# On the Xenology of Comets and Other Primitive Reservoirs in the Solar System

A thesis submitted to The University of Manchester for a PhD in the faculty of Science and Engineering

**2021**

**Thomas Peter Lawton**

**Department of Earth and Environmental Sciences**

**Contents** Page

Total Word Count: 68709

**Figures** Page

**Figures cont.** Page

**Figures cont.** Page

**Tables** Page

**Equations** Page

**Appendices** Page

**Abstract**

University of Manchester
Thomas Peter Lawton
Doctor of Philosophy (PhD)
On the Xenology of Comets and Other Primitive Reservoirs in the Solar System

The composition of xenon contained within planetary materials can elucidate the conditions within which they were formed and the environments in which they have resided since formation. This work focused on extracting and interpreting xenon isotopic compositions from primitive materials with the development of new methodologies for measuring cometary xenon from 81P/Wild 2, measurement of xenon in primitive volcanic glasses from the lunar interior, and development of modelling software which is used to explore the role of cometary xenon from 67P/Churyumov-Gerasimenko in the delivery of volatiles to the terrestrial planets. The unique combination and development of protocol for Closed-System Stepped Etching (CSSE) with the Refrigerator Enhanced Laser Analyser for Xenon (RELAX) is described, as is a summary of problematic phenomena which may be encountered in its implementation. A noble gas modelling platform, Automaton, is designed, validated, and explained in this work. Automaton can extract the probability and nature of mixtures of xenon components in any given composition, featuring any combination of fractionation before or after mixture. Automaton is employed in determining the role of comet 67P/Churyumov-Gerasimenko in the evolution of the atmospheres of Earth and Mars, and U-Xe. Pristine lunar volcanic glasses are candidates for retaining an indigenous lunar noble gas composition. Individual xenon isotopic compositions of volcanic glasses from Apollo 15 and 17 are reported in this work. Their possible retention of an indigenous lunar noble gas composition and their historical residence on the Moon since crystallisation are discussed. The procedural development and a preliminary analogue experiment for measuring the xenon contained within discrete phases of material collected from comet 81P/Wild 2 by Stardust is described in this work. Results indicate that separately extracted xenon components can be measured by a combination of CSSE and RELAX, so ground truth cometary xenon measurements are possible.

## Declaration

No portion of the work referred to in the thesis has been submitted in support of an application for another degree or qualification of this or any other university or other institute of learning.

## Copyright Statement

**Acknowledgements**

This thesis is dedicated to everyone who has persisted with me through the monumental journey I have been on over the past few years. To even have imagined I would come out of the other end of this would have been impossible at times, were it not for your support. You should be as proud in your contribution to this work as I am, even if you don't understand any of it (as most of you insist).

This would not exist were it not for the generosity of people willing to lend their time and ears to me at the darkest times. Dark times brightened by my family and closest friends, to whom I owe the greatest debt.

Jamie, your patience and generosity cannot be overstated, you have made a more significant impact on my life than you could imagine. Sarah, Vera, your help and support has been invaluable over the past few years. Katie, Mike, your time and empathy convinced me that my life could be changed for the better. To all the staff at the university who have helped in any way, thank you for your patience, it is greatly appreciated.

To everyone reading this, if you are struggling, then seek help in family, friends, and professionals. It may seem like you are alone, but you are not. My life was transformed by reaching out, and yours can be too.

This thesis is also partially dedicated to coffee, and the high school teacher who advised that I was not smart enough to study mathematics and physics A-levels.

I must also thank the Science and Technology Facilities Council, STFC, for funding this research, and all of the training, travel, etc., which made it possible.

Finally, I would like to thank the examiners for their help in thoroughly polishing multiple iterations of this thesis.

## The Author

1992
Stockport
Birth

2008 – 2010
Tytherington Sixth Form College
A-Levels: Mathematics, Physics, Chemistry, Biology

2010 – 2014
University of Manchester, School of Earth, Atmospheric, and Environmental Sciences
MEarthSci Geology with Planetary Science - 2:1
Thesis: Aluminium-26 Distribution Modelling in Protoplanetary Disks

2016 – 2021
University of Manchester, School of Earth and Environmental Sciences
STFC PhD Studentship

# 1. Introduction

## 1.1. Noble gas cosmochemistry

Noble gas cosmochemistry is an invaluable tool for understanding the origin, evolution, and current state of the Solar System. All noble gases are barely chemically reactive (Grochala, 2007; Lodders et al., 2009), limiting the possible mechanisms with which they can be contained or transported, relative to non-noble elements. This property limits the number of processes which can modify compositions, and results in noble gas components recording different historical profiles than their reactive cousins. Noble gases are highly volatile and require extremely low temperatures or high pressures to condense (Owen and Bar-Nun, 1995; Lodders, 2003), hence noble *gases*. Noble gases are abundant in the galaxy (Lodders et al., 2009), helium in our Solar System is the second most abundant element in the Sun, Saturn, Jupiter, Uranus, and Neptune. Apart from those locations, the environments required to collect and retain noble gases are not common in the Solar System. Despite this, most Solar System solids contain noble gases; although the volatility and incompatibility of the noble gases is reflected in their low concentrations in Solar System materials (such as the lunar volcanic glasses of this work which contain $1 \times 10^{-10}$ cm$^3$ STP g$^{-1}$ < $7 \times 10^{-10}$ cm$^3$ STP g$^{-1}$ of $^{132}$Xe).

This low abundance is reflected in the increasing sensitivity of noble gas mass spectrometry, where pioneering ground-based instruments capable of detecting ~ $0.5 \times 10^6$ Xe atoms (or $1.9 \times 10^{-14}$ cm$^3$ STP) (Reynolds, 1956) have now been replaced by modern instruments with detection limits of ~ 950 Xe atoms (or $3.5 \times 10^{-17}$ cm$^3$ STP) (Crowther et al., 2008), and spacecraft instruments capable of measuring noble gas compositions of extraterrestrial bodies such as planets (Conrad et al., 2016) and comets (Marty et al., 2017) in situ. The low chemical abundance of noble gases is compounded by the relative

depletion of low abundance isotopes, for example, the Rosetta spacecraft's ROSINA instrument could not resolve any $^{124\text{-}126}$Xe (Marty et al., 2017). While this scarcity clearly presents an issue with regards to detection, requiring highly sensitive instruments, it also means that secondary contributions are more pronounced. For example, solar wind ion implantation and galactic cosmic ray spallation can change the isotopic and elemental composition of materials they are incident upon, lower initial abundances mean this contribution is proportionally larger relative to typical non-noble abundances (Ott, 2014). Similarly, blank and isobaric interference signals, what is essentially 'noise', become more pronounced with decreased sample signal.

The Sun contains the majority of matter in the Solar System and dominates the overall elemental and isotopic signature of noble gases, however, noble gases in Solar System materials regularly deviate from this composition. Solar wind implantation, galactic cosmic ray spallation, and radioactive decay of parent isotopes (e.g., $^{40}$K, $^{129}$I) constitute the significant externally-derived modifiers of original noble gas components. These processes belong to a suite of in situ modifications of trapped noble gases which leave diagnostic elemental and isotopic composition 'fingerprints', which may dominate some materials. For example, young lunar regolith can be used as a proxy for solar noble gas compositions, along with in situ results from NASA's Genesis mission (Benkert et al., 1993; Pepin et al., 1995; Crowther and Gilmour, 2013; Meshik et al., 2014). Analyses of noble gases contained in Solar System materials, specifically meteorites, find numerous familiar isotopic and elemental signatures repeated in related hosts. These characteristic compositions are typically referred to as 'components', which often correspond to related origins and hosts.

These trapped or 'planetary' components constitute an alphabet of discrete phases and origins for each noble gas. For example, the ubiquitous carbonaceous chondrite

component ‘Q’ which may be of solar descent (Lewis et al., 1975; Ott et al., 1981; Gilmour, 2010), and the potentially supernova-derived ‘HL’ contained in pre-solar materials (Lewis et al. 1987). These components may be ‘exotic’, not processed by our Solar System, or ‘local’, ultimately derived from the solar composition, although the exact identities and origins of some components and their chemical hosts remain in contention (Reynolds and Turner, 1964; Huss and Alexander, 1987; Ozima et al., 1998; Crowther and Gilmour, 2013). It is worth noting that ‘planetary’ components do not necessarily correspond to actual planetary noble gas reservoirs. The evidence for the origin of these trapped components is contained in their isotopic and elemental abundances; enrichments and depletions in particular isotopes and elements arise from specific nucleosynthetic and/or fractionational processes, signatures of the environments in which they were emplaced in their host.

Discerning the elemental or isotopic composition of noble gases in a sample can provide a wealth of information. Cosmic ray exposure ages can be determined from excesses in specific noble gas isotopes produced by their interaction with matter, the origins of materials can be determined by relating the isotopic features of contained components to signatures of known formational processes, reservoirs of noble gases can be traced back to specific sources, formational and alteration ages can be determined with numerous isotope decay systematics, and there are more applications based on relative elemental abundances.

### 1.2. Fractionation

Fractionation processes are mechanisms which separate, or 'sort', a reservoir of material according to a specific characteristic. The fractionation processes which affect noble gases are typically related to mass (leading to isotopic fractionations) or first ionisation potential (leading to elemental fractionations) (Bernatowicz and Fahey, 1986; Bodmer and Bochsler, 1998, 2000; Gloeckler and Geiss, 2000; Marrocchi and Marty, 2013); for example, slow solar winds feature isotopic depletions in heavy isotopes of He, Ne, and Ar suggesting a mass-dependent fractionation (Heber et al., 2012). In general, Solar System materials become more dominated by in situ components with increasing petrological order, as the primordial 'trapped' components are lost or contaminated, either physically or through an increasing in situ proportion (essentially overprinting the original signature). As an extreme example, the most planetary component-rich materials for xenon are the primitive carbonaceous chondrites, which features mostly Q-Xe xenon in concentrations of $2 \times 10^{-8}$ $cm^3$ STP $g^{-1}$ (or 0.1 ppb), a figure which also makes them the most noble gas-rich solids in the Solar System (Marti, 1967; Mazor et al., 1970; Ott, 2014). Whereas young lunar regoliths, after subjection to multiple episodes of physical and chemical processing over the history of the Solar System, are almost entirely composed of implanted solar wind, and any planetary component is diluted until practically absent (Pepin et al., 1995).

Thermal and aqueous processing are known to ease the diffusion of noble gases in materials (a fact exploited by thermal diffusion being an established noble gas extraction technique), but the means by which the noble gases are initially trapped in their host phases is sometimes unclear. There are three major processes by which noble gases can be trapped inside host materials, with the dominant trapping process being component or host specific (Wieler and Franchi, 2006; Ott, 2014). These processes are adsorption, radioactive decay

of parent isotopes, and ion implantation. As an example, noble gas components in presolar grains are understood to be mostly (or entirely) trapped by ion implantation from noble gases contained in stellar winds (Wieler and Franchi, 2006), and an $^{129}$Xe abundance may represent the trapped decay product of its unstable parent isotope $^{129}$I; whereas Q-Xe has been proposed as physically adsorbed (Wacker, 1989), buried (Hohenberg et al., 2002), and implanted (Matsuda et al., 2010).

Atmospheric loss to interplanetary space, predominantly by hydrodynamic escape, causes planetary atmospheres to become depleted in low mass elements and isotopes contained in the upper atmosphere (Hunten, 1973). In this process, high fluxes of ultraviolet radiation heat the planetary atmosphere and heavier gases are liberated as a result of energetic hydrogen escaping (Hunten et al., 1987), gases are liberated as a function of their mass, such that heavier isotopes of particular elements are preferentially retained. A similar, yet less significant process by which gases can be sputtered from the upper atmosphere by solar wind interaction causes a similar phenomenon (Chassefière and Leblanc, 2004).

### 1.3. Xenology

Reynolds (1963) proposed ‘Xenology’ as the detailed study of Xe isotopic abundances in meteorites towards a better understanding of the history of meteorites and the Solar System. As with the other noble gases, xenon features helpfully low abundances in Solar System material, so deviations are particularly pronounced. Xenon, along with the other heavy noble gases, also features particularly low fluences in the solar wind relative to the light noble gases (Meshik et al., 2014), thus reducing the ‘overprinting’ phenomenon in materials exposed to solar wind. However, the power of xenology lies in xenon’s nine stable isotopes, which can be traced to distinct nucleosynthetic (s-, r- and p-processes)

(Burbidge et al., 1957; Reynolds, 1963; Arnould and Goriely, 2003; Gilmour and Turner, 2007), radiogenic and cosmogenic origins (Table 1.1).

***Table 1.1*** *Stable xenon isotopes and their production in various nuclear processes.*

| Process | Parent | $^{124}$Xe | $^{126}$Xe | $^{128}$Xe | $^{129}$Xe | $^{130}$Xe | $^{131}$Xe | $^{132}$Xe | $^{134}$Xe | $^{136}$Xe |
|---|---|---|---|---|---|---|---|---|---|---|
| Nucleosynthetic processes | p-process | ✓ | ✓ | | | | | | | |
| | s-process | | | ✓ | ✓ | ✓ | ✓ | ✓ | | |
| | r-process | | | | ✓ | | ✓ | ✓ | ✓ | ✓ |
| $\beta^-$ decay | $^{129}$I | | | | ✓ | | | | | |
| | $^{130}$Te | | | | | ✓ | | | | |
| $2\beta^+$ decay | $^{132}$Ba | | | | | | | ✓ | | |
| Spontaneous Fission | $^{238}$U | | | | ✓ | | ✓ | ✓ | ✓ | ✓ |
| | $^{244}$Pu | | | | ✓ | | ✓ | ✓ | ✓ | ✓ |
| Neutron Irradiation* | $^{128}$I | | | ✓ | ✓** | | | | | |
| | $^{130}$Ba | | | | | | ✓ | | | |
| | $^{130}$Te | | | | | | ✓ | | | |
| | $^{235}$U | | | | | | ✓ | ✓ | ✓ | ✓ |
| Spallation | Ba | ✓ | ✓ | ✓ | ✓ | ✓ | ✓ | ✓ | ✓ | |
| | REE | ✓ | ✓ | ✓ | ✓ | ✓ | ✓ | ✓ | | |

**Neutron irradiation production of these isotopes may be artificially or naturally derived, requiring a high neutron flux. ** for $^{128}I + {}^{1}n \rightarrow {}^{129}Xe$, indicates the relatively minor production relative to $^{128}Xe$.*

Nucleosynthesis refers to a collection of processes attributed to extreme environments outside those of our Solar System in which nuclear processes produce xenon isotopes of three specific profiles (Reynolds, 1963). The processes are referred to as r-, s-, and p- (Burbidge et al., 1957; Arnould and Goriely, 2003).

The r-process, or rapid neutron capture process involves the rapid addition of neutrons to a nucleus and produces neutron-rich nuclei. This incorporation of additional

neutrons into increasingly unstable nuclei must be fast enough to overcome their tendency to decay for heavier isotopes to be produced. This process is unique to environments of extremely high neutron flux, although the exact site of the r-process is unknown. Supernovae cores which eject r-process nuclides, magnetic jets from collapsing massive stars (over seven solar masses), and neutron star or black hole collisions have been proposed, along with less energetic scenarios within less massive stars, yet modelling of the process in those environments cannot recreate observations (Hillebrandt, 1978; Mathews and Cowan, 1990; Cowan et al., 1991). The r-process produces the heaviest xenon isotopes (shown in Table 1.1) (Burbidge et al., 1957; Reynolds, 1963).

The s-process, or slow neutron capture process is the gradual addition of neutrons into a nucleus which is either stable and accumulates additional neutrons until instability causes $\beta^-$ decay, or is unstable and $\beta^-$ occurs (Burbidge et al., 1957). This process requires a less extreme flux of neutrons and a longer time (to allow for $\beta^-$ decay) compared to the r-process, and is probably located in the cores of massive stars (over around 15 solar masses) which ejects the material in strong winds (Lamb et al., 1977; Truran and Iben, 1977), and the helium burning shell in AGB (Asymptotic Giant Branch) stars (Burbidge et al., 1957; Schwarzschild and Härm, 1967). The s-process produces xenon isotopes of intermediate masses $^{128\text{-}132}$Xe (Reynolds, 1963).

The p-process, or rapid proton capture process is the production of neutron deficient nuclei by the addition of protons and subsequent $\beta^+$ decay (Arnould and Goriely, 2003). Similar to the r-process, the p-process requires a large proton flux and high temperature to overcome the large coulomb barrier associated with adding positively charged particles to a proton-saturated nucleus. This process produces the lightest xenon isotopes of $^{124}$Xe and $^{126}$Xe, and is most likely produced in massive stars (over ten solar

masses) on their evolution towards Type II supernovae (SNII) (Arnould and Goriely, 2003).

The conditions required for nucleosynthesis of all noble gas isotopes (apart from $^{3}$He and $^{4}$He which are both produced in the Sun) do not naturally exist inside our Solar System. They can be produced artificially by man-made nuclear reactions, but are otherwise only produced in conditions which exist outside of our Solar System. This means any deviations from the initial compositions of noble gases and their isotopes (apart from $^{3}$He and $^{4}$He) when the Solar System was formed are due to processes other than nucleosynthesis.

Radiogenic contributors lead to excesses in particular isotopes; for example, excesses in $^{129}$Xe can be attributed to the decay of the extinct radioactive nuclide $^{129}$I (Reynolds, 1960), and decays of unstable $^{244}$Pu and $^{238}$U, which produce characteristic heavy isotope excesses (Swindle, 2002). The iodine-xenon decay chronometer is of particular importance in xenology, $^{129}$I was the first (Reynolds, 1960; Reynolds and Turner, 1964), extinct radionuclide discovered in cosmochemistry (Swindle, 2002). $^{129}$I was present in the Solar System during planetary accretion but is now extinct due to its short half-life (~ 16.1 Ma). However, in minerals containing this ancient iodine, radiogenic $^{129}$Xe is retained at the site of the extinct $^{129}$I, thus the present excess $^{129}$Xe/I ratio represents the $^{129}$I/$^{127}$I ratio when the material became closed to xenon loss (Jeffery and Reynolds, 1961; Swindle, 2002; Gilmour et al., 2006). Artificial neutron irradiation of these materials produces $^{128}$Xe from $^{127}$I by $^{127}$I (n,$\beta^{-}$)$^{128}$Xe, allowing the measurement of $^{129}$Xe/$^{128}$Xe to essentially represent $^{129}$Xe/$^{127}$I after a number of corrections (Jeffery and Reynolds, 1961; Swindle, 2002; Gilmour et al., 2006). Absolute ages derived from other chronometers are then combined with this method to provide references for xenon closure ages of materials containing excess iodine over the first ~ 100 Ma of the Solar System

(Gilmour et al., 2009). Artificial neutron irradiation also provides a means of indirectly measuring a number of parent isotopes of different elements through their artificial neutron irradiation-derived, xenon-producing, unstable daughters. Natural irradiation by galactic cosmic rays can also be quantified through its production of excesses in low mass isotopes of xenon, provided the host material is rich in target elements such as barium and rare Earth elements, quantifying the excesses derived from this source allows cosmic ray exposure ages to be resolved (Hohenberg et al., 1978).

$^{129}$I, $^{244}$Pu and $^{238}$U feature more nuclear particles than the heaviest, stable nucleus of $^{209}$Bi, therefore they can only be produced by the rapid neutron capture process of nucleosynthesis. Discovering significant excesses of xenon isotopes produced by the decay of parent isotopes which originate from specific nucleosynthetic processes can therefore provide the basis of identification of materials from these nucleosynthetic environments, or materials containing them. For example, the component Xe-HL features enrichments in heavy (H) r-process ($^{134}$Xe and $^{136}$Xe) and light (L) p-process ($^{124}$Xe and $^{126}$Xe) xenon isotopes, which most likely correspond to a supernova origin (Reynolds and Turner, 1964; Heymann and Dziczkaniec, 1979; Lewis et al., 1987). Silicon carbide grains and diamonds featuring isotopic anomalies resembling solar and Xe-HL are therefore likely to have interacted with these presolar environments (Lewis et al., 1987; Huss and Lewis, 1994; Gilmour et al., 2005, 2016).

### 1.3.1. Xenon in our Solar System

While all xenon is ultimately derived from nucleosynthesis, radioactive decays and nuclear interactions, its composition within reservoirs of the Solar System is often a complex modified mixture of many sources. The Solar System can be considered a

closed-system with regards to nucleosynthesis, and many extinct radioactive sources. It is often more convenient to redefine Solar System xenon reservoirs in their current context.

As is the case for 99.9% of all matter in the Solar System, the overwhelming majority of xenon in our Solar System is contained in the sun, a reservoir which best matches the protosolar nebula from which the Solar System formed. Xenon trapped in Solar System solids and atmospheres may be directly related to this inferred initial composition (provided they are of 'local' origin) through simple mass fractionations (Jupiter and young lunar regoliths, for example) (Pepin et al., 1995; Mahaffy et al., 2000; Crowther and Gilmour, 2013), although many require more complex models featuring additions from other sources (Marti and Mathew, 1998; Wieler, 2002; Gilmour, 2010; Caracausi et al., 2016; Marty et al., 2016). For example, Q-Xe, the component which tends to dominate the primitive meteorite budget of all the heavy noble gases (Ott, 2014), has an isotopic composition which may be derived from solar Xe with the addition of $^{129}$I decay and excesses of presolar Xe-HL (Gilmour, 2010). Another example is the atmospheres of Earth and Mars, with their strongly fractionated isotopic signature of xenon relative to solar abundances (Pepin, 1991; Harper and Jacobsen, 1996; Marti and Mathew, 1998; Caracausi et al., 2016; Marty et al., 2016).

### 1.3.2. The Sun

When discussing noble gases of local origin, cosmochemists often refer to deviations from solar abundances. The Sun is assumed to represent the solar nebula composition from which most Solar System matter is derived. However, determining this composition has not been straightforward. Spectrometric measurements using absorption lines from the photosphere are capable of resolving the presence of noble gases, the famous example being helium, which was discovered by this technique. Spectrometric

measurements struggle with relative elemental and isotopic abundances, which are inferred from other element signals (Asplund et al., 2009). The uppermost couple of metres of lunar regolith contain abundant implanted solar wind noble gases (Bogard et al., 1973; Pepin et al., 1995), which provided the basis of our understanding of solar noble gas abundances for some time (Burnett et al., 2003). However, the lunar regolith has been 'gardened' (or mixed) by meteorite bombardment for billions of years, so the 'antiquity', or age of trapping, of the implanted solar wind in a regolith grain (which could be < 4 Ga) is not easily determined, with an additional complication being the evolving elemental abundance of the solar wind with time (Bogard et al., 1973; Pepin et al., 1995; Wieler et al., 1996; Wieler, 2002; Burnett et al., 2003). Results from the Genesis mission, which returned samples of targets exposed to the solar wind at Earth's L1 Lagrangian point (outside the influence of Earth's magnetosphere) (Burnett et al., 2003), now provide the basis of our understanding of the composition of heavy noble gases in the sun and their solar wind flux (Vogel et al., 2011; Crowther and Gilmour, 2013; Meshik et al., 2014).

The solar wind exerts elemental isotopic fractionations on He, Ne, and Ar from ionisation and acceleration in the solar atmosphere which distinguish it from the true solar composition for those elements (Heber et al., 2012), as does the fact that the solar wind is more representative of the outer convective zone than the bulk sun (Heber et al., 2009); however, the outer convective zone has largely preserved the original isotopic composition of the solar nebula (Turcotte and Wimmer-Schweingruber, 2002). Figure 1.1 shows that the solar wind xenon compositions from Genesis and the lunar regolith generally resemble one another (Pepin et al., 1995; Meshik et al., 2014), although lunar estimates of krypton feature a mass fractionation favouring the heavier, more deeply implanted isotopes (due to more shallowly implanted light isotopes being lost to surficial erosion and diffusion) (Meshik et al., 2014). The solar wind composition as measured by the Genesis mission is the most complete representation of the composition of the xenon isotopic composition of

the Sun, and subsequently the solar nebula which preceded it (Vogel et al., 2011; Heber et al., 2012; Crowther and Gilmour, 2013; Meshik et al., 2014).

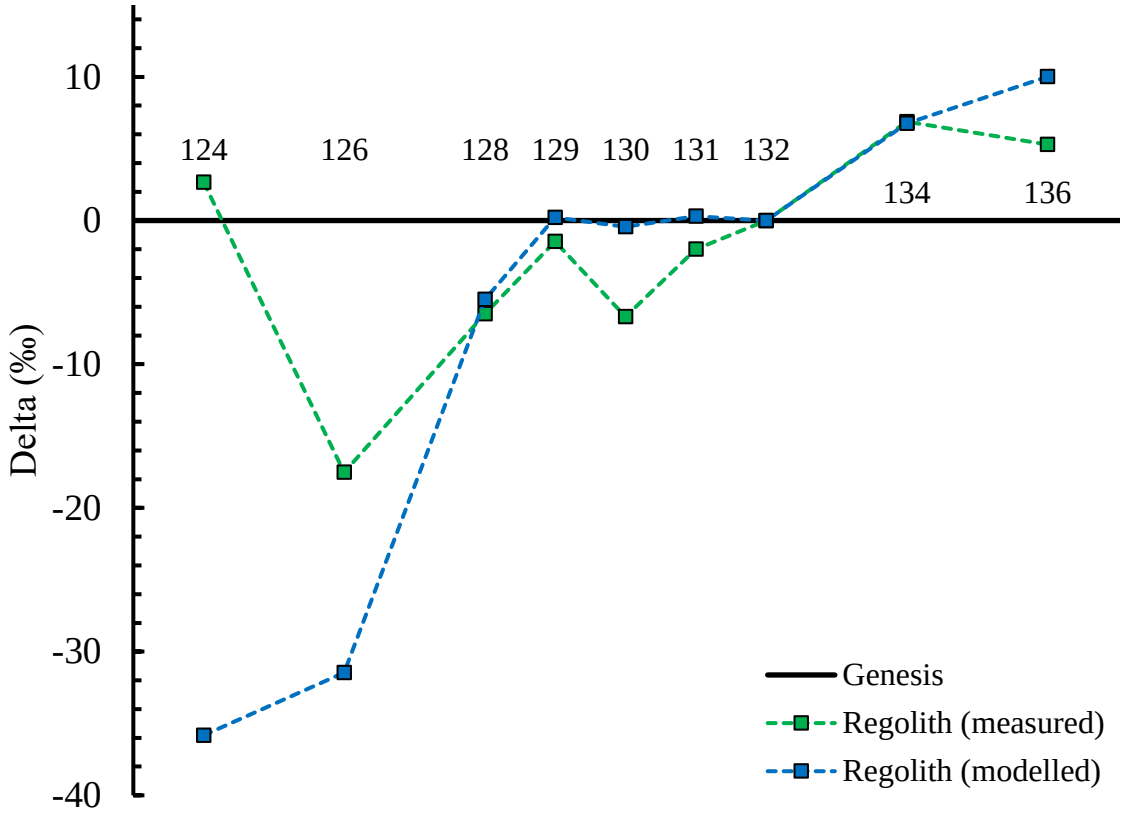


***Figure 1.1*** *Permille (delta) deviations of the 9 stable xenon isotopes of solar xenon as measured (green squares and dashed line) and modelled (blue squares and dashed line) compositions of young lunar regolith, compared to solar wind xenon as measured by Genesis (black line ≡ 0). Both regolith-derived solar xenon values are taken from Pepin et al. (1995), solar composition derived from Genesis is taken from Meshik et al. (2014).*

Ion implantation of solar wind noble gases into lunar regolith and the resulting fractionation provides an excellent case study into the complexities of mass fractionation and the nature of hosting noble gases in materials. Prior to the direct measurement of the solar wind with the Genesis mission, there were apparently two separate noble gas components in materials exposed to the stream of particles ejected from the sun, solar energetic particles (SEP) and solar wind (SW). SEP appeared to feature enrichments in the heavier isotopes of all noble gases and resided deeper in materials compared to the lighter isotope enriched SW nearer to the surface. These compositions were assumed to represent two distinct reservoirs of noble gases within the Sun. Their existence was justified by a

mixing line observed between the two noble gas compositions when analysing gas extracted from increasing sample depth (as in Figure 1 of Etique et al., 1981). Additionally, the lack of SW and presence of the SEP compositions in samples with damaged or lost surface material corroborated their discrete existence. The samples collected by the Genesis mission found these components to be two separate measurements of solar wind fractionated by depth, with heavier isotopes more enriched deeper into samples due to their increased mass resulting in deeper implantation (Grimberg et al., 2006).

### 1.3.3. "Q"

The heavy noble gas inventory of the primitive carbonaceous chondrite class of meteorites is dominated by 'Q', a noble gas reservoir for which the respective origin, trapping mechanism and host chemistry remains unclear (Lewis et al., 1975; Wieler et al., 1992; Busemann et al., 2000). Q-gases comprise ~ 95% of the total trapped $^{132}$Xe budget of the highly primitive meteorite, 'Orgueil', with comparably high proportions in other primitive meteorites (Huss et al., 1996; Ott, 2014). As with all trapped noble gas components, Q-gases become decreasingly prevalent in meteorites of higher metamorphic grade (Matsuda et al., 1980; Huss et al., 1996). Despite its ubiquity, the host phase of Q-gas remains enigmatic beyond an operational definition (Lewis et al., 1975), and convincing evidence that it is organic (Ott et al., 1981). Q-gas is defined as the gas released by the application of nitric acid to the residue of primitive meteorites treated with hydrofluoric and hydrochloric acid (Lewis et al., 1975).

Attempts to deduce the Q host by simulating diagnostic trapping environments have led to a number of suggestions (summarised in Ott (2014)); the preferred theory from these investigations is physical adsorption on the interior surfaces of a pore labyrinth in amorphous carbon (Wacker, 1989; Ott, 2014), although the burying of anomalously

adsorbed low energy noble gases in the growing host phase (Hohenberg et al., 2002), a 'plasma model' of ion implantation into now-amorphised presolar diamonds (Matsuda and Yoshida, 2001; Matsuda et al., 2010), and the simultaneous trapping of noble gases and formation of organic matter in the ionised region of the protoplanetary disk (Kuga et al., 2017). The isotopic composition of Q-Xe helps provide some constraints on the nature of the trapping mechanisms and host composition of phase Q, such as the 'plasma model' favouring recreations of observed Q-Xe mass fractionations by ion implantation experiments (Bernatowicz and Fahey, 1986; Koscheev et al., 2001), and the suggestions of more conventional mixture modelling analyses (Ozima et al., 1998; Gilmour, 2010). Amari et al. (2013) conducted an electron microscopy and noble gas investigation into colloidal separations of phase Q-rich HF-HCL residue of the Saratov meteorite (L4), finding individual noble gas atoms are associated with only a minor component of the porous carbon, suggesting either a structural rearrangement leading to trapping of noble gas atoms in existing carbon phases, or a distinct nanometre scale minor carbon phase which could not be resolved.

The isotopic signatures of Q-Kr and Q-Xe suggest a mass-dependent fractionation from a gas of solar wind composition, with an additional contribution of $^{129}$Xe from $^{129}$I decay in the case of Q-Xe (Ozima et al., 1998; Crowther and Gilmour, 2013; Meshik et al., 2014), as illustrated in Figure 1.2. However, an alternate possibility where Q-Xe represents the true solar composition is possible with the addition of a couple of percent of Xe-HL and $^{129}$Xe (potentially through retrapping of mobilised components) (Gilmour, 2010; Crowther and Gilmour, 2013; Meshik et al., 2014). Despite these models, the origin and host of Q remains unknown in xenology and the entire field of noble gas cosmochemistry.

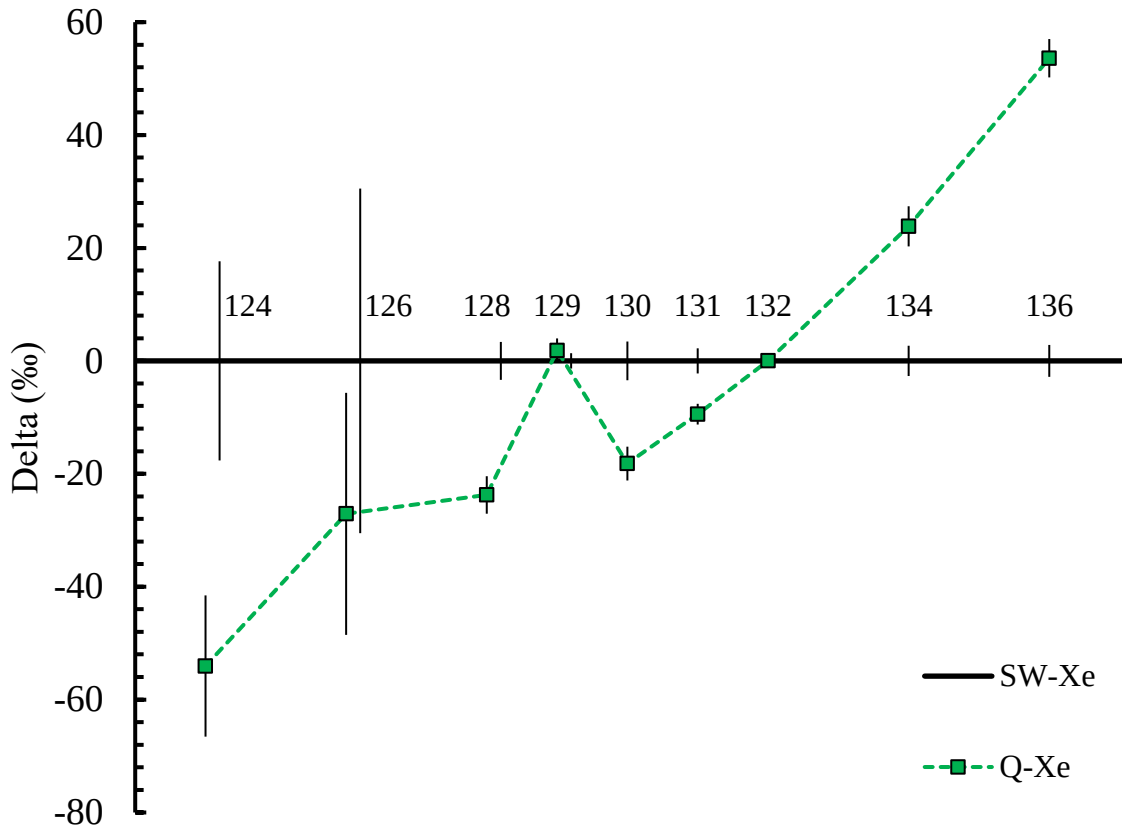


***Figure 1.2*** *Permille (delta) deviations of the 9 stable xenon isotopes in component Q-Xe of Busemann et al. (2000), from solar wind (SW-Xe) of Pepin et al. (1995). SW-Xe normalised to ≡ 0. Errors show one standard deviation.*

### 1.3.4. Earth and Mars

Direct determination of the bulk noble gas inventory of the terrestrial planets is impossible due to their inaccessible interiors (Pepin, 1991; Pepin and Porcelli, 2002; Porcelli and Ballentine, 2002; Wieler, 2002). The noble gas inventories of their atmospheres are often used as proxies for their noble gas content, and are mostly presumed to represent the degassed noble gas composition of the bulk planet (Pepin, 1991; Pepin and Porcelli, 2002; Porcelli and Ballentine, 2002). Xenon and the other heavy noble gases in planetary atmospheres are assumed to more closely match the degassed planetary interior due to their mass making them more resistant to hydrodynamic escape from atmospheres than lighter gases (Hunten, 1973; Hunten et al., 1987; Pepin, 1991; Porcelli and Ballentine, 2002; Chassefière and Leblanc, 2004).

Earth is depleted in volatiles relative to the parental solar nebula, and xenon is particularly depleted in Earth's atmosphere relative to expected abundances inferred from concentrations of solar argon and krypton (Anders and Owen, 1977; Pepin and Porcelli, 2002). This 'missing Xe' of the Earth's primordial gas budget has been proposed as being up to 90% (Ozima and Podosek, 1999). Relative to solar abundances, Earth's atmospheric xenon is fractionated in favour of the heavy isotopes, enriched in $^{129}Xe/^{132}Xe$, and deficient in its two heaviest isotopes ($^{134}Xe/^{132}Xe$ and $^{136}Xe/^{132}Xe$), Figure 1.3 shows its composition relative to solar wind xenon. This is unlike any known meteoritic component, or indeed any Solar System components, apart from the Martian atmosphere which it shares a fractionated isotopic composition and enrichment in $^{129}Xe/^{132}Xe$ relative to solar xenon (Takaoka, 1972; Porcelli and Ballentine, 2002; Conrad et al., 2016). Retracing hypothetical mass fractionations by ancient atmospheric loss are unable to satisfactorily trace it back to a known solar or chondritic composition (Pepin, 1991; Pepin and Porcelli, 2002; Porcelli and Ballentine, 2002). Specifically, the problem is that the precursor of atmospheric Xe features depletions in heavy xenon isotopes ($^{134}Xe/^{132}Xe$, $^{136}Xe/^{132}Xe$) relative to solar and chondritic compositions, depletions which cannot be explained by contributory nuclear processes (Pepin and Porcelli, 2006). These unexplained depletions led to the proposal of a hypothetical 'U-Xe' component, of essentially solar composition with heavy isotope depletions, which represents the original (solar nebula derived) terrestrial xenon signature (Pepin and Phinney, 1982; Pepin, 1991; Pepin and Porcelli, 2006). The Earth's mantle presents another problem; contributions from primordial Xe, fissiogenic Xe from $^{244}Pu$ and $^{238}U$, and atmospheric Xe provide valuable chronometers for processes and systems in the early Earth, but constraining relative proportional contributions to the overall composition is challenging without complex modelling (Pepin and Porcelli, 2002; Caracausi et al., 2016).

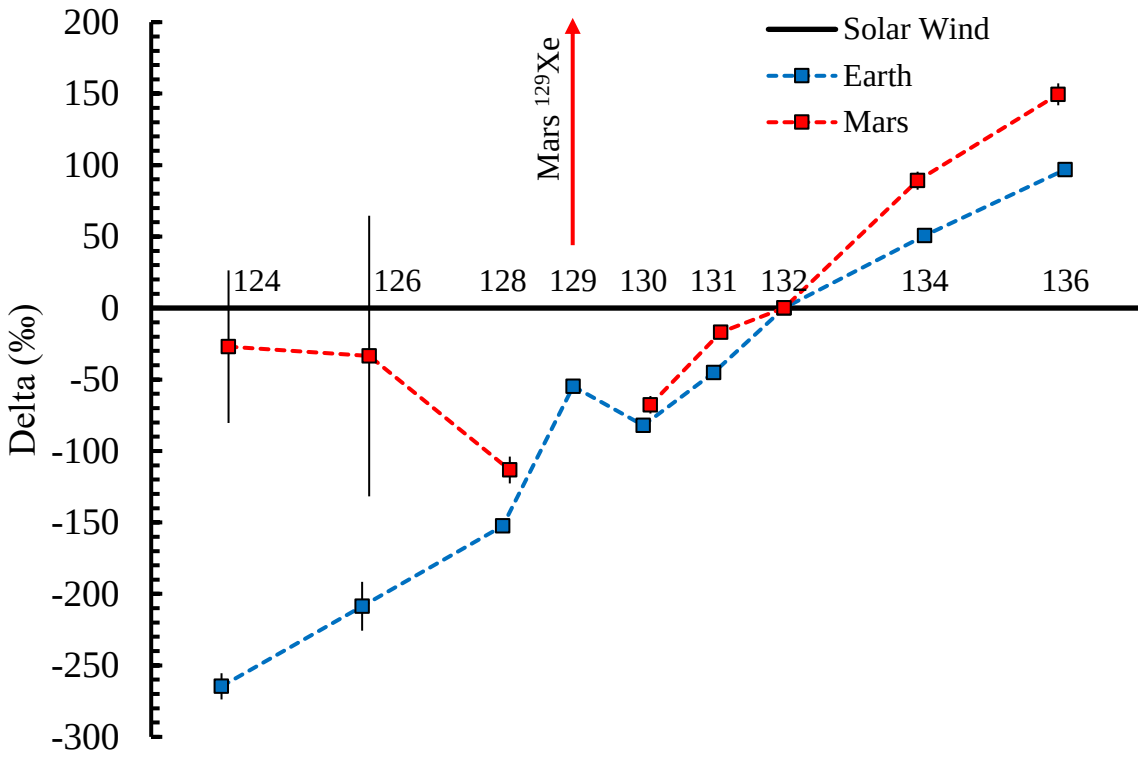


***Figure 1.3*** *Permille (delta) deviations of the 9 stable xenon isotopes measured on Earth (blue squares and dotted line) and Mars (red squares and dotted line) relative to solar wind xenon (black line ≡ 0). Red arrow indicates large excess in delta value of Mars $^{129}$Xe relative to solar wind (‰ = 1400). Earth's atmosphere xenon data from this work, Mars' atmosphere data from Conrad et al. (2016), and solar wind data from Pepin et al. (1995). Errors show one standard deviation.*

The Viking lander provided the first noble gas measurement of the Martian atmosphere from surface measurements, discovering a thin atmosphere with a xenon depletion relative to the other noble gases (as on Earth), and an isotopic composition of nitrogen, argon, and xenon suggesting a different evolutionary history to Earth (Owen and Biemann, 1976; Owen et al., 1976, 1977). This was followed by the discovery of several noble gas compositions within three rare groups of igneous achondrites; the shergottites, nakhlites, and chassignites (the SNC meteorites) were found to contain noble gases of Martian origin (Bogard and Johnson, 1983; Bogard et al., 1984; Ott and Begemann, 1985). There are three distinct noble gas reservoirs trapped within Martian meteorites, corresponding to an ancient Martian atmospheric composition, a more recent composition of the Martian atmosphere, and a Martian interior composition (Bogard et al., 2001; Swindle, 2002). These gases are trapped, sometimes together, in different phases within the

meteorites, and sometimes mixed with cosmogenic gases or terrestrial atmospheric contamination (Schwenzer et al., 2012; Ott et al., 2019).

The Martian interior features a xenon isotopic composition resembling solar wind (Ott, 1988; Mathew and Marti, 2001), apart from some radiogenic contributions from decay of $^{244}$Pu, and elemental ratios of $^{36}$Ar/$^{132}$Xe and $^{84}$Kr/$^{132}$Xe which are fractionated relative to its modern composition and solar wind (Ott, 1988; Mathew and Marti, 2001, 2002). The Martian meteorite ALH84001 contains an ancient (around 4 Ga) trapped xenon composition resembling a fractionated version of the current Martian atmosphere with a lower $^{129}$Xe/$^{132}$Xe than its current value (Murty and Mohapatra, 1997; Gilmour et al., 1998; Mathew and Marti, 2001). Whether this component represents a primordial unfractionated Martian atmosphere complemented by fission xenon from $^{244}$Pu which has since been fractionated and received the remaining $^{129}$Xe from $^{129}$I decay, or other Martian reservoirs altered by weathering, shock incorporation of other components, and mixture with Martian soil is unclear (Drake et al., 1994; Treiman, 1998; Gilmour et al., 1999; Swindle et al., 2000; Mathew and Marti, 2002).

The more recent Martian atmospheric composition present in meteorites is defined by its similarity to the Martian atmosphere as measured in situ by spacecraft and landers. Since measurement by the Viking landers (Owen and Biemann, 1976), the composition of the Martian atmosphere has been measured in situ by the Mars Science Laboratory's Sample Analysis at Mars (SAM) mission (Mahaffy et al., 2012), and the Neutral Gas and Ion Mass Spectrometer (NGIMS) on the Mars Atmosphere and Volatile Evolution Mission (MAVEN) (Mahaffy et al., 2015). The modern Martian atmosphere is significantly thinner than Earth's atmosphere and differs in its heavy isotopic enrichment of nitrogen and deuterium , and heavy noble gas abundances two orders of magnitude lower than Earth's atmosphere (Anders and Owen, 1977; Owen et al., 1977; Bogard et al., 2001; Wong et al.,

2013). Xenon in both atmospheres is fractionated in favour of the heavy isotopes relative to the composition of solar wind (Anders and Owen, 1977; Bogard et al., 2001; Conrad et al., 2016). The enrichments in heavy species and heavy isotopes of xenon form the basis of models in which fractionations occurred due to atmospheric loss, mostly by hydrodynamic escape, and to a lesser extent solar wind interactions on Mars (Hunten, 1973; McElroy et al., 1977; Hunten et al., 1987; Bogard et al., 2001; Chassefière and Leblanc, 2004; Jakosky et al., 2018).

These mass fractionations somewhat contradict the relative elemental and isotopic abundances of the noble gases of the Martian atmosphere exhibiting a similarity with those of Earth, where models for fractionation require different mechanisms which satisfy the significantly reduced relative atmospheric escape (Anders and Owen, 1977; Pepin, 1991; Bogard et al., 2001; Chassefière and Leblanc, 2004; Dauphas and Morbidelli, 2013; Marty et al., 2016). Comparisons between Martian atmospheric evolution and Earth's atmospheric evolution must also satisfy the $^{129}Xe/^{132}Xe$ excess in the Martian atmosphere relative to Earth. Whereas Earth's excess $^{129}Xe$ can be attributed to the decay of now extinct $^{129}I$ and $^{244}Pu$ radionuclides, as corroborated by complimentary excesses of the heavier isotope decay products, Mars only features a disproportionate excess of $^{129}Xe$, presumably from the decay of $^{129}I$. The missing products of fission yet not $^{129}I$ decay in the Martian atmosphere imply degassing of $^{129}Xe$ occurred without the degassing of the products of $^{244}Pu$ and $^{238}U$ fission (Pepin, 2000; Marty and Marti, 2002; Mathew and Marti, 2002), possibly by selective sequestration of fission products within Mars, or a heterogeneous distribution of the short-lived radionuclides amongst the terrestrial planets.

The consensus of cosmochemical analyses and simulations suggest that the terrestrial planets gained their volatile inventory by contributions from highly enriched objects, after initially forming as volatile depleted bodies (Pepin and Porcelli, 2002;

Raymond et al., 2004; Marty, 2012; Albarede et al., 2013; Barnes et al., 2016; Marty et al., 2016). These highly enriched objects may have been primitive asteroids (potentially resembling carbonaceous chondrites), or comets (Owen et al., 1992; Conrad et al., 2016; Marty et al., 2017) or some mixture of both (Anders and Owen, 1977; Owen and Bar-Nun, 1995; Marty and Dauphas, 2002; Albarede et al., 2013; Barnes et al., 2016; Caracausi et al., 2016; Marty et al., 2016). However, tracing the true identity and source of these volatile-rich bodies is complicated by billions of years of planetary processing since enrichment, and a poor understanding of the nature of volatiles on small bodies, particularly the nature of cometary noble gases (Anders and Owen, 1977; Marty and Dauphas, 2002; Marty et al., 2016), which have only recently been measured (Balsiger et al., 2015; Marty et al., 2016, 2017). The answer may lie in the relationship between the elemental and isotopic signatures of the terrestrial planets, and their potential sources of enrichment (Anders and Owen, 1977; Pepin, 1991; Mandt et al., 2015; Caracausi et al., 2016; Marty et al., 2016).

### 1.3.5. The Moon

Understanding the noble gases contained in the Moon would help enormously in our understanding of the volatile evolution of the Earth-Moon system and other terrestrial planets. Geophysical and geochemical data and modelling suggest the Moon's formation resulted from the impact of Theia (Halliday, 2000), a differentiated planetary embryo similar in mass to Mars, and the already differentiated proto-Earth (Hartmann and Davis 1975; Cameron 1997; Canup and Asphaug 2001; Canup 2004, 2012; Reufer et al. 2012). This formation event may have occurred between 50-120 My after Solar System formation (Touboul et al., 2007; Borg et al., 2011; Bottke et al., 2015; Thiemens et al., 2019). The relationship between the volatile inventories of the Earth-Moon system to the timing and

nature of the formation event, and its implications for the volatiles on both bodies is not well constrained.

Constraining the Moon's noble gas inventory could help us elucidate the timing and nature of the volatile evolution of the Earth-Moon system, or expose a primitive noble gas reservoir (e.g. U-Xe or a fissiogenic composition from $^{244}$Pu) preserved by the relatively geologically inactive Moon (Pepin, 1991). Dynamic recycling of Earth's crust makes finding materials containing these primitive noble gases difficult, yet the moon is a one plate planet that has remained mostly inactive since formation, so may be more likely to contain primitive materials. This model is complicated by the fact the lunar sample inventory is mostly composed of materials from the lunar surface, which is subject to processes which have replaced or altered most primitive materials.

The main process changing the lunar surface is "gardening" resulting from massive impacts which have pulverised, ejected, buried, and heated materials on the lunar surface in a decreasing flux since the first billion years after Solar System formation (Tera et al., 1974; Gomes et al., 2005; Fernandes et al., 2013). Smaller impacts still occur to this day with a lower frequency. Since the initial peak impactor flux at ~ 1 Ga after formation gardening has been dominated by micrometeorite bombardment, although their impacts have been heating, shocking, and burying materials on the lunar surface since its formation. The solar and galactic particle flux is similarly ever-present, constantly interacting with the materials on and near the lunar surface, producing cosmogenic noble gases and implanting solar wind. These factors have combined to overprint or degas an ancient internally-derived lunar noble gas composition in all materials analysed up to now, replacing it with mostly solar wind xenon (to the extent where it once defined the solar wind composition) and cosmogenic products of spallation (Pepin et al., 1995; Heber, 2002; Wieler, 2002; Füri et al., 2015, 2018). Noble gases indigenous to the Moon's interior or

transient atmosphere have not been constrained beyond excesses in fission products of xenon and argon (Xe: Reynolds et al. 1974; Bernatowicz et al. 1978; Swindle et al. 1985; Ar: Fernandes et al. 2004; Fernandes and Burgess 2005).

Materials produced in the lunar interior may still preserve trapped noble gases from the environments they formed in, assuming their subsequent residence on the lunar surface is sufficiently shielded from particle flux and processing. Until we can recover samples directly from the lunar interior, research must focus on untangling a composition from the best preserved and most primitive lunar materials collected by the lunar missions. Many pristine volcanic glasses sample lunar mantle melts and remain in their whole vitrified form since quenching after their eruption in fire fountaining (Delano and Livi, 1981; Delano, 1986; Shearer and Papike, 1993; Elkins et al., 2000). These glasses are the best candidates for retaining noble gases from their source region in the lunar interior and potentially a volatile-rich transient lunar atmosphere they were erupted into and quenched within.

### 1.4. Comets

The following explanation of our current understanding of comets is provided to give context to the investigations in Chapters 3 and 5. Comets are small bodies of rock and ice (on the order of tens of metres up to ~ 100 km) which are understood to be some of the most primitive bodies in the Solar System, containing mixtures of volatile ices, refractory interstellar dust and early solar/planetary nebula material, and organic compounds (Weidenschilling, 1997; Brownlee et al., 2006; Mckeegan et al., 2006; Sandford et al., 2006; Simon et al., 2008; Altwegg et al., 2016). The significance of the variety, nature and preservation of materials contained in comets cannot be understated; studying them has significantly changed our views on a range of processes in the early Solar System (Jewitt,

2004; Huebner, 2008; Brownlee, 2014; Guilbert-Lepoutre et al., 2015), potentially provided a source for the origins of life (Elsila et al., 2009; Altwegg et al., 2016), and shed light on the volatile budget of the inner Solar System (Sill and Wilkening, 1978; Owen et al., 1992; Owen and Bar-Nun, 1995; Owen, 2008; Mandt et al., 2015; Barnes et al., 2016; Caracausi et al., 2016; Marty et al., 2016).

Comets are thought to be composed of a central core of fractal aggregates coated in a layered pile of distorted, post-accretionary material in a nucleus featuring interconnected macroscopic voids and microscopically porous networks which serve as conduits for sublimated volatiles and entrained dust particles which are liberated during the comet's 'active' phase (Weissman, 1986; Weidenschilling, 1997; Belton et al., 2007; Dones et al., 2015). The active phase of a comet is dominated by extensive thermal processing by solar radiation upon passage through the inner Solar System, sublimating volatiles of progressively higher condensation temperatures as a function of stellar proximity (Huebner, 2006). Upon sublimation these gases entrain dust particles with an efficiency linked to gas speed and flux, and the mass to cross sectional area ratio of the dust grains (Huebner, 2008). The weak gravitational attraction of the small cometary nuclei mean the liberated dust and gas is weakly bound to the nucleus, hence it expands outwards to form a coma and tail, features which define an active comet (Cochran et al., 2015). An active comet is undoubtedly spectacular and interesting, but the preceding 'storage' phase and formation is the reason studying comets is particularly important for understanding the evolution of the Solar System in a cosmochemical context.

The storage phase of a comet is defined by its residence in the near-pristine cryogenic environment of the outer Solar System, where temperatures are usually low enough ($10\ K < T < 70\ K$) for most cometary volatiles (typically $H_2O$, CO, $CO_2$, $CH_3OH$, and most noble gases) to remain condensed, and impacts are rare and gentle relative to the

congested inner Solar System (Bar-nun and Kleinfeld, 1989; Lodders, 2003; Dones et al., 2004; Gibb et al., 2004; A'Hearn et al., 2012; Balsiger et al., 2015; Guilbert-Lepoutre et al., 2015). Thermal and physical processing may not be unprecedented during storage (Stern and Shull, 1988; Stern, 2003), but it is rare enough for comets in storage to avoid chemical alteration and heating to comprise some of the most pristine samples of primitive Solar System and presolar material available (Stern, 2003; Schlebusch et al., 2010; Guilbert-Lepoutre et al., 2015); early observations of enrichments in highly volatile elements (H, N, and O) relative to CI chondrites suggested this (Altwegg et al., 1999), later discoveries of minimal thermal and aqueous alteration of cometary dust containing refractory calcium-aluminium-rich silicates, chondrules and silicon carbide grains confirmed it (Tsou et al., 2004; Zolensky et al., 2006; Simon et al., 2008; Brownlee, 2014; Paquette et al., 2016).

Prior to the Rosetta mission, the view of how material assembled to form comets was an uncertain topic with significantly different competing theories, each with major implications for constraining the timing and ingredients of their formation. Weissman (1986) saw a rubble pile of primordial protosolar nebula condensates, similar to the icy-conglomerate 'dirty snowball' theory of Whipple (1950), and the Belton et al. (2007) 'talps' model of gentle interpenetrated fractal aggregates. These data-starved speculations prompted the need for dedicated missions to trans-neptunian objects (Guilbert-Lepoutre et al., 2015). Explaining the residence of highly refractory inner Solar System solids which appear to have resisted the inward gravitational collapse of the protoplanetary disk is similarly troublesome (Huebner, 2008). Their presence may be the result of turbulent mixing of the protoplanetary disk (Bockelée-Morvan et al., 2002; Ciesla, 2007), or a model-derived 'X-wind' which selectively delivered them to the outer Solar System (Shu et al., 1996; Simon et al., 2008).

A heavily generalised ‘typical’ evolution of a comet involves the formation and accretion of its (cometisimal or particulate) constituents during the earliest stages of Solar System formation, followed by a giant planet-induced orbital evolution to the relatively pristine reservoirs of the outer Solar System in which most comets currently reside, and finally the chance of some form of gravitational perturbation leading to the comet entering the inner Solar System, a catastrophic development which ultimately ends in complete volatile loss or collision with a larger body (see Guilbert-Lepoutre et al. (2015), Stern (2003), and Balsiger et al. (2008) for a more comprehensive overview). However, one must be careful when using terms such as ‘typical’ with regards to comets, as the picture of their formation and orbital/chemical evolution becomes increasingly diverse as our understanding increases (A’Hearn et al., 1995; Tsou et al., 2004; 2008; Huebner, 2008; Guilbert-Lepoutre et al., 2015).

Completing the story of where these comets originally came from (or whether they formed in situ) and what they consist of requires the retracing of the earliest history of the Solar System up to planetary formation and migration, an incomplete story in itself (Dones et al., 2004; Charnoz and Morbidelli, 2007; Desch, 2007; Walsh et al., 2011); a summary of our current theories regarding cometary origins is provided when discussing specific populations in more detail (in Section 1.4.1). One of the few constants of cometary science is the identification of their present reservoirs in the inner and outer Solar System, where they share defining orbital characteristics (Levison, 1996). Typically, outer Solar System comets are contained in two main reservoirs; the Oort cloud and the trans-neptunian region, with the latter encompassing the Kuiper belt and the Scattered disk (Guilbert-Lepoutre et al., 2015). The shared orbital parameters of comets in these reservoirs provide the best current means of classification due to a potential common origin (Levison, 1996), but the variety of compositions and overlaps in each family suggest caution when

projecting inferences across classes (Levison, 1996; A'Hearn et al., 2012; Guilbert-Lepoutre et al., 2015).

Huebner (2008) stated "The question whether comets are diverse objects that can be grouped according to their place of origin or whether each comet is intrinsically inhomogeneous, remains unanswered", however, this has not deterred attempts (see Mumma and Charnley (2011) for a review). The task of pigeonholing comets with their varied catalogue of compositional traits in our limited yet diverse data is preliminary at best (Levison, 1996; A'Hearn et al., 2012; Meech et al., 2016). Classification by orbital period ('long-period' - orbital periods exceeding 200 years, 'short-period' under 200 years), has given way to the more refined scheme of Levison (1996) based on Carusi et al. (1987) which uses a perturbation-resilient Tisserand parameter, *T*, as defined in Equation 1.1.

$$T = a_j/a + 2\sqrt{(1-e^2)\,a/a_j}\,\cos(i)$$

***Equation 1.1*** *Definition of Tisserand parameter. $a_j$ is Jupiter's semi-major axis, and a, e, and i, are the comet's semi-major axis, orbital eccentricity, and orbital inclination, respectively.*

The divisions of Levison (1996) into nearly-isotropic (T < 2) and ecliptic (T > 2), groups where orbits form a nearly isotopic swarm around the sun, or orbits are generally near the ecliptic, respectively. Further divisions split the ecliptic comets into three sub-categories, Jupiter family (T < 3), Encke-type ($a < a_j$, and T > 3), and Chiron-type/Centaur comets ($a > a_j$, T > 3) (Levison, 1996). This classification scheme retains some familiar comet groupings of the traditional model, and it also suffers from the same issue of qualitatively constraining a natural continuum of comet properties, but the relative stability of classifications provided by the Levison (1996) taxonomical application of the dynamic Tisserand parameter means that it is more appropriate and more indicative of common source regions, but by no means complete (Levison, 1996; Dones et al., 2015). The two

comets best characterised by sample return or remote missions, 81P/Wild and 67P/Churyumov-Gerasimenko both belong to the Jupiter-family group.

### 1.4.1. Populations and origins

From sungrazers within a couple of solar radii from the sun, to the limits which define the edge of the Solar System, the orbital characteristics of comets mean that they can occupy almost anywhere in the Solar System (albeit not necessarily for long periods of time); however, the compositional nature of comets (amongst other characteristics) suggests that they could not have formed in all of the regions they occupy (or pass through). Minor populations of varying stability are found in the main asteroid belt (Hsieh and Haghighipour, 2016), and as centaur objects (Horner et al., 2004), amongst other regions, although the majority of comets are now contained in the Oort cloud and the trans-neptunian region.

Most comets orbit the sun in a swarm between $0.5 \times 10^5$ AU < $1 \times 10^5$ AU as the principal components of the diffuse Oort cloud (Öpik, 1932; Oort, 1950), an inferred structure beyond the heliopause in interstellar space, where it is understood that long-period and Halley-type comets reside before their deflection into the inner Solar System (Levison, 1996; Dones et al., 2004, 2015). It is estimated that roughly $4 \times 10^{11}$ comets occupy the outer Oort cloud ($a > 2 \times 10^5$), but problems such as detection bias make this figure hard to constrain, a problem reflected in the ~ 2 < 40 Earth masses estimates for total outer Oort cloud mass (Francis, 2005; Charnoz and Morbidelli, 2007; Dones et al., 2015). At such great distances from the sun, Oort cloud comets are vulnerable to slight perturbatory influences which can ultimately lead to their orbital evolution towards active comets in the inner Solar System (Öpik, 1932; Byle, 1983; Dybczyński and Królikowska, 2016). Perturbations within the Oort cloud are usually derived from two main sources,

galactic tides (Byle, 1983), the gravitational influence of matter in the galactic disk relative to the sun, and stellar perturbations (Öpik, 1932), the gravitational influence of passing stars. Galactic tides are thought to be the major perturbatory influence leading to the orbital evolution of Oort cloud comets to perihelia in the planetary region (Delsemme, 1987; Dybczyński and Królikowska, 2016). External stellar perturbations are understood to influence the long term orbital evolution of the Oort cloud to a lesser extent than galactic tides (Öpik, 1932; Oort, 1950; Dybczyński and Królikowska, 2016), but have been identified as a plausible and proven cause of injection into the inner Solar System (Öpik, 1932; Fouchard et al., 2013; Bailer-Jones, 2014; Dybczyński and Królikowska, 2016).

Primitive Solar System materials can be found in the inner Solar System, but cometary residence in the relatively gentle conditions of the outer Solar System makes their contents more likely to be better preserved. The comets of the outer Solar system are likely to have undergone less thermal, aqueous and impact-derived processing than inner Solar System materials. The extent of this processing was explored in modelling and direct observations of comets in the outer Solar System, suggesting low speed collisions ($0.2$ km $s^{-1}$) and thermal processing from exotic sources (Stern and Shull, 1988; Guilbert-Lepoutre et al., 2015). Passing luminous stars and supernovae could bathe around 20% of Oort cloud comets in enough radiation to heat their outer layers (on the scale of tens of metres) to at least 30 K and 45 K, respectively (Stern and Shull, 1988). These processes may mobilise noble gases, thus affecting interpretations of their provenance. Despite their current residence in the outer reaches of the Solar System, it is generally accepted that Oort cloud comets formed at 5 AU < 40 AU from the sun, with most originating from 20 AU < 40 AU (Dones et al., 2004; Guilbert-Lepoutre et al., 2015). The outward migration of the giant planets is understood to have been the mechanism of this ejection to the outer edges of the Solar System; this process provides some constraint on the timing of

the start of cometary formation (Gomes et al., 2005; Morbidelli et al., 2005; Walsh et al., 2011).

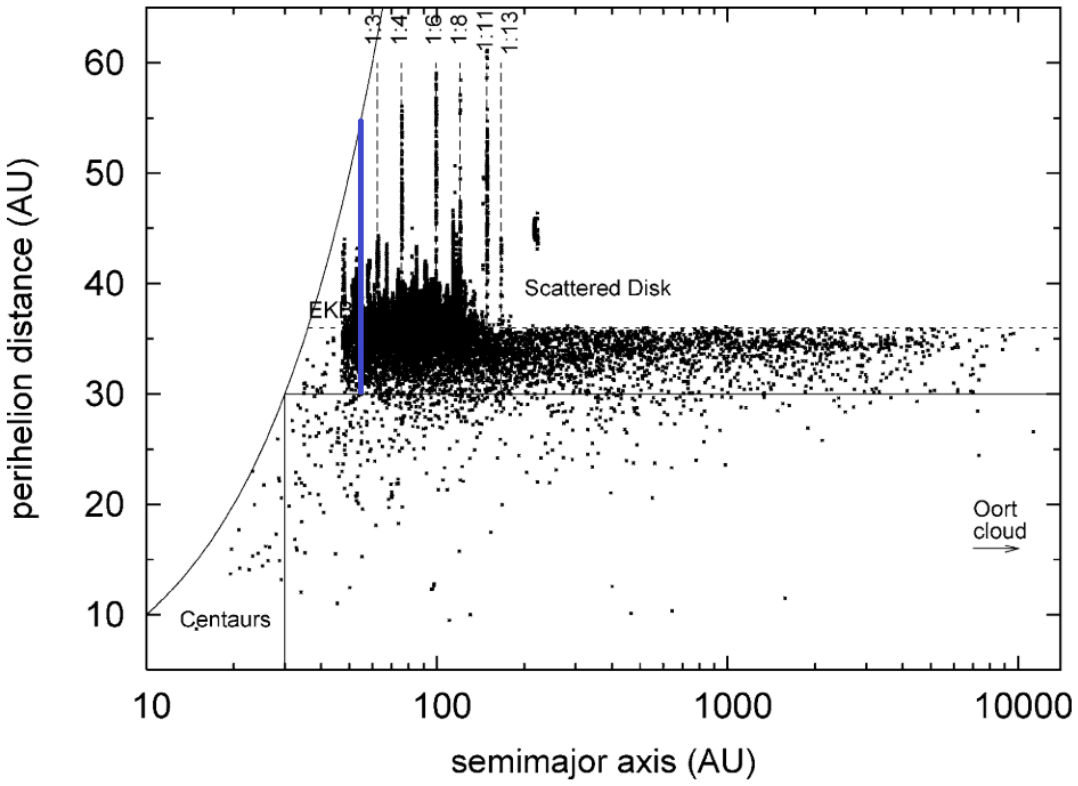


***Figure 1.4*** *Evolving orbital parameters of 475 real and cloned scattered disk objects over 5 Ga. Dots record simulated parameters after 0.25 years up to 5 Ga until ejected to Jupiter family, Oort cloud, interstellar space, or destroyed. Blue line shows Neptune location, ratios indicate orbital resonances. From Fernández et al. (2004).*

The Kuiper Belt lies beyond the orbit of Neptune (at ~ 30 AU < 50 AU from the sun) and appear to have formed either in situ or were dynamically emplaced during the migratory evolution of the giant planets, particularly Neptune (Levison and Morbidelli, 2003; Dones et al., 2004).

The Scattered Disk is a dynamically unstable structure at heliocentric distances of 30 AU < 50 AU (and probably beyond 50 AU) thought to contain around $10^9$ objects with generally higher inclinations ($0.2^o$ < $46.8^o$), and more eccentric orbits than the Kuiper Belt (Figure 1.4) (Duncan and Levison, 1997; Brown, 2001; Gomes et al., 2008; Dones et al., 2015). It is composed of objects which probably formed within the region of 25 AU < semimajor axis < 35 AU, prior to the migratory dynamical evolution of the giant

planets, specifically Neptune, which is understood to have scattered them into their current unstable and erratic configuration (Duncan and Levison, 1997; Dones et al., 2004; Morbidelli et al., 2004; Charnoz and Morbidelli, 2007; Guilbert-Lepoutre et al., 2015). The scattered disk's proximity to Neptune results in a dynamic instability (Figure 1.4) which causes its objects to be sent inwards to be the major source of Jupiter family comets, or outwards to the Oort cloud and interstellar space (Duncan and Levison, 1997; Fernández et al., 2004; Gomes et al., 2008).

The populations of comets and the modelling of their dynamical evolutions suggest the comets formed within our Solar System, mostly within the current orbits of the ice giants. Subsequent scattering and perturbation have placed them in the various populations explained above, or collisional paths with other celestial bodies. Their seemingly chaotic distribution within various stages of the Solar System's evolution, and apparently large overall mass of volatile-enriched, well-preserved contents, makes cometary science crucial to many facets of Solar System formation.

### 1.4.2. Stardust

Stardust was the first mission to retrieve samples from a comet, and also the first to retrieve solid samples from an astronomical body other than the moon (Tsou et al., 2003; Brownlee et al., 2006), comet 81P/Wild 2. The orbit of 81P/Wild 2 was perturbed by a close encounter with Jupiter in 1974 from an initial perihelion of 5 AU and aphelion of 24.7 AU, to post-perturbation figures of 1.5 AU and 5.2 AU respectively (Pozuelos et al., 2014). Given the low number of close passes of the sun since perturbation, the surface of 81P/Wild 2 is thought to have experienced minimal alteration since its formation.

The Stardust spacecraft intercepted the tail of 81P/Wild 2 in 2004, where it deployed sample collection trays containing silica aerogel (3 cm thick), an ultra-low density (5 kg $m^{-3}$ < 50 kg $m^{-3}$, decreasing towards surface), highly porous, slightly transparent solid (Pierre and Pajonk, 2002; Tsou et al., 2003, 2004). Aerogel was chosen as a result of these properties (Tsou et al., 2003), which made decelerating the expected hypervelocity comet particles (~ 6 km $s^{-1}$) produce lower impact shocks (and therefore less thermal processing) relative to previously suggested materials (Tsou, 1990), preserving more of the structural and mineralogical properties of the mostly intact incident particles (Tsou, 1990; Tsou et al., 2003; Brownlee et al., 2006), before the transparency could allow for easy identification and removal (Tsou et al., 2003).

The collected particles, which represent a sample of the non-volatile material in the interior of the comet 81P/Wild 2, were ejected from freshly exposed material on the comet nucleus which had lost its original surface to sublimation upon recent deflection towards the inner Solar System (Tsou et al., 2003; Brownlee et al., 2006). The Stardust samples provide the basis of our understanding of the refractory dust composition of comets, previously limited to remote sensing and interplanetary dust particles. Results from the Rosetta mission continue to build upon the advances in cometary science provided by Stardust samples, but in general, its in situ nucleus analyses are intended to answer different questions to the Earth-based characterisation of refractory dust offered by Stardust.

The discovery of refractory crystalline silicates in 81P/Wild 2 (Brownlee et al., 2006; Simon et al., 2008) provides the strongest evidence for large scale radial transport of materials in the early Solar System (Simon et al., 2008; Wooden, 2008; Brownlee, 2014). This is because the refractory crystalline silicates are formed in the hot inner region of the protoplanetary disk, whereas the comet formed in the cold outer Solar System. The fact

that CAIs and a number of chondrules were both accreted into 81P/Wild 2 suggests that its accretionary formation coincided with the chondrule formation periods in the early Solar System (~ 1.5 Ma after CAI crystallisation) (Cochran et al., 2015).

81P/Wild 2 also contains crystalline silicates featuring a comprehensive range of Fe compositions (mostly ~ 0% < 50%, and some near 100%) (Wooden, 2008), yet no evidence of their aqueous alteration in the form of accompanying phyllosilicates (despite their susceptibility to aqueous alteration) (Wogelius and Walther, 1992; Zolensky et al., 2006, 2008). Evidence of aqueous alteration the form of nickel-, copper-, and zinc-bearing iron sulphides in 81P/Wild 2 is present, but only in trace amounts (Hanner and Zolensky, 2010; Berger et al., 2011). This is in contrast to equivalently primitive material-rich meteorites, which often feature significant evidence of thermal and aqueous alteration (Brownlee, 2014). The primitive nature of the samples collect by Stardust from 81P/Wild 2 and their lack of thermal and aqueous alteration means they constitute some of the most pristine collections of early Solar System material available on Earth (Zolensky, et al. 2006; 2008).

The volatile ices in which these refractory solids are embedded are likely to be equally as well preserved and primitive, and thus preserve the volatile composition of the area of the early solar nebula in which 81P/Wild 2 formed. Noble gases trapped in these materials could preserve the signature of reservoirs and processes which were present in these early stages of the Solar System, possibly without the thermal and aqueous resetting of meteoritic equivalents, or the radiation and spallation damage and overprinting exhibited by interplanetary dust particles (IDPs) (Guilbert-Lepoutre et al. 2008; Scott and Krot 2005; Wooden 2008). Considering the importance of cometary enrichment in many models of terrestrial atmosphere formation, and the potential to constrain ancient reservoirs of xenon, determination of 81P/Wild 2 xenon (81P-Xe) would be invaluable. A key question is

whether these compositions resemble or differ from those measured in the coma of comet 67P/Churyumov-Gerasimenko (returning isotopic data for $^{128\text{-}136}$Xe) (Marty et al., 2017).

### 1.4.3. General composition

In the years preceding spacecraft missions to comets, spectral analyses of their volatile-derived coma and tails were all that was available for determining, or inferring, the composition and structure of the obscured cometary nuclei which released them (Cochran et al., 2015); more recently, spacecraft have sought to study comet tails comae and surfaces in situ or with sample return (Reinhard, 1986; Tsou et al., 2004; Altwegg et al., 2015). An active comet's coma and tail give indirect insight into the comet's chemical and physical properties (Gudipati et al., 2015). However, tails and comae are often composed of fragmented chemical products of the true cometary nuclei particles, and are selectively released by chemical and physical processes which are poorly constrained (A'Hearn et al., 2012; Cochran et al., 2015; Guilbert-Lepoutre et al., 2015). The rates and composition of the ejected material comprising cometary tails and comae could be controlled by structural inhomogeneities and thermal processing of the nucleus (Huebner and Benkhoff, 1997, 1999; De Sanctis et al., 2010; A'Hearn et al., 2012). Such features are also reliant on a small sample of the cometary population. The flow of results from the first cometary nucleus-focussed mission, Rosetta, continue to elucidate our understanding of cometary composition, despite the unplanned Philae landing (Altwegg et al., 2017). While refractory materials contained in comets pose interesting questions of our models of protoplanetary disk evolution, their abundant volatile content and its role in terrestrial planet formation is the focus of this work.

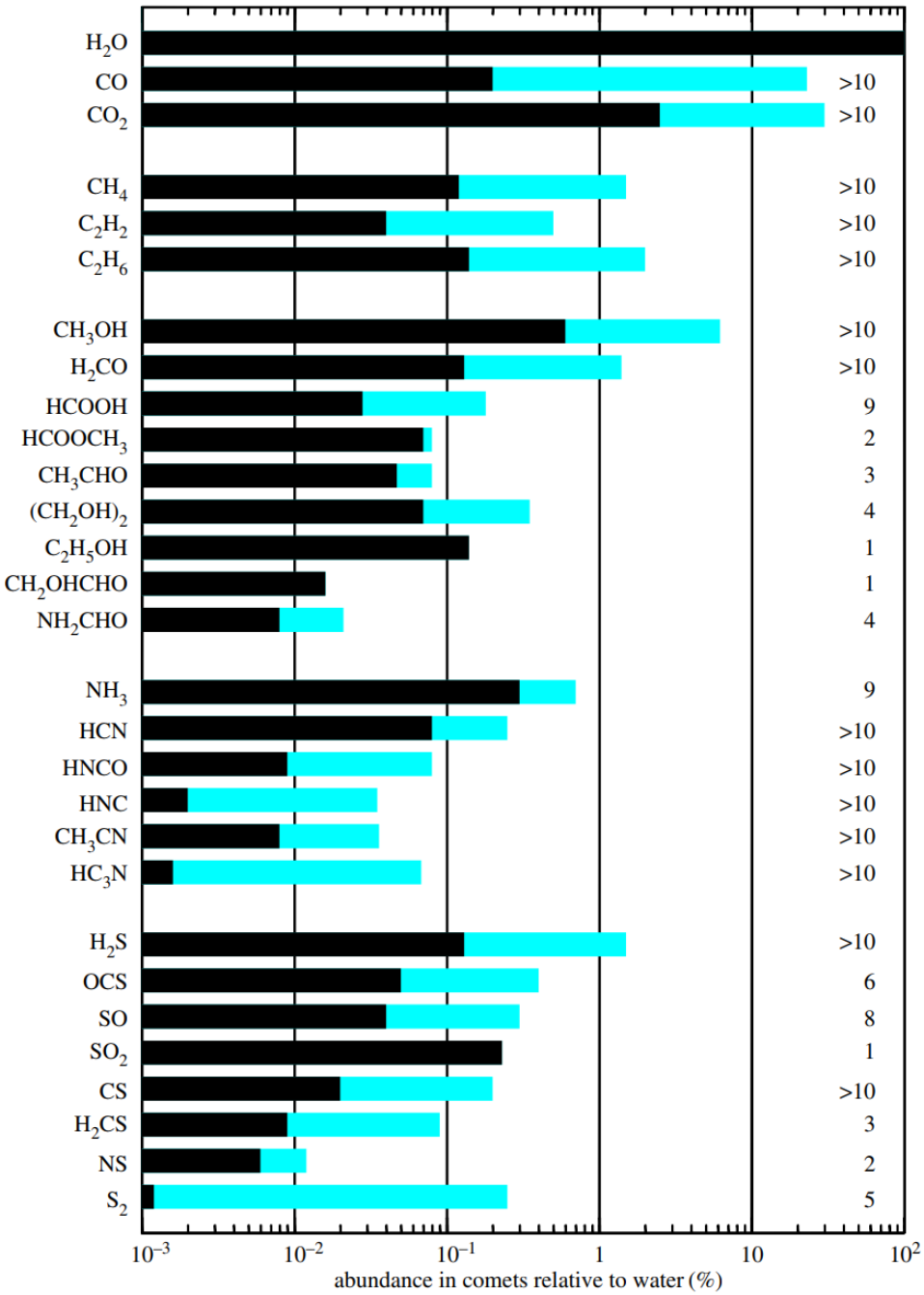


***Figure 1.5*** *Molecules detected in comets from spectroscopy (leftmost column) and their abundances relative to water ($H_2O \equiv 10^2\%$). Horizontal black bars terminate at lowest observed relative abundance, blue bars highlight range of observed abundances up to highest observation. Numbers of comets from which measurements of specific abundances were taken is shown on right. Chart includes measurements up to 2015. From Bockelée-Morvan and Biver (2017).*

The discovery of the volatile-rich nature of most comets, along with their inner Solar System excursions, has led to proposals of comets as a mechanism for the enrichment of the originally depleted volatile inventory of the inner planets (Sill and Wilkening, 1978; Caracausi et al., 2016; Marty et al., 2016), and the seeding of Earth with

volatile prebiotic building blocks (Owen et al., 1992; Owen and Bar-Nun, 1995; Owen, 2008; Altwegg et al., 2016). A diverse suite of familiar volatiles ($H_2O$, CO, $CO_2$, etc.), and other complex comet-specific volatiles ($H_2CS$, $HCOOCH_3$, etc.) have been identified in numerous cometary comae and nuclei (Figure 1.5). Relative abundances of common volatiles vary by orders of magnitude between comets, with no apparent population correlations with existing classifications (Crovisier, 2007; Mumma and Charnley, 2011; A'Hearn et al., 2012).

Water constitutes the largest volatile fraction of most comets (A'Hearn et al., 2012), but how it resides in cometary nuclei is not fully understood (Huebner, 2008). Laboratory experiments based on the expected temperatures, chemical species, and observed processes of cometary nuclei volatiles provide strong arguments for the presence of water in the form of amorphous ice and hydrate clathrates (Delsemme and Swings, 1952; Blake et al., 1991; Huebner, 2008; Gudipati et al., 2015), but no direct observations of either in comets exist. The potential presence of water in amorphous ices or hydrate clathrates has implications for cometary formation, structure, and also the nature of the residence of noble gases (for which relevant trapping mechanisms have been proposed (Sill and Wilkening, 1978; Bar-Nun et al., 1987), but not proven). Crystalline water ice has been found on the surface of comet 67P/Churyumov-Gerasimenko, but its presence is thought to be the result of near-surface processes and may not indicate the structure of ice at depth (Filacchione et al., 2016).

The difficulties of direct nuclei measurements have restricted our understanding of noble gas residence in comet nuclei to spectroscopy and comae measurements. Spectroscopy detected Argon in the comae of comets 67P/Churyumov-Gerasimenko and Hale-Bopp (Stern et al., 2000; Balsiger et al., 2015). A number of interplanetary dust particles of possible cometary origin contain trapped noble gas components (Busemann et

al., 2010; R. L. Palma et al., 2013). Samples returned from the Stardust mission contain an implanted noble gas component of coma origin, as well as noble gases trapped in refractory particles (Marty et al., 2008; Palma et al., 2009, 2012; Mohapatra et al., 2011, 2013; 2013).

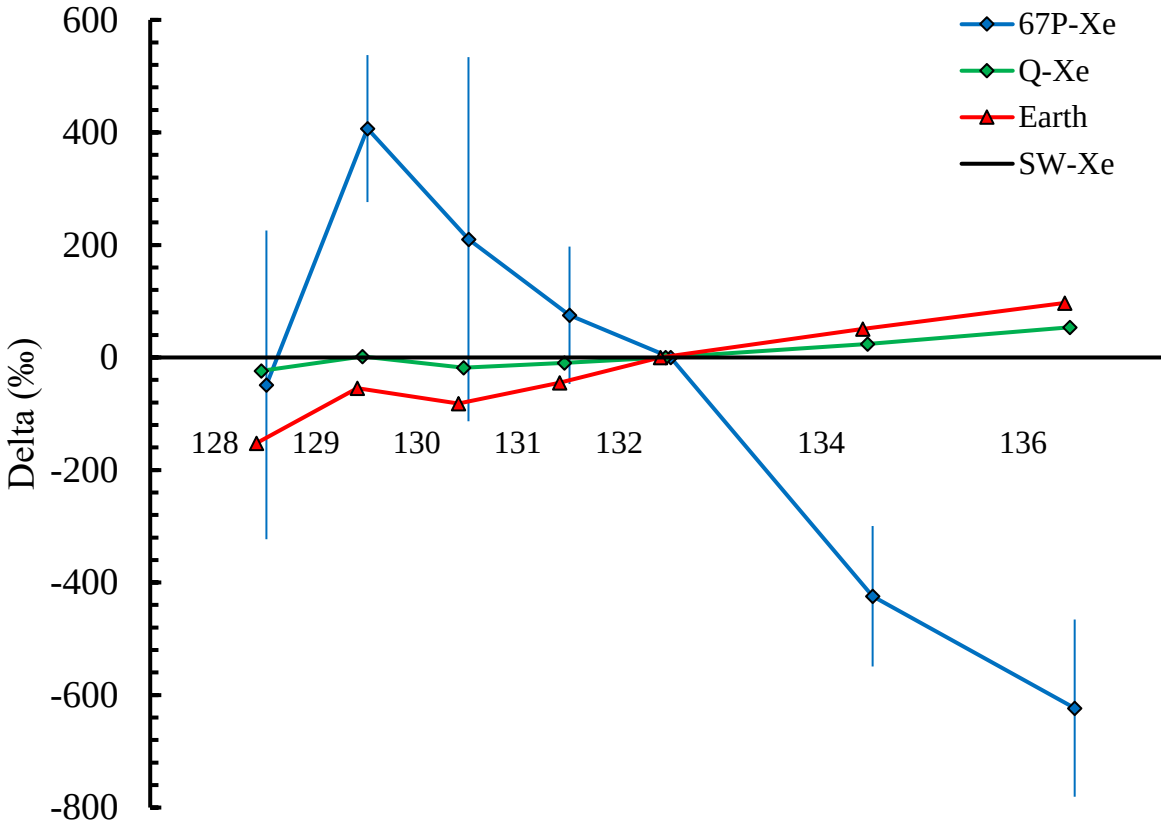


***Figure 1.6*** *Delta plot of various xenon isotopic compositions relative to solar wind. Compositions normalised to $^{i}Xe/^{132}Xe$ and SW-Xe ≡ 0. Errors correspond to one standard deviation. 67P-Xe data (blue line/diamonds) from Marty et al. (2017). Q-Xe data (green line/diamonds) from Busemann et al. (2000). Earth data (red line/triangles) as measured in this work. SW-Xe data (horizontal black line) from Meshik et al. (2014).*

Rosetta's ROSINA mass spectrometer provides the best current example of the noble gas composition in comets. Data were collected for argon, krypton, and $^{128\text{-}136}$Xe (Figure 1.6) during a series of low-altitude (7 km < 10 km) orbits within the coma of the comet 67P/Churyumov-Gerasimenko (Marty et al., 2017; Rubin et al., 2018). These measurements found that xenon was significantly depleted in $^{134}$Xe and $^{136}$Xe, and enriched in most of the lighter isotopes $^{129\text{-}131}$Xe, relative to solar, except for $^{128}$Xe. The origin and implications of this composition is explored in detail in Chapter 3.

The extremely low temperatures required to retain noble gases in the comet nucleus also aide the preservation of pre-accretionary refractory grains in a relatively unaltered state. Wild 2 samples appear to show no signs of aqueous alteration (Brownlee et al., 2006), unlike most meteorites which have undergone some degree of thermal or aqueous alteration (Guilbert-Lepoutre et al. 2008; Scott and Krot 2005; Wooden 2008). Our understanding of the composition of refractory cometary dust is currently dominated by the returned samples of the Stardust mission. Results from Stardust confirmed the presence of a suite of high-temperature inner Solar System minerals, and a lack of amorphous silicates and presolar materials (potentially due to the nature of sample collection) (Brownlee et al., 2006; Zolensky et al., 2006; Roskosz et al., 2008; Simon et al., 2008; Floss et al., 2013). The Rosetta spacecraft's gas and particle instrument suite also suggested the presence of material resembling calcium-aluminium-rich inclusions on 67P/Churyumov-Gerasimenko (Paquette et al., 2016), material which is suspected to be the first solids to condense in the Solar System (Connelly et al., 2012).

Apart from the remotely sensed, or physically collected, refractory grains which can be directly attributed to specific comets, there are other, passive means of studying refractory comet dust in the form of interplanetary dust particles and Antarctic micrometeorites. Cometary dust tails can extend multiple astronomical units, and comets frequently cross Earth's orbital path as near-earth objects (Francis, 2005), so Earth is continually showered in cometary material (Messenger, 2002). Interplanetary dust particles (< 100 μm in diameter) and Antarctic micrometeorites (100 μm < 200 μm) collected from the stratosphere and Antarctic circle respectively, are potential fragments of comets (Brownlee, 1985; Engrand and Maurette, 1998; Maurette et al., 2000; Imae, 2013). For example, the collection of interplanetary dust particles which coincided with the close passage of comet 26P/Grigg-Skjellerup feature particularly pristine assemblages and exotic isotopic signatures, suggesting a cometary origin (Messenger, 2002; Busemann et al.,

2009). Cometary interplanetary dust particles have been shown to feature particularly primitive materials such as presolar grains and disordered carbon, as well as familiar rock-forming minerals, such as olivine and pyroxene, featuring highly variable compositional ranges (Ishii et al., 2008; Zolensky et al., 2008; Busemann et al., 2009). Some interplanetary dust particles feature presolar and disordered organic compositions containing more primitive assemblages than 81P/Wild, whose samples are more dominated by inner Solar System materials (Ishii et al., 2008; Busemann et al., 2009). Such observations add weight to the argument that materials contained in comets represent a continuum, so any addition to our catalogue of cometary data is incredibly important for resolving compositional homogeneity. For the volatiles such as xenon, compositional ranges expressed in comets are of particular importance given their potential roles in terrestrial atmosphere formation (Owen and Bar-Nun, 1995; Owen, 2008; Marty, 2012; Marty et al., 2017).

### 1.5. Aims, objectives, and structure

The aims of the work contained in this thesis are as follows:

- *Understand the relationships amongst current and primordial xenon isotopic compositions of volatile reservoirs in the Solar System.*
- *Discover and constrain primordial xenon from the lunar interior.*
- *Work towards a better understanding of cometary xenon and its role in contribution to the volatile reservoirs of the terrestrial planets.*
- *Measure the composition of cometary xenon as contained within 81P/Wild 2 samples.*

The research described in this thesis works towards the aims by attempting to achieve the following objectives:

- *Develop a spectral decomposition modelling platform for relative abundance signatures of xenon isotopes.*
- *Conduct the most precise measurements of xenon contained within erupted lunar volcanic glasses to date.*
- *Develop a novel methodology for analysing xenon in cometary samples from 81P/Wild 2 on Earth.*

Chapter 6 contains a summary of whether each chapter successfully achieved the previously outlined aims and objectives, and a summary of future work related to their outcome.

The multidisciplinary foci of the research topics covered in each chapter mean they require additional background information outside the scope of the introduction preceding this section, this background information is presented as a brief introduction at the start of each chapter. Similarly specific methodologies are contained within their respective chapters, for instruments or techniques not used in the other sections of the thesis. Each chapter then contains the results, discussions, and conclusions of the research contained within them. The following sections are included to guide the reader to the contents of Chapters 2, 3, 4, and 5, by describing the tasks which were fulfilled within each chapter.

### 1.5.1. Instrumentation

Chapter 2 provides an introduction to the common instruments and techniques used and developed in this thesis, and some of the problems which may be encountered in their implementation. The tasks fulfilled within the contents of Chapter 2 are as follows:

- *Describe the Refrigerator Enhanced Laser Analyser for Xenon (RELAX) mass spectrometer.*

  Explain the process by which xenon isotopic information is extracted from samples using RELAX in comparison to other mass spectrometers, and why it is useful for this work.

- *Describe the Closed-System Stepped Etching (CSSE) apparatus.*

  The design and functionality of CSSE with RELAX is explained and protocols for their use together are developed and described.

- *Develop and describe the data reduction protocols for use of RELAX and CSSE.*

  The extraction of useful data from sample etching is developed and described by a summary of the various procedures which are conducted alongside etching.

- *Explore the problems which may be encountered during sample analysis contained in this work.*

  The potential for unwanted features which may detract from the precision of results are explained physically and mathematically. Proposals for physical and mathematical mitigation are then presented.

### 1.5.2. Modelling mixture of Solar System reservoirs

Chapter 3 presents, tests, and employs Automaton, a new modelling platform for determining the mixtures and fractionations of end members which constitute xenon isotopic compositions. Prior to this work, there was no modelling platform using xenon isotopic ratios for the unmixing of end members from one another. There was also no implementation of fractionation in similar modelling applications, apart from bespoke models. The tasks fulfilled within the contents of Chapter 3 are as follows:

- *Create and describe the modelling platform, Automaton.*

  A program for this purpose, Automaton, is written and described. The mathematical functions which control its operation, and how a user may interact with the program and results are compared to other similar programs.

- *Validate Automaton's results against a similar modelling platform and explore the limitations of employing Automaton in various modelling scenarios.*

  Increasingly complicated synthetic mixtures of end members are created for modelling by Automaton and a similar noble gas modelling platform, and the results are compared, to explore the precision and accuracy of Automaton. Modelling of other synthetic mixtures explores the limitations of using Automaton on end member compositions featuring different uncertainties.

- *Modelling of the xenon composition of comet 67P/Churyumov-Gerasimenko with notable noble gas reservoirs.*

  Modelling of the potential origins of the xenon isotopic composition of 67P/Churyumov-Gerasimenko is conducted with Automaton and other significant primitive noble gas reservoirs in the Solar System.

- *Modelling of significant xenon reservoirs in Solar System with composition of comet 67P/Churyumov-Gerasimenko.*

  The likelihood and nature of cometary contributions to the terrestrial reservoirs is modelled with Automaton in light of in situ noble gas measurements of xenon from comet 67P/Churyumov-Gerasimenko. Automaton is used to untangle xenon end member contributions to the Earth's atmosphere, Earth's primordial U-Xe composition, and the Martian atmosphere.

- *Explore the reliance of particular models on the isotopic composition of xenon from 67P/Churyumov-Gerasimenko.*

  Fractionated solutions to modelling involving 67P/Churyumov-Gerasimenko are modelled with and without the corrected composition of $^{128}Xe/^{132}Xe$ from Marty et al. (2017) to explore the reliance of results upon its composition. The influence of the uncertainty of the reported composition of xenon from 67P/Churyumov-Gerasimenko is discussed in the context of the solutions proposed by modelling.

### 1.5.3. Xenon isotopes in individual lunar volcanic glasses of Apollo 15 and Apollo 17

Chapter 4 contains an investigation into the presence of an indigenous lunar xenon composition contained within primitive lunar volcanic glasses. Prior to this work, similar analyses of primitive lunar materials have focussed on other noble gases or have been conducted by mass spectrometers less sensitive than RELAX. The tasks fulfilled within the contents of Chapter 4 are as follows:

- *Optically classify samples of lunar regolith to separate volcanic glass candidates.*

  Procedures for the optical classification of glasses which are candidates for having a volcanic origin are developed. These glasses are cleaned and prepared for major element confirmation of their volcanic origin.

- *Develop procedure which allows for major element classification by electron microprobe analysis and xenon isotopic measurement by RELAX.*

  Procedures which balance the reliability of major element measurement by electron probe microanalysis and xenon measurement with RELAX are developed. Both analytical techniques require different approaches to sample preparation which impact the reliability of the other's data. A procedure which minimises the potential for damaging the data or instrument during xenon analysis in RELAX while producing major element data reliable enough for volcanic classification is developed, explained, and discussed.

- *Confirm the volcanic classification of candidate glasses with major element data from electron probe microanalysis.*

  Major element data for the volcanic glass candidates of the two lunar regolith samples are produced to confirm their origin as volcanic or not.

- *Measure and characterise the xenon isotopic compositions contained within the volcanic glasses using the RELAX mass spectrometer.*

  Measure the xenon isotopes contained within individual pristine volcanic glasses from the lunar interior.

- *Interpret the xenon isotopic and major element data to reconstruct the history of the volcanic glasses analysed by both methods, and comment on any indigenous lunar xenon.*

  The measured compositions reported by both analyses are interpreted and explained in the context of their possible indigenous lunar xenon composition and history through xenology.

### 1.5.4. Towards noble gas analysis of Stardust samples with closed-system etching

Chapter 5 contains the validation and testing of a novel approach to noble gas extraction from samples such as those collected by Stardust from 81P/Wild (Tsou et al., 2003). Prior to this work, there had been no measurement of xenon contained within definitely cometary material measured in situ or in returned samples. At the time of writing, the composition of xenon contained within cometary material is confined to in situ measurements of comet 67P/Churyumov-Gerasimenko without the compositions of $^{124}$Xe and $^{126}$Xe. A ground truth analysis would double the inventory of cometary xenon and is more likely to have an increased precision only available to Earth-based instruments. The tasks fulfilled within the contents of Chapter 5 are as follows:

- *Develop an experimental procedure for xenon extraction from a Stardust sample with CSSE for isotopic analysis with RELAX.*

  The procedures detailed in Chapter 2 are tested and refined in preparation for application on real samples of Stardust material from comet 81P/Wild 2. The difficulties in measuring this composition conventionally are discussed, along with the benefits of the approach proposed in this work.

- *Detail the characteristics of a Stardust sample and propose analogous materials which can test the applicability of the gas extraction approach.*

  A typical Stardust sample is described, along with the reasons why it is difficult to extract a xenon composition conventionally. Analogous materials are proposed for a test to prove whether the proposed technique is capable of sequential extraction of xenon components.

- *The xenon contained in the Stardust sample analogue materials are measured conventionally and discussed.*

  The analogue materials PCA 02007 and organic residue “Q” from meteorite Vigarano II are analysed individually by stepped heating with the RELAX mass spectrometer. The xenon compositions of each material are discussed in their individual contexts and their use as a Stardust analogue.

- *The Stardust analogue is prepared and analysed with CSSE and RELAX.*

  Analogue materials are simultaneously loaded into the CSSE apparatus and etches of increasing severity are treated and analysed with RELAX. Etching of siliceous material with HF is conducted until no sample gas is observed, the acid is then swapped with $HNO_3$ to repeat the process for the organic sample material.

- *The analogue test results are discussed before applying the techniques and procedures to a real Stardust sample.*

  A discussion of the analogue test results is presented and refinements to the procedures are proposed for its ultimate use with a real Stardust sample.

- *CSSE and RELAX extract the xenon isotopic composition of 81P/Wild 2 from a real Stardust sample.*

  The refined techniques advised by the analogue test are employed on a real Stardust sample of material collected from 81P/Wild 2 to determine another cometary xenon composition.

# 2. Instrumentation

## 2.1. Refrigerator Enhanced Laser Analyser for Xenon (RELAX)

Noble gas mass spectrometers all share a similar structure. They extract noble gases from a sample, clean or separate the extracted gases, ionise a fraction of the atoms of all noble gases, employ a means of mass separation, then create a signal from the ionised gas. This signal is then converted to useful data using calibrations and standards. This section specifically describes the instrument used to collect the majority of the data presented in this work, the Refrigerator Enhanced Laser Analyser for Xenon (RELAX). Its physical construction and the process by which it produces signal are explained, as is the means by which signal is typically converted to data. The end of the chapter discusses some analytical considerations for the signal to data conversion relevant to the later chapters. Many of these processes and concepts are shared with other noble gas spectrometers.

RELAX is a resonance ionisation time of flight mass spectrometer for xenon built to make maximum use of the smallest possible amounts of precious extraterrestrial materials (Gilmour et al., 1994; Crowther et al., 2008). The greater sensitivity of RELAX relative to conventional mass spectrometers means it requires less sample material, preserving the maximum amount of sample material for other work. It can also resolve the xenon contained within individual samples of smaller sizes than less sensitive mass spectrometers (as in the volcanic glass of Chapter 5, for instance). RELAX follows the typical time of flight (TOF) mass spectrometer structure, where the atoms are ionised in the ion-source then accelerated by electric plates to a microchannel plate (MCP) detector which converts ion counts to signal (Figure 2.1). This approach is specifically suited to xenon as it allows for simultaneous analysis of all isotopes, where a magnetic sector approach often needs multiple collectors to detect all xenon isotopes.

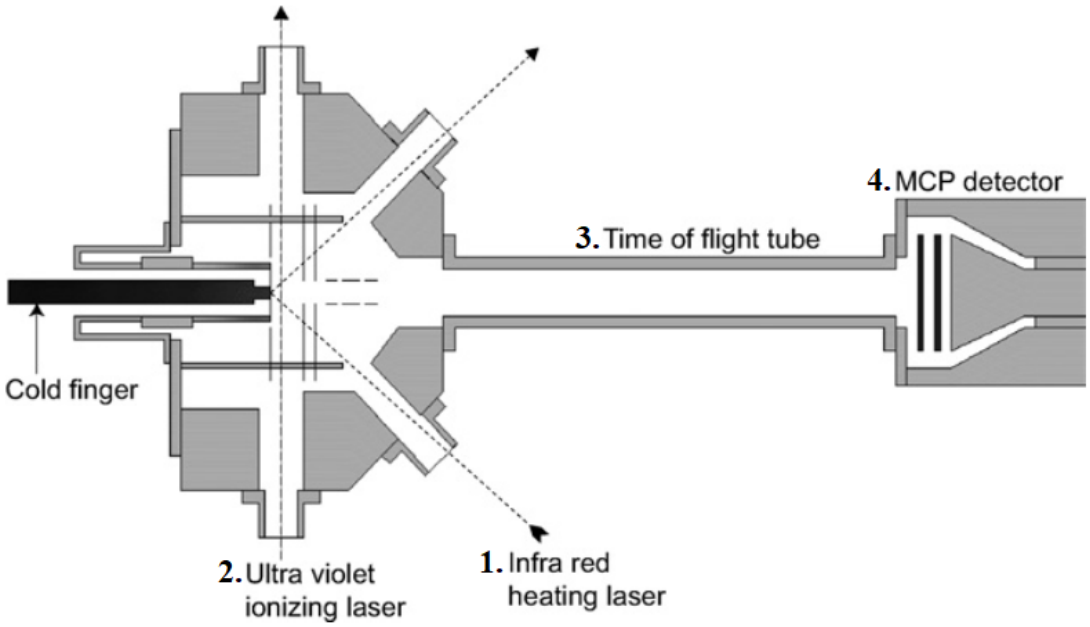


***Figure 2.1*** *Diagram of ion source, mass separation, and ion detection modules of RELAX mass spectrometer adapted from Crowther et al. (2008).*

All noble gas instruments require the maintenance of a vacuum for a number of reasons. A vacuum increases the mean free path of ions so they are unlikely to collide during travel down the flight tube, potentially changing flight time by perturbing ion velocity and direction. A vacuum also reduces the signal attributable to sources other than the sample, such as atmospheric xenon. RELAX maintains an ultrahigh vacuum (UHV, defined as $< 10^{-9}$ mbar). An ultrahigh vacuum is achieved by constructing the instrument out of stainless-steel tubing sealed by copper gaskets compressed with knife-edge flanges (ConFlat, or CF flanges), connected to three stages of pumping, each successively increasing the vacuum until the pumping method's efficiency diminishes. 'Rough' rotary pumps reduce the pressure to $\sim 10^{-3}$ mbar, after which turbo pumps reduce the pressure to $\sim 10^{-7}$ mbar, finally ion pumps create an ultrahigh vacuum by reducing the pressure below $10^{-9}$ mbar. Pumping of these systems requires the extraction of gases initially contained in the volume, gases which may be leaking through improper seals (which prevent UHV unless sealed), and the release of gases adsorbed to the internal surface of the vacuum volume. Sealing leaks and reducing instrument volume ease the production of this vacuum

and ultimately improve instrument sensitivity, as does the selection of materials which 'degas' less, diffusing smaller volumes of adsorbed gases from their surfaces under vacuum. UHV instruments are typically constructed from stainless steel for this reason, as the lower near-surface partial pressures exhibited under vacuum outweigh the benefits of other physical properties such as transparency and conductivity (glass, plastic, ceramics), or cost.

Liberation of surface-correlated gases from their adsorption sites when introducing new modules or after exposure to atmosphere is aided by a process called 'baking', in which the vacuum walls are heated (to a temperature limited by the resilience of glass-metal seals and microchannel plates, < 200 ℃ for RELAX), hastening the liberation of volatiles from their adsorption sites so they can be pumped from the vacuum chamber. Pumping must be continuous to maintain this vacuum due to incomplete degassing despite baking and inherently imperfect seals between enormous pressure differential. This unavoidable build-up of gas is referred to as a blank, whose rate is monitored closely so that its signal influence can be quantified and removed mathematically.

***Table 2.1*** *Schematic diagram of typical noble gas mass spectrometer structure and examples of each module.*

| Gas Extraction | Ion Source | Mass separation | Detectors |
|---|---|---|---|
| Infrared laser* | Resonance Ionisation* | Acceleration & Time of Flight (TOF)* | Multichannel Collector plates* |
| Closed System Stepped Etching (CSSE)* | Electron Impact | Magnetic Field Deflection | Faraday Cups |
| Crucible Heating | | Quadrupole Mass Selection | Ion to Photon Detector (IPD) |
| Crushing | | | |

*Asterisks denote use in conjunction with RELAX. Note that most combinations of these components would constitute a functional mass spectrometer.*

Sample gases are typically extracted in steps of increasingly intense heating applied by illumination of the sample in an infrared laser beam. For each step, extracted gases are treated by exposure to a SAES getter for two minutes to remove active gases, crack long-chain hydrocarbons, and absorb $H_2O$ and $CO_2$ (producing H). The sample gas is then introduced to the ion source chamber (left side of Figure 2.1). This volume contains a cold spot cooled by a cryogenerator operating at 40 K, onto which the extracted xenon atoms condense. The cold spot is exposed to the sample aliquot for 45 seconds, after which the flight tube and ion source are sealed from the rest of the instrument. The 45 second condensation duration on the cold spot was optimised by previous RELAX operators in order to condense the maximum amount of sample gas while minimising the time for blank gas to accumulate. While this duration is proven to only condense around 90% of xenon in the exposed volume, condensation of the remaining 10% takes significantly longer, making experiments last longer and increasing the blank contribution. The condensed gas is then liberated from the spot by exposure to a pulsed heating laser ($\lambda$ = 1064 nm, 5 mJ, 10 ns), which temporarily raises the temperature of the cold spot and releases the condensed xenon into a plume (‘1.’ of Figure 2.1). The plume propagation from a point source also inhibits the Maxwell-Boltzmann distribution of atom speeds after liberation, as the particles cannot travel backwards through the cold spot, effectively halving the velocity distribution of particles relative to a cloud, whose tighter grouping aids instrument resolution. The duration of plume expansion is controlled by a trigger box which Q-switches an ionising laser to illuminate the plume after a delay optimised to maximise the xenon illuminated by the beam (‘2.’ of Figure 2.1). The illuminated section of the plume is subsequently saturated in photons of $\lambda$ = 249.6 nm required for two-state ionisation, which allows for their acceleration down the flight tube by electrostatic repulsion.

Resonant ionisation is significantly more efficient than the degree of non-resonant ionisation of unwanted contaminants from the sample gas, increasing the signal relative to noise, which is particularly useful for an instrument optimised for low sample concentration. The employed ionisation scheme uses two photons to excite a *5p* electron to a 6*p* orbital in xenon via a virtual state. The excited electron is then ionised by a third photon. This ionisation scheme avoids hyperfine structures introduced by interaction between electron angular momentum and nuclear spin which would manifest in isotopic biases, and allowed for development of the instrument using commercially available lasers. The ultraviolet ionising beam is produced by a Continuum YAG ($\lambda = 1064$ nm) pumping a Sirah dye laser containing Coumarin 503 to produce a 499.2 nm beam which is frequency doubled by a BBO crystal to achieve a wavelength of 249.6 nm. This beam is maintained at an energy of 2 mJ per pulse, beyond which sensitivity is not improved, suggesting unit probability of ionisation upon illumination within the plume.

The ionised parcel of xenon is then accelerated in an electric field by three charged plates perpendicular to the flight tube length, one in front (0 kV), one in the middle (of variable voltage) and one behind (+3 kV). These charged plates are arranged in a Wiley-McLaren configuration (Wiley and McLaren, 1955), featuring a relatively small potential difference between the back and middle charged plates, such that ions across the plume volume are accelerated more with increasing proximity to the cold spot. This potential difference serves to concentrate the ions before they exit the furthest charged plate and enter the flight tube. Introducing this correlation between velocity and location in the ion source reduces the length of the ion cloud parallel to the flight tube, and the non-mass related velocity distribution of the packet of ions, ultimately improving the mass resolution.

The electric field subjects the ions to identical potential energies and all ions created at the same point accelerate in proportion to their mass/charge ratio, resulting in ions of each isotope exiting the ion source with identical kinetic energies but different velocities. The middle plate voltage is optimised to maximise the mass resolution, compensating for different formation positions and formation velocities. Prior to their entry into the flight tube, the ion beam is converged by an einzel lens to reduce spread and ensure its perpendicular contact with the detector plates. This further improves mass resolution by ensuring all ions are focussed on the detector plates, and are not lost in transit. The xenon ions take between 8.9 and 9.1 μs to arrive at the end of the flight tube (48 cm, '3.' of Figure 2.1), with lighter isotopes arriving first.

The end of the flight tube contains microchannel plate detectors ('4.' of Figure 2.1) perpendicular to the beam path in a chevron configuration. These plates are composed of an array of channels which produce an electrical signal depending upon the incident flux of ions. In isolation, each channel is temporarily consumed by the detection of one ion, whose impact creates a cascade of secondary electron emission when a high voltage is applied across the channel length. This electron cascade is reported as the binary incidence of an ion (a 'count'), regardless of mass or charge. The channel is refreshed prior to the next pulse of ions, but cannot detect multiple ions in one pulse. The implications of this saturation are explored in Section 2.3.2, and are addressed by the method of data reduction.

The condensation, plume generation, ionisation, and acceleration cycle repeats continuously at 10 Hz for five minutes, after which the sample gas has mostly been recondensed, liberated, ionised and detected. The resultant signal is processed by an Aquiris 8-bit digitiser card capable of writing and storing the < 2 GS/s of data, before it is passed to a conventional computer for storage, treatment, and interpretation. The data are recorded in sets of 100 spectra which are transferred to a computer every 10 seconds, a

total of 30 times. Each group of 100 spectra are summed to produce a single mass spectrum for the xenon analysed over the ten second interval of their recording. The data reported throughout this work correspond to the summed composition of xenon contained in the first six sets of 100 spectra, therefore the first 60 seconds of data acquisition. This roughly corresponds to a third of the total xenon as detected by the mass spectrometer during measurement of the 30 spectra. All sets of spectra are not used as they introduce more instrument fractionation and have worse signal to noise ratios.

While the resonant ionisation of xenon reduces the probability of unwanted ion production, non-resonant ionisation of hydrocarbons is regularly observed. Some of these hydrocarbons are supposed to originate from rough pumps attached elsewhere on the vacuum system; they are notably introduced with new MCPs, which require significant degassing before data collection. They are condensed, liberated, ionised, and detected in the same action as the xenon atoms, introducing noise to the recorded signal, and saturating channels which could otherwise have detected xenon ions. Systematic removal of the hydrocarbon signal in post-acquisition data processing is not possible due to their irregular migration and concentration throughout the instrument, their influence is subsequently reduced by physical means. In between analyses the cold spot is heated by the pulsed infrared laser to a temperature above 40 K. This results in a more complete liberation of condensed materials, such as hydrocarbons, which are subsequently removed by ion pump, or recondensed elsewhere within the instrument. Their condensation elsewhere in the instrument satisfactorily reduces their influence on signal collection, until its concentration reduces the vacuum quality, or the species are liberated by a stray laser during beam alignment. The hydrocarbon signal is monitored closely during analyses, and the instrument is cleaned by baking if the signal is high enough to affect signal height by MCP saturation (as explained in Section 2.3.2), or is creating a signal interference with isobaric isotopes.

### 2.1.1. RELAX blanks and calibration

All analyses with RELAX reported in this work are conducted alongside blank quantification and air calibration procedures. These are conducted before, during, and after all analyses in order to determine any instrumental drift in sensitivity or potential sources of atmospheric blank.

Procedural blanks constrain the signal not attributable to sample gases by conducting analyses which are nearly identical to those of sample analyses, without introduction of sample gases. This signal is measured before and after all sample analyses, and after particularly large sample releases to ensure no 'memory' effect (non-complete removal of previously analysed xenon). Xenon compositions reported in this work are those which exceeded the average blank signal plus three standard errors at any isotope during the period of data collection. The blanks related to the CSSE apparatus are more complicated due to the variable periods of accumulation in between analyses and the additional, mostly unpredictable additional reservoirs of blank xenon it introduces (summarised in Section 2.2.1).

Calibration of RELAX is conducted before and after all sample analyses, and also after every four or so sample analyses. Calibration is achieved by measuring the reported signal for a known volume of atmospheric xenon (~ $1.2 \times 10^5$ $^{132}$Xe atoms). Air calibrations outside the typical range of signals cause sample measurements to cease until a cause is determined. The most frequent explanations for reduced instrument sensitivity are related to either the power of the ionising laser beam, or poor alignment of the ionising or plume generating lasers, described as follows:

- *A drop in the ionising beam power may result in incomplete ionisation of the illuminated plume of xenon atoms.*

  The two-photon ionisation of xenon requires a high power-density to achieve near-unity ionisation of the illuminated atoms. Powers below this critical flux result in only some of the plume being ionised, so fewer ions are accelerated and measured by the detectors. Typical causes are losses in beam production efficiency from mirrors getting covered in dust or receiving burn damage, and more commonly a photochemical degradation of the dye chemical (Coumarin 503) used in laser production. Remediation typically requires replacing the laser dye, cleaning the beam path, or increasing the power of the 'pumping' laser to improve the efficiency of the dye laser.

- *Misalignment of the heating laser which produces the plume of xenon atoms for illumination in the ionising laser can result in a reduction in ionisation efficiency.*

  Such a reduction is simply the result of the ionising beam not ionising the typical fraction of the plume. This is a regular occurrence during analyses due to the number of components through which the beam path can be altered during heating and vibration of the instrument during use. The user must manually 'tune' the beam path to maximise signal in the event of this misalignment.

### 2.2. Closed-System Stepped Etching (CSSE)

All noble gas mass spectrometers require the extraction of noble gases from the sample. For solid sample analysis, there are a number of options for sample gas extraction, each with traits lending themselves to particular samples or instruments. Every technique must find a way of removing gases trapped inside crystal lattices, adsorbed to surfaces, or sealed in structures they cannot permeate. The preferred means of noble gas extraction is to heat samples until atoms are liberated from the surfaces they are adsorbed to, or the sample's physical structure is broken down or relaxed enough for noble gases to diffuse into the surrounding volume. Such techniques subject samples to increasingly higher temperatures in order to liberate gases from more thermally resilient sites, or simply melt the entire sample in a furnace and analyse the released gases. The user can vaguely target more or less deeply implanted noble gases, materials of different thermal properties, and adsorption sites of differing strengths with increased temperatures. However, accurately targeting specific depths or phases is impossible without an intimate knowledge of the thermal properties of the materials involved, the proportions of noble gases escaping by fractures or through the chemical structures, and complete control of where and by what temperature a sample is heated. Closed-system stepped etching is an approach to noble gas extraction which places an emphasis on depth resolution and the targeting of specific phases.

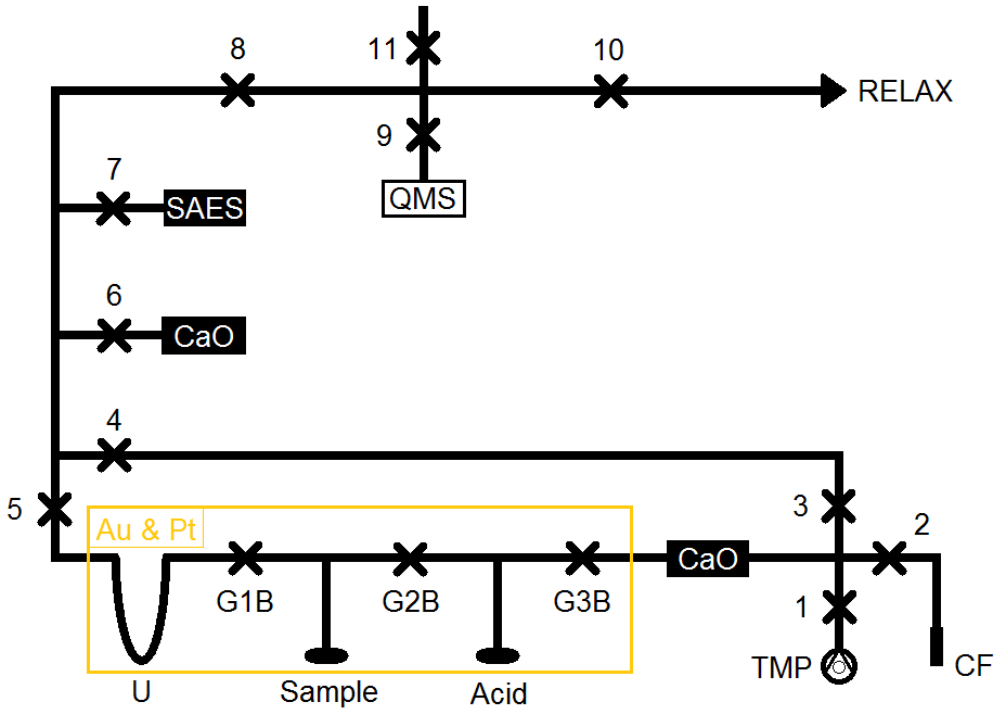


***Figure 2.2*** *Schematic diagram of the closed-system stepped etching line as connected to the RELAX mass spectrometer during this work.*

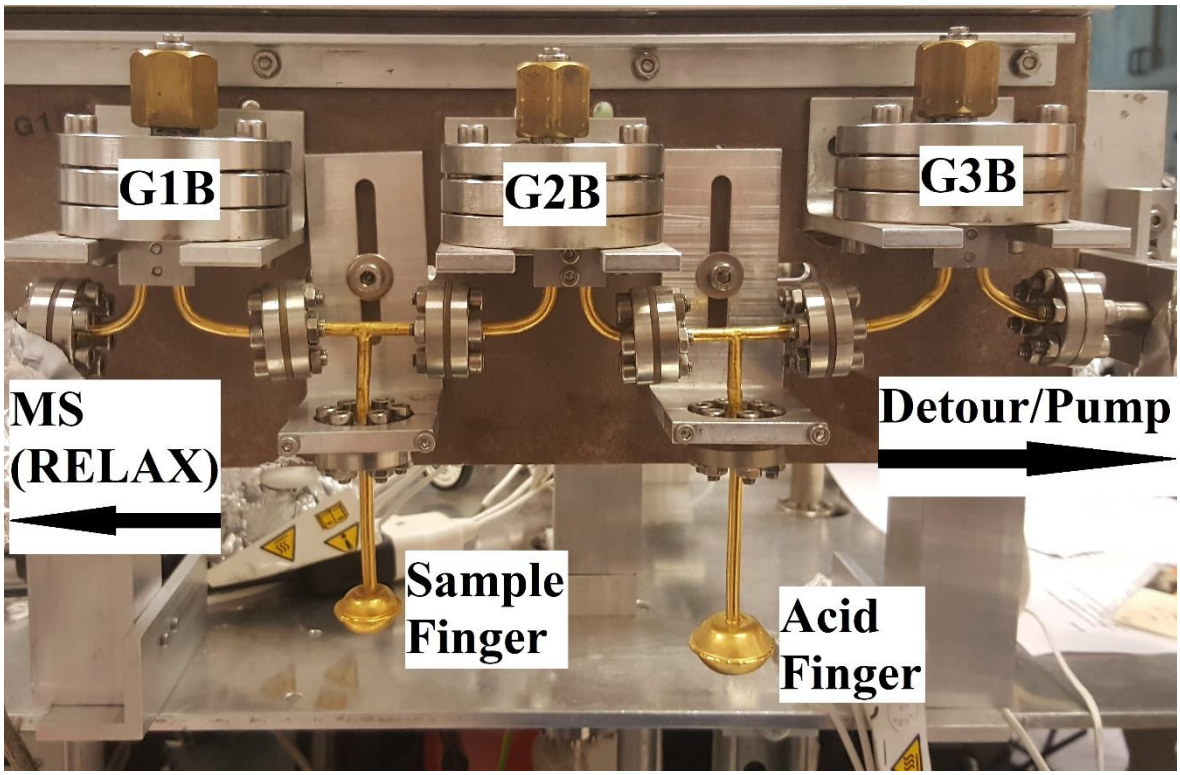


***Figure 2.3*** *Annotated image of 'gold section' of closed-system stepped etching line (G1B to G3B of Figure 2.2). Valves (G1B, G2B, G3B), gold fingers (sample & acid), and paths leading from the gold section are labelled (with arrows indicating ultimate destination).*

Closed-system stepped etching (CSSE) is a means of sample extraction which liberates trapped components in vacuo by chemically etching a sample to release the contained gases to be treated and measured by an attached mass spectrometer (Weiler et al., 1986; Benkert et al., 1993). Of the two CSSE apparatus currently in use, both were built in ETH Zürich, where one remains, while the other is on loan at the University of Manchester. The CSSE apparatus used during this work is the one located in the University of Manchester, which can be explained in two sections, the gold section (within the gold box labelled 'Au & Pt' on Figure 2.2, and mostly contained within Figure 2.3) and the gas treatment line (the area outside of the aforementioned box on Figure 2.2). Both are of a near identical structure apart from the attached mass spectrometers (beyond valve 8 of Figure 2.2).

The gold section houses two gold vessels with wide bases and thin necks, and a gold tube connecting it to the rest of the apparatus (labelled in Figure 2.2, and shown in Figure 2.3). One vessel is designated to contain an acid (acid finger), and the other a sample (sample finger). These vessels are attached in a modular construction in which modules contact one another with platinum valves and gaskets which can be removed and replaced to facilitate sample and acid transfer. The line is composed of gold and platinum due to their inert interaction with the acids used for etching, and the platinum gaskets and valves prevent cold welding between the contacts of gold modules. All valves on the gold section (G1B, G2B, G3B, as shown in Figure 2.3) are of identical construction; a tapped stainless-steel rod is pressed against a platinum sheet until it forms a seal to close the valve and separate the two gold input lines.

The gold tube ('U' on Figure 2.2, and to the left of the image in Figure 2.3) is the start of the gas treatment section of the CSSE apparatus, and is the last gold module. The remainder of the apparatus is composed of standard stainless-steel tubing modules which

ultimately lead to a turbomolecular pump or the mass spectrometer. This transition to material susceptible to acid etching indicates the boundary after which the majority of acid has been removed from the vacuum (roughly defined by valve five), although there are additional gas treatment modules before gas can be treated as ‘clean’ and be introduced to the attached mass spectrometer. Three separate cleaning modules are sequentially exposed to the extracted gases on their way to the mass spectrometer. Any gases travelling from the sample chamber towards the mass spectrometer are initially exposed to the gold U bend externally cooled to −70 ℃, then two separate cleaning modules containing CaO (behind valve six) and an SAES getter at 250 ℃ (behind valve seven). Additionally, a quadrupole mass spectrometer is attached in the volume between the gas cleansing line and the mass spectrometer volume. This quadrupole mass spectrometer is used for leak detection and ensuring the gas cleansing modules are working as intended.

Extracting and treating gases released from a single etching step without contaminating the acid-susceptible line or leaving the sample exposed to acid requires following a strict and exact procedure (included in appendix). This procedure was optimised for RELAX during this work, and verified to have sufficiently removed any detectable partial pressure of acid vapour by periodic testing with the quadrupole mass spectrometer.

### 2.2.1. Stepped etching in practice

The nature of the etching is dependent upon the following conditions:

- *The type of acid being used, typically either HF or $HNO_3$ to target siliceous or organic compounds, respectively.*
- *The chemical composition, or compositions, of the material being etched and their relation to the acid employed in the etching (Brady and Walther, 1989).*
- *The geometry and topography of the material being etched, whether it is porous, or polished. Essentially a measure of the surface area onto which acid can react.*
- *The partial pressure of acid in the sample volume. Increasing this allows for more sample material to be etched.*
- *The duration of etching. Longer durations generally etch greater volumes.*
- *The ambient temperature of the sample chamber during etching. Raising the temperature accelerates the etching reaction.*

Manipulation of the controllable conditions allows the technique to target specific materials, the volume or location of material being etched, and the volume of noble gases extracted from the sample. In practice, combinations of these variables control the etching of any sample during etching. The following sequence describes the variables which are regularly changed in a methodical stepped etching analysis to control the gas released from a sample in stepped etching analyses, these parameters are described in multiple previous examples of sample analyses with CSSE (Weiler et al., 1986; Wieler et al., 1991; Wieler and Baur, 1994; Busemann et al., 2000; Riebe et al., 2017) and summarised here:

1. Initial etching steps may incrementally increase the duration over which a sample is exposed to acid vapour from an acid sample held at −70 ℃. Acids typically used in closed-system stepped etching, HF and $HNO_3$, are well below liquidus at this temperature, so the sample is exposed to acid vapour sublimated from the condensed acid. Durations of acid vapour exposure steps are advised by the volume of released sample gas and behaviour of similar samples (if available). Etching durations for acid vapour etching steps are increased until the duration of etching is impractical, or the volume of released gas is small enough that the simultaneous accumulation of atmospheric blank becomes significant. In the case of this work, the acid vapour etching step duration was limited by the impracticality of maintaining an isopropanol bath at −70 ℃ for extended period). The etching proceeds in severity by changing the etching severity according to the second stage.

2. In this stage the temperature of the acid finger is gradually increased to increase sublimation from the condensed acid, raising the partial pressure of acid vapour exposed to the sample. As in the first stage, the duration of etching steps at any given temperature is optimised according to the amount of sample gas released during etching, and the relative significance of the atmospheric blank accumulation. Once the duration of a particular etching temperature reaches the limit according to the previous criteria, the temperature can be increased and the cycle of longer etching durations is repeated. This process repeats up to room temperature, at which point all of the acid is in the vapour phase. Given the removal of the impracticalities in changing the specific temperatures from ambient room temperature, the ultimate control of etching duration at this stage is limited purely by the relative significant of atmospheric blank.

3. In particularly resilient samples where the duration of room temperature etching is impractically long, or when atmospheric blank accumulation is significant, the acid may be distilled from the acid finger into the sample finger, this is known as a wet etch. A wet etch increases the partial pressure of the acid exposed to the sample further, by reducing the volume it occupies. Etching severity can be increased further by heating the sample finger after acid distillation. This approach is typically employed at the end of sample analysis, or when there is little sample material remaining, as it is relatively hard to control. For example, etching occurs while distilling acid in to and out of the sample finger, a time-consuming and complicated procedure (~ 12 hours) which is hard to quantify.

The sequence and exact timing or temperature of these three approaches is mostly decided prior to analysis of a sample, and based on previous analyses with similar sample masses and concentrations of equivalent compositions. Once a rough template for the etching procedure is enacted, and the experiment begins, the step nature, duration, and temperature are mostly revised according to the concentration of gas released in the previous step. For a sample which has not been etched before, as is the case with the stepped etching in Chapter 5, the previous etching step release and the atmospheric blank accumulation as a function of sample signal height is typically the only qualitative measure advising etching and its progression. Quantification of the blank accumulation in most of the etching conditions is attempted to ensure the most precise information advises step progression, however, the variety and duration of many of the etching steps mean blank accumulation often has to be estimated.

## 2.3. Development of data reduction

### 2.3.1. Blanks

The closed-system stepped etching apparatus' attachment to RELAX added volume and other sources from which atmospheric gases can accumulate. These sources increase the given proportion of signal which is not attributable to the sample, and are known as blanks. Quantification of these blanks and their systematic addition to the sample signal when using certain parts of instruments or apparatus allows their precise determination and subtraction from any given sample gas extraction, thus increasing the precision and accuracy of the data. The range of approaches to etching and their unique contributions to the blank accumulation rate make blank quantification particularly important for CSSE, especially when its combined use with RELAX had not been previously investigated. This section contains the approach to blank quantification for CSSE and RELAX developed during this work.

Significant, non-xenon, blanks due to improper seals of flanges or atmospheric gases adsorbed to recently added and rough vacuum exposed components were mostly removed by replacement and baking, respectively. Baking is conducted at slightly lower temperatures than the stainless-steel components (~ 150 ℃) around the gold-platinum-gold and gold-platinum-steel flanges (~ 100 ℃) of the CSSE apparatus due to the differing thermal expansion properties of each metal potentially introducing leaks. This approach required two stages of baking so that volatiles liberated from higher temperature steel components did not condense on the lower temperature gold components. Before the xenon blanks were quantified, an extensive review of other volatiles was conducted using a quadrupole mass spectrometer, mostly to ensure the acid chamber was properly sealed from sensitive parts of the RELAX mass spectrometer. Once this process was complete

and the acid finger valves were capable of being reliably opened and shut without significant leaking of acid, the blanks were designed around the most sensitive aspect of the mass spectrometer, RELAX, which quantified atmospheric accumulation by measuring the xenon concentration.

CSSE introduced new and more complicated reservoirs of xenon blanks compared to those typical of RELAX. Only some of these blanks were able to be quantified conventionally, by measuring a xenon accumulation rate for a particular volume which can be scaled for different times and volumes, for example. The majority of blank quantification required the development of entirely new procedures, outlined below. The characterisation of CSSE blanks is split into two categories depending upon whether they quantify the blank gases expected in the sample extraction and treatment section of the line (‘procedural blanks’), or whether they are concerned with the gases dissolved in the acid (‘acid blanks’).

#### 2.3.1.1. Procedural blanks

The first blank (‘procedural blank without sample’) follows the typical sample extraction procedure of a normal etching step of CSSE, but the gold section remains isolated. Blank gases in the line up to the sample finger valve (G1B) are exposed to a cooled U-tube and expanded to the CaO and SAES getters for the typical times, before analysis with RELAX. This procedure quantifies the general blank characteristics of the vacuum line up to the sample finger valve, and is conducted before and after each day of etching.

The second blank involves a near identical procedure to the ‘procedural blank without sample’, but includes the opening of the platinum valve (G1B) connecting the

sample finger to the gas treatment line. This ‘procedural blank without acid’ involves the cooling of the U-tube and expansion to the gas treatment section as in a real etching step, and concludes with analysis using RELAX. If the valve separating the sample finger from the acid (G2B) is leaking, or the acid was not fully removed from the sample finger during the condensation stage of the previous step, this blank may contain gases extracted from uncontrolled etching of the sample. Conducting this blank before the first etching step of the day is an easy means of checking the condition of the platinum valve separating the acid and sample fingers (G2B) and the effectiveness of the acid condensation during typical etching steps.

#### 2.3.1.2. Acid blanks

The acids used during etching are a reservoir of noble gases which may be dissolved during etching, dissolved since their exposure to atmosphere before incorporation into the CSSE apparatus, or from blank accumulation through the valves and seals surrounding the acid finger.

When a new volume of acid is introduced to the acid finger, a particularly large release of sample gas is observed, or the CSSE line is left to accumulate blank gases through valves etc., it is subjected to a process called degassing, which attempts to minimise the atmospheric noble gas component. Without this process, etching steps would mix any existing ‘acid-xenon’ component already in the acid finger with newly extracted sample xenon liberated during etching. Xenon remains gaseous during the etching process so is partially trapped in the acid finger once etching is stopped. This process repeats, mixing an equilibrated xenon composition composed of fractions of all xenon released in preceding steps.

Reducing this ‘dissolved’ component by degassing requires condensing the acid as though etching, extracting the gaseous xenon, neutralising the contained acid vapour (by exposure to CaO after G3B, and the cold finger behind valve 2), and removing the gas by turbomolecular pump (behind valve 1). This process is repeated by thawing, refreezing and pumping the acid. Periodic detour measurement of treated xenon degassed from the acid, an acid blank, determines the success of this technique.

An acid blank involves cooling the acid finger until condensed, and extracting a sample of the vapour via valve G3B and sequential exposure to CaO, the cold finger trap behind valve 2, and the detour line (between valve 3 and 4). The gas is then treated again by exposure to the sample-side CaO and getter (valves 6 and 7), before exposure to the mass spectrometer for measurement. Acid blanks are useful for determining the composition of the noble gas contained in the acid finger, but their unusual route to measurement compared to the sample gas extraction procedure renders their data qualitative. Acid blanks are therefore conducted after particularly large releases of sample gas to monitor the composition of the noble gas contained in the acid finger, and its evolution during etching. They also have a qualitative value in their measure of the efficiency of acid degassing, which is repeated until the acid blank concentration stabilises, ensuring a minimal contribution from this source during etching.

The acid blanks are conducted to quantify the contribution of gases dissolved in the acid to the analysed aliquots. There are two methods of measuring the acid blank, one for when the sample is fully etched or not present (‘sample extraction blank’) and another which bypasses the sample finger using the detour line (‘detour acid blank’).

The sample extraction blank follows the typical sample etching steps including the condensation and gas expansion times outlined previously in Section 2.2.1. This approach provides the best means of determining the contribution of gases associated with the acid to each etching step, but suffers from the requirement that it must include the sample finger. This sample finger inclusion means that a sample extraction blank cannot be conducted when a sample has not been fully etched, otherwise the acid would etch and release sample gases too.

The detour acid blank technique avoids the complications associated with passing the acid through the sample finger by utilising the alternate route to the mass spectrometer (via valve G3B). The acid finger and bypass cold finger is first cooled to −70 °C for two hours, as in the typical condensation stage of a sample etching step. The valve between the acid finger and detour line (G3B) is then opened, allowing the gas to expand into the volume containing the cold finger and CaO. After the typical exposure duration, the gas is then expanded through the detour line to the remaining gas purification line typically used for sample etching, where it is treated as a normal sample etch step would be (see Section 2.2.1). This acid blank method is conducted after particularly large etch steps, and at the start and end of each day of etching.

### 2.3.2. Saturation

RELAX is designed to extract xenon isotopic data from the smallest possible amounts of sample material such as from extra-terrestrial sample return missions or individual mineral separates. Sample gas extraction is optimised where possible to measure roughly the same amount of xenon as in a typical air calibration volume, $1.2 \times 10^5$ atoms of $^{132}Xe$. Many of the samples analysed in this work, in particular the aerogel and Stardust analogue, are expected to feature significantly larger amounts of xenon which may not be

able to be predicted and avoided. Every attempt is made during sample gas extraction in this work to avoid the analysis of large amounts of xenon, but the possibility of larger releases of sample gas is more likely with CSSE than stepped heating. If the cautious, evidence-based approach to sample gas extraction with CSSE results in large amounts of xenon, instrument dependent effects can affect the results.

This section considers the signal features that result from the physical phenomenon occurring within RELAX when a significantly large amount of sample gas is analysed. The probable cause of these effects as observed in signal analysis is proposed according to the components and processes occurring within the RELAX instrument during data collection. Mathematical models of the processes which may cause these phenomena are proposed and compared to real world data to confirm their accuracy. If the influence of these phenomena can be accurately predicted and quantified by models, then it may be possible to work backwards from data compromised by large signals towards their true compositions corrected for the large signal effects.

One of the phenomena observed with larger amounts of sample gas in RELAX is instrument dependent fractionation. Instrument dependent fractionation describes a preferential enrichment or depletion of particular elements, or isotopes of xenon in the case of RELAX, by mass from the sample gas as extracted from the sample, and the signal as recorded by the instrument. This artificial enrichment in favour of heavier or lighter isotopes is symptomatic of physical and/or chemical processes which create a disparity between the true isotopic composition of sample gas and the signal data. Within RELAX, instrument dependent fractionation is most significantly controlled by the microchannel plates (MCP) employed for ion detection.

Each spectrum captured by RELAX is a record of signal with respect to time, where time of flight is proportional to the square root of mass, and isotopes of increasing mass are detected in sequence. RELAX's ion detection module is a microchannel plate composed of an array of individual detectors called channels. Each of these channels will emit a signal when struck with an ion, and once triggered, each channel cannot detect subsequent ions until refreshed. Considered in isolation, a channel is essentially a cylinder containing a large potential difference, where upon incidence of an ion, a cascade of secondary electrons is produced which indicates the binary incidence of an ion. The potential difference required for the electron cascade must then be recharged after each triggering, meaning ~ 8 ms have to elapse before another ion can be detected by that channel (Seko and Kobayashi, 1973; Wiza, 1979). The 'idle' recharge time of ~ 8 ms for each channel is longer than the duration of one mass spectrum ~ 9 μs, so individual channels are not recharged by the time the subsequent packet of ions reaches the detector.

Considering collection of a single packet of ionised xenon, one individual mass spectrum, the number of available channels decreases as they are 'consumed' by lighter isotopes, resulting in a diminishing fraction of available channels for subsequent heavier ions, which share the same target area. This fraction of available channels is essentially a measure of the efficiency with which ions are detected, as the next packet of heavier ions has a greater chance of reaching an idle channel before it has refreshed, and thus does not produce a signal. This effectively translates as a lower efficiency for conversion of ion incidence to signal with increased isotopic mass. With increasing time and mass, detection efficiency is reduced, so the heavier isotopes are less efficiently detected; this leads to an instrument dependent fractionation called the saturation effect herein (illustrated in Figure 2.4). The following model attempts to simulate the saturation effect with real data in order to test its statistical plausibility, and potentially allow for its quantification, so that its effect can be corrected in samples featuring large xenon concentrations.

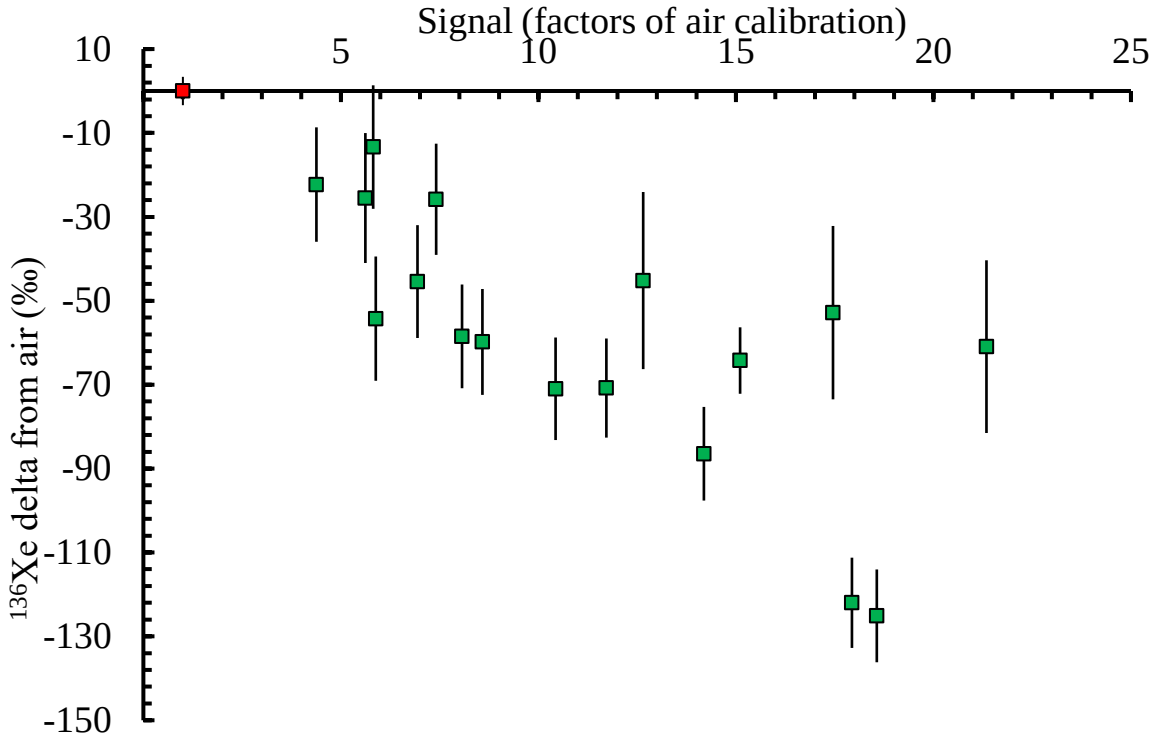


***Figure 2.4*** *Permille delta deviations of $^{136}Xe/^{132}Xe$ measured in large air analyses (green squares) from expected composition of $^{136}Xe/^{132}Xe$ (air calibration signal ≡ 0, red square). Abscissa exhibits signal height in factors above air calibration signal (hence air calibration ≡ 1). Data were collected for this work by measuring increasingly large aliquots of atmospheric xenon. Errors represent propagated standard deviation.*

#### 2.3.2.1. Saturation model

As we do not know the maximum number of detector channels in the MCP which can be discharged to record a signal, we suppose a hypothetical maximum signal per spectrum which would discharge all of the channels. The efficiency of detection is defined as the ratio of discharged to available channels, where prior to a spectrum analysis the efficiency is perfect (100% detection), and if the cumulative signal preceding equals the available channels the efficiency is zero (no detection). The model takes the cumulative peak area up to each isotope and subtracts it from a total predefined to be the hypothetical maximum signal able to be detected in each spectrum. This model calculates an isotope-specific correction for the saturation effect using real examples of large analyses and their expected counterparts. The initial number of available channels, N, is the unknown variable which dictates the detection efficiency for all but the first isotope.

The reason that the initial number of available channels, N, is unknown, despite any MCP having a finite and defined number of available channels, is because of the way it is used within RELAX. On a day-to-day basis the ion beam can be incident upon a range of channels due to the 'tuning' of the infrared laser which creates the plume of xenon atoms, or as the distances and volume within the instrument change with temperature. From step to step, the atmospheric blank and non-xenon ion concentration in the ionisation volume can change. After routine maintenance of the ionising lasers, every 6 months or so, the exact location of ionisation within the ion source is refocussed, slightly changing the ion beam. Over years, channels are gradually destroyed, ultimately necessitating the replacement of the MCP.

$$C_j = \frac{N}{N - \sum_{i=1}^{j-1} S_i}$$

***Equation 2.1*** *Correction factor, $C_j$ defined as the inverse of the efficiency of detection, a measure of the cumulative signal preceding isotope j, and its proportional consumption of the number of available channels, N.*

$$C_{134} = \frac{N}{N - \sum_{i=124}^{132} S_i}$$

***Equation 2.2*** *Example of signal correction for $^{134}Xe$ according to Equation 2.1.*

The detection efficiency for an isotope is defined as the fraction of channels which have not been deactivated by previous isotopes. The number of available channels is defined as the cumulative signal preceding isotope *j*, subtracted from the initial number of channels. Each isotope is then subject to a correction factor, $C_j$, calculated as an inverse of the efficiency (Equation 2.1). Multiplying the original signal by the correction factor results in the saturation corrected signal. Equation 2.2 is an example of the signal correction for $^{134}$Xe.

The data chosen to validate the model were those composed of predictably pure concentrations of known end members in which some analyses produced signals exhibiting mass dependent deviations from the expected composition. The larger analyses were paired with their ideal expected Xe composition. The ideal analyses acted as target compositions for comparison to the saturation corrected larger samples, and a chi-squared statistic based on their permille deviations from one another would act as a measure of plausibility.

The data used in the modelling were from multiple air calibration aliquots (as in Figure 2.4), closed-system stepped etching of aerogel conducted in 2014, the Stardust analogue stepped heating analyses of PCA 02007 and HF/HCl resistant “Q” residue from Vigarano II (detailed in Chapter 5). Reliable ‘target’ compositions are averages of typically sized analyses of materials containing identical xenon compositions. Their large counterparts were purely selected based on their signal exceeding the normally acceptable range. Durations between the large and target analyses selection were kept to a minimum to minimise the effect of long-term instrument drift and data collection differences. Given the fact large amounts of xenon within the instrument are avoided, and can significantly affect subsequent data collection by introducing gases other than xenon into the ionisation volume, the data used in this modelling were mostly confined to scattered examples of large xenon analyses from multiple experiments.

The model varies the starting number of channels to minimise the chi-squared statistic comparing the target and saturation corrected compositions. This process is conducted for each large release and target pair, producing a corresponding total for the modelled number of channels and a chi-squared goodness of fit statistic. Individual isotopes could be excluded from the chi-squared statistic calculation comparing the corrected and target compositions should there be reasonable grounds for it, for example, when an unexpected hydrocarbon interference affects the isotopic composition as well as

the saturation effect. However, all the signal, including the isotopes excluded from the corrected and target composition comparison are included in the quantification of channel deactivation. If the modelling can reliably reproduce a consistent value for the starting number of channels, and reasonable chi-squared statistics for the corrected and target compositions, the model would validate the hypothesis that channel deactivation is causing the saturation effect. Results from this modelling are shown in Figure 2.5.

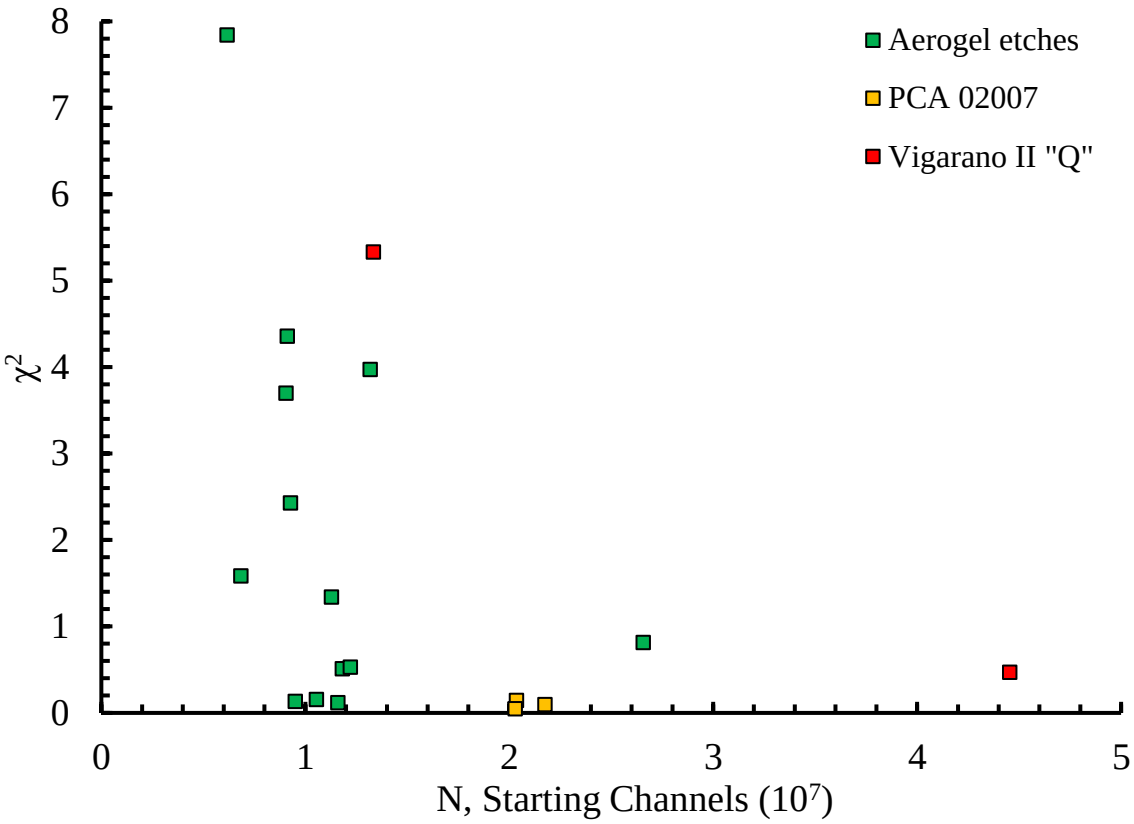


***Figure 2.5*** *Modelled solutions to the number of MCP starting channels (abscissa, in $10^7$ channels) initially available to incident xenon ions of aerogel etches (green squares), PCA 02007 (orange squares), and Vigarano II "Q" (red squares). Ordinate exhibits reduced chi-squared 'goodness of fit' statistic of modelled scenario.*

For large volume aliquots such as these, some secondary effects became significant, and clearly affected the model. Isobaric hydrocarbon interference is a problem for $^{128}$Xe and $^{131}$Xe, and a lack of quantification means it cannot be systematically accounted for, thus these isotopes were not included in the target and corrected composition comparison. The relatively small and inconsistent peak areas for $^{124}$Xe and $^{126}$Xe, yet significant influence of the chi-squared statistic, resulted in their omission from

the target and corrected comparison too. A convolution of the peaks of $^{129}Xe$ and $^{130}Xe$ resulted in the omission of $^{130}Xe$ from the chi-squared statistic (see Section 2.3.2.2 for a more detailed explanation of this). Subsequent to these omissions, the results presented here are for model runs where only $^{129}Xe$, $^{132}Xe$, $^{134}Xe$, and $^{136}Xe$ were included in the chi-squared statistic comparing the corrected and target compositions. Note that the omission of isotopes from the chi-squared statistic did not remove their effect on channel deactivation and detection efficiency.

Figure 2.5 illustrates a wide range of modelled starting channels and many chi-squared statistics which did not sufficiently match the target and corrected compositions (generally the chi-squared statistic values above two). Of the acceptable modelled solutions (chi-squared statistics were below two), the modelled number of available starting channels exhibits significant variability (from ~ $1 \times 10^7$ to $4.5 \times 10^7$). However, when focussing on the different datasets used for the modelling, the modelled starting channel numbers for reproducing the saturation-induced fractionation for the aerogel etch data appear to group around $N = 1.2 \times 10^7$. The modelled PCA 02007 scenario channel totals appear to group around $N = 2.1 \times 10^7$, with all models exhibiting excellent goodness of fit. The Vigarano II "Q" scenarios rendered two results, one significantly higher than those of PCA 02007 or the aerogel, and the other featuring a poor goodness of fit ($\chi \sim 5$).

The difference between the two more consistent modelled solutions for the number of starting channels, the PCA 02007 and aerogel etch data, could be the result of multiple differences in their data collection. The aerogel etch data are from experiments conducted in 2014 using the CSSE apparatus, whereas the PCA 02007 data are from stepped heating experiments two years later. The two analyses feature different methods of data analysis, with the PCA 02007 experiment employing stepped heating within a smaller volume, with

the sample gas exposed to less atmospheric blank accumulation before measurement. The aerogel etch would have accumulated more atmospheric blank before measurement, and was not condensed within the ionisation volume, unlike PCA 02007. The subsequent difference between the target and corrected compositions of the aerogel etches and PCA 02007 stepped heating data are not accurately modelled by fractionation of the saturation effect, as processes which are not included in the model are influencing the chi-squared statistic. The number of available channels may also have changed in the time between aerogel and PCA 02007 measurement, mostly due to instrument tuning and channels permanently deactivating, although this would presumably be evident in a gradual decline in air calibration signal (measuring what is assumed to be an identical volume of atmospheric xenon), yet this is not observed.

The difference between the PCA 02007 and "Q" Vigarano II modelling of the starting number of channels is most probably not due to different instrument conditions, given their measurement within days of one another, using an identical MCP, and mostly identical instrument conditions, yet they were also modelled with different numbers of starting channels. One potential explanation is a fundamental difference between the measured and target composition. In these examples a pure target composition was used, and while this is perfectly applicable to the aerogel, which is known to only feature Earth's atmospheric xenon (this sample was not used by the Stardust mission), the same cannot be said of PCA 02007. For instance, surface correlated air contamination on PCA 02007 could be mixed with the solar wind xenon. The model cannot distinguish this mixture, so the applied saturation fractionation correction would be optimised for the wrong target composition (the regular PCA 02007 composition, instead of air with PCA 02007). Similarly, as with any natural sample measurement, the expected composition is not entirely predictable, so the target composition may simply be fundamentally different from the true unfractionated PCA 02007 composition. For even the largest of these releases, the

total fraction of modelled channels which were consumed never reached 40%, and was around 16% on average.

The wide range of modelled numbers of starting channels which feature reasonable chi-squared statistics are indicative of the model unsuccessfully capturing the processes affecting different analyses of large amounts of xenon. When considered in isolation, the experiment specific data (apart from “Q” Vigarano II) produced relatively consistent values for available channels with reasonable chi-squared statistics. Apart from the differences between the input data outlined above, there are two significant assumptions which undoubtedly affect the applicability of this model:

- *The ions which consume channels prior to the arrival of the xenon isotopes are not counted.*

  These ions impact the fraction of available channels, yet they are not accounted for in the correction factor. For example, two otherwise identical compositions may be preceded by different amounts of indirectly ionised hydrocarbons, whose compositions regularly fluctuate within RELAX. Greater or lesser volumes of hydrocarbons will directly affect the true number of starting channels available for Xe detection, whereas the ideal model assigns exactly the same starting number for all examples.

- *The starting and target compositions are assumed to be identical, except for the saturation effect.*

  As with any sample, they are not perfectly homogeneous, nor is the instrument in an identical configuration from analysis to analysis. The model’s chi-squared statistic is a measure of the similarity of two volumes of gas extracted from different locations within a sample, where heterogeneities, interferences, and instrument precision cannot be entirely removed.

The good fit for many of the models when considered in isolation indicates that the model could accurately predict the physical process causing the saturation effect. The variable acceptable number for the initial number of starting channels is most probably a reflection of differences between experiment approaches, although the PCA 02007 and "Q" Vigarano data express a difference despite nearly identical methodology and instrument conditions. The difference between modelling the PCA 02007 and "Q" Vigarano data may be due to complexity which this model ignores, as discussed in the previous two bullet points. A more comprehensive experiment to quantify the saturation effect is unlikely, given the fact that measuring large amounts of xenon at one time with RELAX defeats the purpose of having such a sensitive instrument, and is almost always an unexpected and unwanted consequence of incorrectly predicting the release of sample gas in stepped etching and heating, it is subsequently a rare occurrence. Given the strength of RELAX is to measure small amounts of sample material, an experiment designed to quantify the effects of large amounts of sample gas is not a priority, and would most probably require repeated analyses of large amounts of xenon and subsequently expose the instrument to larger than normal amounts of other gases which would accelerate the need for instrument cleaning. Ironically, an experiment designed to quantify the starting number of channels in the MCP detectors would accelerate the deactivation of MCP channels, and reduce the time before a new MCP is installed. These factors, along with the results of the modelling, make the saturation model presented here a tool for diagnosis of the effect and the complexity of introducing large amounts of xenon into RELAX, which are grounds for its mitigation.

#### 2.3.2.2. $^{130}$Xe excess

In large samples the signal of $^{130}$Xe can be affected by the scale of the $^{129}$Xe isotope signal preceding it. This phenomenon arises from the way the raw data is reduced by measuring signal areas exceeding the noise, defined by a baseline. The $^{129}$Xe baseline noise signal is typically easily established as the 'tail' of the $^{128}$Xe isotope signal peak preceding it is close to the noise baseline by the time the first $^{129}$Xe ions are detected. However, large $^{129}$Xe signals 'bleed' into the following $^{130}$Xe signal. Whether this occurs by slower $^{129}$Xe ions arriving at the detector as the first $^{130}$Xe ions are arriving, or by some means of signal broadening within the instrument electronics, is unclear.

The means of establishing isotope signal with the RELAX mass spectrometer requires measuring the area of signal peak above a baseline. This baseline, of what is essentially noise, is typically established before and after each isotope signal, then averaged and subtracted from the ion signal area. However, the baseline cannot be easily established when the signals of $^{129}$Xe and $^{130}$Xe cannot be resolved from one another.

Isotope signal peak areas measured with the spectrum topography are subsequently flawed in the instances where individual isotope peaks cannot be resolved. Either the baseline is defined by the average values defined elsewhere, leading to part of the $^{129}$Xe signal tail being attributed to $^{130}$Xe, or the user could define a new baseline specifically for the $^{130}$Xe peak, in which the definition of where it begins is difficult to establish.

For evaluating this phenomenon, it is most useful to consider its effect upon the $^{130}$Xe/$^{129}$Xe ratio in the circumstance where an average baseline is applied. In this circumstance, the reported $^{130}$Xe signal features an excess proportional to the $^{129}$Xe signal preceding it. However, as proven in the previous section, the instrument sensitivity

changes with each isotope as channels are deactivated by ions. The combination of the tail bleed and saturation effect makes any interpretation of $^{130}$Xe in large releases difficult, as its attribution to either phenomena, or the sample itself, are hard to quantify.

A dataset with a known composition measured with and without tail bleed, and corrected for saturation (with the model of Section 2.3.2.1), should allow us to isolate the tail bleed effect. Once corrected for saturation, any enrichment of the $^{130}$Xe/$^{129}$Xe ratio from its expected concentration can be assumed to result from the tail bleed effect. If this theory is correct, increasing amounts of $^{129}$Xe signal should progressively encroach upon the $^{130}$Xe signal peak area, increasing the $^{130}$Xe signal above its expected area. This $^{130}$Xe/$^{129}$Xe excess should also positively correlate with $^{129}$Xe signal.

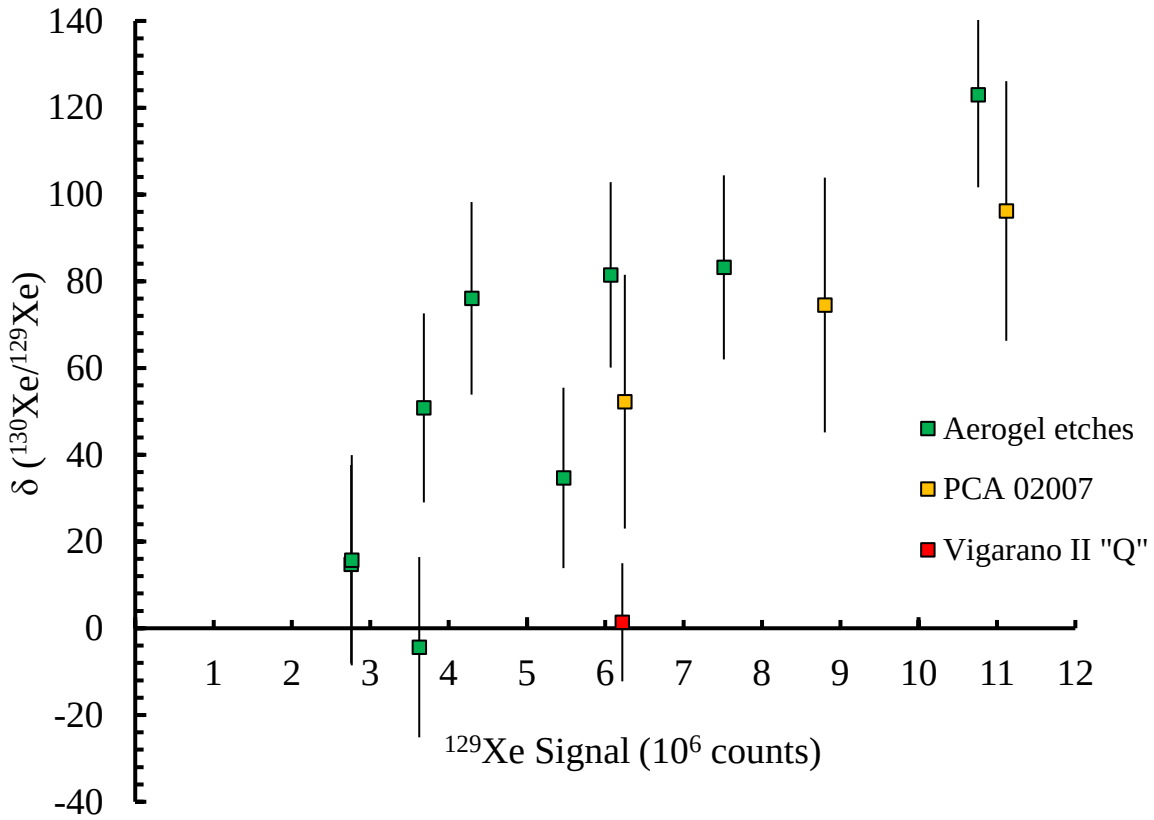


***Figure 2.6*** *$^{136}$Xe excess as a function of $^{129}$Xe signal for large amounts of xenon in RELAX. Ordinate exhibits $^{130}$Xe/$^{129}$Xe excess relative to expected ratios (expressed as a ratio). Abscissa exhibits $^{129}$Xe signal in millions of counts.*

Figure 2.6 illustrates the tail bleed effect as an increased excess in $^{130}Xe/^{129}Xe$ with an increased $^{129}Xe$ signal. This relationship appears to be expressed as a roughly linear correlation. In its current state, these results only provide a proof of concept, as deducing a 'true' $^{130}Xe/^{129}Xe$ ratio requires extrapolating the linear relationship between $^{130}Xe/^{129}Xe$ excess from Figure 2.6 (which would be fairly straightforward), and use of the saturation model of Section 2.3.2.1 to correct for saturation. Given the fact the saturation model as described in Section 2.3.2.1 does not entirely model the phenomenon it was designed to capture, a tail bleed correction is not available by this method. With more data from large releases, the tail bleed could be better quantified, but the existence of this phenomenon is ironically grounds for avoiding large releases. As in the case of the saturation effect modelling, a comprehensive review of the effect would require an experiment in which large amounts of xenon are introduced to RELAX, the adverse effects of this and reasons why this is inappropriate for the fundamental purpose of RELAX are outlined at the end of Section 2.3.2.1.

An alternative method for determining and correcting for tail bleed may be provided in modelling the $^{129}Xe$ peak shape using isolated isotope signal peaks. Changing the size of the peak of such an isotope, such as $^{136}Xe$, to reflect the $^{129}Xe$ signal peak, would allow its subtraction from the $^{130}Xe$ signal area where their signal areas overlap. This technique assumes the shape of each isotope signal is identical, which is unproven, but avoids the use of the saturation model, which is unreliable at present. In practice, samples where large releases of xenon from a sample are expected are treated with caution, and every attempt is made to reduce the chance of the phenomena which accompany and change the composition of large releases. The RELAX user has a number of options to avoid the amount of gas which causes these effects:

- *Anticipate samples with large concentrations.*

  Research published concentrations of sample being analysed. If a concentration is known, and there is a precedence for how similarly composed samples diffuse xenon, the amount of sample material or gas extraction approach can be tailored for a particular amount of xenon (such as is attempted in Chapter 4 for the volcanic glasses of Apollo 15 and 17). However, this information is not always available.

- *Alter the ionisation process to reduce sensitivity.*

  If an unexpectedly large signal is measured, the delay between the heating laser and ionising laser can be changed, decreasing the efficiency of ionisation and ion flux to the detector. This approach reduces the sensitivity (lower ionisation efficiency), so artificially reduces the ions incident upon the detector. However, it also affects mass discrimination by ionising atoms of a different energy distribution to normal (see Section 2.1). Quantifying this affect would require an investigation similar to that for saturation and tail bleed using air calibrations featuring the same delay. Given that this approach introduces an instrument mass fractionation which has not been quantified, it considered a last resort alternative before pumping the sample gas out of the ionisation volume.

- *Measure an aliquot of the sample gas.*

  Gas extracted from a sample may be partitioned before introduction to the mass spectrometer if it is expected to be large volume. This technique requires isolating a known portion of sample gas for analysis while the rest of the sample aliquot remains outside the ionisation volume.

- *Leave the gas uncondensed within the ionisation volume.*

  In this instance, the cold spot within the ionisation volume can be left at ambient temperature, so that xenon is not condensed upon it. Again, this technique is purely employed in situations where the amount of xenon being analysed is assumed to be large enough to cause problems in detection or interpretation. However, this approach introduced its own interpretation problems in that it has an effect upon the velocities of the xenon atoms before ionisation, which would otherwise be in a relatively predicable plume. This affects mass resolution more significantly than saturation or tail bleed, so is only employed when a high ionisation efficiency is expected to significantly saturate the detectors.

# 3. Modelling mixtures of Solar System reservoirs

## 3.1. Introduction

All reservoirs of noble gases in the Solar System may be defined as end members, or mixtures and modifications of any number of end members, defined by their isotopic compositions (see Table 3.1 and Section 1.3). Such end members are useful compositions of known provenance, history or prominence in our Solar System, and are the first reference for identifying an unusual noble gas composition. Reconstructing compositions using mixtures and modifications of end members allow us to trace the environments and processes which produced them and their host materials.

A fundamental tool used to explore noble gas compositions is the three-isotope coordinate plot, in which isotope ratios are plotted in two-dimensional space. Three isotope plots feature two isotope ratios as their ordinate and abscissa, both with common denominators. Compositions are then plotted accordingly alongside end members they are suspected to be composed of. For example, you may expect low temperature heating steps of a lunar regolith sample to release noble gases of adsorbed terrestrial atmospheric composition, high temperature steps to release a solar wind composition, and intermediate steps to be a fractional evolution of low temperature to high temperature component. A three-isotope plot of this would feature atmosphere and solar wind as end members, and measured compositions for each heating step showing a linear progression from former to latter (left plot of Figure 3.1). This simple linear feature indicating two-component mixtures is known as a mixing line. If such a sample contains an additional component, such as radioactive decay, then you would plot this as another end member, creating an area defined by the three mixing lines between each end member. The data would then plot according to the fraction of each end member they contain (see Figure 3.1).

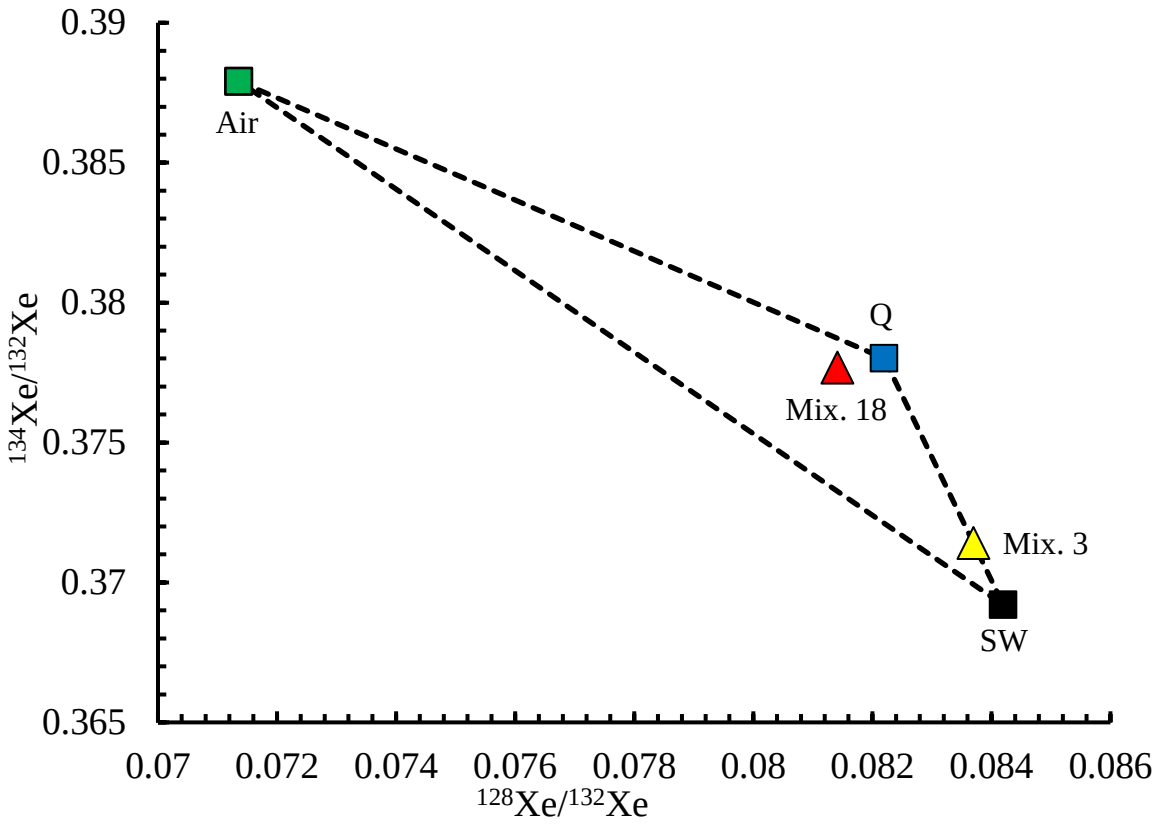


***Figure 3.1*** *Three-isotope plot of $^{128}Xe/^{132}Xe$ (abscissa) and $^{134}Xe/^{132}Xe$ (ordinate) with synthesised mixtures 3 (yellow triangle) and 18 (red triangle) of Table 3.2, and end members; Earth's atmosphere (green square), Q-Xe (blue square), and solar wind (black square). End member compositions listed in Table 3.1. Dashed lines indicate two-component mixing lines between the two attached end members. Mixture 3 is composed of a two-component mixture, Mixture 18 is composed of a three-component mixture.*

Three isotope plots are particularly useful for elements with fewer isotopes and samples with fewer predictable and pure end members, but encounter problems as these variables increase in complexity and number. Which isotopes do you plot when end members are defined by more than three isotope ratios? Which of these plots do you trust if their interpretations conflict? How do you account for fractionation within a multiple component mixture? These questions may be answered with multiple plots and a comprehensive understanding of the isotopic system of an element, but they expose the limitations of this tool. Even with this understanding, it is difficult to extract statistical and numerical measures of the interpretations you may draw from three isotope plots.

Compositional analyses in noble gas geochemistry frequently describe bespoke mathematical models for a more focussed untangling of noble gas compositions in specific problems. For example, Pepin (1991) describes models for terrestrial planet and meteoritic noble gas reservoirs. Elemental and isotopic ratios of noble gases and hydrogen are mixed and fractionated in order to reconstruct present reservoirs. Modelled solution fits are improved by trial and error, with the user tweaking variables in a spreadsheet. Marty et al. (2017) describes models in which xenon isotopes measured in comet 67P/Churyumov-Gerasimenko is recreated by varying mixtures of other noble gas reservoirs. Data are generated by Monte Carlo simulations of incrementally changing combinations of variables, with the best fit solution being the one with the lowest chi-squared value. These models combine mathematical simulations of real-world phenomena into bespoke solutions for a specific scenario (such as a component composed of multiple end members) without provision for interchangeability (by considering fractionation, or adding/removing isotopes), or public accessibility (beyond rebuilding the models).

There are fewer examples of widely available models with more general applications. One example is Isoplot (Ludwig, 2008), a toolkit for Microsoft Excel which can extract isochron data from two and three dimensional plots (three isotope ratios with common denominator), along with a suite of other isochron related features. Gilmour (2018) describes Samaritan, a Microsoft Excel workbook built with Visual Basic for Applications functions and macros to model linear combinations of xenon end members to a given isotopic composition in atoms. The model solution is presented as fractional contributions from chosen end members and a chi-squared per degree of freedom goodness of fit. Samaritan provides a more automated approach to modelling xenon isotopic compositions than the trial-and-error approaches described in Pepin (1991) and Marty et al. (2017), yet lacks their versatility in being able to apply fractionations and the inclusion of other volatiles.

A modelling platform which combines the automation and functionality of Samaritan with the scope of processes described in Pepin (1991) and Marty et al. (2017), and the accessibility of Isoplot would be invaluable as a laboratory and theoretical modelling tool in noble gas cosmochemistry. Automaton is a noble gas modelling platform developed for this work to satisfy these criteria for the modelling of mixtures and fractionations of noble gas reservoirs (Lawton, 2020).

### 3.2. Automaton

The following section describes the architecture, function, and testing of Automaton, a noble gas modelling platform written in Visual Basic for Applications macros and functions in a Microsoft Excel workbook (Lawton, 2020). Automaton creates a modelled xenon composition using user-defined end members and automatically optimises its constituent fractions and fractionations by minimising a chi-squared statistic in order to match a target composition. Automaton can process any number of isotopes, and account for fractionation of any input component of choice, or the ultimate modelled composition. Each stage accounts for the precision of input components, and propagates the errors throughout. This may be repeated in a Monte Carlo simulation with as many iterations as desired, and produces an array of possible solutions. The coding and databases referenced herein are contained within macros and spreadsheets embedded in a central Automaton Microsoft Excel workbook. Data concerning end member and target compositions, and fractionation regimes are entirely contained within the central Microsoft Excel workbook, to allow for easy replacement. Similarly, the addition, removal, and limiting of variables is conducted in the central Microsoft Excel workbook. A description of the mathematical methodology of optimising and manipulating modelled compositions in Automaton is presented in Section 3.2.1, followed by an evaluation of Automaton's performance and limitations compared to Samaritan (Gilmour, 2018), the most similar existing modelling

platform, in Section 3.2.2, and finally an example of how a user may interact with Automaton's interface in Section 3.2.3.

### 3.2.1. Methodology

The user must first define a 'target' xenon composition for Automaton to recreate. This may be a measured or hypothetical composition featuring any number of isotope ratios with any denominator. The target composition is then 'expanded' into a list of compositions corresponding to the amount of Monte Carlo simulations the user wishes Automaton to consider, all defined and executed within a spreadsheet of the Automaton workbook. In this expansion, probability density functions are defined for each isotope ratio in which the area beneath a normal distribution between compositional limits is the probability of measuring a value between those limits (Equation 3.1). The input data are assumed to follow a Gaussian distribution, where the probability density function can be defined as in Equation 3.2, using the standard deviation and mean of the measured values.

$$\int f(x)dx = 1$$

***Equation 3.1*** *Normalisation of isotope composition distribution such that the area reaches unity, a probability density function.*

$$f(x|\mu,\sigma^2) = \frac{1}{\sqrt{2\pi\sigma^2}} e^{-\frac{(x-\mu)^2}{2\sigma^2}}$$

***Equation 3.2*** *Probability density function relating isotope ratio mean, $\mu$, and standard deviation, $\sigma$, to probability of attaining isotope ratio, $x$, assuming Gaussian distribution.*

The uncertainties around an isotope ratio actually follow a Cauchy distribution, but can be approximated by a normal distribution if the error is small compared to the ratio, and the ratio is less than one. This approximation is improved by the fact most major reservoirs of xenon share $^{132}$Xe as their most abundant isotope, and feature relatively minor uncertainties relative to their isotopic ratio values (see Table 3.1), although its implications

are exposed in the modelling of a Section 3.2.2.1. The use of isotope ratios, which is unavoidable when modelling with end members, also means the errors of each ratio are subsequently related by their normalising isotope. Apart from propagating errors through the normalising equations, Automaton's calculations assume isotopic ratio uncertainties are independent.

The probability function is rearranged to produce an isotope ratio when fed an evenly distributed random real number greater than or equal to zero and less than one. Automaton applies this process to each isotope ratio of the input target composition for as many iterations as the user wants to be considered in the Monte Carlo simulation, populating an array of expanded target compositions where $\mu_{Array} = \mu_{Input}$, and $\sigma_{Array} = \sigma_{Input}$ for every isotope. The inclusion of errors in the input target composition, or the choice of whether an input target composition featuring errors is expanded, is optional, so Automaton can be fed a list of identical 'absolute' target compositions for modelling. Each iteration of the expanded target composition is ultimately solved individually in sequence by Automaton.

Before Automaton models any composition, the user must define the parameters within which Automaton can recreate each expanded target composition. These parameters are defined by changing values of cells acting as switches and limits within the Automaton workbook. The user must first define at least one end member to include in the modelling. Selection of one end member limits the model to fractionation of that composition, whereas multiple end members may be mixed, fractionated, or both. The parameters for mixing and fractionation of each end member are customisable as follows:

- *Which isotopes should Automaton consider?*

  This is particularly useful for compositions featuring large monoisotopic excesses, such as artificially irradiated samples containing large amounts of iodine, or for compositions with a particular isotope ratio featuring large uncertainties.

- *Is the end member composition 'absolute'?*

  This option changes whether end member compositions are to be 'expanded' before modelling according to their errors as in Equation 3.1 and Equation 3.2, or treated as absolute, with a static composition. Expansion of end members may be useful when a target composition is defined as absolute.

- *Define a minimum, maximum, or fixed fraction coefficient.*

  This may be of use when a radioactive contribution is known, such as after artificial irradiation with a known neutron flux and target isotope concentration.

- *Define the polarity of the fraction coefficient.*

  This could be used to simulate the removal of a reservoir, such as atmospheric loss, or material loss due to giant impact.

- *Should the model apply fractionation to this end member?*

  Each end member may be subject to fractionation prior to homogenisation, or the target composition may simply be a fractionated version of one end member.

- *Which model of fractionation should be used?*

  Non-linear fractionation models may be considered, and added as needed.

- *Define a minimum or maximum for fractionation.*

  This parameter limits the degree of fractionation applied to each end member. Possibly used in a situation where the degree of fractionation is already known, or it is beneficial to be limited to a more realistic magnitude.

- *Define the polarity of the fractionation.*

  The target composition may be considered an unfractionated precursor to an end member if fractionation is negative. Likewise, a positive fractionation posits a target composition resulting from fractionation of the end member.

- *Define whether to introduce post-mixture fractionation.*

  This allows the entire mixture to be fractionated as though the modelled mixture were a finished article. Automaton can vary this simultaneously with all previous variables such as the fractional contributions of end members and their individual fractionation. The user may also define limits and the nature of fractionation employed.

Different fractionation models are implemented using the mass dependent fractionation laws of Young et al. (2002), which uses a mass relationship parameter, β, as an exponent to calculate the difference between a pair of isotope ratio in a reference composition, and a fractionated composition, as in Equation 3.3. Three models for fractionation from Young et al. (2002) were included in Automaton during this work, defined by mass relationship parameters for equilibrium fractionation (Equation 3.4), kinetic fractionation (Equation 3.5), and gravity/centrifugal fractionation (Equation 3.6), each defined by separate mass relationship parameters.

Figure 3.2 compares the application of each of these fractionation models on ratios of terrestrial air xenon, showing that they barely deviate from linearity outside of extreme fractionation. The modelling in this work generally uses the equilibrium fractionation model unless stated, which uses the mass relationship parameter, β, as defined as in Equation 3.4. This model was selected due to it most closely resembling linear mass fractionation, which is typically the standard in noble gas cosmochemistry.

$$^{2/1}R = {}^{3/1}R^{\beta}\left({}^{2/1}R_{ref}/{}^{3/1}R_{ref}^{\beta}\right)$$

***Equation 3.3*** *Formula for fractionation curve in three-dimensional space where $^{2/1}R$ and $^{3/1}R$ are the isotope ratios between isotopes of masses 1, 2, and 3, and $^{2/1}R_{ref}$ and $^{3/1}R_{ref}$ are the isotope ratios for a reference material on the curve. The reference material data in Automaton are isotopic compositions prior to the application of fractionation. Uses a mass law exponent, β, as defined in Equation 3.4, 3.5, and 3.6. From Young et al. (2002).*

$$\beta = \left({}^{1}/_{m_1} - {}^{1}/_{m_2}\right)/\left({}^{1}/_{m_1} - {}^{1}/_{m_3}\right)$$

***Equation 3.4*** *Definition of mass law exponent, β, in equilibrium fractionation of Young et al. (2002), used to relate fractionation of isotopes 1, 2, 3, of atomic masses $m_1$, $m_2$, and $m_3$, respectively. Note requirement that $m_1 < m_2 < m_3$.*

$$\beta = ln\left({}^{m_1}/_{m_2}\right)/ln\left({}^{m_1}/_{m_3}\right)$$

***Equation 3.5*** *Definition of mass law exponent, β, in kinetic fractionation of Young et al. (2002), used to relate fractionation of isotopes 1, 2, 3, of atomic masses $m_1$, $m_2$, and $m_3$, respectively. Note requirement that $m_1 < m_2 < m_3$.*

$$\beta = (m_1 - m_2)/(m_1 - m_3)$$

***Equation 3.6*** *Definition of mass law exponent, β, in gravitational fractionation of Young et al. (2002), used to relate fractionation of isotopes 1, 2, 3, of atomic masses $m_1$, $m_2$, and $m_3$, respectively. Note requirement that $m_1 < m_2 < m_3$.*

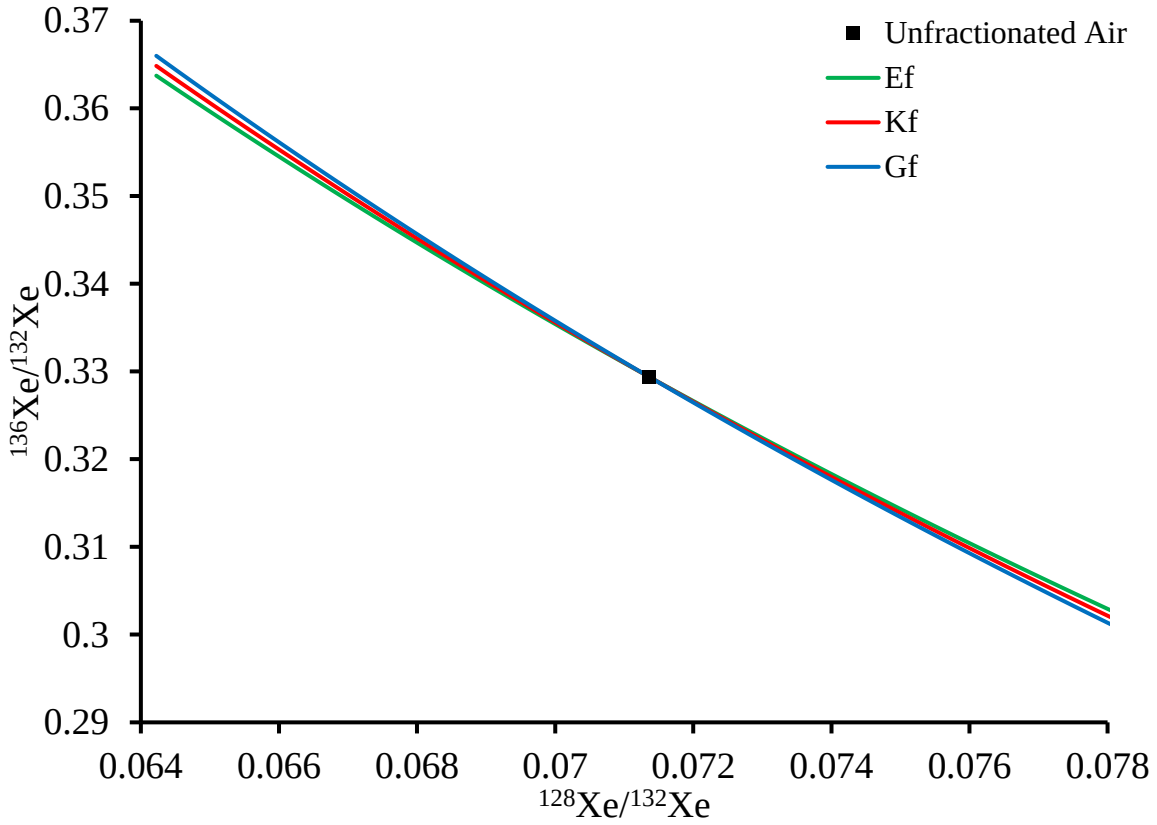


***Figure 3.2*** *Fractionation models available to Automaton and their effects upon air ratios of $^{136}Xe/^{132}Xe$ when $^{128}Xe/^{132}Xe$ is varied by ± 100 ‰. Fractionation models from Young et al. (2002): Ef, equilibrium fractionation (green), Kf, kinetic fractionation (red), and Gf gravity/centrifugal fractionation (blue).*

$$\chi^2 = \sum_{i=1}^{n} \frac{(x_i - \mu_i)^2}{\sigma_i^2}$$

***Equation 3.7*** *Chi-squared statistic ($\chi^2$) definition, with n independent variables $x_i$ normally distributed with mean $\mu_i$, and variance $\sigma_i^2$. In an ideal solution, the fraction approaches unity. The chi-squared value is divided by degrees of freedom to give the reduced chi-squared statistic.*

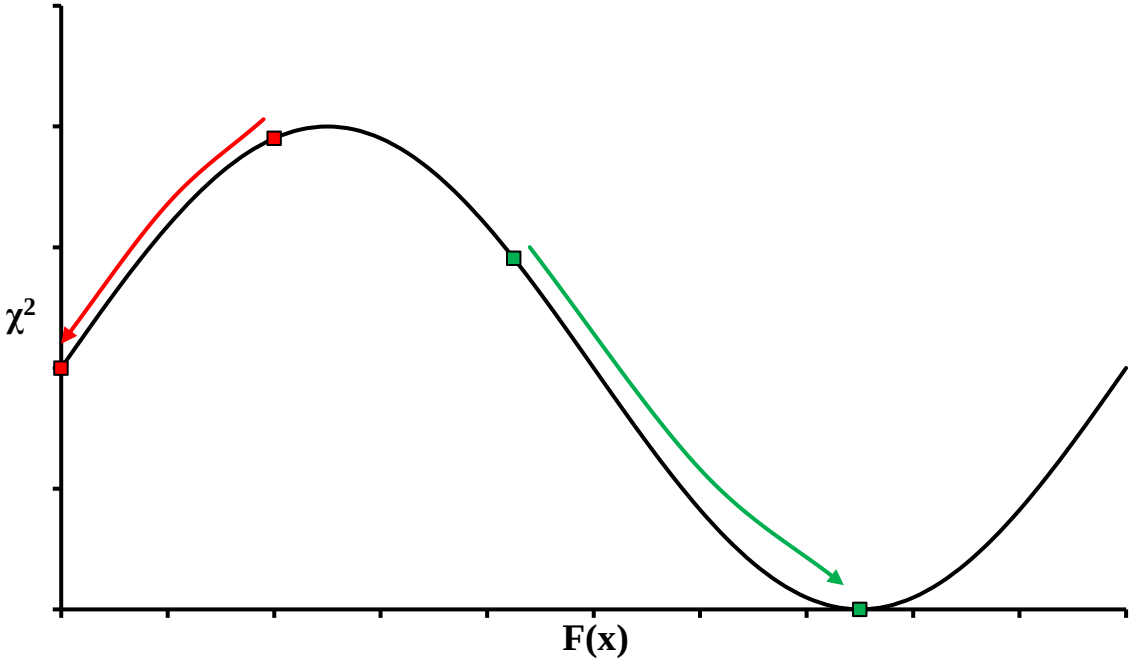


***Figure 3.3*** *Example of variable seeding finding two local chi-squared minima solutions. Arrows indicate optimisation direction of minimisation algorithm, green and red points indicate starting and resultant values of the variable, x, after optimisation.*

Once all parameters have been defined, Automaton is ready to consider the first iteration of the expanded target composition. Automaton retrieves the selected end members and their parameters, which are seeded by random number selection within the user-defined ranges, and combines them to produce a modelled composition. This modelled composition is the product of mixing each simulated end member composition after all modifications and fractions are applied, and is continually compared to the target composition using a chi-squared statistic (Equation 3.7). This chi-squared value is a measure of how closely the target and modelled compositions match, and by extension the accuracy of the modelled composition. Excel's Solver function iteratively reduces this chi-squared value by changing the variables within the user-defined limits, and settles on a

final set of variables when the chi-squared value is minimised. This optimised suite of values for each variable is recorded with its corresponding chi-squared goodness of fit statistic in a separate array. This process is then repeated with the next synthesised target composition and fresh seeds for each variable, until the entire array of target compositions has an equivalent array of solutions. The array of solutions subsequently contains a probabilistic measure of what combination of variables combine to produce the target composition within the defined parameters, and how closely these solutions match the target composition. Additionally, the solutions being presented as an array allows the user to scrutinise each individual 'sub-solution' in order to identify features only evident on the scale of a singular iteration (such as in Figure 3.8 and Figure 3.13).

Automaton's algorithm for minimising a chi-squared statistic by optimising variables could result in the discovery of false minima. In these instances, the optimisation algorithm becomes 'stuck', where an incremental increase or decrease in the variables results in a larger chi-squared statistic, despite being closer to the true solution. This results from the minimisation algorithms employed by Automaton being unaware of multiple minima in the chi-squared statistic. A partial solution written into Automaton is its random selection of initial values for each variable within the predefined parameters before running each optimisation routine. With multiple simulations this routine will find the local minima based on the input variable as it follows the minimisation algorithm to the closest chi-squared statistic minima (as in Figure 3.3). This approach will find more of these solution minima as a function of the number of simulations, the number of variables included in the fit, and the magnitude of variation allowed. Automaton allows the user to define variables as absolute, or confine them within defined limits, if physically implausible minima are disproportionately favoured, thus reducing the frequency of false minima solutions. Individual sub-solution scrutiny can also make false minima more evident, and allow the user to revise parameters to avoid or explore them (as in Figure 3.9).

### 3.2.2. Validation and limitations

The following sections attempt to validate and constrain the functionality, precision, and accuracy of modelling with Automaton. These attributes are first tested by modelling synthesised compositions with known fractions of end members (Section 3.2.2.1). This testing is run in parallel with Samaritan (Gilmour, 2018), the closest equivalent modelling platform for xenon isotopic mixtures. This is followed by a more focussed exploration of the effects that input data uncertainty have on Automaton's modelling results, in which the results of Automaton modelling synthesised compositions with identical isotope ratios but different uncertainties are compared to one another (Section 3.2.2.2). Synthesised compositions in this section are linear fractional mixtures of end members contained in Table 3.1. Both subsections give an insight into the modelling limitations of Automaton, and how its results should be interpreted.

These validations are not intended to be comprehensive; selections containing different end members, more components, and finer incremental variations in fractions of components would uncover more statistical curiosities with implications for nuances of the applications of Automaton. This testing also neglects the theoretical physical implications of the modelling, advised by knowledge of the system the mixtures were produced in. For example, a model may be numerically satisfied with a mixture containing a large fraction of a spallation component, yet the composition was measured in a material whose chemistry forbids the physical plausibility of the modelled solution. The user must therefore consider the numerical and physical implications of all solutions, and iteratively improve the input parameters based on those results. The results must then be interpreted in light of the limitations explored in the following sections.

***Table 3.1*** *Isotopic compositions of significant xenon end member reservoirs, radiogenic yields, and compositions used herein.*

| End Members | Xenon Isotopic Compositions Normalised to $^{132}Xe \equiv 100$ | | | | | | | | | | | | | | | | Reference |
|---|---|---|---|---|---|---|---|---|---|---|---|---|---|---|---|---|---|
| | 124 | | 126 | | 128 | | 129 | | 130 | | 131 | | 134 | | 136 | | |
| *Earth Atmosphere (Air-Xe)* | 0.35 | - | 0.33 | - | 7.14 | - | 98.32 | - | 15.14 | - | 78.90 | - | 38.79 | - | 32.94 | - | *n/a* |
| *Primordial Earth Atmosphere (U-Xe)* | 0.48 | (0.002) | 0.42 | (0.002) | 8.41 | (0.013) | 103.95 | (0.14) | 16.54 | (0.02) | 82.62 | (0.13) | 35.16 | (0.07) | 27.40 | (0.06) | *a* |
| *Martian Atmosphere* | 0.47 | (0.025) | 0.40 | (0.04) | 7.47 | (0.077) | 252.21 | (0.63) | 15.37 | (0.094) | 81.23 | (0.29) | 40.21 | (0.26) | 34.52 | (0.22) | *b* |
| *Martian Atmosphere (Spall. Corrected)* | 0.40 | (0.028) | 0.31 | (0.048) | 7.27 | (0.08) | 252.21 | (0.63) | 15.29 | (0.98) | 78.82 | (1.66) | 40.26 | (0.27) | 34.51 | (0.23) | *b* |
| *67P/Churyumov-Gerasimenko* | - | - | - | - | 8.01 | (2.3) | 146.00 | (13.5) | 19.90 | (5.33) | 88.80 | (10) | 21.20 | (4.6) | 11.30 | (4.72) | *c* |
| *Solar Wind (SW-Xe)* | 0.48 | (0.006) | 0.42 | (0.009) | 8.42 | (0.02) | 104.01 | (0.1) | 16.49 | (0.04) | 82.63 | (0.13) | 36.92 | (0.07) | 30.03 | (0.06) | *d* |
| *Q-Xe* | 0.46 | (0.002) | 0.41 | (0.002) | 8.22 | (0.02) | 104.20 | (0.2) | 16.19 | (0.03) | 81.85 | (0.08) | 37.80 | (0.11) | 31.64 | (0.08) | *e* |
| *Ba Spallation* | 51.7 | (16.21) | 95.0 | (29.76) | 153.9 | (48.27) | 151.9 | (60.91) | 118.5 | (37.25) | 414.0 | (129.8) | 6.55 | (2.446) | - | - | *f* |
| *REE Spallation* | 1283.0 | (1497) | 1666.0 | (1944) | 2033.0 | (2372) | 2666.0 | (3181) | 66.6 | (168) | 2733.0 | (3213) | 0.00 | (0) | - | - | *f* |
| *Martian Spallation* | 120.8 | (3.41) | 198.4 | (5.118) | 299.4 | (8.97) | 350.2 | (12.43) | 131.3 | (4.38) | 632.9 | (33.95) | 6.2 | (0.25) | - | - | *b* |
| *$^{235}U$ Fission* | - | - | - | - | - | - | - | - | - | - | 67.6 | (1.1) | 183.0 | (2.1) | 148.8 | (1.3) | *g* |
| *$^{238}U$ Fission* | - | - | - | - | - | - | 0.1 | (0) | - | - | 14.4 | (0.11) | 143.5 | (0.3) | 173.3 | (0.3) | *h* |
| *$^{244}Pu$ Fission* | - | - | - | - | - | - | 5.4 | (6.2) | - | - | 27.8 | (2.4) | 106.1 | (3.7) | 112.9 | (3.8) | *h* |

*Ratios normalised to $^{132}Xe \equiv 100$. Empty cells indicate no production of the certain isotope by the process in the respective end member. Parentheses contain standard deviations. References: [a] Pepin (1991) [b] Conrad et al. (2016) [c] Marty et al. (2017) [d] Meshik et al. (2014) [e] Busemann et al. (2000) [f] Hohenberg et al. (1981) [g] Ragettli et al. (1994) [h] Podosek and Ozima (2000).*

#### 3.2.2.1. Comparing results of Automaton and Samaritan

The following section considers the results of modelling a number of increasingly complicated synthesised mixtures of end members (listed in Table 3.1) to validate the accuracy and precision of Automaton compared to the same mixtures run in the Samaritan program of Gilmour (2018), the closest equivalent modelling platform for noble gas mixtures. Both models share a similar architecture, being written within macros and functions of Microsoft Excel workbooks, optimising goodness of fit with a chi-squared statistic using Microsoft Excel's Solver, and employing Monte Carlo simulations. Samaritan differs from Automaton in that it starts with a target isotopic composition in atoms, so is better suited to model with data acquired from laboratory samples. Samaritan also features less functionality with modelling fractionation compared to Automaton. Automaton was written specifically to model end members, so purely considers isotopic ratios.

Synthetic mixtures were produced by combining linear fractions of end members (listed in 'True fractions' column of Table 3.2), where isotope ratios normalised to $^{132}Xe$ were multiplied by their corresponding 'True fractions' coefficient and added together. Errors for the synthesised mixtures were calculated by assuming a total of one million atoms of $^{132}Xe$ for each synthesised mixture (by multiplying the isotope ratios by one million), and defining the error for each isotope as the square root of the corresponding number of atoms (listed in atoms in Appendix 3A.1). In the case of Automaton, each synthesised mixture was then normalised to $^{132}Xe$ again and expanded to 100 compositions to be run sequentially as part of a Monte Carlo simulation. This expansion is identical to the method explained in 3.2.1. Samaritan is designed to model with the isotopic composition in numbers of atoms, so the input compositions were the data after the one million atom multiplication and error definition (exactly as contained in Appendix 3A.1).

Automaton and Samaritan were then set up to recreate each synthesised mixture by modelling all xenon isotopes of the end members used to produce each synthetic mixture (compositions in Table 3.1), with no limits on the allowed fractions, and no fractionation. The results of this validation are presented in Table 3.2.

The two-component mixture tests (1 − 10) of SW-Xe and Q-Xe in varying proportions were correctly solved by Automaton and Samaritan which both returned fractional percentages within a standard deviation (all below 4%) of the true value. The end members constituting the largest fractions of the synthesised three-component mixtures were solved to within a few percent of the true value for each mixture, typically being within one standard deviation of the true value. However, Automaton exhibited a consistent underestimation of the synthesised Ba spallation fractions of 10% (mixtures 11 - 19), returning a value of ~ 9.5% and a small standard deviation ($\sigma_{Ba}$ <0.03%) which does not envelop the true value. Samaritan exactly determined the true fraction of Ba spallation in all of the three-component synthesised mixtures reliably (with similarly low standard deviations ($\sigma_{Ba}$ < 0.04%).

Apart from the standard deviations for the Ba spallation fractions, Automaton's solution arrays exhibited consistent standard deviations throughout the two and three-component modelling. Samaritan exhibited modelled fractions with increased scatter (apart from Ba spallation) for three-component mixtures with larger disparities between their true fractions, as shown by the larger standard deviations for modelled Q and SW fractions in solutions 11 ($\sigma_Q$ = 8.7, $\sigma_{SW}$ = 8.9) and 19 ($\sigma_Q$ = 14.9, $\sigma_{SW}$ = 15.4), compared to the solutions for mixtures 14, 15 and 16 (with average $\sigma_Q$ = 3.67, and average $\sigma_{SW}$ = 3.77), which featured less pronounced end member fraction disparities.

The results suggest both Automaton and Samaritan are reliably precise in modelling the fractions of two-component mixtures of Q-Xe and SW-Xe compositions. Automaton and Samaritan expressed no decreased precision or accuracy with an increased disparity between fractional contributions of mixtures, and both modelling platforms returned similar standard deviations for all two-component synthesised mixtures. Automaton and Samaritan also appear capable of modelling three-component mixtures of Q-Xe, SW-Xe and Ba spallation consistently to within a couple of percent of the true value (typically within one standard deviation).

Automaton's consistent underestimation of the fraction of Ba spallation in the three-component synthesised mixtures (~ 0.5% from the true value) is not reflected in similarly low true fractions of SW-Xe and Q-Xe (as in mixtures 11, 12, 18, and 19), suggesting its cause is related to its handling of Ba spallation as an end member. The Ba spallation specificity of this phenomenon is backed up by the Ba spallation fraction standard deviations being two orders of magnitude lower than those of SW-Xe or Q-Xe, a feature also expressed in the Samaritan results. Automaton's modelled Monte Carlo simulation solutions for the three-component mixtures (excluding Ba spallation) exhibited a consistently low average standard deviation of 3.4% ± 0.7%. Samaritan's equivalent average standard deviation was 8.3% ± 5.4%, mostly as a result of the increased scatter for the solutions concerning synthesised mixtures with more disparate end member fractions (11, 12, 18, 19). This suggests Automaton could more accurately model minor contributions from end members than Samaritan.

The barium specific modelling uncertainty expressed by Automaton may be the product of its consideration of isotopic ratios normalised to a common denominator. The composition of Ba spallation is significantly enriched in $^{124}$Xe, $^{126}$Xe, and $^{131}$Xe, which are significantly more abundant than $^{132}$Xe. The normalisation to $^{132}$Xe therefore introduces a

significant error, as this isotope is defined with less certainty, as evident in the relative uncertainties between isotopic compositions of other end members compared to Ba and REE spallation in Table 3.1, as neither feature $^{132}Xe$ as their most abundant isotope. The relatively large uncertainties of these isotope ratios may result in the assumption of a Gaussian distribution being incorrect, which manifested in a systematic underestimation of the contribution of Ba spallation. Samaritan, on the other hand, modelled Ba spallation as a variable component normalised to the more abundant isotope $^{126}Xe$, so did not introduce significant systematic error.

The reduced scatter of Automaton's results compared to Samaritan for modelling of three-component mixtures excluding barium may be the result of the difference in both models considering isotopic ratios or atomic compositions. In Samaritan, the mathematical solution can feature negative numbers of atoms, so numbers of atoms corresponding to the less abundant components may spill into negative values. This increased range of solutions will result in a larger scatter than a model such as Automaton, that did not allow negative values in this modelling. Samaritan may also express different scatter due to its atomic approach resulting in different handling of covariances compared to Automaton's ratio-based modelling. In normalising to a particular isotope, ratios introduce the stochastic error of the normalising isotope as a systematic error in all other normalised ratios. Automaton and Samaritan ignore the introduction of this systematic error and treat errors as stochastic. The effect of these different approaches is possibly evident in the different scatter of modelled solutions, as the models otherwise function similarly in this application.

Automaton is clearly a capable modelling platform for linear mixtures of end members, matching and sometimes exceeding the performance of Samaritan in all but the modelling of Ba spallation, which is still fairly precisely modelled (to within half a percent of the true value). The peculiarities in these results are sufficiently explained and are

unlikely to be problematic in the application of Automaton to modelling scenarios where all components are normalised to a major isotope (as is observed in the end members used in Section 3.3). The results of Section 3.3 illustrate that even if an end member normalised to a minor isotope were used, the precision being incorrect within a few percent is frequently insignificant compared to the uncertainty in the modelled solutions.

***Table 3.2*** *Synthesised Xe mixtures solved with Automaton and Samaritan.*

| Synthesised Mixtures | | | Modelled Solutions | |
|---|---|---|---|---|
| Reference # | End Members | True Fractions (%) | Automaton (% ± σ) | Samaritan (% ± σ) |
| 1 | Q-Xe | *5* | 5 ± 2.6 | 5.2 ± 2.6 |
| | SW-Xe | *95* | 95.2 ± 2.6 | 94.8 ± 2.6 |
| 2 | Q-Xe | *15* | 14.9 ± 3 | 14.5 ± 2.5 |
| | SW-Xe | *85* | 85.1 ± 3 | 85.5 ± 2.5 |
| 3 | Q-Xe | *25* | 24.9 ± 3 | 24.5 ± 3.3 |
| | SW-Xe | *75* | 75.1 ± 3 | 75.1 ± 3.3 |
| 4 | Q-Xe | *35* | 35 ± 3 | 35.1 ± 3.1 |
| | SW-Xe | *65* | 65 ± 3 | 64.9 ± 3.2 |
| 5 | Q-Xe | *45* | 45.3 ± 3 | 45.1 ± 2.7 |
| | SW-Xe | *55* | 54.7 ± 3 | 54.9 ± 2.7 |
| 6 | Q-Xe | *55* | 59.6 ± 5.7 | 55 ± 2.7 |
| | SW-Xe | *45* | 40.4 ± 5.7 | 45 ± 2.7 |
| 7 | Q-Xe | *65* | 64.9 ± 3.1 | 65.6 ± 2.9 |
| | SW-Xe | *35* | 35.1 ± 3.1 | 34.4 ± 2.9 |
| 8 | Q-Xe | *75* | 74.8 ± 3.5 | 75.4 ± 3.5 |
| | SW-Xe | *25* | 25.2 ± 3.5 | 24.6 ± 3.6 |
| 9 | Q-Xe | *85* | 84.7 ± 3.5 | 84.7 ± 2.8 |
| | SW-Xe | *15* | 15.3 ± 3.5 | 15.4 ± 2.8 |
| 10 | Q-Xe | *95* | 95.3 ± 3 | 95.3 ± 2.8 |
| | SW-Xe | *5* | 4.7 ± 3 | 4.7 ± 2.8 |
| 11 | Q-Xe | *5* | 6.1 ± 4.1 | 4.2 ± 8.7 |
| | SW-Xe | *85* | 84.4 ± 4.1 | 85.8 ± 8.9 |
| | Ba Spall. | *10* | 9.55 ± 0.02 | 10 ± 0.04 |
| 12 | Q-Xe | *15* | 14.3 ± 2.9 | 12.5 ± 1.9 |
| | SW-Xe | *75* | 76.2 ± 2.9 | 77.6 ± 1.74 |
| | Ba Spall. | *10* | 9.5 ± 0.02 | 10 ± 0.03 |
| 13 | Q-Xe | *25* | 24.8 ± 5 | 25.2 ± 4.7 |
| | SW-Xe | *65* | 65.7 ± 5 | 64.8 ± 4.8 |
| | Ba Spall. | *10* | 9.5 ± 0.03 | 10 ± 0.03 |
| 14 | Q-Xe | *35* | 35.7 ± 3 | 33.9 ± 1.3 |
| | SW-Xe | *55* | 54.7 ± 3 | 56.1 ± 1.3 |
| | Ba Spall. | *10* | 9.5 ± 0.02 | 10 ± 0.04 |
| 15 | Q-Xe | *45* | 44.5 ± 3 | 45.2 ± 4.8 |
| | SW-Xe | *45* | 46 ± 3 | 44.8 ± 5 |
| | Ba Spall. | *10* | 9.5 ± 0.03 | 10 ± 0.03 |
| 16 | Q-Xe | *55* | 54.4 ± 3.2 | 55.2 ± 4.9 |
| | SW-Xe | *35* | 36 ± 3.2 | 34.8 ± 5 |
| | Ba Spall. | *10* | 9.5 ± 0.02 | 10 ± 0.03 |
| 17 | Q-Xe | *65* | 65.7 ± 3.3 | 64.1 ± 1.11 |
| | SW-Xe | *25* | 24.8 ± 3.3 | 25.9 ± 2.59 |
| | Ba Spall. | *10* | 9.5 ± 0.02 | 10 ± 0.03 |
| 18 | Q-Xe | *75* | 75.5 ± 2.5 | 74.6 ± 4.25 |
| | SW-Xe | *15* | 14.9 ± 2.5 | 15.4 ± 4.3 |
| | Ba Spall. | *10* | 9.5 ± 0.03 | 10 ± 0.03 |
| 19 | Q-Xe | *85* | 85.8 ± 3.4 | 83.5 ± 14.9 |
| | SW-Xe | *5* | 4.6 ± 3.4 | 6.6 ± 15.4 |
| | Ba Spall. | *10* | 9.5 ± 0.02 | 10 ± 0.03 |

*Synthesised mixtures are the result of fractional contributions of isotope ratios featuring the percentages in the "true fractions" column. Solutions to mixtures are exhibited for Automaton and Samaritan of Gilmour (2018). End member compositions are listed in Table 3.1.*

#### 3.2.2.2. Uncertainty and Automaton

The following section explores the effect that the uncertainty of compositions fed into Automaton has on resultant solutions, to understand the relationship between data uncertainty and model precision. Uncertainty is accounted for in the input data expansion step (Equation 3.2), is propagated throughout the modelling, and is ultimately contained in the chi-squared statistic (Equation 3.7). Synthesised linear mixtures of end members were created as isotope ratios normalised to $^{132}$Xe, then multiplied by arbitrary numbers of 'atoms' and given uncertainties equal to the square root of that number (Equation 3.8). Uncertainty being the square root of isotope signal height is consistent with real instrument data, since signal typically depends on the number of ions counted and is governed by Poisson statistics. The synthesised mixtures were then re-normalised to isotope ratios over $^{132}$Xe, with propagated errors (table containing synthesised ratios contained in Appendix 3A.2). One hundred Monte Carlo simulations of the expanded synthesised mixtures were then modelled with Automaton with the known end members allowed to vary freely. This process was repeated in Monte Carlo simulations for three synthesised mixtures containing hypothetical measurements of $10^4 \leq$ atoms of $^{132}$Xe $\leq 10^{14}$, with 100 Monte Carlo simulations for each order of magnitude increase in hypothetical atoms for each synthesised mixture (results presented in Table 3.3).

$$^{132}Xe\ (atoms) \times {}^{i}Xe_f \Big/ {}_{^{132}Xe_f} = \sigma^2$$

***Equation 3.8*** *Relationship between test uncertainties, $\sigma$, and modelled number of atoms for fraction $f$, of isotope, i.*

***Table 3.3.*** *Permille deviations of Automaton solutions to synthesised Xe mixtures of decreasing uncertainty.*

| Modelled atoms of $^{132}Xe$ | | | $10^4$ | $10^5$ | $10^6$ | $10^7$ | $10^8$ | $10^9$ | $10^{10}$ | $10^{11}$ | $10^{12}$ | $10^{13}$ | $10^{14}$ |
|---|---|---|---|---|---|---|---|---|---|---|---|---|---|
| Test 1 | $f_Q \equiv 40$ % | Modelled $f_Q$ | 5.1 | -20.7 | -7.73 | -3.54 | -0.35 | 0.085 | 0.084 | -0.042 | 0.001 | 0.000 | 0.000 |
| | | St. Error | 66.7 | 23.3 | 7.39 | 2.73 | 0.85 | 0.26 | 0.079 | 0.029 | 0.008 | 0.003 | 0.001 |
| | $f_{SW} \equiv 60$ % | Modelled $f_{SW}$ | -3.4 | 13.8 | 5.15 | 2.36 | 0.23 | -0.06 | -0.055 | 0.028 | 0.000 | 0.001 | 0.000 |
| | | St. Error | 44.5 | 15.5 | 4.92 | 1.82 | 0.56 | 0.17 | 0.053 | 0.019 | 0.005 | 0.002 | 0.001 |
| Test 2 | $f_Q \equiv 80$ % | Modelled $f_Q$ | -107 | -13.0 | -2.65 | -0.02 | -0.06 | 0.08 | -0.071 | -0.001 | -0.002 | -0.001 | 0.000 |
| | | St. Error | 31 | 11.6 | 1.58 | 1.44 | 0.52 | 0.15 | 0.058 | 0.017 | 0.005 | 0.002 | 0.000 |
| | $f_{SW} \equiv 20$ % | Modelled $f_{SW}$ | 428 | 52.2 | 10.62 | 0.08 | 0.26 | -0.34 | 0.284 | 0.005 | 0.006 | 0.006 | 0.000 |
| | | St. Error | 124 | 46.5 | 6.34 | 5.77 | 2.07 | 0.60 | 0.231 | 0.067 | 0.022 | 0.007 | 0.002 |
| Test 3 | $f_Q \equiv 65$ % | Modelled $f_Q$ | -51 | -11.5 | -3.31 | -2.50 | 0.115 | -0.045 | 0.075 | -0.035 | -0.012 | -0.012 | -0.010 |
| | | St. Error | 44 | 16.9 | 4.84 | 1.69 | 0.500 | 0.145 | 0.048 | 0.018 | 0.006 | 0.002 | 0.002 |
| | $f_{SW} \equiv 25$ % | Modelled $f_{SW}$ | 132 | 29.6 | 8.36 | 6.55 | -0.296 | 0.117 | -0.195 | 0.092 | 0.032 | 0.032 | 0.028 |
| | | St. Error | 115 | 44.2 | 12.60 | 4.40 | 1.303 | 0.377 | 0.125 | 0.047 | 0.014 | 0.006 | 0.004 |
| | $f_{Ba} \equiv 10$ % | Modelled $f_{Ba}$ | 0.27 | 0.51 | 0.62 | -0.116 | -0.011 | 0.002 | 0.000 | -0.002 | -0.003 | -0.003 | -0.002 |
| | | St. Error | 2.78 | 1.07 | 0.31 | 0.103 | 0.033 | 0.010 | 0.003 | 0.001 | 0.0005 | 0.0003 | 0.0002 |

*Results of three synthesised 'Test' mixtures of fractions ($f_x$) with increasingly larger numbers of atoms run in Automaton. Errors of isotopes in each synthesised mixture are equal to the square root of the modelled number of atoms, presented as atoms of $^{132}Xe$ on the second row. Automaton's modelled solutions to the synthesised mixtures are presented as permille deviations of each fractional component from the true coefficient, errors correspond to the standard error of 100 Monte Carlo simulations.*

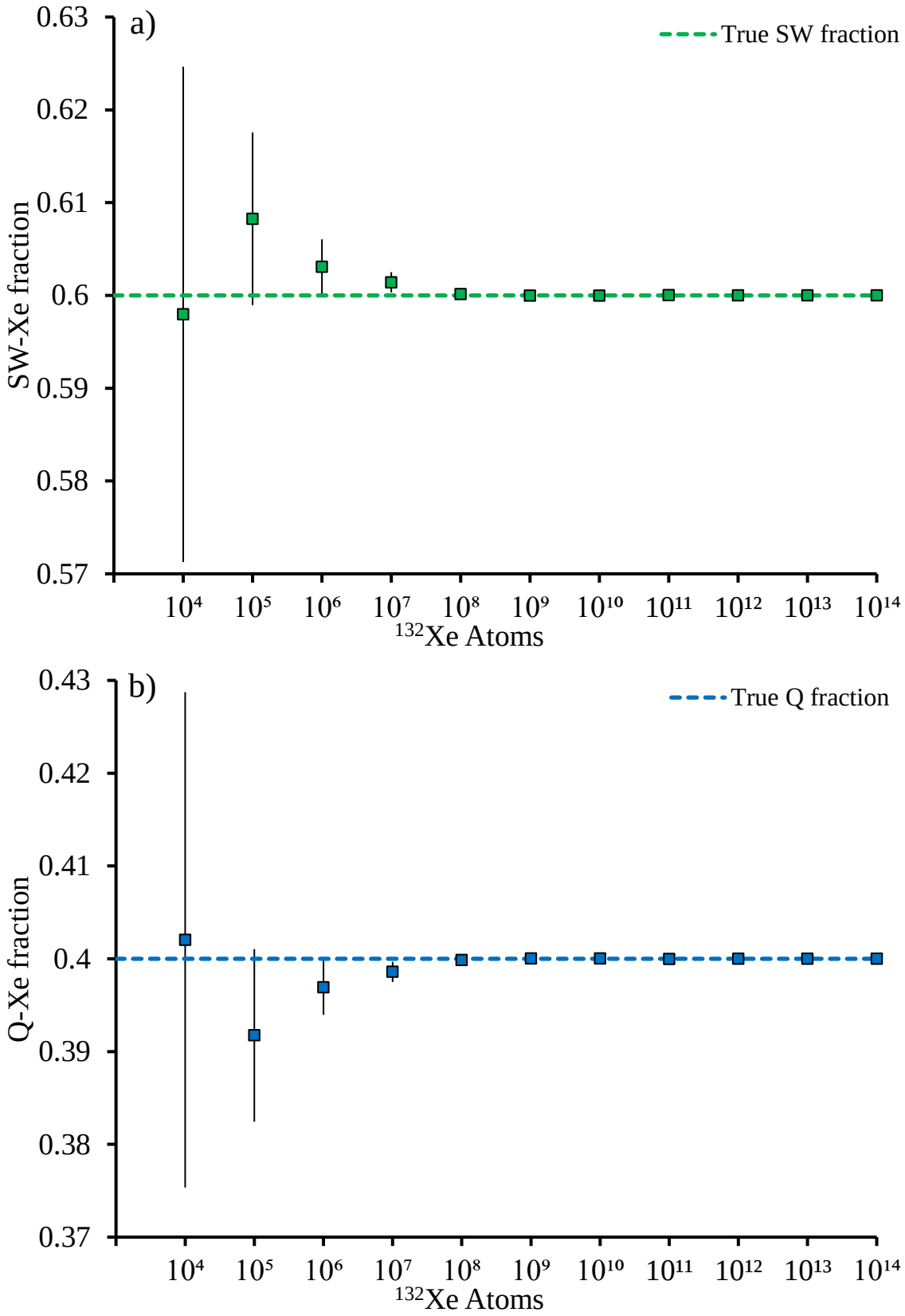


***Figure 3.4*** *Incremental convergence of Automaton solution fractions to 'True' two-component synthesised compositions of 'Test 1' in Table 3.3. Figure a) shows modelled SW-Xe fraction (green squares) compared to 'True' SW-Xe fraction (green dashed line). Figure b) shows modelled Q-Xe fraction (blue squares) compared to 'True' Q-Xe fraction (blue dashed line). Horizontal axes in modelled number of $^{132}$Xe atoms, with uncertainty negatively correlating with quantity of xenon (as in Equation 3.8). Error bars indicate standard errors of 100 simulated mixtures.*

The chi-squared statistic (Equation 3.7) optimised by Automaton as a measure of a solution's goodness of fit is defined in part by the difference between the fit and the target value. Increasing the input data or target errors allows for a particular chi-squared statistic value to be optimised for a modelled value further from the target composition value. Equation 3.8 shows that the synthesised mixtures of this section feature a lower uncertainty with an increased number of atoms (explicitly detailed in Appendix 3A.2). It follows that the chi-squared statistic of Automaton's modelled solutions should be optimised closer to the target value for the synthesised mixtures of this test containing more atoms. Additionally, the precision with which Automaton can settle on the true fractions of end members should improve with decreased uncertainty.

Table 3.3 shows the permille deviations of the modelled solutions from the true fractions clearly decrease with an increased number of atoms. Each two-component test renders solutions within 5% of the true fractions with $10^5$ modelled atoms of $^{132}$Xe. An additional factor of ten increase in $^{132}$Xe atoms to $10^6$ improves the fits to within 10 ‰, and 1 ‰ in simulations exceeding $10^8$ atoms of $^{132}$Xe (Table 3.3). The three-component mixture tests are solved within 10 ‰ for tests with more than $10^6$ $^{132}$Xe atoms, and 1 ‰ in simulations exceeding $10^8$ atoms of $^{132}$Xe.

Figure 3.4 exhibits the solutions of modelling one of these two-component mixtures (Test 1) with Automaton, showing all solutions being correct within error, and a clear convergence to within a scale not visible on either figure at around $10^8$ modelled atoms of $^{132}$Xe. Figure 3.5 exhibits a similar convergence of modelled end member fractions to their true values with an increased number of $^{132}$Xe atoms in the three-component Test 3, although the model with $10^4$ $^{132}$Xe atoms overestimated SW-Xe and underestimated Q-Xe, such that their errors did not envelop the true fraction. This may be due to the magnitude of

the target composition uncertainties representing significant fractions of the isotope ratios, such that the assumption of their Gaussian distribution breaks down.

Figure 3.5 and Table 3.3 show that the three-component results (Test 3) are less precise than their equivalent two-component tests in only the modelling featuring $10^4$ atoms of $^{132}$Xe, and only for SW-Xe and Q-Xe fractions (Ba-Xe was precisely modelled to its true value). Apart from that result, the precision and accuracy of all iterations of Test 3 featuring atoms of $^{132}Xe > 10^4$ typically achieved similar precisions and errors to the equivalent two-component mixtures.

The errors modelled in these tests are more typical of ground truth samples (such as in Table 4.5) and refined end member measurements (Table 3.3), data that precise modelling with Automaton is well suited to. For less precise measurements, such as 67P-Xe of Marty et al. (2017) and Mars-Xe of Conrad et al. (2016), the maximum certainty of a solution can be expected to be much lower, especially with increased numbers of components, as evident in the solution for $10^4$ atoms of $^{132}$Xe in Test 3 (Figure 3.5 and Table 3.3). Additionally, the mixtures in these tests represent fractions of pure end members, which are unrealistic with sample inhomogeneity, and various instrumental and user-derived impurities.

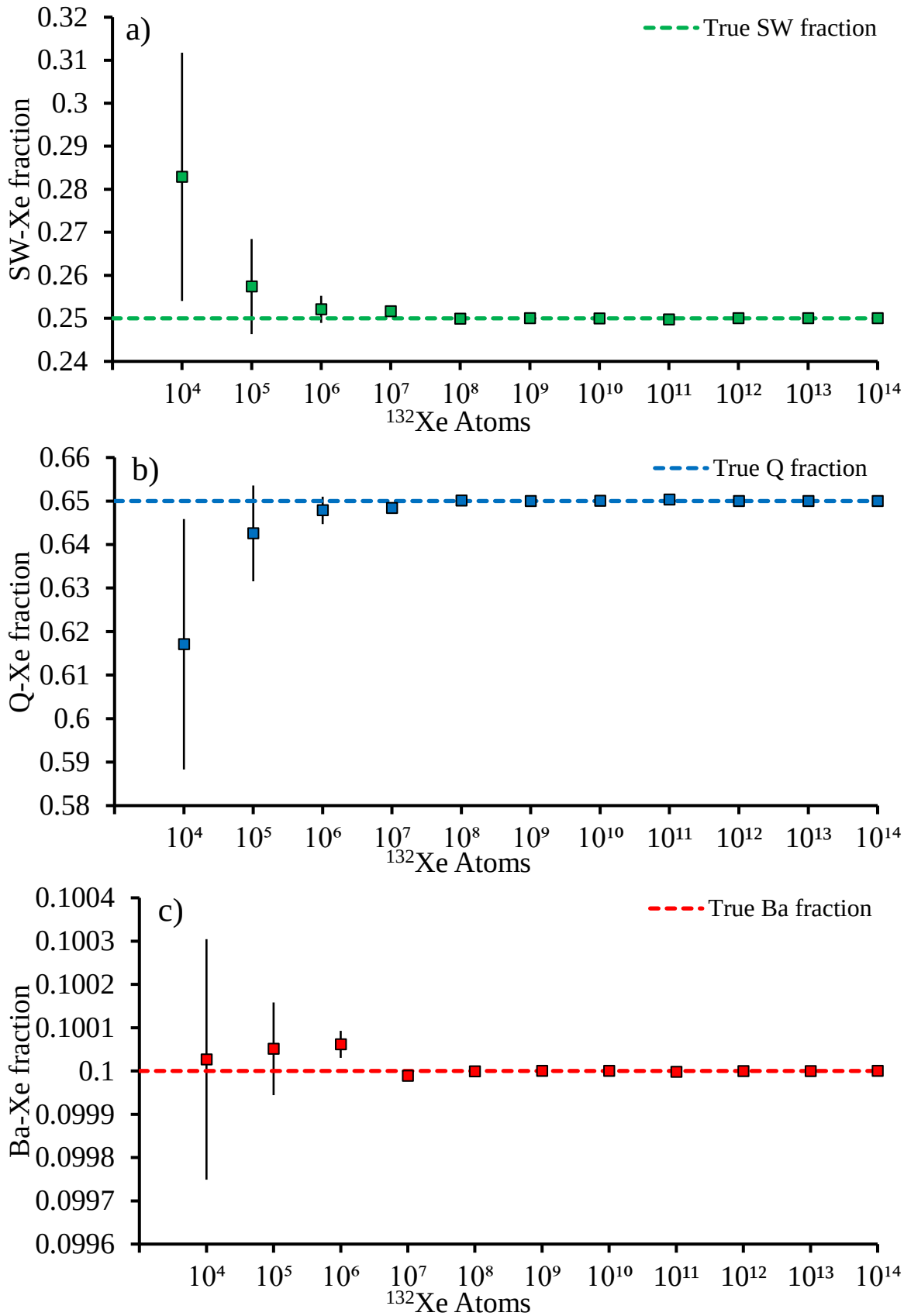


***Figure 3.5*** *Incremental convergence of Automaton solution fractions to 'True' three-component synthesised compositions of 'Test 3' in Table 3.3. Figure a) shows modelled SW-Xe fraction (green squares), Figure b) shows modelled Q-Xe fraction (blue squares), Figure c) shows modelled Ba-Xe fraction (red squares), 'True' fractions of each component are shown as dashed lines in respective colours. Horizontal axes in modelled number of $^{132}$Xe atoms, with uncertainty negatively correlating with quantity of xenon (as in Equation 3.8). Error bars indicate standard errors of 100 simulated mixtures.*

### 3.2.3. Example

The following section follows the process of modelling a composition with Automaton, with relevant examples of the user interface at each stage. The user must first expand the xenon isotopic composition they wish to recreate into the desired number of Monte Carlo simulations. Figure 3.6 illustrates this process in the ‘target expansion’ spreadsheet of the workbook which Automaton uses to synthesise an array of target compositions. The composition to be expanded, and the number of iterations desired, are entered into the relevant cells, then the user clicks a button to initiate a macro which generates the desired number of compositions. The user may also select whether these compositions can have an asymmetrical error in which the error is different depending upon polarity, such as in the 26 – 31 May 2016 67P-Xe data of Marty et al. (2017). Each expanded composition as listed is ready for sequential consideration in Automaton.

The user now moves to the central Automaton spreadsheet from which all other variables are controlled (Figure 3.7). The user can change cell values acting as switches for features, or values of input data such as end member compositions and how fractionation is implemented. A list of end members are contained in an array allowing easy replacement, revision and inclusion in the modelling. Similarly, mass dependent fractionation models are stored as an array of cell values corresponding to the mass relationships of each isotope in a particular fractionation regime. Limits can be placed on the minimum and maximum allowed fractions of each end member and fractionation of each member by changing values of cells. Another set of cells control the application and magnitude of fractionation which can be applied to the entire mixture of end members (which may themselves be fractionated). The user then selects which xenon isotopes they would like Automaton to try and match with the input composition, and clicks a button to start modelling either one composition, or the entire expanded array of isotope compositions.

| | A | B | C | D | E | F | G | H | I | J | K | L | M | N | O | P | Q | R | S | T | U |
|---|---|---|---|---|---|---|---|---|---|---|---|---|---|---|---|---|---|---|---|---|---|
| 1 | **Input** | 124 | σ | 126 | σ | 128 | σ | 129 | σ | 130 | σ | 131 | σ | 132 | σ | 134 | σ | 136 | σ | | |
| 2 | Example ID | 0.00354 | 0.00018 | 0.0033 | 0.00017 | 0.07136 | 0.00357 | 0.9832 | 0.04916 | 0.15136 | 0.00757 | 0.789 | 0.03945 | 1 | 0.05 | 0.3879 | 0.0194 | 0.3294 | 0.01647 | Generate | |
| 3 | **Asymmetrical errors?** | **0** | 0 | | 0 | | 0 | | 0 | | 0 | | 0 | | 0 | | 0 | | 0 | | |
| 4 | | | | | | | | | | | | | | | | | | | | | |
| 5 | | | | | | | | | | | | | | | | | | | | **Rows to output** | |
| 6 | | | | | | | | | | | | | | | | | | | | | 10 |
| 7 | | | | | | | | | | | | | | | | | | | | | |
| 8 | Expanded Ratios | 124 | σ | 126 | σ | 128 | σ | 129 | σ | 130 | σ | 131 | σ | 132 | σ | 134 | σ | 136 | σ | | |
| 9 | | 0.00406 | 0.00018 | 0.00344 | 0.00017 | 0.07137 | 0.00357 | 1.00093 | 0.04916 | 0.15375 | 0.00757 | 0.75084 | 0.03945 | 1 | 0.05 | 0.36977 | 0.0194 | 0.32641 | 0.01647 | | |
| 10 | | 0.00343 | 0.00018 | 0.00291 | 0.00017 | 0.07204 | 0.00357 | 0.94425 | 0.04916 | 0.15379 | 0.00757 | 0.6992 | 0.03945 | 1 | 0.05 | 0.42291 | 0.0194 | 0.32693 | 0.01647 | | |
| 11 | | 0.00326 | 0.00018 | 0.00328 | 0.00017 | 0.07706 | 0.00357 | 1.06695 | 0.04916 | 0.13069 | 0.00757 | 0.81507 | 0.03945 | 1 | 0.05 | 0.37838 | 0.0194 | 0.30852 | 0.01647 | | |
| 12 | | 0.00354 | 0.00018 | 0.00301 | 0.00017 | 0.06657 | 0.00357 | 1.02576 | 0.04916 | 0.13911 | 0.00757 | 0.80488 | 0.03945 | 1 | 0.05 | 0.37367 | 0.0194 | 0.3455 | 0.01647 | | |
| 13 | | 0.00341 | 0.00018 | 0.0034 | 0.00017 | 0.06844 | 0.00357 | 0.98639 | 0.04916 | 0.14455 | 0.00757 | 0.78744 | 0.03945 | 1 | 0.05 | 0.3929 | 0.0194 | 0.31897 | 0.01647 | | |
| 14 | | 0.00378 | 0.00018 | 0.00336 | 0.00017 | 0.07532 | 0.00357 | 0.95497 | 0.04916 | 0.14518 | 0.00757 | 0.81342 | 0.03945 | 1 | 0.05 | 0.38923 | 0.0194 | 0.35338 | 0.01647 | | |
| 15 | | 0.00371 | 0.00018 | 0.00331 | 0.00017 | 0.07427 | 0.00357 | 1.02638 | 0.04916 | 0.15625 | 0.00757 | 0.83655 | 0.03945 | 1 | 0.05 | 0.37609 | 0.0194 | 0.34068 | 0.01647 | | |
| 16 | | 0.00369 | 0.00018 | 0.00327 | 0.00017 | 0.07402 | 0.00357 | 0.98299 | 0.04916 | 0.15056 | 0.00757 | 0.8543 | 0.03945 | 1 | 0.05 | 0.37737 | 0.0194 | 0.33704 | 0.01647 | | |
| 17 | | 0.00359 | 0.00018 | 0.00308 | 0.00017 | 0.06935 | 0.00357 | 0.9659 | 0.04916 | 0.16065 | 0.00757 | 0.77745 | 0.03945 | 1 | 0.05 | 0.40708 | 0.0194 | 0.32429 | 0.01647 | | |
| 18 | | 0.00354 | 0.00018 | 0.00344 | 0.00017 | 0.07611 | 0.00357 | 0.98902 | 0.04916 | 0.16539 | 0.00757 | 0.79956 | 0.03945 | 1 | 0.05 | 0.41385 | 0.0194 | 0.38155 | 0.01647 | | |
| 19 | | | | | | | | | | | | | | | | | | | | | |

***Figure 3.6*** *Example of Automaton's user interface for 'target expansion' of isotope ratio. Figure is divided into coordinate system by cell for reference purposes (a − u horizontally, and 1 − 19 vertically). Green cells indicate values which can be changed as follows; Input composition reference (A2), Input xenon isotopic composition (B2 − S2), Asymmetrical error switch (B3), Errors treated as -σ if asymmetrical error switch is "1" (C3 -S3), Rows to output/number of iterations for Automaton to consider (U6). Note that selection of asymmetrical errors treats the input composition error as +σ. Once all variables have been set, the user clicks on the grey 'Generate' button (T2 – U3) to produce the expanded ratios. Expanded compositions are output sequentially in the rows beneath B9 – S9.*

| A | B | C | D | E | F | G | H | I | J | |
|---|---|---|---|---|---|---|---|---|---|---|
| MDF? | End Member Selection | | Force +Ve? | Absolute? | Limits? | Max fraction | Min fraction | | | 1 |
| 0 | 10 | 67P-Xe | 1 | 1 | 1 | 0.3 | 0 | | | 2 |
| 0 | 6 | Uranium-238 | 1 | 1 | 0 | 1 | 0 | | | 3 |
| 1 | 2 | SW-Xe | 1 | 1 | 0 | 1 | 0 | Post-Mix fractionation? | | 4 |
| | | #N/A | | | | 1 | 0 | 0 | | 5 |
| | | #N/A | | | | 1 | 0 | Isotopes to include | | 6 |
| | | #N/A | | | | 1 | 0 | 124 | 0 | 7 |
| | | #N/A | | | | 1 | 0 | 126 | 1 | 8 |
| | | #N/A | | | | 1 | 0 | 128 | 1 | 9 |
| | | #N/A | | | | 1 | 0 | 129 | 1 | 10 |
| | | #N/A | | | | 1 | 0 | 130 | 1 | 11 |
| | | #N/A | | | | 1 | 0 | 131 | 1 | 12 |
| | | #N/A | | | | 1 | 0 | 132 | 1 | 13 |
| | | #N/A | | | | 1 | 0 | 134 | 1 | 14 |
| | | #N/A | | | | 1 | 0 | 136 | 1 | 15 |
| | Fractionation Model Selection | | | | | | | | | 16 |
| | 1 | Equilibrium Fractionation (Ef) | | | | | | | | 17 |
| | 200 | Upper Fractionation Limit (‰/amu) | Individual end members | | | | | | | 18 |
| | 0 | Lower Fractionation Limit | | | | | | | | 19 |
| | 200 | Upper Fractionation Limit (‰/amu) | post-mix | | | | | | | 20 |
| | 0 | Lower Fractionation Limit | | | | | | | | 21 |

***Figure 3.7*** *Example of Automaton's central worksheet user interface. Figure is divided into coordinate system by cell for reference purposes (A - J horizontally, and 1 - 21 vertically). Green cells indicate values which can be changed: End member compositions (C2 – C15) and reference numbers (B2 - B15), switches allowing end member fractionation (A2 – A15), switch to allow end member removal (D2 – D15), switch to define end member composition as absolute (E2 – E15), switch (F2 – F15) to limit fractions to minimum (G2 – G15) and maximum (H2 – H15) values between zero and one, switch to allow post-mixture fractionation (I5), fractionation model selection and identity (B17 - C17), maximum and minimum fractionation limits for most mixture and individual end member fractionation (B18 – B21), switches for xenon isotopes to include in model (J7- J15).*

Once running, Automaton works on minimising a chi-squared statistic by varying each variable within the defined ranges. This optimisation is conducted by Microsoft Excel's Solver, which references equations and macros within the central spreadsheet of the workbook. Once the chi-squared statistic is minimised, it is printed, along with the corresponding values for each variable, in a separate spreadsheet of the workbook. Automaton then copies the next expanded input composition into the central spreadsheet and optimises the chi-squared statistic for this new variant. This process repeats until the pre-defined number of Monte Carlo simulations are modelled.

The user may then refer to the results in a spreadsheet which contains the optimised solutions for each expanded iteration of the input composition (Figure 3.8). This array keeps a record of the options and limits selected before modelling, the optimised values of each corresponding variable, and the chi-squared statistic for each solution. These data may be used to determine the average and standard deviation of the end member fractions and fractionations, as in Table 3.2 and Table 3.3. It may be more useful to plot each variable as a function of one another, or the chi-squared value, as in Figure 3.9, in order to expose false chi-squared statistic minima. This presentation of the results as an array of sub-solutions allows flexibility in the way the modelling can be refined, presented, and interpreted. For example, clear correlations between low chi-squared statistic values and an absence of an end member may suggest further modelling should not consider that end member. Another example may yield reproducible end member fractions, yet unsatisfactory values for chi-squared statistics, in which case refinement by removing particular isotopes, or adding new end members, may be beneficial. As with any numerical modelling of physical conditions, proposed solutions may satisfy the scenario mathematically, but defy physical plausibility. Solutions must therefore be iteratively revised to improve the suitability of any solutions provided by Automaton.

| Sub-solution | | 1 | 2 | 3 | 4 | 5 | 6 | 7 | 8 | 9 | 10 |
|---|---|---|---|---|---|---|---|---|---|---|---|
| Fractionation model | | Ef | Ef | Ef | Ef | Ef | Ef | Ef | Ef | Ef | Ef |
| Post-Mix frac. (‰/amu) | | 0.80 | 0.00 | 0.22 | 0.00 | 0.23 | -62.76 | 0.00 | 0.28 | 0.00 | 0.00 |
| 67P-Xe | Coeff | 0.87 | 0.85 | 0.87 | 0.86 | 0.86 | 0.85 | 0.86 | 0.87 | 0.86 | 0.47 |
| | ‰/amu | 0.00 | 0.00 | 0.00 | 0.00 | 0.00 | 0.00 | 0.00 | 0.00 | 0.00 | 0.00 |
| Uranium-238 | Coeff | 0.13 | 0.15 | 0.13 | 0.14 | 0.14 | 0.15 | 0.14 | 0.13 | 0.14 | 0.11 |
| | ‰/amu | 0.00 | 0.00 | 0.00 | 0.00 | 0.00 | 0.00 | 0.00 | 0.00 | 0.00 | 0.00 |
| SW-Xe | Coeff | 0.00 | 0.00 | 0.00 | 0.00 | 0.00 | 0.00 | 0.00 | 0.00 | 0.00 | 0.42 |
| | ‰/amu | 0.00 | 0.00 | 0.00 | 0.00 | 0.00 | 0.00 | 0.00 | 0.00 | 0.00 | 0.00 |
| End member 4 | Coeff | #N/A | #N/A | #N/A | #N/A | #N/A | #N/A | #N/A | #N/A | #N/A | #N/A |
| | ‰/amu | #N/A | #N/A | #N/A | #N/A | #N/A | #N/A | #N/A | #N/A | #N/A | #N/A |
| End member 5 | Coeff | #N/A | #N/A | #N/A | #N/A | #N/A | #N/A | #N/A | #N/A | #N/A | #N/A |
| | ‰/amu | #N/A | #N/A | #N/A | #N/A | #N/A | #N/A | #N/A | #N/A | #N/A | #N/A |
| End member 6 | Coeff | #N/A | #N/A | #N/A | #N/A | #N/A | #N/A | #N/A | #N/A | #N/A | #N/A |
| | ‰/amu | #N/A | #N/A | #N/A | #N/A | #N/A | #N/A | #N/A | #N/A | #N/A | #N/A |
| End member 7 | Coeff | #N/A | #N/A | #N/A | #N/A | #N/A | #N/A | #N/A | #N/A | #N/A | #N/A |
| | ‰/amu | #N/A | #N/A | #N/A | #N/A | #N/A | #N/A | #N/A | #N/A | #N/A | #N/A |
| End member 8 | Coeff | #N/A | #N/A | #N/A | #N/A | #N/A | #N/A | #N/A | #N/A | #N/A | #N/A |
| | ‰/amu | #N/A | #N/A | #N/A | #N/A | #N/A | #N/A | #N/A | #N/A | #N/A | #N/A |
| End member 9 | Coeff | #N/A | #N/A | #N/A | #N/A | #N/A | #N/A | #N/A | #N/A | #N/A | #N/A |
| | ‰/amu | #N/A | #N/A | #N/A | #N/A | #N/A | #N/A | #N/A | #N/A | #N/A | #N/A |
| End member 10 | Coeff | #N/A | #N/A | #N/A | #N/A | #N/A | #N/A | #N/A | #N/A | #N/A | #N/A |
| | ‰/amu | #N/A | #N/A | #N/A | #N/A | #N/A | #N/A | #N/A | #N/A | #N/A | #N/A |
| | $\chi 2$ | 0.349649 | 1.61722 | 1.111783 | 0.608906 | 0.559475 | 0.553123 | 0.484647 | 0.782742 | 0.461895 | 0.285725 |
| | CpD | 0.06993 | 0.323444 | 0.222357 | 0.121781 | 0.111895 | 0.110625 | 0.096929 | 0.156548 | 0.092379 | 0.057145 |
| | Isotopes included | 1011111 | 1011111 | 1011111 | 1011111 | 1011111 | 1011111 | 1011111 | 1011111 | 1011111 | 1011111 |
| | Notes | Example | Example | Example | Example | Example | Example | Example | Example | Example | Example |

***Figure 3.8*** *Example of Automaton's solution array, a spreadsheet containing results of the modelling. Values in this example are arbitrary, but contained in a similar format to the actual solution array. Note the columns corresponding to each sub-solution.*

### 3.3. Reservoir building

The following sections explore the nature of and relationships among notable reservoirs of xenon in the Solar System by modelling their compositions with Automaton. The section is split into subsections describing scenarios and results for modelling of the reservoirs described in this subsection. The modelling is focussed on the xenon isotopic composition of comet 67P/Churyumov-Gerasimenko (67P-Xe herein) of Marty et al. (2017), and how this measurement may change our idea of the evolution of various xenon reservoirs in the Solar System, such as Earth's atmosphere, U-Xe, and the Martian atmosphere.

Modelling these compositions with Automaton is conducted using a suite of xenon isotopic end member compositions representing significant or ubiquitous reservoirs thought to be present during their formation. Other, more specific, minor reservoirs are explained in their relevant sections. All end member compositions are contained in Table 3.1. The two recurring end member compositions throughout the modelling are solar wind xenon (SW-Xe herein) (Meshik et al., 2014), and the xenon associated with the organic residue, phase Q, contained in carbonaceous meteorites, used as a proxy for chondritic xenon (Q-Xe herein) (Busemann et al., 2000). Both SW-Xe and Q-Xe are assumed to represent their original compositions in the Solar System around the time of the formation of each modelled reservoir (explained in more detail in Section 1.3).

Section 3.3.1 contains modelling of the origin of 67P-Xe with Automaton. The modelling takes two approaches. In one approach, the reported composition of 67P-Xe is assumed to be representative of a cometary xenon composition, and modelling explores how 67P-Xe could be produced by chondritic (Q-Xe) or solar wind (SW-Xe) xenon. The other approach questions the proposed $^{128}$Xe composition of Marty et al. (2017). Marty et

al. (2017) numerically disentangled the composition of $^{128}Xe$ (127.9030 amu) from an overlapping $^{32}S_4$ (127.8877 amu) signal by unmixing the sum of two Gaussian signal peak shapes which are reproducible in isotopes without isobaric interference. The models then test the extent to which conclusions drawn upon the composition of 67P-Xe depend upon the corrected isotope.

Automaton is used to explore the implications of removing this isotope, such as its enrichment ruling out the origin of 67P-Xe as fractionated solar wind. The modelling following this section follows a similar pattern of exploring the differences in modelling with and without assuming $^{128}Xe$ of 67P-Xe was correctly reported in other reservoirs of the Solar System. All following approaches assume the compositions of 67P-Xe as representative of the xenon contained in all comets, and thus its contribution in models is a proxy for cometary enrichment.

Modelling of the origin of Earth's atmospheric xenon composition with Automaton is split into Section 3.3.2 and Section 3.3.3. Each section contains modelling which approaches the topic in two distinct methods. Section 3.3.2 contains modelling of Earth's atmospheric xenon composition as it exists today explicitly with the components and processes suggested by the atmospheric evolution of Pepin (1991), along with other significant reservoirs of the Solar System, and 67P-Xe. Modelling is conducted in scenarios using the fissiogenic contributions and atmosphere-scale fractionation as described in the derivation of U-Xe by Pepin (1991), along with SW-Xe, Q-Xe, and 67P-Xe. Section 3.3.3 contains modelling of Earth's atmospheric xenon composition by accepting the proposal of U-Xe as its primordial precursor, as described in Pepin, (1991), and in more detail within the section. U-Xe is recreated by modelling mixtures containing Q-Xe, SW-Xe, and 67P-Xe, in order to test the suggestion of Marty et al. (2017) that U-Xe can be derived from a 67P-Xe dominated mixture containing those end members. The

modelling would also test whether the composition of 67P-Xe has any influence on the suggestion of Caracausi et al. (2016) that the light isotopic composition of Earth's mantle xenon suggests a chondritic origin.

Section 3.3.4 contains modelling of the xenon composition of the Martian atmosphere. Modelling attempts to recreate the most recent in situ measurement of the Martian atmospheric xenon composition by the Mars Science Laboratory's Sample Analysis at Mars (SAM) investigation reported by Conrad et al. (2016). This composition is recreated using various xenon reservoirs, including the Martian isolated spallogenic component of Conrad et al. (2016). This composition is used in favour of Martian meteoritic measurements due to their susceptibility to modification or loss of their original compositions by weathering, shock, spallation in interplanetary space, mixture with Martian soil, and fission (Drake et al., 1994; Gilmour et al., 1999; Swindle et al., 2000; Mathew and Marti, 2002).

Data presented in these sections represent the results of modelling two hundred Monte Carlo simulations of the defined compositions with Automaton. Results are presented in tables containing the averages and standard deviations of the two hundred resultant solutions. Fractionations are presented as averages and standard deviations of the equivalent linear fractionation values, in the format of enrichment/depletion in permille per atomic mass unit (‰/amu). Fractionation of a magnitude which could result in significant non-linear deviations is discussed in context. Delta plots contain reconstructed mixtures of modelled solutions using the average fractions and fractionations for each end member. A summary of the results of the modelling is contained at the end of each of the following sections. A discussion of the results and implications of this modelling are contained in equivalent subsections of the discussion, in Section 3.4.

### 3.3.1. 67P/Churyumov-Gerasimenko

The xenon isotopic composition of comet 67P/Churyumov-Gerasimenko was measured by the ROSINA instrument on board the Rosetta spacecraft in May 2016, and the measured composition is reported and discussed in Marty et al. (2017). Relative to solar wind and normalised to $^{132}$Xe, Xenon in 67P/Churyumov-Gerasimenko (67P-Xe) features depletions of $^{128}$Xe/$^{132}$Xe, $^{134}$Xe/$^{132}$Xe, $^{136}$Xe/$^{132}$Xe, and enrichments in $^{129}$Xe/$^{132}$Xe, $^{130}$Xe/$^{132}$Xe, and $^{131}$Xe/$^{132}$Xe (Figure 1.6 and Figure 3.9). The data do not contain a $^{124}$Xe or $^{126}$Xe signal, but the available isotopic abundances appear to resemble a significantly mass fractionated SW-Xe composition with relative enrichments in all other isotopes lighter than $^{132}$Xe except for $^{128}$Xe/$^{132}$Xe, which is depleted relative to SW-Xe. The results and methodology of measuring 67P-Xe are presented in Marty et al. (2017), where the authors attempt to explain this composition in the context of other Solar System reservoirs.

The following modelling uses Automaton to consider the origin of 67P-Xe. By removing or modifying the reported $^{128}$Xe composition and assuming 67P-Xe has undergone some form of fractionation prior to measurement, the origin of 67P-Xe as a fractionated version of an existing Solar System reservoir is modelled. Table 3.4 presents the results of this modelling. Modelling Scenarios 1, 2, and 3 of Table 3.4 attempted to determine the degree of fractionation required for 67P-Xe to resemble a fractionated SW-Xe composition. Scenario 1 of Table 3.4 attempted to fit all of the isotopes except for the missing isotopes in 67P-Xe ($^{124}$Xe/$^{132}$Xe and $^{126}$Xe/$^{132}$Xe), and $^{128}$Xe/$^{132}$Xe, upon the assumption that the isobaric interference with $^{128}$Xe rendered its signal unreliable. Scenario 2 and 3 of Table 3.4 considered scenarios in which $^{128}$Xe/$^{132}$Xe was fit by the model, but the reported uncertainty of $^{128}$Xe/$^{132}$Xe was increased by a factor of two and three, the results are presented with respect to SW-Xe in Figure 3.9.

Scenarios 1, 2, and 3 of Table 3.4 with enlarged $^{128}Xe/^{132}Xe$ uncertainties, or an absence of $^{128}Xe/^{132}Xe$ from fitting, all suggested mixtures in which SW-Xe is reproduced by 67P-Xe being extremely fractionated (124 ‰/amu < 132 ‰/amu), yet still expressed pronounced depletions in the heavy isotopes (~ 250 ‰ for $^{134}Xe/^{132}Xe$ and ~ 400 ‰ $^{136}Xe/^{132}Xe$ relative to solar). The modelled scenarios in which 67P-Xe was derived purely from fractionated SW-Xe, or SW-Xe purely from 67P-Xe, produced fractionation values surprisingly independent of the certainty or inclusion of $^{128}Xe/^{132}Xe$ in modelling.

The solutions for Scenario 3 in which 67P-Xe was recreated with fractionated SW-Xe required fractionations equivalent to 129 ‰/amu ± 0.3 ‰/amu, and a physical mechanism which could have resulted in such a pronounced fractionation which also explains the depletions of the heavy isotopes (shown in Figure 3.9). A similarly extreme fractionation and heavy isotope depletion is required in the modelled solutions to Scenario 4, where it is assumed that 67P-Xe and Q-Xe are derived from their counterpart's fractionation (results contained in Table 3.4, and plotted in Figure 3.10), along with similar requirements for a significant and selective fractionation which does not account for depletions of $^{134}Xe/^{132}Xe$ and $^{136}Xe/^{132}Xe$ relative to Q-Xe.

Scenario 5 of Table 3.4 considered a more complex model of the origin of 67P-Xe in which SW-Xe was modelled by a mixture of freely fractionated Q-Xe and 67P-Xe. This solution resulted in a proposed degree of fractionation for 67P-Xe equivalent to 20 ‰/amu ± 4.4 ‰/amu, and Q-Xe fractionated to a magnitude which expressed significant non-linearity, and significant scatter, with fractionations ranging from 214 ‰/amu < 1305 ‰/amu.

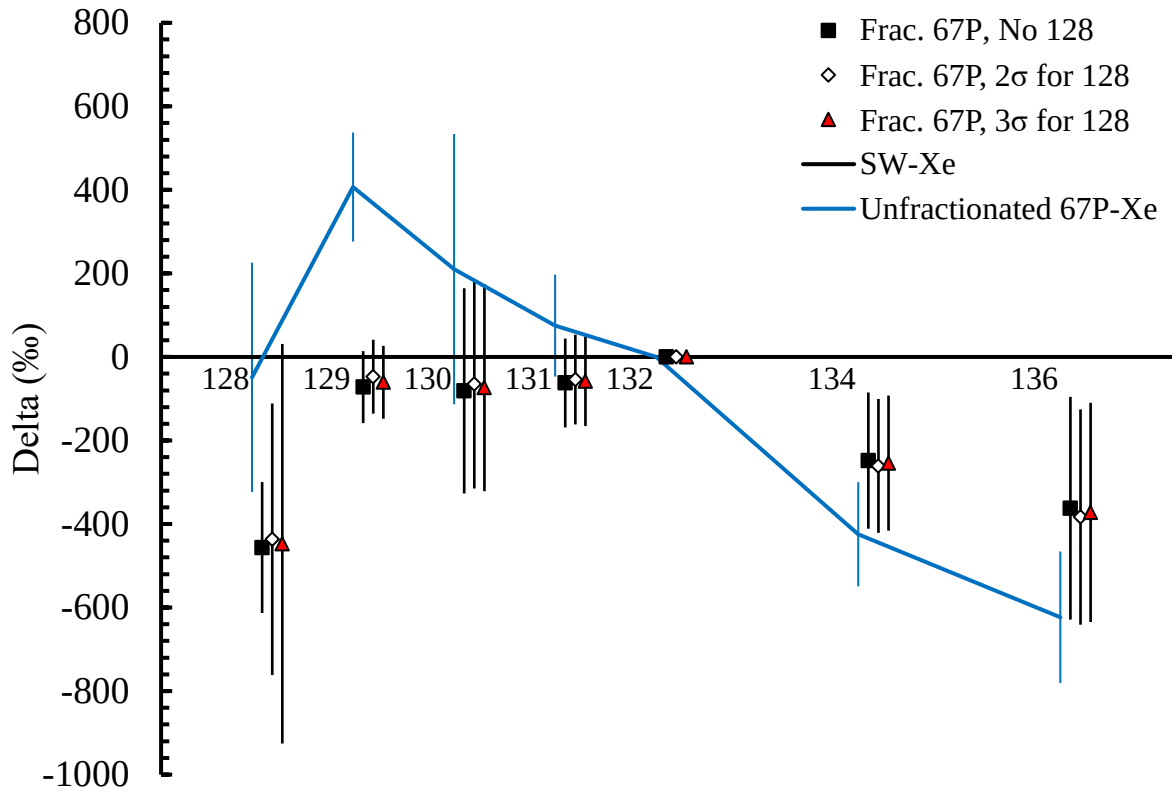


***Figure 3.9*** *Permille deviations of xenon isotope ratios in Automaton solutions for SW-Xe from fractionated 67P-Xe, with various $^{128}$Xe uncertainties for 67P-Xe. SW-Xe normalised to ≡ 0. Ratios normalised to $^{132}$Xe. Errors represent one standard deviation except for $^{128}$Xe/$^{132}$Xe, whose uncertainty, or omission from fit, is listed in the legend. Scenario 1 (black squares), Scenario 2 (white diamonds), and Scenario 3 (red triangles), of Table 3.4 plotted. Unfractionated 67P included for reference (blue line).*

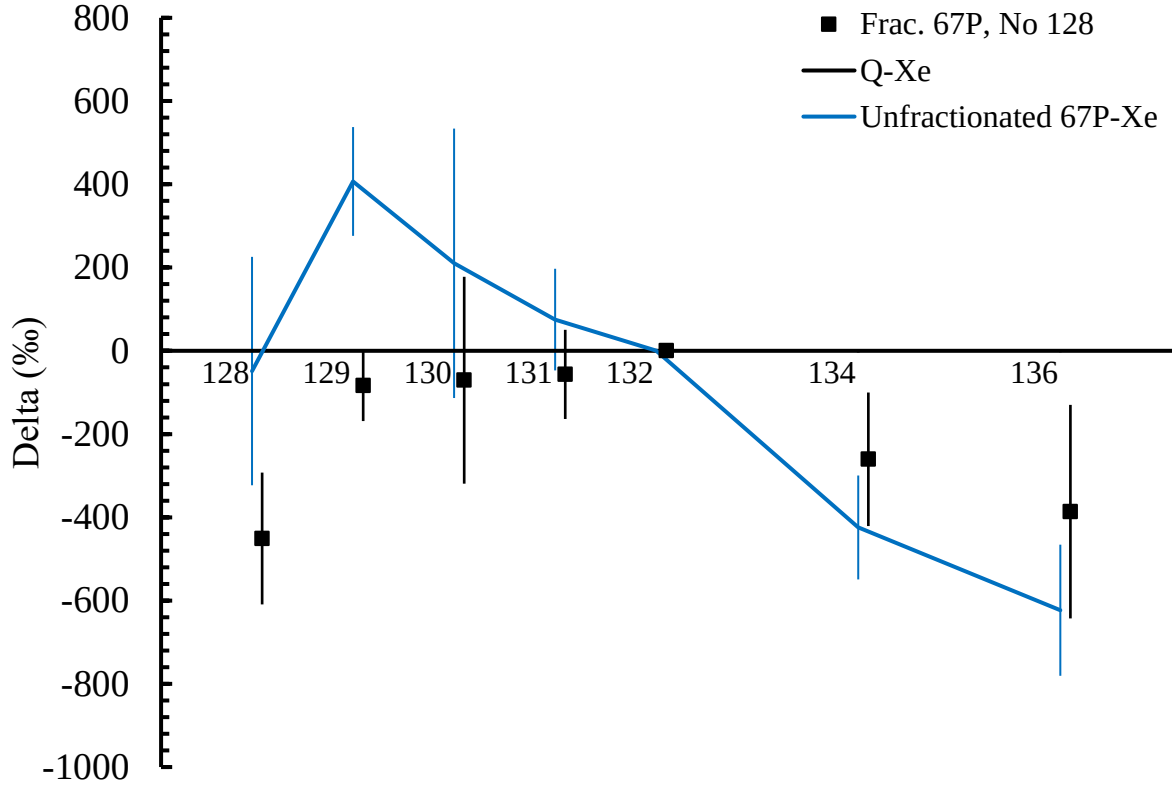


***Figure 3.10*** *Permille deviations of xenon isotope ratios in Automaton solutions for fractionated 67P-Xe from Q-Xe, according to the conditions described in Scenario 4 of Table 3.4. Q-Xe normalised to ≡ 0. Ratios normalised to $^{132}$Xe. Errors represent one standard deviation. Unfractionated 67P-Xe included for reference (blue line).*

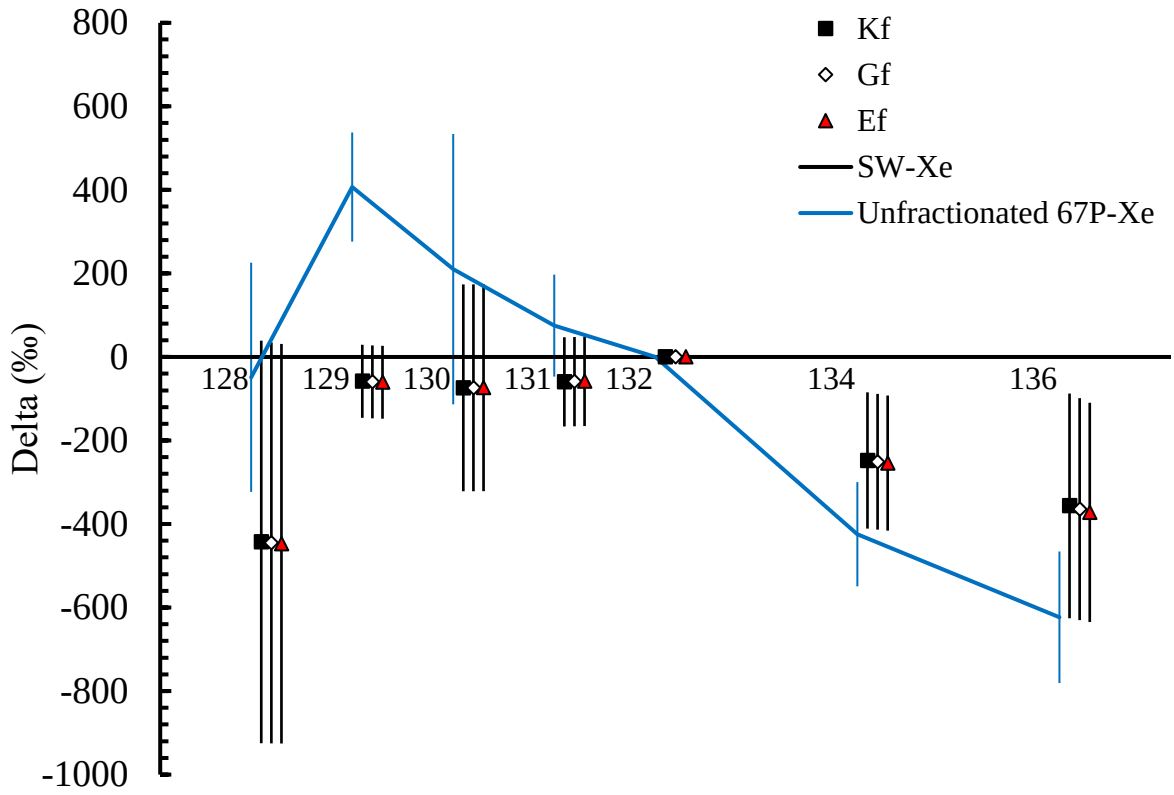


***Figure 3.11*** *Permille deviations of xenon isotope ratios in Automaton solutions for fractionated 67P-Xe from SW-Xe, using three differing fractionation models. SW-Xe normalised to ≡ 0. Ratios normalised to $^{132}$Xe. All plotted isotopes were included in the fit. Unfractionated 67P included for reference (blue line). Kinetic fractionation (Kf, black squares), Gravitational fractionation (Gf, white diamonds), and Equilibrium fractionation (Ef, red triangles). Errors represent one standard deviation except for $^{128}$Xe where errors represent 3σ.*

The results of modelling Scenarios 1, 2, and 3 which considered 67P-Xe as fractionated SW-Xe using different or absent $^{128}$Xe/$^{132}$Xe uncertainties for 67P-Xe produced solutions with significant enough fractionations that differences between fractionation models could be apparent. As explained in Section 3.2.1, the fractionation model initially applied (and used throughout the rest of the work unless stated) was the Equilibrium fractionation model of Young et al. (2002), due to its relatively minor deviation from linear fractionation compared to the other fractionation models available to Automaton (as shown in Figure 3.2). Figure 3.11 shows that even at this magnitude, the differences between the solutions of Automaton's modelling using the fractionation models of Young et al. (2002), Equilibrium (Ef), Kinetic (Kf), and Gravitational (Gf) fractionation, were insignificant, especially in relation to the expressed uncertainties.

The results of the modelling of 67P-Xe can be summarised as follows. Removing $^{128}Xe/^{132}Xe$ or increasing the uncertainty of $^{128}Xe/^{132}Xe$ in 67P-Xe when modelling with either SW-Xe or Q-Xe results in similarly fractionated modelled compositions. These compositions are extremely depleted in $^{134}Xe/^{132}Xe$ and $^{136}Xe/^{132}Xe$, but otherwise match either SW-Xe or Q-Xe, including the $^{129}Xe/^{132}Xe$ composition. 67P-Xe is also modelled with extremely fractionated Q-Xe and slightly fractionated SW-Xe, but the sub-solutions express significant scatter.

***Table 3.4*** *Modelling 67P-Xe.*

| Scenarios | 1 | 2 | 3 | 4 | 5 | |
|---|---|---|---|---|---|---|
| Target composition | SW-Xe | SW-Xe | SW-Xe | Q-Xe | SW-Xe | |
| Conditions | $^{128}$Xe not fitted | 2σ for $^{128}$Xe | 3σ for $^{128}$Xe | $^{128}$Xe not fitted | $^{128}$Xe not fitted | |
| | Fractionated 67P-Xe | Fractionated 67P-Xe | Fractionated 67P-Xe | Fractionated 67P-Xe | Fractionated 67P-Xe & Fractionated Q-Xe | |
| End members | Fractions (% ± σ) | Fractions (% ± σ) | Fractions (% ± σ) | Fractions (% ± σ) | Fractions (% ± σ) | End member fractionation (‰ / amu ± σ) |
| Q-Xe | - | - | - | - | 65 ± 13 | 537 ± 132* |
| SW-Xe | - | - | - | - | - | - |
| 67P-Xe | ≡ 100 | ≡ 100 | ≡ 100 | ≡ 100 | 35 ± 13 | 20 ± 4.4 |
| Post-mixture fractionation (‰ / amu ± σ) | 132 ± 0.3 | 124 ± 0.2 | 129 ± 0.3 | 136 ± 0.5 | - | |

*67P-Xe, SW-Xe and Q-Xe compositions listed in Table 3.1. Automaton's solutions to the scenarios described in each column. Solutions represent the results of Monte Carlo simulations of 200 mixtures containing all xenon isotopes except for $^{124}$Xe, $^{126}$Xe, unless stated. Numbers indicate averages and standard deviations of all sub-solutions. Hyphens designate exclusion of corresponding variable from solution. Fractionation listed as linear equivalents to non-linear equilibrium fractionation, which approaches linearity at these magnitudes. *This value of fractionation introduces significant non-linear differences between isotopes, described in the text.*

### 3.3.2. Earth's atmosphere

The following modelling used Automaton to consider the origin of Earth's atmospheric xenon as it is today. Modelling scenarios recreated it using various combinations of 67P-Xe, Q-Xe, SW-Xe, and fission products of $^{238}U$ and $^{244}Pu$ as end members. Xenon isotopes $^{128}Xe/^{132}Xe$, $^{130}Xe/^{132}Xe$, $^{131}Xe/^{132}Xe$, $^{132}Xe/^{132}Xe$, $^{134}Xe/^{132}Xe$, and $^{136}Xe/^{132}Xe$ were included in the following models. Isotopes $^{124}Xe$ and $^{126}Xe$ were not fitted because of their exclusion from the reported 67P-Xe data (Marty et al. 2017), $^{129}Xe/^{132}Xe$ was not fitted due to the ease with which its composition can be attributed to $^{129}I$ decay, whose initial concentration in the Earth is hard to determine. Table 3.5 contains the results of modelling the Earth's atmosphere in the scenarios explained herein.

Scenario 6 of Table 3.5 contains the results of modelling with Automaton of a simple mixture of 67P-Xe, Q-Xe, SW-Xe, and fission products of $^{238}U$ and $^{244}Pu$, without any limitations on fractions, and no fractionation. The solution results in a 67P-Xe dominated mixture for Earth's atmosphere composed of 53% ± 15% 67P-Xe, and fissiogenic contributions accounting for 14% ± 5% of the atmosphere. The majority of this fission xenon contribution was derived from the decay of $^{244}Pu$, 12% ± 2% (with an additional 2% ± 3% from $^{238}U$ fission).

Modelling Scenarios 7, 8, 9, and 10 of Table 3.5 assumed the prevailing idea that Earth's atmosphere has undergone some degree of mass fractionation by hydrodynamic escape (Hunten et al., 1987; Pepin, 1991). This was achieved by applying post-mixture fractionation to the fractional mixture of end members, and allowing its optimisation by Automaton. This essentially simulates a scenario in which Earth's atmosphere was closed after a cometary contribution, and has subsequently been fractionated by hydrodynamic

escape. Fractionation was limited to positive values (resulting in heavy isotopic excess), consistent with hydrodynamic escape.

Scenario 7 of Table 3.5 describes the results of modelling a scenario containing a mixture of 67P-Xe, Q-Xe, SW-Xe, and fission products of $^{238}$U and $^{244}$Pu, as in Scenario 6, but allowed post-mixture fractionation. This solution expresses a similarly 67P-Xe dominated mixture to Solution 6 (52% ± 15%), yet Automaton applied an average post-mixture fractionation equivalent to 0.7 ‰/amu ± 1.4 ‰/amu.

Scenario 8 of Table 3.5 describes modelling of a scenario in which the reported composition of 67P-Xe is one which has undergone fractionation since its incorporation into Earth's atmosphere, so the cometary xenon contained in Earth's atmosphere prior to hydrodynamic escape is an unfractionated precursor to 67P-Xe. In this case, Automaton is allowed to freely vary the individual fractionation of 67P-Xe, and the post-mixture fractionation of the atmosphere after mixture of its constituents. The results of Scenario 8 are nearly indistinguishable from Scenario 7 (which differs in its lack of 67P-Xe fractionation) in terms of contributions from components and post-mixture fractionation (0.6 ‰/amu ± 1.3 ‰/amu), apart from the occasional application of a significant fractionation to 67P-Xe roughly equivalent to 39.4 ‰/amu.

Scenarios 9 and 10 of Table 3.5 describe modelling of Earth's atmosphere if the contributions of fissiogenic components are constrained according to literature values. Scenario 9 considers the fractional contribution of fissiogenic xenon fixed at 2.26% ± 0.28%, and assumes it entirely consists of $^{244}$Pu, as suggested by Caracausi et al. (2016). Automaton was set up to simulate Earth's atmospheric xenon composition with a mixture containing a fixed $^{244}$Pu fraction, and variable fractions of Q-Xe, SW-Xe, and 67P-Xe. The model also allowed Automaton to vary post-mixture fractionation. This

resulted in a solution where Earth's atmosphere was composed of 81% ± 4% SW-Xe and 67P-Xe contributed 16% ± 0.2% prior to a significant and consistent mass fractionation equivalent to 35.4 ‰/amu ± 0.2 ‰/amu.

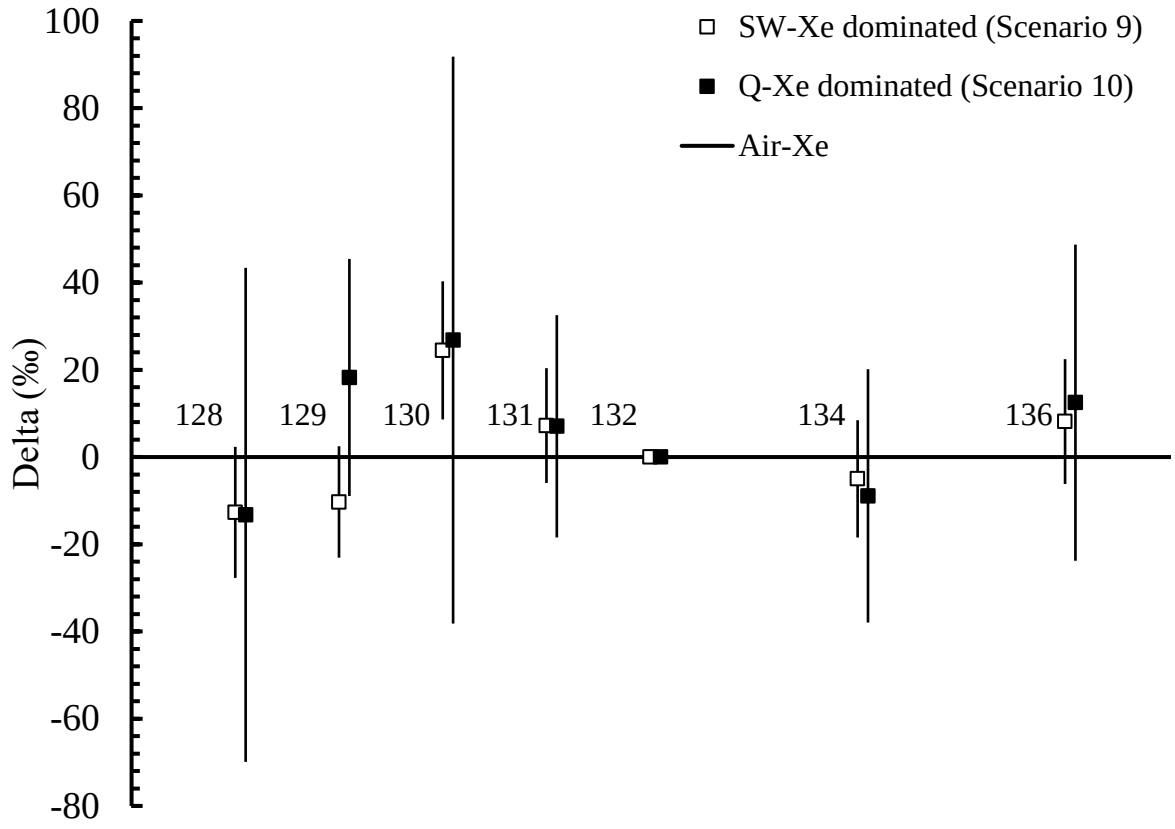


***Figure 3.12*** *Delta plot of Automaton solutions for Earth's atmospheric xenon from SW-Xe and Q-Xe dominated mixtures. Data are permille deviations of averages and standard deviation of isotope ratios of modelled solutions to Scenario 9 (SW-Xe dominated, white squares) and Scenario 10 (Q-Xe dominated, black squares) of Table 3.5, with respect to atmospheric xenon (horizontal line). All ratios normalised to* $^{132}$*Xe. Note that* $^{129}$*Xe was not fit in these solutions. End member compositions reported in Table 3.1.*

The ease with which the results of modelling Scenario 9 of Table 3.5 disregarded any notable contribution of chondritic xenon begged the question of whether a scenario in which only Q-Xe was considered would satisfy the modelling in a similar manner. Scenario 10 of Table 3.5 presents the results of modelling in which Earth's atmosphere is reconstructed with Q-Xe, 67P-Xe, $^{244}$Pu fission xenon (fixed at 2.26%), and post-mixture fractionation. The solution presents a marginally smaller degree of post-mixture fractionation than the results of Scenario 9, equivalent to 30.5 ‰/amu ± 0.02 ‰/amu, and

an atmosphere containing 78% Q-Xe and 19% 67P-Xe with minimal scatter in sub-solutions ($\sigma = 0.005\%$). The suggested fractional components contained in Scenario 9 and Scenario 10 of Table 3.5 are mixed to produce the modelled composition of Earth's atmosphere, and compared to the true composition in Figure 3.12.

Scenarios 9 and 10 of Table 3.5 which modelled Earth's atmosphere with the fixed fissiogenic contributions of Caracausi et al. (2016) are plotted in Figure 3.12, and clearly satisfy the $^{129}Xe/^{132}Xe$ ratio of atmospheric xenon, despite the solution not including any $^{129}I$ decay.

The results of the modelling of Earth's atmosphere can be summarised as follows. A non-fractionated simple mixture of end members produces Earth's atmospheric composition from Q-Xe, SW-Xe, fission products of $^{238}U$ and $^{244}Pu$, and over 50% of 67P-Xe, although this model exhibits significant scatter. Similarly 67P-Xe dominated solutions for Earth's atmosphere are presented for scenarios which added atmospheric fractionation, and atmospheric fractionation with individual fractionation of 67P-Xe. SW-Xe and Q-Xe dominated scenarios for a fractioned atmosphere when the fraction of $^{244}Pu$ is fixed at 2.26% produced two different contributions from 67P-Xe and similar values for fractionation.

***Table 3.5*** *Modelling Earth's atmospheric xenon with SW-Xe, Q-Xe, 67P-Xe, and fissiogenic contributions from $^{244}Pu$ and $^{238}U$.*

| Scenarios | 6 | 7 | 8 | | 9 | 10 |
|---|---|---|---|---|---|---|
| Target composition | Air-Xe | Air-Xe | Air-Xe | | Air-Xe | Air-Xe |
| Conditions | All end members | All end members | All end members | | Fixed fission, Q-Xe, SW-Xe, and 67P-Xe | Fixed fission, Q-Xe, and 67P-Xe |
| | No fractionation | Post-mixture fractionation | 67P-Xe fractionation & post-mixture fractionation | | Post-mixture fractionaton | Post-mixture fractionaton |
| End members | Fractions (% ± σ) | Fractions (% ± σ) | Fractions (% ± σ) | End member fractionation (‰ / amu ± σ) | Fractions (% ± σ) | Fractions (% ± σ) |
| Q-Xe | 26 ± 20 | 27 ± 21 | 28 ± 22 | - | 0.4 ± 4 | 78 ± 0.005 |
| SW-Xe | 8 ± 14 | 8 ± 14 | 10 ± 16 | - | 81 ± 4 | - |
| $^{244}Pu$ | 12 ± 2 | 12 ± 1 | 12 ± 2 | | ≡ 2.26 | ≡ 2.26 |
| $^{238}U$ | 2 ± 3 | 2 ± 3 | 1 ± 2 | | - | - |
| 67P-Xe | 53 ± 15 | 52 ± 15 | 49 ± 14 | 39.4 ± 24.9 | 16 ± 0.2 | 19 ± 0.005 |
| Post-mixture fractionation (‰ / amu ± σ) | - | 0.7 ± 1.4 | 0.6 ± 1.3 | | 35.4 ± 0.2 | 30.5 ± 0.02 |

*End member compositions listed in Table 3.1. Automaton's solutions to the scenarios described in each column. Solutions represent the results of Monte Carlo simulations of 200 mixtures containing all xenon isotopes except for $^{124}Xe$, $^{126}Xe$, unless stated. Numbers indicate averages and standard deviations of all sub-solutions. Hyphens designate exclusion of corresponding variable from solution. Fractionation listed as linear equivalents to non-linear equilibrium fractionation, which approaches linearity at these magnitudes.*

### 3.3.3. U-Xe

U-Xe is the hypothetical primordial composition of Earth which upon the addition of $^{129}$Xe $^{132}$Xe, $^{134}$Xe, and $^{136}$Xe by $^{129}$I, $^{244}$Pu, and $^{238}$U decay, and fractionation by hydrodynamic escape, resulted in the current atmospheric xenon composition (Hunten et al., 1987; Pepin, 1991). This section follows from the modelling of Marty et al. (2017) in which the composition of U-Xe is modelled upon the assumption of 67P-Xe representing a cometary xenon composition which could have contributed to the primordial precursor to Earth's atmosphere. Table 3.6 contains the results of modelling with Automaton of the composition of U-Xe using various combinations of Q-Xe, SW-Xe, and 67P-Xe, and fractionations of end members and mixtures. Isotopes of $^{128}$Xe/$^{132}$Xe, $^{129}$Xe/$^{132}$Xe, $^{130}$Xe/$^{132}$Xe, $^{131}$Xe/$^{132}$Xe, $^{132}$Xe/$^{132}$Xe, $^{134}$Xe/$^{132}$Xe, and $^{136}$Xe/$^{132}$Xe are included in the following models unless stated. Note the inclusion of $^{129}$Xe/$^{132}$Xe in these simulations. Also note that the modelling with Automaton excluded the light isotopes of $^{124}$Xe/$^{132}$Xe and $^{126}$Xe/$^{132}$Xe, due to their composition not being measured in 67P-Xe.

Scenario 11 of Table 3.6 presents the results of modelling U-Xe from 67P-Xe, Q-Xe, and SW-Xe under no fractional limitations or fractionation with Automaton. Under these conditions, U-Xe was created with a simple mixture of 15% ± 2% of 67P-Xe, 30% ± 23% of Q-Xe, and 56% ± 25% of SW-Xe. The large standard deviations of the Q-Xe and SW-Xe fractions were elucidated by viewing the results of individual sub-solutions to each Monte Carlo simulation. Figure 3.13 shows the fractional contributions of all components in each modelled sub-solution to Scenario 11 of Table 3.6, illustrating the interchangeability of Q-Xe and SW-Xe in this modelled scenario as a negative correlation between either component's fractional contribution to U-Xe. Automaton's sub-solutions to this scenario expressed percentages of $0\% < f_{Q\text{-}Xe} < 81\%$ for fractions of Q-Xe and $0\% < f_{SW\text{-}Xe} < 88\%$ for fractions of SW-Xe, and a contribution from

67P-Xe ranging from 12% (in SW-Xe dominated solutions) to 19% (in Q-Xe dominated solutions).

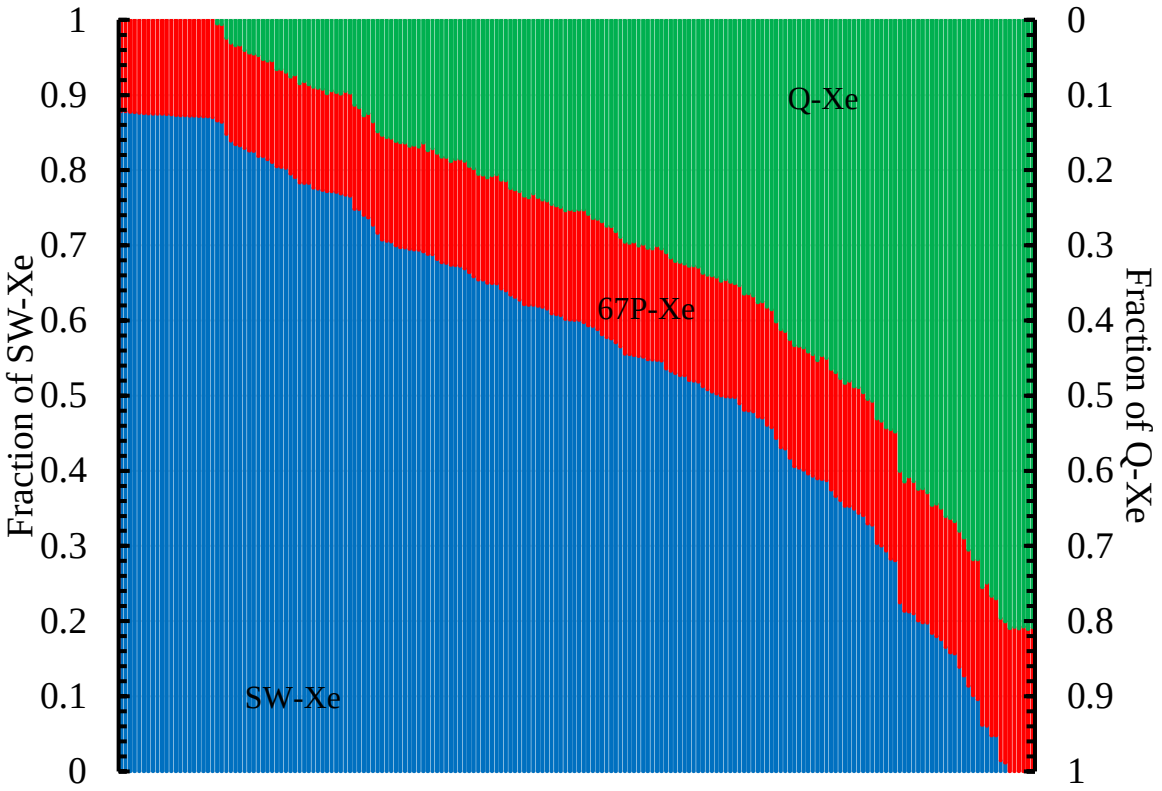


***Figure 3.13*** *Plot of Automaton's sub-solutions to modelling U-Xe from Q-Xe, SW-Xe and 67P-Xe, as in Scenario 11 of Table 3.6. Figure contains 200 vertical bars, each representing one sub-solution with corresponding fractional contributions of SW-Xe (blue bar, plotted from bottom to top, with corresponding values on left vertical axis), Q-Xe (green bar plotted from top to bottom, with corresponding values on right vertical axis), and 67P-Xe (red bar, plotted between other end members) stacked on top of one another.*

Given the mutual exclusion of Q-Xe or SW-Xe still satisfied U-Xe in the modelling, the subsequent modelling in Scenario 12 and 13 sought to simulate the difference in the amount of 67P-Xe required to produce U-Xe with the addition of either Q-Xe or SW-Xe, respectively. The results reflect those of Scenario 11, in that U-Xe can be produced with a mixture containing a larger proportion of 67P-Xe, 19% ± 0.2%, when only mixed with Q-Xe (Solution 12), compared to a mixture of only SW-Xe and 67P-Xe (Scenario 13), which contains on average 13% ± 0.2% of 67P-Xe. Results of modelling Scenario 12 and 13 with Automaton both returned substantially more accurate fractions of end members (percentage fractions all expressing a standard deviation of 0.2%) compared

to Scenario 11, confirming the large standard deviations were a result of SW-Xe and Q-Xe interchangeability. The average results of Scenarios 12 and 13 are plotted on a delta plot relative to U-Xe in Figure 3.14. Note that the solutions contain a significant excess of $^{129}Xe/^{132}Xe$ relative to U-Xe, a feature which is also evident in the sub-solutions to Scenario 11.

Scenario 14 and 15 of Table 3.6 show the results of modelling U-Xe with Automaton from SW-Xe, Q-Xe, and 67P-Xe whilst allowing 67P-Xe to fractionate with and without the inclusion of $^{128}Xe/^{132}Xe$ (in Scenario 14 and Scenario 15, respectively). This modelling attempts to determine how fractional contributions of Q-Xe or SW-Xe to U-Xe are dependent upon fractionation of 67P-Xe, and how reliant such a fractionation is on the composition of $^{128}Xe/^{132}Xe$ in 67P-Xe.

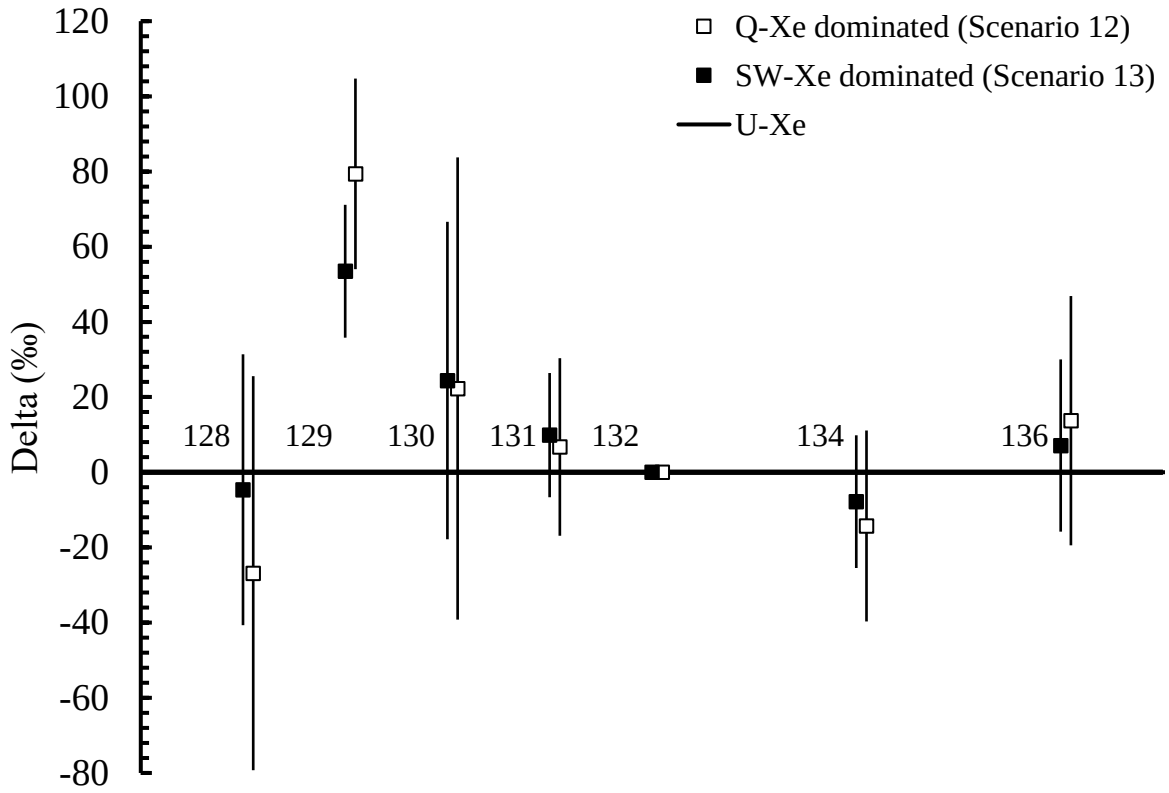


***Figure 3.14*** *Delta plot of Automaton solutions for U-Xe from SW-Xe with 67P-Xe, and Q-Xe with 67P-Xe. Data are permille deviations of averages and standard deviation of isotope ratios of modelled solutions to Scenario 12 (Q-Xe dominated, white squares) and 13 (SW-Xe dominated, black squares) of Table 3.6, with respect to U-Xe (horizontal line). All ratios normalised to $^{132}Xe$. End member compositions reported in Table 3.1.*

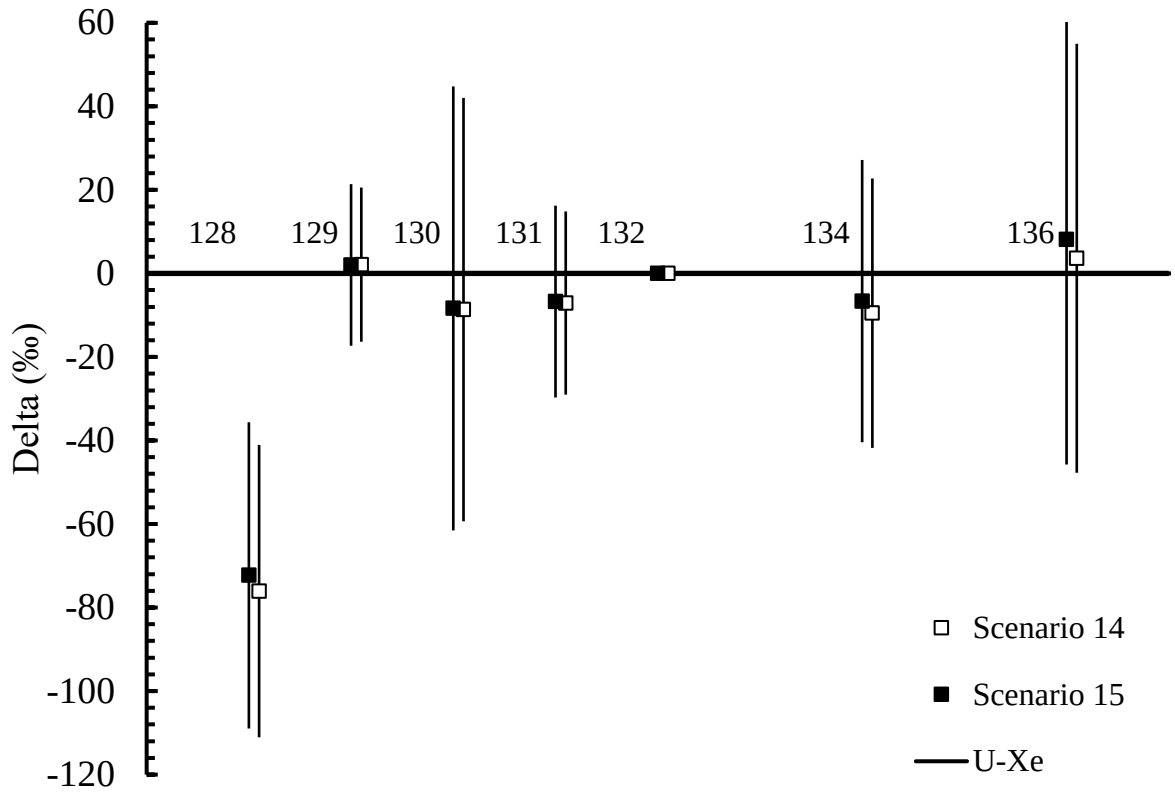


***Figure 3.15*** *Delta plot of Automaton solutions for U-Xe from SW-Xe and fractionated 67P-Xe, with and without the inclusion of $^{128}Xe/^{132}Xe$ in the fit. Data are permille deviations of averages and standard deviation of isotope ratios of modelled solutions to Scenario 14 (including $^{128}Xe/^{132}Xe$) and 15 (not including $^{128}Xe/^{132}Xe$) of Table 3.6, with respect to U-Xe (horizontal line). All ratios normalised to $^{132}Xe$. End member compositions reported in Table 3.1.*

Scenario 14 of Table 3.6, in which Automaton was set up with the freedom to fractionate 67P-Xe with $^{128}Xe$, produced U-Xe with a contribution of 8.9% ± 0.2% 67P-Xe, fractionated to amounts equivalent to 78 ‰/amu ± 1.9 ‰/amu. Scenario 15 of Table 3.6, in which $^{128}Xe/^{132}Xe$ was not included in the fit, resulted in a solution containing 8.4% ± 0.2% 67P-Xe fractionated to the equivalent of 106 ‰/amu ± 2.2 ‰/amu. Both modelled solutions featured compositions dominated by SW-Xe which did not express the interchangeability with Q-Xe such as in the modelled solutions to Scenario 11, which featuring free fractions of SW-Xe, Q-Xe and 67P-Xe without 67P-Xe fractionation.

The equivalent SW-Xe dominated solutions to Scenario 13 featuring unfractionated 67P-Xe contained 13% ± 0.2% of 67P-Xe. The addition of fractionation to a SW-Xe dominated origin of U-Xe with 67P-Xe, therefore amounts to a reduction of roughly 4.1%

in the fraction of 67P-Xe when assuming $^{128}Xe/^{132}Xe$ in 67P-Xe is correctly reported (Scenario 14), and 4.6% in the fraction of 67P-Xe when assuming $^{128}Xe/^{132}Xe$ in 67P-Xe is incorrectly reported (Scenario 15), compared to their unfractionated equivalent (Scenario 13). Figure 3.15 illustrates the modelled compositions of solutions to Scenario 14 and 15 in comparison to U-Xe, both modelled compositions no longer have an excess of $^{129}Xe/^{132}Xe$, but now express a significant deficit in the $^{128}Xe/^{132}Xe$ composition relative to U-Xe.

The results of the modelling of U-Xe can be summarised as follows. A non-fractionated simple mixture of Q-Xe, SW-Xe, and 67P-Xe can produce U-Xe with any combination of either SW-Xe or Q-Xe, or both components, with a 67P-Xe contribution of around 15%. Modelling of U-Xe with 67P-Xe and either SW-Xe or Q-Xe features 13% ± 0.2% of 67P-Xe and 19% ± 0.2% of 67P-Xe, respectively, and both solutions express a larger $^{129}Xe/^{132}Xe$ than U-Xe. Allowing 67P-Xe to fractionate reduces the contribution of 67P-Xe to U-Xe and matches the $^{129}Xe/^{132}Xe$ with its value in U-Xe, although a deficit in $^{128}Xe/^{132}Xe$ relative to U-Xe is observed. Removal of $^{128}Xe/^{132}Xe$ from the modelling increases the modelled fractionation, reduces the contribution from 67P-Xe by roughly half a percent, and resembles the scenario which included $^{128}Xe/^{132}Xe$ in its isotopic composition.

***Table 3.6*** *Modelling U-Xe with SW-Xe, Q-Xe, and 67P-Xe.*

| Scenarios | 11 | 12 | 13 | 14 | | 15 | |
|---|---|---|---|---|---|---|---|
| Target composition | U-Xe | U-Xe | U-Xe | U-Xe | | U-Xe | |
| Conditions | All end members | Q-Xe and 67P-Xe | SW-Xe and 67P-Xe | Q-Xe, SW-Xe, and 67P-Xe | | All end members, $^{128}$Xe not fitted | |
| | No fractionation | No fractionation | No fractionation | 67P-Xe fractionation | | 67P-Xe fractionation | |
| End members | Fractions (% ± σ) | Fractions (% ± σ) | Fractions (% ± σ) | Fractions (% ± σ) | End member fractionation (‰/amu ± σ) | Fractions (% ± σ) | End member fractionation (‰/amu ± σ) |
| Q-Xe | 30 ± 23 | 81 ± 0.2 | - | 0 ± 0 | - | 0 ± 0 | - |
| SW-Xe | 56 ± 25 | - | 87 ± 0.2 | 91.1 ± 0.2 | - | 91.6 ± 0.2 | - |
| 67P-Xe | 15 ± 2 | 19 ± 0.2 | 13 ± 0.2 | 8.9 ± 0.2 | 78 ± 1.9 | 8.4 ± 0.2 | 106 ± 2.2 |

*End member compositions listed in Table 3.1. Automaton's solutions to the scenarios described in each column. Solutions represent the results of Monte Carlo simulations of 200 mixtures containing all xenon isotopes except for $^{124}$Xe, $^{126}$Xe, unless stated. Numbers indicate averages and standard deviations of all sub-solutions. Hyphens designate exclusion of corresponding variable from solution. Fractionation listed as linear equivalents to non-linear equilibrium fractionation, which approaches linearity at these magnitudes.*

### 3.3.4. Martian atmosphere

The Mars Science Laboratory's Sample Analysis at Mars (SAM) investigation measured the composition of Martian atmospheric xenon. This composition, reported in Conrad et al. (2016) and discussed in Section 1.3.4, features a significant monoisotopic excess of $^{129}$Xe, presumably due to the decay of $^{129}$I, but otherwise appears to resemble fractionated SW-Xe (Pepin, 2000). This section uses Automaton in modelling of the possible contribution of cometary xenon, assumed to be 67P-Xe, to the Martian atmosphere using combinations of SW-Xe, Q-Xe, and the isolated spallogenic component of Conrad et al. (2016) (containing REE and Ba spallation derived xenon). Fractionation is introduced in all but the initial modelled scenarios as the Martian atmosphere's fractionated solar resemblance is well established (Swindle and Jones, 1997; Mathew et al., 1998; Pepin, 2000; Conrad et al., 2016). All the modelling described in this section considered $^{128}$Xe/$^{132}$Xe, $^{130}$Xe/$^{132}$Xe, $^{131}$Xe/$^{132}$Xe, $^{132}$Xe/$^{132}$Xe, $^{134}$Xe/$^{132}$Xe, and $^{136}$Xe/$^{132}$Xe in the chi-squared statistic measuring goodness of fit. $^{129}$Xe/$^{132}$Xe excess was not included due to its excess in Martian atmospheric xenon being easily attributed to decay of $^{129}$I. $^{124}$Xe/$^{132}$Xe and $^{126}$Xe/$^{132}$Xe were not included as they are not contained in the 67P-Xe composition.

Scenario 16 of Table 3.7 contains the results of modelling with Automaton of a scenario in which Q-Xe, SW-Xe, 67P-Xe, and fissiogenic xenon from $^{244}$Pu and $^{238}$U decay are mixed in a simple model of fractional contributions with no fractionation to the Martian atmospheric xenon composition. This scenario was solved by a large range of acceptable fractional contributions of each end member, as evident in the large standard deviations expressed by their sub-solutions (standard deviations up to 16%). As in the case of the similarly simple model of Earth's atmosphere (Solution 6 of Table 3.5), the model attributed a significant portion of Martian xenon (65% ± 16%) to cometary contributions.

Scenario 17 of Table 3.7 describes the results of modelling a scenario in which a Martian atmosphere containing the same end members as Scenario 16 was also subject to a post-mixture fractionation which Automaton could optimise. Despite the unconstrained post-mixture fractionation variable, the solution applied negligible fractionation (average and standard deviation of 0.002 ‰/amu ± 0.03 ‰/amu), and returned near identical results to the equivalent unfractionated Scenario 16.

Scenario 18 of Table 3.7 posited a negligible fissiogenic contribution to the Martian atmosphere, as is frequently suggested (Swindle and Jones, 1997; Pepin, 2000; Conrad et al., 2016), so only modelled the Martian atmosphere with the end members SW-Xe, Q-Xe, and 67P-Xe, and applied a variable post-mixture fractionation. This scenario resulted in sub-solutions expressing a significant scatter in their proposed fractions of components, with the average mixture containing 28% ± 22% Q-Xe, 23% ± 8% 67P-Xe, no contribution from SW-Xe, and a post-mixture fractionation equivalent to 54 ‰/amu ± 10.6 ‰/amu. The sub-solutions revealed that this scatter was the result of a complimentary increase in the fraction of 67P-Xe with increased fractionation in favour of the heavier isotopes, between mixtures containing no 67P-Xe fractionated to an equivalent of 22 ‰/amu, up to mixtures containing 40% 67P-Xe fractionated to an equivalent of 76 ‰/amu.

Scenario 19 of Table 3.7 contains the results of modelling with Automaton of a Martian atmosphere in which Q-Xe does not contribute, and the only modelled end members are 67P-Xe and SW-Xe, to which an unconstrained post-mixture fractionation was added and optimised. The solutions to this scenario contained 41% ± 7% 67P-Xe, and significant average post-mixture fractionation equivalent to 82 ‰/amu ± 7.6 ‰/amu. Figure 3.16 illustrates that the scale of fractionation applied in the modelled sub-solutions exhibited a negative correlation with the fractional contribution of 67P-Xe. These sub-solutions illustrate that the scenario can result in the Martian atmospheric composition

with fractional contributions of 67P-Xe between extremes of 20% and 58% when post-mixture fractionations of 60 ‰/amu and 97 ‰/amu, are applied, respectively.

Scenarios 20 and 21 of Table 3.7 contain modelling with Automaton of scenarios in which the contribution of spallation to Martian atmospheric xenon is explored. Scenario 20 considers the Martian spallation composition as described in Conrad et al. (2016) as an end member along with SW-Xe and 67P-Xe, and allows Automaton to optimise an unconstrained post-mixture fractionation to reproduce the Martian atmospheric composition. This scenario returned a Martian atmosphere composed of 2% spallation, 48% ± 3% SW-Xe and 50% ± 3% 67P-Xe, all significantly fractionated to an equivalent of 148 ‰/amu ± 10 ‰/amu.

Scenario 21 modelled the spallation corrected Martian atmospheric composition of Conrad et al. (2016) as the target composition, which is recreated by a mixture of the end members SW-Xe and 67P-Xe, and an unconstrained post-mixture fractionation. This scenario resulted in a spallation corrected Martian atmosphere consisting of 83% ± 17% SW-Xe and 17% ± 17% 67P-Xe, with a post-mixture fractionation equivalent to 59 ‰/amu ± 21 ‰/amu. Figure 3.17 illustrates that Scenario 21 provided another example of a correlation between the fractions of components and the applied fractionation, similarly to Scenario 19, an increased 67P-Xe contribution was matched by an increase in the degree of post-mixture fractionation applied.

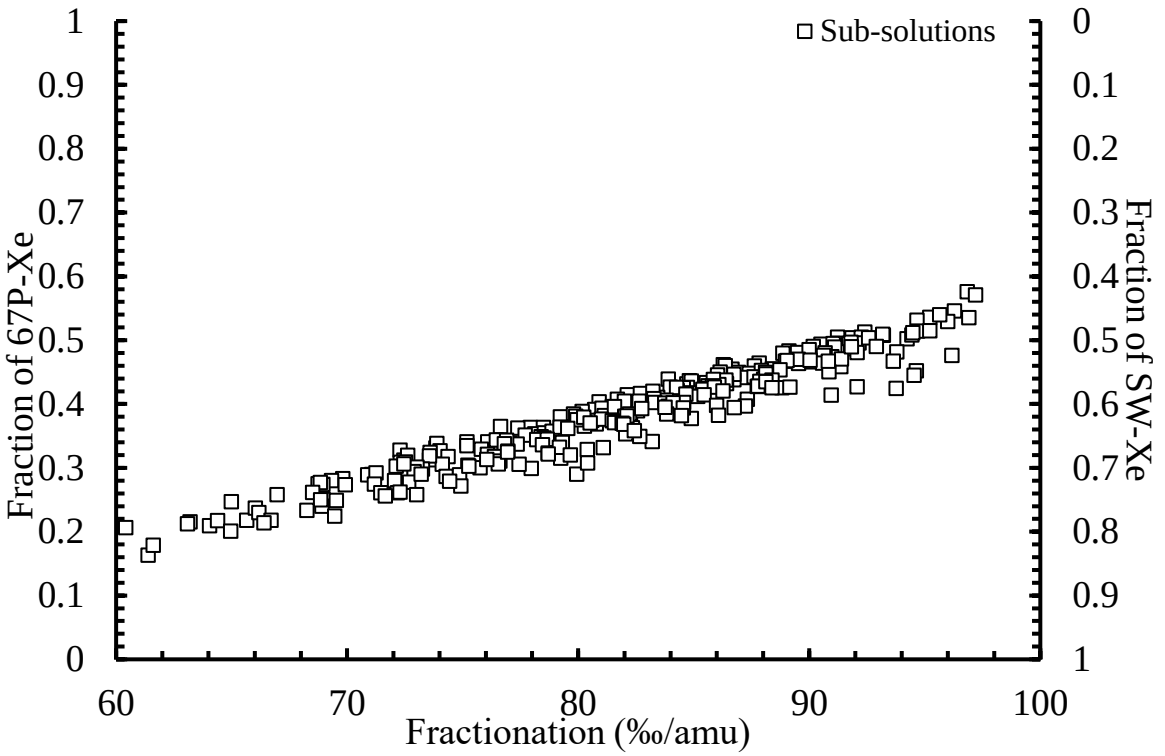


***Figure 3.16*** *Automaton's 200 sub-solutions to modelling the Martian atmosphere with a fractionated mixture of 67P-Xe and SW-Xe. Data correspond to Scenario 19 of Table 3.7. Each point represents one Monte Carlo simulation in which the corresponding values for fractions of 67P-Xe (left axis) and SW-Xe (right axis) are shown on the two vertical axes. The horizontal axis shows the equivalent linear fractionation (as ‰/amu) applied to each sub-solution. End member compositions in Table 3.1.*

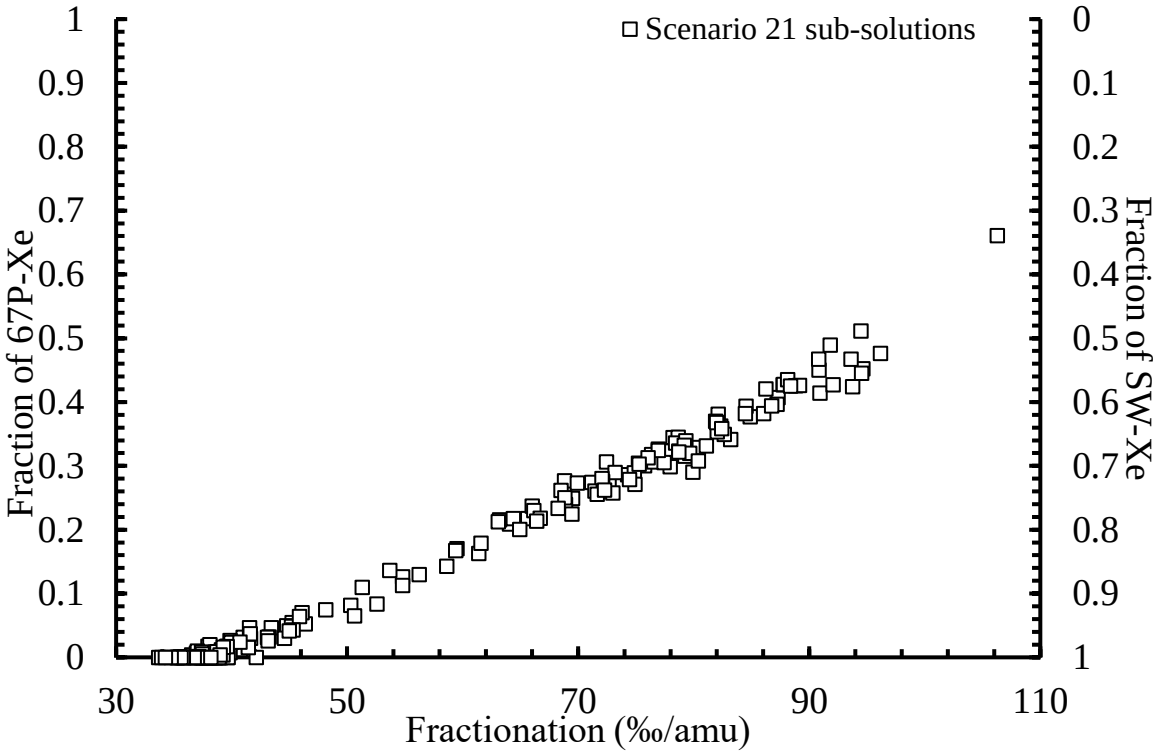


***Figure 3.17*** *Automaton's 200 sub-solutions to modelling the spallation corrected Martian atmosphere with a fractionated mixture of 67P-Xe and SW-Xe. Data correspond to Scenario 21 of Table 3.7. Each point represents one Monte Carlo simulation in which the corresponding values for fractions of 67P-Xe (left axis) and SW-Xe (right axis) are shown on the two vertical axes. The horizontal axis shows the equivalent linear fractionation (as ‰/amu) applied to each sub-solution. End member compositions in Table 3.1.*

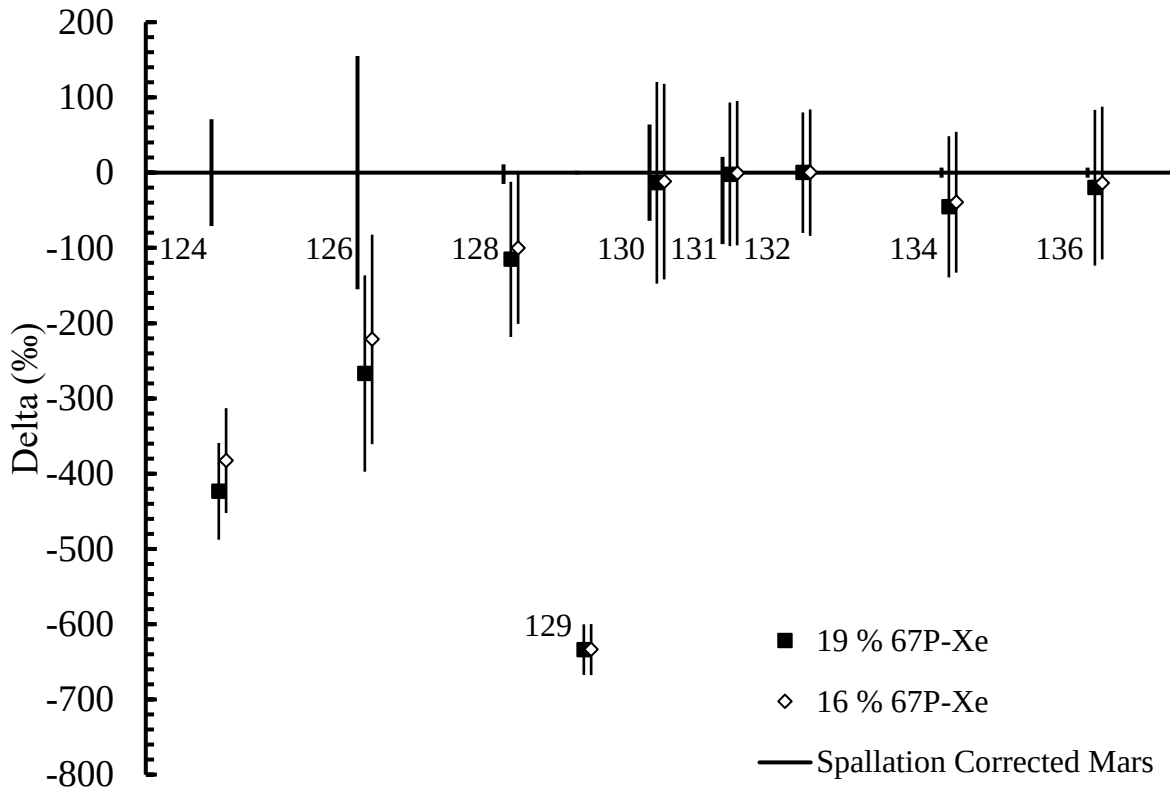


***Figure 3.18*** *Delta plot of Automaton solutions for spallation corrected Martian atmospheric xenon from SW-Xe with 16% and 19% 67P-Xe, and post-mixture fractionation. Data are permille deviations of isotopic ratios normalised to $^{132}$Xe from spallation corrected Martian atmospheric xenon (horizontal line). 16% 67P-Xe mixture plotted as white diamonds, 19% 67P-Xe mixture plotted as black squares, remaining composition is SW-Xe fractionated according to the text. Errors are propagated representations of one standard deviation. Note that $^{124}$Xe, $^{126}$Xe, and $^{129}$Xe was not fit in these solutions, yet their corresponding compositions in such mixtures are still plotted. End member compositions in Table 3.1.*

Figure 3.17 exhibits a mathematical relationship between the sub-solutions of Automaton to a model of the spallation corrected Martian atmosphere composed of 67P-Xe and SW-Xe. Using this relationship, we can extract a figure for the post-mixture fractionation applied for any given fractional contribution of 67P-Xe within that range. Assuming that the spallation corrected Martian atmosphere was composed of the same fractional contribution of 67P-Xe as Earth's atmosphere as modelled in Scenarios 9 and 10 of Table 3.5 (16% and 19%, respectively), we can extract values for the corresponding post-mixture fractionation. In this scenario, the degree of fractionation experienced by the spallation corrected Martian atmosphere would be roughly equivalent to 59 ‰/amu for the 16% 67P-Xe scenario and 63 ‰/amu for the 19% 67P-Xe scenario. Figure 3.18 shows a

delta plot of the spallation corrected Martian atmospheric mixtures containing the assumed 67P-Xe contributions of 16% and 19% (with the remaining percentage composed of SW-Xe) and suggested fractionation values (from relationship shown in Figure 3.17).

The results of the modelling of the Martian atmosphere can be summarised as follows. A non-fractionated simple mixture of Q-Xe, SW-Xe, 67P-Xe, and the fission products of $^{244}$Pu and $^{238}$U produces Martian atmospheric xenon with a large 67P-Xe contribution (65%) and significant scatter (Scenario 16). A nearly identical solution is proposed when post-mixture fractionation is added (Scenario 17). A model without any fission contribution, only Q-Xe, SW-Xe, 67P-Xe, and post mixture fractionation (Scenario 18), contains no SW-Xe and significant scatter of most variables as a result of a mathematical relationship with complementary increases in both the fraction of 67P-Xe (up to 40%) and post-mixture fractionation (between 22 ‰/amu and 76 ‰/amu). A SW-Xe and 67P-Xe origin of the Martian atmosphere with post-mixture fractionation (Scenario 19) expresses a similar complementary relationship for an increased post-mixture fractionation (between 60 ‰/amu and 97 ‰/amu) and fraction of 67P-Xe (between 20% and 58%). A model including SW-Xe, 67P-Xe, spallation, and post-mixture fractionation (Scenario 20) features a significant fractionation (around 148 ‰/amu) and around 50% 67P-Xe. A model of the spallation corrected Martian atmospheric xenon composition containing SW-Xe, 67P-Xe and post-mixture fractionation (Scenario 21) expresses another relationship between the fraction of 67P-Xe and the amount of post-mixture fractionation. Extrapolating the post-mixture fractionation from this relationship assuming either a 16% or 19% contribution from 67P-Xe (as in Earth's atmosphere from Scenario 9 and 10), results in a spallation corrected Martian atmosphere composed of SW-Xe and a post-mixture fractionation of either 59 ‰/amu (for the 16% 67P-Xe scenario) and 63 ‰/amu (for the 19% 67P-Xe scenario). All models feature a significant deficit in the amount of $^{129}$Xe/$^{132}$Xe relative to the Martian atmosphere.

***Table 3.7*** *Modelling Martian atmospheric xenon with Q-Xe, SW-Xe, $^{244}$Pu, $^{238}$U, and spallation.*

| Scenarios | 16 | 17 | 18 | 19 | 20 | 21 |
|---|---|---|---|---|---|---|
| Target composition | Martian atmosphere | Martian atmosphere | Martian atmosphere | Martian atmosphere | Martian atmosphere | Spallation corrected Martian atmosphere |
| Conditions | All end members except Martian spallation | All end members except Martian spallation | Q-Xe, SW-Xe, and 67P-Xe | SW-Xe and 67P-Xe | SW-Xe, 67P-Xe, and Martian spallation | SW-Xe and 67P-Xe |
| | No fractionation | Post-mixture fractionation | Post-mixture fractionation | Post-mixture fractionation | Post-mixture fractionation | Post-mixture fractionation |
| End members | Fractions (% ± σ) | Fractions (% ± σ) | Fractions (% ± σ) | Fractions (% ± σ) | Fractions (% ± σ) | Fractions (% ± σ) |
| Q-Xe | 5 ± 14 | 5 ± 13 | 28 ± 22 | - | - | - |
| SW-Xe | 17 ± 15 | 18 ± 16 | 0 ± 0 | 59 ± 7 | 48 ± 3 | 83 ± 17 |
| $^{244}$Pu | 2 ± 2 | 2 ± 2 | - | - | - | - |
| $^{238}$U | 11 ± 3 | 11 ± 3 | - | - | - | - |
| 67P-Xe | 65 ± 16 | 65 ± 15 | 23 ± 8 | 41 ± 7 | 50 ± 3 | 17 ± 17 |
| Martian spallation | - | - | - | - | 2 ± 0.2 | * |
| Post-mixture fractionation (‰ / amu ± σ) | - | 0.002 ± 0.03 | 54 ± 10.6 | 82 ± 7.6 | 148 ± 10 | 59 ± 21 |

*End member compositions listed in Table 3.1. Automaton's solutions to the scenarios described in each column. Solutions represent the results of Monte Carlo simulations of 200 mixtures containing all xenon isotopes except for $^{124}$Xe, $^{126}$Xe, unless stated. Numbers indicate averages and standard deviations of all sub-solutions. Hyphens designate exclusion of corresponding variable from solution. Fractionation listed as linear equivalents to non-linear equilibrium fractionation, which approaches linearity at these magnitudes. *Spallation is already removed from target composition.*

## 3.4. Discussion

### 3.4.1. 67P/Churyumov-Gerasimenko

Two versions of 67P-Xe were considered in the modelling of its composition with SW-Xe and Q-Xe. The use of one version is signified by the fitting of $^{128}Xe/^{132}Xe$, thus assuming its reported composition is correct. The other version of 67P-Xe assumes the reported $^{128}Xe$ composition is incorrect, and subsequently removes the isotope from the fit. $^{128}Xe/^{132}Xe$ is the lightest reported isotope in the composition of 67P-Xe, and mass fractionation more significantly affects isotopic compositions of the lightest and heaviest isotopes, so exclusion of $^{128}Xe/^{132}Xe$ from a fit, or increasing the uncertainty of the $^{128}Xe/^{132}Xe$ composition may significantly change the applied fractionation in models containing 67P-Xe. This is of particular importance given the apparent depletion of $^{128}Xe/^{132}Xe$ in the composition of 67P-Xe in comparison to fractionated SW-Xe or Q-Xe as reported in Section 3.3.1.

These results suggest the initial concerns about the unmixing of $^{128}Xe$ from isobaric interference do not significantly affect the interpretation of the origin of 67P-Xe from either SW-Xe or Q-Xe. A narrow range of significant fractionation in favour of the heavy isotopes (between 124 ‰/amu < 136 ‰/amu) producing acceptable solutions for the Scenarios 1, 2, 3, and 4, is surprising given the dependency of fractionation on the composition of $^{128}Xe/^{132}Xe$, and the fact the 67P-Xe composition excluding $^{128}Xe/^{132}Xe$ appears to resemble fractionated solar wind. The numerically acceptable solutions of modelling these scenarios also contain a significant depletion of $^{134}Xe/^{132}Xe$ and $^{136}Xe/^{132}Xe$ relative to the target compositions (as shown in Figure 3.9 and Figure 3.10). An even greater fractionation, as afforded by the removal of $^{128}Xe/^{132}Xe$ from the fit, or inflation of its uncertainty, could have allowed the depletions in $^{134}Xe/^{132}Xe$ and

$^{136}Xe/^{132}Xe$ to be corrected, yet all modelled solutions feature this depletion, and roughly similar fractionation.

Figure 3.9 and Figure 3.10 may illustrate why this was the case, as a greater fractionation would have resulted in the more abundant and more precise $^{129}Xe/^{132}Xe$ (and potentially $^{131}Xe/^{132}Xe$) composition not matching the SW-Xe or Q-Xe compositions within error.

The results of the modelling of SW-Xe with freely fractionated Q-Xe and 67P-Xe in Scenario 5 contained a wildly variable range of solutions with enormous degrees of fractionation in favour of the heavy isotopes (214 ‰/amu < 1305 ‰/amu). This solution requires the physical explanation of a degree of fractionation which has not been observed elsewhere in the Solar System, and is likely a purely mathematical solution.

The more reasonable results of scenarios in which fractionation in favour of the heavy isotopes in 67P-Xe resembles either SW-Xe or Q-Xe with large depletions in the heaviest xenon isotopes present competing scenarios with individual problems:

- *The fractionation required to produce SW-Xe or Q-Xe with 67P-Xe.*

  Fractionation of the magnitude suggested by the most acceptable models is unfamiliar in the inner Solar System, but cannot be ruled out in the relatively unknown outer Solar System. If we assume a process exists which can produce such a fractionation, then elemental fractionation may be expected to express similarly extreme fractionations. Marty et al. (2017) estimate an $^{132}Xe/^{36}Ar$ ratio of $2.5 \times 10^{-2}$ for 67P from in situ mass spectrometer measurements, a value much higher than the solar ratio of $1.8 \times 10^{-5}$ (Anders and Grevesse, 1989).

- *The fractionation required to produce SW-Xe or Q-Xe with 67P-Xe continued.*

  There are two ways of approaching this difference, if 67P-Xe is precursor to SW-Xe which is mass fractionated in favour of the heavy isotopes, then a complimentary enrichment in the heavier chemical species could agree with the enriched $^{132}Xe/^{36}Ar$ ratio in 67P relative to SW-Xe. In a scenario in which 67P-Xe is derived from SW-Xe mass fractionated in favour of the light isotopes, the $^{132}Xe/^{36}Ar$ ratio should correspondingly feature a larger relative $^{36}Ar$ contribution, and should be lower. Applying the same process to the 67P ratio of $^{84}Kr/^{132}Xe = 4.7 \pm 1.1$ (Rubin et al., 2018), which is depleted by a factor of around five compared to the solar ratio of $20 < {}^{84}Kr/^{132}Xe < 29$ (Wieler, 2002), discovers the opposite. A scenario in which SW-Xe is a precursor to 67P-Xe which has been enriched in the light isotopes may correspond to a similarly enriched ratio of $^{84}Kr/^{132}Xe$ in 67P relative to solar, which is not the case. The Q-Xe equivalent of this thought experiment with the ratio $^{84}Kr/^{132}Xe = 1.2 \pm 0.36$ in phase Q (Busemann et al., 2000), implies an origin of 67P-Xe from Q-Xe fractionated in favour of the light isotopes and elements. However, inferring elemental fractionations of other noble gases from isotopic fractionations of xenon is problematic given the unknown nature of the process which fractionated the xenon, can we assume that such a process also affects elemental fractionation between noble gases? Such contradictions are perhaps an illustration of the unlikely nature of all such scenarios, especially when considering the further problems listed below.

- *How can the depletion in $^{134}Xe/^{132}Xe$ and $^{136}Xe/^{132}Xe$ be explained?*

  Assuming the fractionation is satisfactorily explained, then the subsequent depletion of $^{134}Xe/^{132}Xe$ and $^{136}Xe/^{132}Xe$ relative to SW-Xe and Q-Xe must be explained. A larger uncertainty for both of these isotopic compositions than was reported by Marty et al. (2017) could mean their compositions match either SW-Xe or Q-Xe. Similarly, a depletion in the $^{132}Xe$ concentration of actual cometary xenon relative to 67P-Xe, or a misreported enrichment in $^{132}Xe$ relative to the true composition would result in higher ratios of $^{134}Xe/^{132}Xe$, $^{136}Xe/^{132}Xe$, and $^{128}Xe/^{132}Xe$, making fractionated 67P-Xe resemble SW-Xe and Q-Xe more closely.

- *When and where were these reservoirs isolated?*

  If the above scenarios are satisfactorily explained, and they are compatible with the subsequent depletion in $^{134}Xe/^{132}Xe$ and $^{136}Xe/^{132}Xe$ relative to SW-Xe and Q-Xe, then when and where did these processes occur? The outer Solar System is likely to contain processes not documented by our mostly inner Solar System observations, but can we assume these processes occurred on all comets which enriched inner Solar System materials, as is the case if we assume 67P is representative of cometary xenon? Assuming the composition of 67P-Xe is a precursor for either Q-Xe or SW-Xe, how would such a composition be reconciled with its measurement only being contained within 67P, surely such a composition would be ubiquitous, or at least preserved in stages heading towards its reported composition.

Whether these problems present scenarios which are more or less probable than an exotic nucleosynthetic signature preserved in comets, as suggested by Marty et al. (2017), is unclear given our current understanding.

The use of the two compositions of 67P-Xe in the other modelling of reservoirs in the Solar System were limited to scenarios expressing large degrees of fractionation specific to 67P-Xe. Scenarios 14 and 15 of Table 3.6 illustrate the difference in modelling of U-Xe with a mixture of Q-Xe, SW-Xe, and fractionated 67P-Xe with and without $^{128}$Xe included in the fit. The exclusion of $^{128}$Xe in the fit resulted in a decreased contribution from 67P-Xe to the modelled composition (9% ± 0.2% reduced to 8.4% ± 3%), and a larger degree of fractionation (78 ‰/amu ± 1.9 ‰/amu increased to 106 ‰/amu ± 2.2 ‰/amu). This is closer to the expected behaviour of the modelling in a scenario containing fractionation with and without the exclusion of $^{128}$Xe/$^{132}$Xe in the fit, as explained before, with $^{128}$Xe/$^{132}$Xe being more significantly affected by fractionation due to it being the lightest reported isotope.

Curiously, modelling of U-Xe in Scenario 11, allowing contributions from SW-Xe, Q-Xe, and 67P-Xe expressed an interchangeability in the contributed fractions of either SW-Xe or Q-Xe (discussed in more detail in Section 3.4.3) unless 67P-Xe was allowed to be fractionated, as in Scenarios 14 and 15, in which case Q-Xe was almost entirely removed from the modelled solutions in favour of a fractionated 67P-Xe and SW-Xe mixture. The results of Automaton effectively substituted Q-Xe with fractionated 67P-Xe. Whether this is indicative of a favoured origin of 67P-Xe from Q-Xe rather than SW-Xe is debatable, especially given the problems listed earlier, and the fact that the proposed fractionations for 67P-Xe are so extreme.

### 3.4.2. Earth's atmosphere

The modelling of xenon in Earth's atmosphere with Automaton and 67P-Xe in this work began with a model containing linear contributions of likely end members with no fractionation, Scenario 6. The solution for Earth's atmospheric xenon in this scenario was most notable for its significant fraction of 67P-Xe (53% ± 15%). The suggestion that the xenon contained in Earth's atmosphere is mostly sourced from comets such as 67P-Xe has implications for other chemical signatures for enriched volatiles in comets. For example, the other noble gases, and D/H, although the modelling of Marty et al. (2017) suggests its contribution to the enormous volume of water on Earth is marginal (A'Hearn et al., 2012; Marty, 2012). Additionally, Bekaert et al. (2020) investigated the contribution from 67P of Kr and a suite of other volatiles (Ar, Kr, $H_2O$, D/H, N, and $^{12}C$) to Earth's volatile budget and suggested they were mostly negligible compared to Earth's existing volatile budget, and mostly contributed from sources other than comets such as 67P. However, their modelling using the volatile content of 67P suggested that a contribution corresponding to around 20% of the terrestrial xenon coincides with tens of percent of the carbon budget of the Earth, and a significant mass of organic molecules such as glycine ($5 \times 10^{18}$ kg, although the preservation of these species during delivery is unclear). These values would be doubled along with the xenon contribution from 67P in the non-fractionated solutions for Scenarios 6 and 7 in which roughly half the xenon budget of Earth's atmosphere came from comets like 67P. The solution's attribution of 14% ± 5% of Earth's atmospheric xenon originating from fissiogenic sources (around 2% $^{238}U$ and 12% $^{244}Pu$), is also inconsistent with other models of atmospheric evolution, being a factor of seven larger than has been suggested by Caracausi et al. (2016) as 2.26% ± 0.28% of mostly $^{244}Pu$ fission.

An additional consideration is that volatiles not accounted for in Bekaert et al. (2020) may be incompatible with over half the xenon budget of Earth's atmosphere coming from comets like 67P. Section 1.4.3 also lists many volatiles contained in comets which are not included in the modelling of Bekaert et al. (2020), a doubling of the cometary contribution to Earth's atmosphere may affect any one of these volatiles in a way which is incompatible or notable within Earth's atmosphere.

A model for Earth's atmosphere without fractionation is also inconsistent with most ideas of Earth's atmospheric evolution. Fractionation of the atmospheres of both Earth and Mars is an established theory (Hunten et al., 1987; Pepin, 1991; Chassefière and Leblanc, 2004; Conrad et al., 2016; Marty et al., 2017), and has arguably been measured in sample analyses (Caracausi et al., 2016; Meshik et al., 2019). The solution to Scenario 7, in which the required post-mixture fractionation of Earth's atmosphere was added to the model containing all likely end members with unconstrained fractions (essentially Scenario 6), produced near identical results to its unfractionated equivalent (as shown in Table 3.5).

Section 3.4.1 explains the interchangeable treatment of Q-Xe or SW-Xe from fractionated 67P-Xe during modelling with Automaton. Perhaps the lack of overall fractionation, even in the models allowing for fractionation, could have been exchanged for a greater contribution of 67P-Xe as the modelling considers both as mostly interchangeable.

The solutions for modelling Earth's atmosphere with little or no fractionation with Automaton must overcome the following problems if they are to be plausible models for Earth's atmosphere:

- *Are comets relatively enriched in xenon to the magnitude that such a large modelled contribution would not be obvious in other cosmochemical tracers?*

  Section 1.4.3 contains a long list of volatiles contained in comets which would have complimented the xenon brought to Earth by comets resembling 67P. A volume of cometary matter consistent with around 50% of Earth's atmospheric xenon would alter the concentration of Earth's volatile budget. Modelling with volatile data from 67P and Earth using roughly half the cometary contribution of this scenario suggest the volatile budget of Earth would not be significantly affected (Marty, et al., 2017; Bekaert et al., 2020). Doubling this contribution and considering volatiles beyond the scope of existing models or measurements from 67P may suggest otherwise.

- *What are the implications for a lack of any observed fractionation of Earth's atmospheric xenon?*

  If we assume the case for the increased contribution from 67P-Xe essentially masking a fractionation, then there are many implications for assuming Earth's atmosphere has not undergone fractionation. How can this be the case with the samples and modelling which strongly suggest fractionation of Earth's atmosphere (Hunten et al., 1987; Pepin, 1991; Chassefière and Leblanc, 2004; Caracausi et al., 2016; Conrad et al., 2016; Marty et al., 2017). Such models also indicate a significant loss of the mass of Earth's atmosphere which facilitated fractionation, as evident in other chemicals and heavy noble gases, what process could have protected the isotopic composition of xenon from these processes? The fractionation of the atmospheres of Earth and Mars are frequently considered in tandem, given their relative similarities in proximity to the sun and size, a lack of fractionation on one body would challenge similar arguments for the other.

- *The fission contribution is inconsistent with other models of atmospheric evolution.* The contribution of xenon derived from the fission of $^{244}Pu$ and $^{238}U$ to Earth's atmosphere in the scenarios with insignificant or no fractionation are in excess of previous modelling and challenge models of the composition of Earth's interior (Pepin, 1991; Caracausi et al., 2016)

Scenarios 6, 7, and 8 of Earth's atmospheric xenon are all solved with large uncertainties on the fractional contributions of end members. This is probably an example of a non-minimal model, in which too many variables are fitted with constraints which are too loose. Having too wide a range of variables makes Automaton capable of solving the model with many combinations of variables, which manifests as a large scatter in the sub-solutions. Table 3.5 contains evidence of this increase of uncertainty with more variables; as the standard deviation of the sub-solutions appears to increase by around one percent with each addition of a variable, such as post-mixture fractionation (in Scenario 7), and fractionation of 67P-Xe (in Scenario 8), neither addition reduces the uncertainty for the modelled solutions, and the solutions express large uncertainties in most variables. Beyond the physical implications of such models, drawing interpretations of models for atmospheric evolution in which the uncertainties of contributions from comets and chondritic material mean they may contribute either 0% or 50% (as is roughly the case with the standard deviation of the fraction of Q-Xe in Scenarios 6, 7, and 8) is not helpful beyond their mathematical possibility.

Scenarios 9 and 10 avoid the non-minimal modelling of the other solutions by applying physical constraints on variables based on existing models for Earth's atmospheric evolution. These two solutions result in a significantly lower contribution of 67P-Xe to Earth's atmosphere, one which coincides with the results of other models of Marty et al. (2017) and Bekaert et al. (2020), including their consideration of

complementary volatile enrichment. Both the SW-Xe and Q-Xe dominated scenarios (9 and 10, respectively), also feature fractionations of a magnitude more consistent with other models for Earth's atmospheric evolution. Pujol et al. (2011) suggested Earth's atmospheric xenon could be formed from chondritic xenon fractionated by a maximum of close to 35 ‰/amu which sharply decayed exponentially to about 10 ‰/amu after 1.5 Ga, and to 0 ‰/amu in the present day. Their proposed fractionation is comparable to the solutions to modelling of Scenario 9 and 10 with Automaton.

The degree of fractionation (35.4 ‰/amu ± 0.2 ‰/amu) suggested by the solution to modelling Earth's atmospheric composition in Scenario 9 with Automaton, a fractionated mixture of mostly SW-Xe (81%), 67P-Xe (16%), negligible Q-Xe and a fixed fission contribution from $^{244}$Pu (2.26%), closely resembles the 37.7 ‰/amu fractionation suggested for the Martian atmosphere by Marti and Mathew (1998). This is despite the Martian atmosphere being a reservoir which has undergone significantly more hydrodynamic escape than Earth's atmosphere.

The solutions for Scenarios 9 and 10 also illustrate the similarity in Automaton's handling of SW-Xe and Q-Xe in modelling containing both or either of them as end members. The solution to Scenario 9 disregarded any notable contribution of Q-Xe, and produced a comparable result to the modelling of Scenario 10, which only differed in a 3% increase in amount of 67P-Xe for the model dominated by Q-Xe instead of SW-Xe (see Table 3.5). Scenario 10 may be a more appropriate model for the reality of such a mixture, as it corresponds with the Caracausi et al. (2016) suggestion of light xenon isotopes in Earth's mantle favouring a chondritic origin instead of SW-Xe. These solutions probably provide the most accurate modelled proposals of Earth's atmosphere with 67P-Xe in this work.

Figure 3.12 plots the modelled solutions for Scenario 9 and 10 in comparison to Earth's atmospheric composition. There are two significant features to this plot which cast doubt on their ability to recreate the composition of Earth's atmospheric xenon. Firstly, the modelled compositions of both scenarios satisfy the $^{129}Xe/^{132}Xe$ composition despite not taking into account the decay of $^{129}I$ and subsequent enrichment of that ratio in Earth's atmosphere during its formation. The $^{129}Xe/^{132}Xe$ composition is likely to be higher than its composition as in these modelled compositions, but such an enrichment may make the modelled compositions exceed the true atmospheric xenon composition. The second point is that the modelled solutions express significant uncertainties, despite the minimal scatter in the modelled solutions. This is a consequence of uncertainties in the input data, mostly from 67P-Xe, which detracts from the validity of the solutions.

### 3.4.3. U-Xe

An interesting feature of modelling U-Xe with 67P-Xe, Q-Xe, and SW-Xe was that sub-solutions expressed an interchangeability between Q-Xe and SW-Xe in which minor differences in 67P-Xe contribution were the only difference between a Q-Xe or SW-Xe dominated composition resembling U-Xe. Scenario 11 provided the most pronounced example of that, as illustrated in Figure 3.13, where a three-component mixture of SW-Xe, Q-Xe, and 67P-Xe was modelled to produce U-Xe, and the sub-solutions expressed a fraction of 67P-Xe ranging from 12% (in SW-Xe dominated solutions) to 19% (in Q-Xe dominated solutions), and a range of intermediate combinations of SW-Xe and Q-Xe between those extreme 67P-Xe fractions.

The two proposed contributions of 67P-Xe to U-Xe in Q-Xe dominated (19% 67P-Xe) and SW-Xe dominated (13% 67P-Xe) mixtures are lower than the results of Marty et al. (2017) in which modelling of U-Xe with Q-Xe and 67P-Xe suggested a 22% ± 5% cometary contribution. This contribution is roughly similar to the value proposed by Bekaert et al. (2020), who modelled the contributions of 67P to Earth's other volatiles (including krypton) if roughly 20% of Earth's atmospheric xenon came from 67P, finding them to mostly be in agreement with that hypothesis if the remaining contribution was from carbonaceous chondrites. In this work, U-Xe made from a mixture of carbonaceous chondrite material (Q-Xe) and 67P-Xe is modelled in Scenario 12, which suggests a contribution of 19% to U-Xe from 67P-Xe. The SW-Xe dominated Scenario 13 contains less of a contribution from 67P-Xe in its modelling of U-Xe but must make up for the deficit in volatiles relative to a carbonaceous chondrite (or Q-Xe) dominated origin. This source of volatiles would also have to account for the incompatibility of a solar and 67P source of the krypton in Earth's atmosphere (Bekaert et al., 2020). Another explanation may be provided by assuming volatile compositions of 67P as measured by

Rosetta are not representative of the rest of the 67P-like comets apart from xenon. Either the measurements of volatiles other than xenon did not measure the entire composition of 67P, or comets express such a range of compositions of volatiles that a bulk dose of comets containing 67P-Xe would correctly enrich the SW-Xe to recreate the primordial atmospheric composition. Both explanations seem unlikely.

As in the models of Marty et al. (2017), the modelled compositions for a SW-Xe or Q-Xe dominated origin of U-Xe with 67P-Xe and no fractionation both contain a significant excess of $^{129}Xe/^{132}Xe$ relative to U-Xe. In this work, the $^{129}Xe/^{132}Xe$ compositions of the modelled solutions exceed U-Xe by around 50 ‰. The evolution of the component U-Xe to Earth's modern atmosphere proposed by Pepin (1991) suggests the decay and degassing of $^{129}I$ is the cause of the subsequent enrichment of $^{129}Xe$ towards its modern composition. In the modelling of Marty et al. (2017) and Scenarios 12 and 13 of this work, contributions from 67P-Xe mean the $^{129}Xe/^{132}Xe$ composition of Earth's primordial atmosphere was close to its modern value, and significantly in excess of U-Xe. Marty et al. (2017) suggests an explanation may be provided by an exotic nucleosynthetic source of $^{129}Xe$ in the reservoir of xenon sampled by comets like 67P-Xe, or enrichment by a different reservoir of $^{129}I$ to the one which contributed to the early Solar System, at least 100 Ma before its formation. An alternate explanation is provided by fractionation of 67P-Xe since its incorporation into U-Xe, as in Scenarios 14 and 15.

Assuming U-Xe is derived from a SW-Xe and 67P-Xe mixture, we can reduce the contribution to U-Xe from 67P-Xe with its fractionation, down to 8.9% of the primordial atmospheric xenon budget. Reducing the contribution of 67P to Earth's primordial atmosphere reduces the requirement of significant atmospheric loss and destruction of organic molecules suggested by Bekaert et al. (2020), removes the $^{129}Xe/^{132}Xe$ excess relative to U-Xe, but introduces a deficit in $^{128}Xe/^{132}Xe$ relative to U-Xe.

A SW-Xe dominated origin of U-Xe with fractionated 67P-Xe, requires a mechanism for 67P-Xe being fractionated in favour of the heavy isotopes and mixed with SW-Xe before its incorporation into U-Xe. Also, a mostly unfractionated SW-Xe origin of U-Xe does not agree with the 67P krypton composition (Bekaert et al., 2020), so would require an explanation similar to the one proposed earlier. The required fractionation of 67P-Xe may have occurred since its incorporation into Earth's primordial atmosphere, before its measurement by Rosetta, or perhaps during measurement with Rosetta. Any explanation would not only need to account for the timing and nature of such a fractionation, but also explain the magnitude of such a fractionation (78 ‰/amu ± 1.9 ‰/amu). Marty et al. (2017) suggest xenon fractionation during measurement, or fractionation of the xenon as it is degassed from the comet nucleus or prior to measurement by Rosetta is unlikely given the consistency of measured values over time and space. Another, more plausible explanation may be that an unknown process has fractionated 67P-Xe during its residence in the outer Solar System since U-Xe formation. Given the exotic and unknown processes acting on materials in the outer Solar System (discussed in Section 1.4), this is not entirely unreasonable. The depletion in $^{128}Xe/^{132}Xe$ relative to U-Xe may be the result of its unmixing from isobaric $^{32}S_4$ underestimating its true value.

Scenario 15 is set up identically to Scenario 14 but without the inclusion of $^{128}Xe/^{132}Xe$ in the chi-squared statistic. Removal of $^{128}Xe/^{132}Xe$ from the fitting resulted in a larger fractionation of 67P-Xe in favour of the heavy isotopes of xenon, and a further reduction in 67P-Xe fraction of U-Xe (from 8.9% down to 8.4%). This scenario essentially exchanges an explanation of more significant fractionation with an incorrect $^{128}Xe/^{132}Xe$ value in 67P-Xe. Scenarios 14 and 15 also illustrate the interchangeability of Q-Xe with fractionated 67P-Xe and SW-Xe, where Q-Xe does not feature in the modelling as a result of its composition being substituted by fractionated 67P-Xe and SW-Xe.

### 3.4.4. Martian atmosphere

The modelled solutions to Scenarios 16 and 17 reflect the similarly non-fractionated scenarios for Earth's atmospheric xenon in their 67P-Xe dominated compositions (around 65% from 67P), and large uncertainties on almost all the included end members. As with the modelling of Earth's atmosphere, these solutions are interesting in that they can apparently satisfy their target compositions without applying fractionation, for which there is a wealth of evidence (Hunten, Pepin and Walker, 1987; Pepin, 1991; Chassefière and Leblanc, 2004; Conrad et al., 2016). This is even less plausible when modelling the Martian atmosphere for which most atmospheric models propose atmospheric loss and hydrodynamic fractionation since its formation (Hunten, 1973; Hunten et al., 1987; Pepin, 1991, 2000; Ott et al., 2019). The non-fractionated solutions also contained significant fractions of fissiogenic xenon from $^{244}$Pu and $^{238}$U amounting to around 13% of the total Martian atmospheric xenon budget. This contradicts other models which suggest a negligible fissiogenic contribution to the Martian atmosphere (Swindle and Jones, 1997; Pepin, 2000; Conrad et al., 2016).

The large uncertainties on the fractions of end members is most probably another example of Scenarios 16 and 17 representing non-minimal models, in which there are too many unconstrained variables, and a large range of mathematical sub-solutions are easily discovered by Automaton (as described in Section 3.4.2). Similar to the non-minimal modelling of Earth's atmosphere, the non-minimal solutions suggestion of a Martian atmospheric xenon composition dominated by 67P-Xe has large implications for the other volatiles on Mars. Given the lack of precision in the modelling of these solutions, and the identification of such a phenomenon corresponding to a poor model of a composition, the subsequent volatile implications of such a large 67P-Xe contribution are not explored in this work. These factors probably combined to remove the requirement for post-mixture

fractionation when introduced as a variable in Scenario 17 along with the end members of Scenario 16, this addition barely changed the results from the non-fractionated equivalent.

The results of modelling Scenarios 18, 19, 20, and 21 more closely resemble reliable models of the Martian atmosphere compared to Scenarios 16 and 17, as they minimised variables according to physical constraints, such as removing the fission products of $^{238}U$ and $^{244}Pu$, and constraining or correcting spallation (in Scenarios 20 and 21). Scenarios 18 and 19 may have provided apparently reasonable solutions for fractionated Martian atmospheric xenon with SW-Xe and Q-Xe dominated compositions, but upon closer inspection they are unlikely to reflect reality. Firstly, the poor precision of the modelled component fractions and fractionation (more evident in Scenario 18) is an indication of the variables in the models combining to provide no clear chi-squared minima, this is in spite of the models containing minimal variables to avoid the similar phenomenon in non-minimal modelling. Another problem is in these models not accounting for the apparently significant spallation contribution in Martian atmospheric xenon, which is assumed to not exist in both scenarios. The fractionation suggested in both solutions also exceeds the magnitude of fractionation suggested by previous models of the Martian atmosphere, such as the 26 ‰/amu < 32 ‰/amu of Conrad et al. (2016).

More specifically to Scenario 18, along with the previously listed issues with such a model, a chondritic origin of the majority of the Martian atmospheric xenon is inconsistent with previous models including other noble gases and volatiles (Swindle and Jones, 1997; Pepin, 2000; Pepin and Porcelli, 2002; Conrad et al., 2016). The most significant discovery of the modelling of Scenario 18 was its exaggerated scatter making the complimentary relationship between post-mixture fractionation and the fractional contribution of 67P-Xe to the Martian atmosphere more obvious, thus helping recognise this feature in Scenario 19.

Scenarios 20 and 21 provide the most well constrained models of the Martian atmosphere in this work, with their modelling including the contribution of Spallation and fractionation, yet their results contain features with significant implications for Martian atmospheric evolution. For example, the solutions for Scenario 20 express the greatest precision of any of the modelling of the Martian atmospheric xenon in this work, with an extremely fractionated atmosphere (equivalent to 148 ‰/amu) composed of around 50% 67P-Xe. This scenario would have to provide an explanation for such an extreme degree of fractionation, exceeding the magnitude of other models of the Martian atmosphere by around 100 ‰/amu (Conrad et al., 2016), and also explain how such a large contribution from 67P would affect the other volatiles on the Martian surface. Models for contributions of 67P to Earth's atmosphere may also require revision in light of this contribution, due to the proximity and similarity of both planets. Scenario 21 removed the Martian spallation variable by recreating a spallation-corrected Martian atmosphere (Conrad et al., 2016), yet produced sub-solutions lacking in precision, and fractionation mostly in excess of previous modelling.

The model which utilises the relationship between the spallation corrected Martian atmospheric 67P-Xe contribution and fractionation to infer a fractionation given two fractions of 67P-Xe (as described in Section 3.3.4) removes the lack of precision in the modelling of Solution 21 in exchange for the assumption that the atmospheres of Earth and Mars contain an identical contribution from comets like 67P. The most important distinction between the two compositions is their inference of the fraction of 67P-Xe from either a SW-Xe or Q-Xe dominated composition of Earth's atmosphere. Both models of the spallation corrected Martian atmosphere are derived from a SW-Xe dominated composition, whereas the 16% 67P-Xe solution to Earth's atmosphere is the only equivalently SW-Xe dominated composition (with the other being dominated by a Q-Xe composition). If we are assuming equivalency in the delivery of 67P-Xe to the atmospheres

of Earth and Mars, then an equivalently SW-Xe dominated composition (16% 67P-Xe) is more likely than both planetary atmospheres differing in their more dominant source of xenon apart from 67P-Xe. In this case, the Martian model for a cometary contribution of 16% 67P-Xe must account for the problems outlined in Section 3.3.4, notably the light isotopic composition of xenon in Earth's mantle favouring a chondritic origin (Caracausi et al., 2016), along with other models suggesting similar origins for Earth's atmosphere from other volatiles including heavy noble gases (Pujol et al., 2011; Marty et al., 2017; Bekaert et al., 2020). The model must also account for the isotopic composition of its solution, as plotted in Figure 3.18, which requires a substantial enrichment in $^{129}Xe/^{132}Xe$ to resemble the spallation-corrected Martian atmosphere, most easily explained by the decay of $^{129}I$. However, such an explanation requires a targeted sequestration of the xenon produced by fission of chemicals other than $^{129}I$, as discussed in Conrad et al. (2016). The light isotopic composition of the solution (which was excluded from the fit) also expresses significant depletions, the hypothetical light isotopic composition of 67P-Xe must therefore account for this depletion with a significant enrichment if this model is correct.

Modelling of the Martian atmosphere with 67P-Xe as reported in Marty et al. (2017) while assuming the Martian atmosphere is mass fractionated and may contain a significant spallation component is significantly hindered by the lack of light isotopes. The values for fractionation in the modelling of this work are frequently compared to modelling using light isotopes of xenon, and spallation xenon which predominantly contains lighter isotopes. It is unclear whether more accurate results would be achieved if Automaton were set up to include the light isotopes of a spallation component, as they would feature significant uncertainties when normalised to the relatively depleted $^{132}Xe$. The uncertainty of the xenon isotopic composition of 67P is already a hindrance in even the most precise modelling of the Martian atmosphere, as illustrated in the large error bars of Figure 3.18, another component with significant uncertainty would compound this problem.

### 3.4.5. General

The uncertainty of the composition of 67P-Xe as used throughout this modelling, and the way that the uncertainty is propagated through Automaton in its calculations of solutions, means some scenarios expressed solutions with a misleading precision. For example, while Automaton's two-component solutions are apparently precise to within roughly 0.2% in Scenarios 12 and 13 of Table 3.6 when estimating the fractions of components, propagation of this error into a delta plot of the solution with respect to the target composition reveals a precision which may otherwise be dissatisfying (such as in Figure 3.12, and perhaps more significantly Figure 3.14, with its excess in $^{129}Xe/^{132}Xe$). Conversely, the apparently poor precision of the solutions to Scenario 6 of Table 3.5, in which Automaton was used to model Earth's atmosphere without fractionation, is an artefact of a range of acceptable component contributions. The sub-solution specific optimisation of the chi-squared statistic employed by Automaton means considering each sub-solution individually may reveal that they each satisfy the composition of Earth's atmosphere. The scenarios which avoided these situations by removing non-minimal modelling of unnecessary variables, and introducing constraints on variables based on physical limitations (such as $^{244}Pu$ fission in Scenarios 9 and 10, and pre-correcting spallation in Scenario 21), provide the best examples of modelling in this work. The exclusion of the light isotopic composition of xenon throughout the modelling is another large caveat to the modelling in this chapter, they comprise two ninths of the data which can be fit to modelled solutions and are of particular importance in resolving fractionation and spallation, yet are unfortunately absent from the composition of 67P-Xe. Their exclusion from this modelling is particularly unfortunate due to the extensive simulation of fractionation of individual and entire compositions that Automaton is capable of, and the role that fractionation is thought to play in the development of the terrestrial atmospheres.

The modelling in which the only difference between scenarios was the exclusion of $^{128}Xe/^{132}Xe$ from the fit, or an increased $^{128}Xe/^{132}Xe$ uncertainty, show that it had little impact on the resultant solutions. $^{128}Xe/^{132}Xe$ was generally removed or modified in scenarios in which a significant fractionation was applied either after the mixture or specifically to 67P-Xe. The expectation was that its exclusion may allow the composition to be more severely fractionated, given the control of the lightest isotopes on isotopic fractionation, and the observation that fractionated 67P-Xe appears to resemble SW-Xe or Q-Xe apart from $^{128}Xe/^{132}Xe$. Scenarios 1 through 4 barely expressed variation despite the removal and modification of $^{128}Xe/^{132}Xe$ and significant fractionation. The most significant change was in the modelling of U-Xe with and without $^{128}Xe/^{132}Xe$, where Scenarios 14 and 15 expressed an increased fractionation (roughly 28 ‰/amu) and half a percent decrease in the amount of 67P-Xe. Apart from the difference in fractionation, Figure 3.15 illustrates that the exclusion of $^{128}Xe/^{132}Xe$ would mean the other isotopic compositions match with U-Xe. This is the only modelled scenario in which the accuracy of the reported composition of $^{128}Xe/^{132}Xe$ for 67P-Xe changes the interpretation of its role in modelling a Solar System reservoir.

Hydrodynamic escape and its preferential removal of the light isotopes is a function of atmospheric loss, which in turn is a function of a planet's mass. Given the difference between the mass of Mars and Earth, and the relatively low concentration of xenon on Mars compared to Earth, presumably due to atmospheric loss, we should see a greater degree of isotopic fractionation on Mars than Earth. In the models which compared the modelled and inferred fractionation on the atmospheres of Earth and Mars with two identical cometary contributions, isotopic fractionation of xenon is roughly a factor of two larger in the Martian atmosphere, as may be expected. Table 3.8 contains a side-by-side comparison of these two scenarios, which are discussed in depth separately in Section 3.4.2 and Section 3.4.4. In summary, the models assume identical cometary contributions to both

planets, they sometimes contradict other volatile models for either Q-Xe or SW-Xe comprising the remaining atmosphere, and the $^{129}Xe/^{132}Xe$ compositions are either depleted (in the Martian atmosphere) or identical to its modern value (in Earth's atmosphere) without modelling $^{129}I$ decay.

***Table 3.8*** *Two fractionated models of the atmospheres of Earth and Mars.*

| Conditions | 16 % 67P-Xe | 19 % 67P-Xe |
|---|---|---|
| Reservoirs | Post-mixture fractionation (‰/amu) | Post-mixture fractionation (‰/amu) |
| Earth's atmosphere with fixed fission | 35.4 | 30.5 |
| Spallation corrected Martian atmosphere | 59* | 63* |

*Both models assume the same fractional contribution of 67P-Xe. Model results are listed as solutions 4 and 5 of Table 3.5 for Earth, and described in Section 3.3.4 for Mars. Martian atmospheric composition is spallation corrected according to Table 3.1, which also contains Earth's atmospheric composition and 67P-Xe. Earth's atmospheric composition as modelled here contains a fixed fission contribution as described in Section 3.3.2. *Fractionation in the case of the Martian atmosphere is inferred from correlation between fraction of 67P-Xe and degree of fractionation explained in Section 3.3.4.*

The modelling of the non-fractionated models of the atmospheres of Earth and Mars were examples of non-minimal models, with significant physical and chemical implications (discussed in Sections 3.4.2 and 3.4.4) provide a. If we assume these scenarios are describing reality, then could these compositions be indicative of a primordial composition shared by the inner Solar System? Table 3.9 is a side-by-side comparison of the two non-fractionated models of the atmospheres of Earth and Mars. Automaton could not settle upon a reliably similar solution (in terms of the fractional contributions), as signified by the large uncertainties relative to the other models, however, both solutions feature roughly similar cometary contributions. The slightly higher proportional contribution of cometary xenon in the Martian atmosphere could be explained by more efficient or less significant degassing of the internal chondritic or solar xenon composition from Mars accretion. The internal xenon budget of both planets is presumably a function of

the volume of material accreted to form them, and their ability to retain it, so Earth's larger internal reservoir is understandably more dominant. It could also be the result of a greater flux of cometary material, possibly a function of heliocentric distance or migration. The difference in contribution of either Q-Xe or SW-Xe xenon for both solutions is inconclusive as it could easily be attributed to their interchangeability, as observed throughout the reservoir building section. The proposal of a non-fractionated atmospheric evolution of Earth and Mars must also account for the existing measurements and modelling which strongly suggest the fractionated evolution of both planetary atmospheres, as discussed in Section 1.3.4, Section 3.4.2, and Section 3.4.4, and the contributions of xenon from fission of $^{238}$U and $^{244}$Pu, which are more significant than other suggested fission contributions to the atmospheres of Mars and Earth (Caracausi et al., 2016; Conrad et al., 2016), although such a scenario does not require the problematic explanation for targeted sequestration of $^{244}$Pu in the Martian atmosphere.

***Table 3.9*** *Models for the modern atmospheres of Earth and Mars without fractionation.*

| End members | Q-Xe | SW-Xe | 67P-Xe | Fission |
|---|---|---|---|---|
| Target compositions | Fractions (% ± σ) | Fractions (% ± σ) | Fractions (% ± σ) | Fractions (% ± σ) |
| Earth's atmosphere | 26 ± 20 | 8 ± 14 | 53 ± 15 | 14 ± 3 |
| Martian atmosphere | 5 ± 14 | 17 ± 15 | 65 ± 16 | 13 ± 3 |

*Automaton solutions using the end members in each column (defined in Table 3.1). 'Fission' column denotes combination of contributions from $^{238}$U and $^{244}$Pu, which are expanded in Table 3.5 and Table 3.7. Errors represent standard deviations of 200 sub-solutions.*

The following points contain the major problems which have become apparent during the modelling of Solar System reservoirs with 67P-Xe conducted in this work:

- *The lack of a light isotopic composition of cometary xenon.*

  This is critical to all of these models, especially given the discussion of the role of fractionation and its particular reliance on the lightest and heaviest isotopes.

- *The heterogeneity of cometary xenon.*

  Comets exhibit little homogeneity in most other aspects of their chemistry, so can we expect that 67P-Xe is representative of the whole cometary reservoir?

- *The uncertainty of 67P-Xe.*

  The focus of the Rosetta mission was unfortunately not to measure the noble gas composition of 67P, as reflected in the poor precision of the returned data. Modelling of this nature is highly sensitive to the uncertainty of the provided data (as explained in Section 3.1.3), so any improvement would be welcomed.

- *The origin of 67P-Xe.*

  Recreating 67P-Xe using known reservoirs of the Solar System with Automaton was not successful without significant fractionation. This may be more likely than a uniquely exotic nucleosynthetic mixture, yet requires experimental or observational justification to explain the process of this fractionation. The timing of the fractionation is also unknown, when and where did this fractionation occur?

- *The interchangeability of SW-Xe and Q-Xe.*

  These compositions are frequently interchangeable in most of the non-fractionated models presented in this work. It would be particularly useful to have some means of distinguishing these two reservoirs, especially given their vastly different sources. This is only possible with lower uncertainties for input and target compositions of end members, or modelling of other elemental and isotopic ratios of end members.

- *The interchangeability of SW-Xe and fractionated 67P-Xe with Q-Xe*

  Models including SW-Xe, Q-Xe, and fractionated 67P-Xe invariably replaced a fractional contribution of Q-Xe with fractionated 67P-Xe and SW-Xe. In the models containing these three components, Q-Xe can be added in exchange for SW-Xe and fractionated 67P-Xe to produce similar solutions. These components clearly resemble one another according to the solutions provided by modelling with Automaton, would this still be the case if we knew the light isotopic composition of 67P-Xe? The fact such extreme fractionations of 67P-Xe are observed in its modelling would make this origin readily apparent if we had that information.

### 3.5. Conclusions

Automaton has clearly proven itself to be a valuable tool in modelling isotopic compositions of xenon reservoirs of the Solar System. Automaton differs from similar models in its dedicated approach to modelling of end members with up to nine isotopes. The comparisons between Automaton and Samaritan, its closest equivalent modelling platform, illustrate Automaton's reliability for modelling of mixtures of end members as isotope ratios. This functionality is complimented by Automaton's unique ability to fractionate the individual components and overall mixtures which combine to produce a target xenon composition.

Automaton's user interface is designed to allow the user to select and constrain as many variables as possible. This approach means modelling can be honed and confined within real physical limitations and produce results closer to reality. The presentation of output data in Automaton also allows the user to easily find and constrain statistical features by navigating individual sub-solutions, which can then advise refinement of subsequent modelling.

Automaton's coding architecture is written with expansion and alteration in mind, so future versions of the software can easily implement new features. For example, a future version could vary both xenon and krypton isotopes simultaneously, which would be particularly useful in modelling the missing xenon paradox. Modifications which allow any combination of isotopic compositions are easily implemented, as are different models of fractionation.

As for the models including 67P-Xe as a proxy for cometary xenon, the uncertainty of the end member composition is clearly problematic for Automaton. Additionally, to

extrapolate one measurement of cometary xenon to a population of such magnitude and variety is optimistic. Our uncertainty regarding formational mechanisms (Dones et al., 2015), dynamical evolutions (Guilbert-Lepoutre et al., 2015), and even the basic attributes of the largest population of comets (Francis, 2005; Charnoz and Morbidelli, 2007) is a testament to that. Many compositional characteristics of refractory particles in 81P differ from interplanetary dust particles of cometary descent and primitive chondrites (H. Ishii et al., 2008; Zolensky et al., 2008), as do the volatile components from remote sensing of comets (Bockelée-Morvan and Biver, 2017). Noble gases may be less susceptible to fractionation than other elements, but it may be more surprising to find the entire cometary xenon reservoir to be compositionally homogenous. As such, any models of Solar System volatile evolution including 67P-Xe should be considered in the context of 67P-like comets, and not comets as a whole.

The lack of 67P-Xe containing compositions for $^{124}$Xe and $^{126}$Xe compounds the problem with modelling such a large reservoir using only one example of cometary xenon, especially in the context of the reservoirs modelled in this work, which are mostly fractionated, a process which affects the lightest and heaviest isotopes most significantly. The best modelled solutions to scenarios for each xenon reservoir were the ones in which variables were constrained within the best current knowledge and the resultant xenon composition more closely resembled the target composition in its isotopic compositions, yet every model has problematic implications for other volatiles and the timing and nature of mixtures and fractionation. It is currently impossible to say whether these solutions would agree with the consequent compositions of $^{124}$Xe and $^{126}$Xe, and these solutions generally required other cosmochemical and physical assumptions which needed explanation.

## 4. Xenon isotopes in individual lunar volcanic glasses of Apollo 15 and Apollo 17

### 4.1. Introduction

Our largest collection of lunar material, the lunar mission inventory, is dominated by materials gathered from the lunar surface. Chemical analyses, including noble gas data, are subsequently confined to materials which were found on or near the lunar surface. The noble gases contained in these materials are subsequently dominated by radiogenic (radioactive decay or fission of parent isotope), cosmogenic (from atom-scale interactions between cosmic rays and specific elements), or implanted solar wind (Eberhardt et al., 1970, 1971; Bogard et al., 1973; Kirsten et al., 1973; Hohenberg et al., 1978; Benkert et al., 1993; Pepin et al., 1995; Heber, 2002; Wieler, 2002).

Surface correlated xenon distinct from solar wind, featuring fission products from extinct radionuclides $^{129}$I and $^{244}$Pu ($^{129}$Xe and $^{136}$Xe, respectively), have been found in some regolith materials, possibly from adsorption of an extinct lunar exosphere (Reynolds et al., 1974; Bernatowicz et al., 1978; Swindle et al., 1985). Additionally, "parentless" $^{40}$Ar produced by the decay of $^{40}$K has been found in regolith breccias and soils, and could derive from ancient crust and mantle outgassing (Fernandes et al., 2004; Fernandes and Burgess, 2005). This is the current extent of the characterisation of an indigenous lunar noble gas composition.

Pristine lunar volcanic glasses are considered good candidates for retaining an internal primitive lunar noble gas component. These basaltic glasses were produced from partial melting in the primitive lunar mantle before extrusion in gas-charged eruptions akin to fire fountaining, quenching and deposition on the lunar surface (Heiken et al., 1974; Meyer et al., 1975; Delano, 1986). Argon dating and petrogenetic work suggest the

volcanic glasses formed around the same time as the mare basalts, ~ 3.6 Ga ago (Huneke et al., 1973; Husain and Schaeffer, 1973; Eberhardt. et al., 1975; Alexander et al., 1978; Huneke, 1978). The volcanic glasses of Apollo 15 and 17 feature textures and major element ratios which suggest their mantle source melt originated from depths of over 400 km below the lunar surface (Delano and Livi 1981). Many of these glasses remain vitrified from their quenching after eruption, and have been preserved from damage and heating in various stages of pristinity as defined in Section 4.2.3, and exhibited in Figures 4.1 and 4.3 (Heiken et al., 1974; Delano and Livi, 1981; Delano, 1986).

These volcanic glasses exhibit evidence of their eruption being gas-charged in the form of vesicles and a surface coating of volatile elements (Heiken et al., 1974; Delano and Lindsley, 1983; Barraclough and Marti, 1985; Delano, 1986; Saal et al., 2008). The most pristine of the volcanic glass spherules can be expected to have undergone minimal heating and thus degassing, since their sudden quenching upon eruption (signified by a lack of devitrification), so they may still contain the noble gases dissolved in the volatile-rich primitive lunar mantle melts which created them (Delano and Livi, 1981; Füri et al., 2018).

The volcanic glasses formed at a time when the Moon was degassing enough to have sustained a transient atmosphere/exosphere of volatile elements into which the volcanic glass plumes may have erupted and quenched within (Needham and Kring, 2017; Saxena et al., 2017; Hui et al., 2018). This transient exosphere was most likely dominated by gases released from the many gas-rich melts from which the eruptions originated. Localised partial pressures beside these eruptions could have featured high enough partial pressures for the inward diffusion of these gases. Volcanic lunar glasses may therefore retain noble gases from the transient lunar atmosphere they passed through. Additionally, the volcanic glasses may contain noble gases acquired from their residence near the lunar surface, in the form of galactic cosmic ray spallation, and implanted solar wind.

Previous noble gas analyses of the volcanic lunar glasses of Apollo 15 and 17 have been limited to establishing the presence of cosmogenic components and solar wind in the heavy noble gases, with various descriptions of exposure histories based upon those findings (Bogard et al., 1973; Kirsten et al., 1973). More recent work has focussed on measuring the light noble gases (He, Ne, Ar) in volcanic lunar glasses (Füri et al., 2015, 2018), and produced results which suggest any internal or atmospheric lunar noble gas component has not been retained. The present work follows attempts to characterise the xenon contained in the volcanic glasses of Apollo 15 and 17, with an emphasis on the determination of a hypothetical indigenous lunar noble gas composition.

Xenon features nine stable isotopes whose relative concentrations are attributable to various nucleosynthetic and radiogenic sources. These nine isotopes can make identification of components more certain relative to elements with fewer isotopes, such as the lighter noble gases, whose characterisation has to rely on fewer independent isotope ratios. Identifying components with certainty could allow us to subtract them and reveal indigenous lunar xenon. Xenon's atomic radius, ~ 2 Å (Bondi, 1964), also renders it less susceptible to problems caused by interference from implanted solar wind, whose xenon is typically implanted in the upper tens of nanometres (Heber, 2002; Grimberg et al., 2006; Wieler et al., 2007). Helium for instance, whose atomic radius is ~ 1 Å (Bondi, 1964), is implanted at depths measured in hundreds of nm at typical solar wind implantation energies (from 'SRIM', Stopping and Range of Ions in Matter, of Ziegler et al. (2010) modelling of a $SiO_2$ glass target and solar wind at < 4 keV/amu). This strong correlation to surface area makes it easier to resolve and subtract it from a potential trapped indigenous component, either numerically or by gas extraction as a function of depth (as described in Section 4.4.3). A larger atomic radius also makes diffusive loss of volume-correlated components, and diffusive incorporation of external components, less efficient.

Such properties lend themselves to measuring an ancient lunar noble gas composition with xenon, but low concentrations require larger samples, bulk analyses, or more sensitive instruments relative to light noble gas work. For example, Kirsten et al. (1973) required analyses of Apollo 17 samples containing multiple glass spherules to measure $^{132}$Xe concentrations of $2 \times 10^{-10}$ cm$^3$ STP g$^{-1}$ < $7 \times 10^{-10}$ cm$^3$ STP g$^{-1}$. If we assume the Apollo 17 $^{132}$Xe concentration range of Kirsten et al. (1973) is applicable to the average mass of individual volcanic glasses of Apollo 15 (~ 80 µg) and Apollo 17 (~ 51 µg) to be analysed individually in this work (from samples 15426 and 74220, respectively), they could feature between $4.4 \times 10^5$ $^{132}$Xe atoms to $15 \times 10^5$ $^{132}$Xe atoms in 15426 and $2.7 \times 10^5$ $^{132}$Xe atoms to $9.6 \times 10^5$ $^{132}$Xe atoms for 74220. These low numbers demand only the most sensitive of instruments for meaningful individual glass spherule measurement. For this reason, the RELAX (Refrigerator Enhanced Laser Analyser for Xenon) mass spectrometer is employed for my measurements, whose typical detection limit is one thousand $^{132}$Xe atoms, close to a tenth of the lower estimate of the total xenon released from a volcanic glass of similar provenance to those of Kirsten et al. (1973). In addition to this exceptionally low detection limit, RELAX is capable of simultaneously measuring all isotopes of xenon, so determination of spallation, fission, and "trapped" (i.e., primordial) xenon can be conducted in tandem with minimal sample gas loss.

The RELAX mass spectrometer allows us the ability to measure and interpret the xenon contained within individual volcanic glass spherules, something which is impossible on less sensitive instruments without using the largest of glass spherules, or settling for bulk or multi-spherule measurements. These data represent the most precise investigation of the existence of an indigenous noble gas composition from the lunar interior to date. Additionally, individual glass analyses allow this work to quantify glass-specific spallation products, exposure ages and burial depths.

### 4.2. Samples

All samples used in this work were loaned to Dr Vera Assis Fernandes via the regular NASA calls for sample allocation. Samples were received within stainless-steel canisters, and were cleaned, picked and processed within the clean room of the Department of Earth and Environmental Science at The University of Manchester. Samples were mounted within acrylic tubes and brass holders for polishing in a sample preparation room. Once prepared, samples were taken to the EPMA and RELAX instruments for analysis.

#### 4.2.1. Apollo 15 sample 15426,189

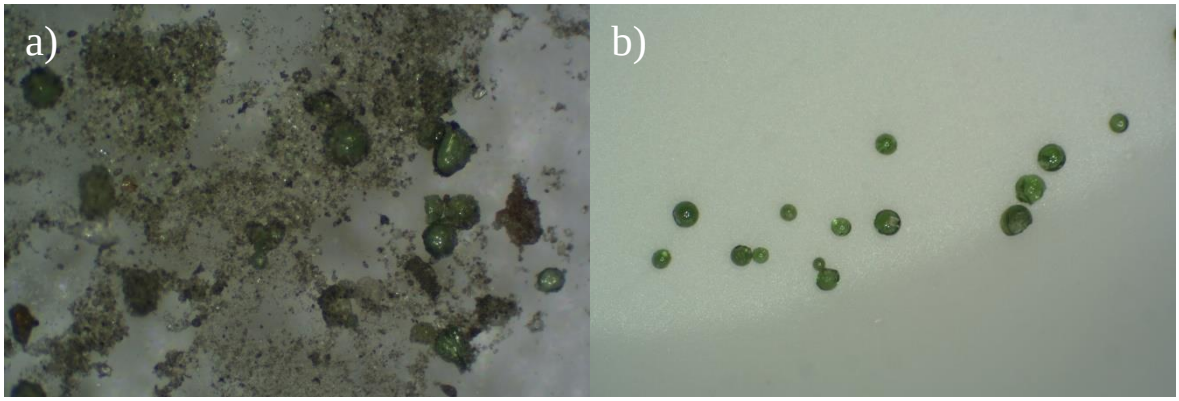


***Figure 4.1*** *a) Partially sorted constituents of Apollo 15 (15426, 189) soil under optical microscope exhibiting lithic and glass fragments, and green glass spherules of variable pristinity. Field of view is ~ 4 mm wide.*
*b) Selection of isolated green glasses after picking. Field of view is ~ 6 mm wide.*

15426 is one of three greenish friable clods (> 1 cm) collected from the lunar surface on the rim of Spur Crater on the Apennine Front during the Apollo 15 mission (Butler et al., 1971). All samples collected from the Apennine Front featured similarly high abundances of green glasses relative to the mare surface (Basu et al., 1981; Nagle, 1981), with many of the clods being almost entirely composed of green glass. The average size of the volcanic glass spherules is less than 0.1 mm, and the samples are often composed of

fragmented glasses and grey powdered regolith breccia and basalts (see Figure 4.1). Black and yellow glasses of impact origin also feature in the clods and loose regolith of Apollo 15 (Delano, 1980; Delano and Livi, 1981; Spangler et al., 1984; Hughes et al., 1988; Zellner, 2019). Modal classification of the materials in 15426 found it to feature 68% white 'matrix' material composed of fine fragments of broken glass (< 25 μm), 15% glass spherules and shards (> 25 μm), 9.5% lithic materials such as regolith breccia and mare basalts, and 6.2% mineral fragments of indeterminable origins (Basu et al., 1981). Some glasses appear to be fused aggregates of individual spherules, indicative of collision while molten which was preserved by quenching. A minority of glasses also contain features such as vesicles, and olivine dendrites, which (along with the fused aggregates) are consistent with an origin from quenching of materials erupted volcanically in a process similar to fire fountaining on Earth (Basu et al., 1979; Delano and Lindsley, 1983; Arndt et al., 1984; Steele et al., 1992).

Major and trace element analyses have grouped the green glasses into up to seven distinct compositional groups (Delano, 1979; Galbreath et al., 1990; Steele et al., 1992), although individual glass analyses can express variability as a function of experimental technique and/or glass composition (Delano, 1986; Steele et al., 1992). All geochemical groups of the green glasses, and individual green glasses, are distinct from the lunar regolith material in their high Ni concentrations and unique refractory element ratios (Delano 1986; Hughes et al. 1990; Galbreath et al. 1990; Zellner et al. 2002; Zellner 2019). Compositional distinction between impact and volcanic glasses is based upon ratios of MgO, $Al_2O_3$ and CaO, established by Delano (1986), with a general rule that glasses in which $MgO/Al_2O_3$ exceeds 1.25 are likely of volcanic origin. These elements form the basis of distinguishing volcanic from impact glasses in this work. Siderophile Ni is tacitly correlated with the $Al_2O_3$ composition in this model, whose abundance is a measure of meteoritic contamination endemic to impact glasses. Delano (1986) also details criteria for

optical distinction of the volcanic glasses, elaborated in Section 4.2.3. The soil and glasses of 15426 are closely matched geochemically, suggesting minimal mixing of the sample material with the surrounding non-volcanic lunar regolith.

The volcanic green glasses of 15426 crystallised simultaneously with the nearby mare basalts, ~ 3.4 Ga ago (Ar-Ar dating of Huneke et al. 1973; Podosek and Huneke 1973; Spangler et al. 1984) a figure which does not significantly change with the recent revisions to the $^{40}$K decay constant (Renne et al., 2011), and is consistent with the Pb/Pb age of 3.41 Ga (Tatsumoto et al., 1987). Cosmogenic exposure ages have been calculated using various cosmogenic isotope production rates, and reported as 300 Ma (Huneke et al., 1973) and 284 ± 22 Ma < 276 ± 20 Ma (Spangler et al., 1984) using $^{38}$Ar, 150 Ma < 370 Ma using $^{3}$He, $^{21}$Ne, and $^{38}$Ar (Lakatos et al., 1973), and 87 ± 9 Ma < 2.1 ± 0.3 Ga using $^{21}$Ne and $^{38}$Ar (Füri et al., 2018). All exposure ages being younger than the crystallisation ages are indicative of variable burial depths since formation. Measurements of the light noble gases (He, Ne, Ar) contained in the green glass spherules of Apollo 15 found them to feature mostly solar-like compositions with cosmogenic contributions from galactic cosmic ray spallation (Huneke et al., 1973; Lakatos et al., 1973; Spangler et al., 1984; Zellner et al., 2009, 2018; Füri et al., 2018).

The particular subsample used in this work is 15426,189, a loose collection of material which fell from the friable clods collected at the lunar surface (Butler et al., 1971). Optical inspection of the sample before and during sorting confirmed the samples exhibited no significant deviations from all aspects of the previously published sample descriptions.

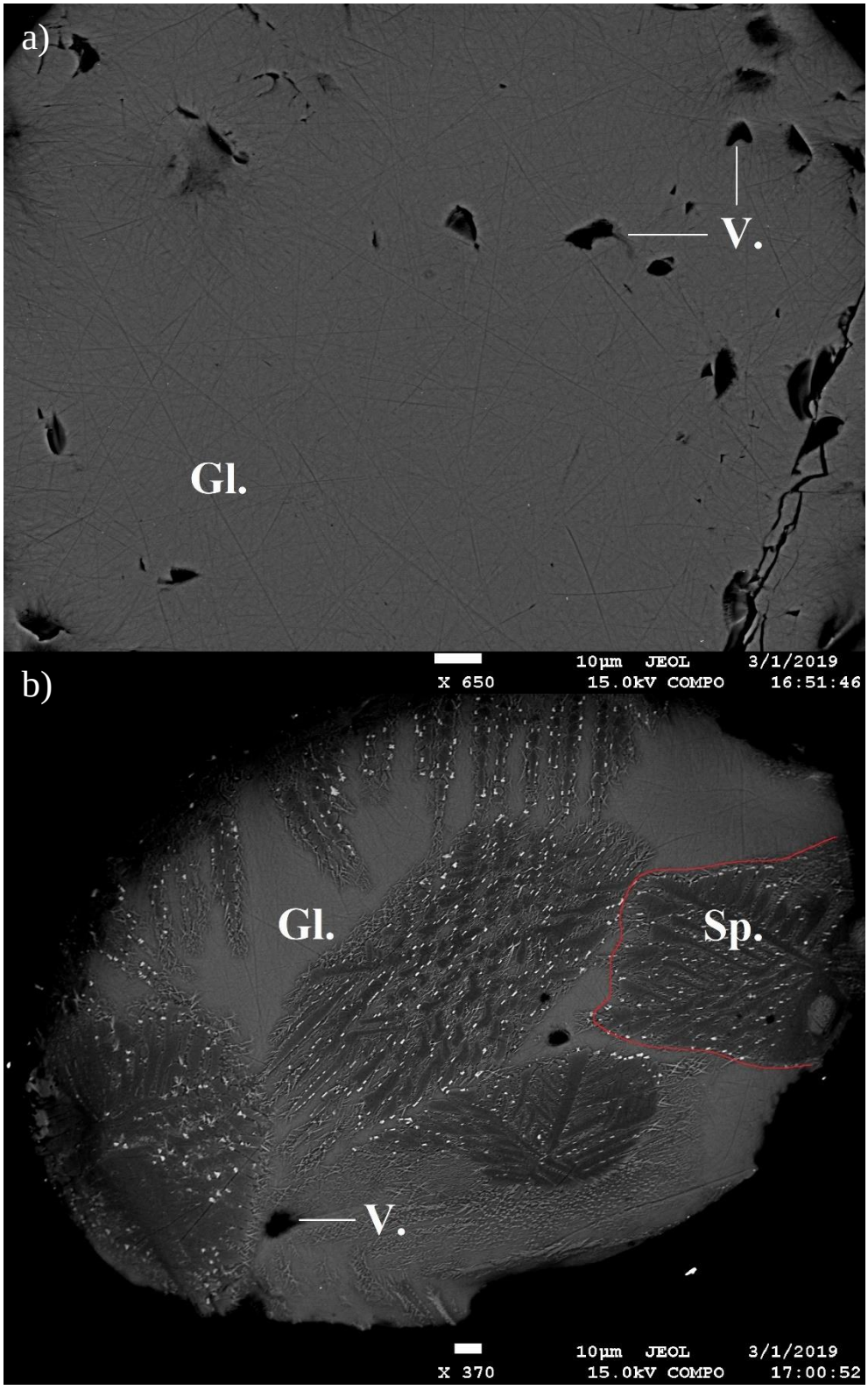


***Figure 4.2*** *Backscattered Electron (BSE) images of polished surfaces of glasses.*
*a) Volcanic glass of 15426,189, "C" exhibiting chemical and structural homogeneity in its complete vitrification (grey area labelled "Gl."), and vesicles resembling dark spots (some examples labelled "V.").*
*b) Impact glass of 15426,189, "E", exhibiting incomplete devitrification (one example surrounded by red line) in the form of spinifex crystals too small to identify (labelled "SP."), remaining vitrified areas (labelled "Gl."), and vesicles resembling dark spots (one example labelled "V."). Bright spots at edges of feathers are likely to be exsolution of either FeS or metallic $^{0}$Fe. Image capture properties and scales listed on bottom right.*

### 4.2.2. Apollo 17 sample 74220,939

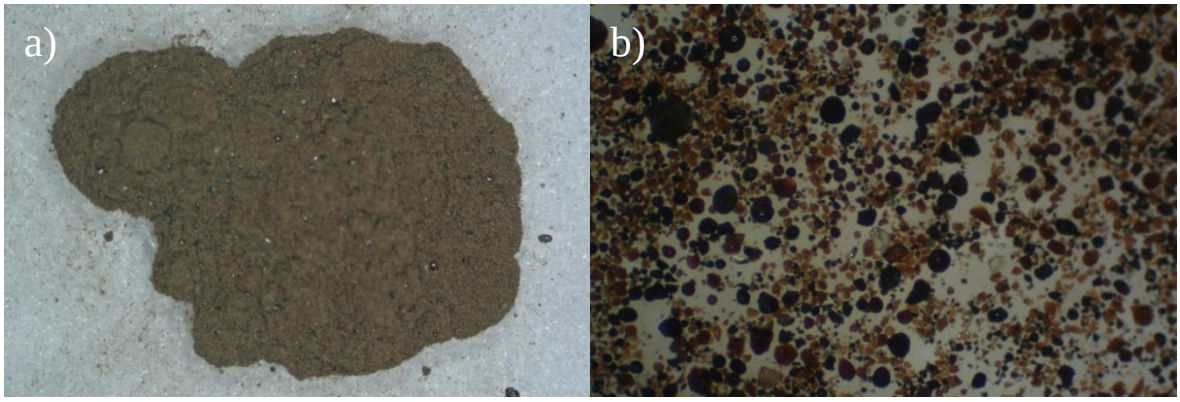


***Figure 4.3*** *a) Apollo 17 (74220,939) orange soil exhibiting characteristic orange colouration and visible glass spherules of variable pristinity. Field of view ~ 20 mm wide b) Partially sorted constituents of 74220,939 exhibiting impact and volcanic glasses alongside regolith material. Note the variable levels of preservation ranging from spherical glass spherules to shards. Field of view is ~ 4 mm wide.*

74220 is a clod of friable surface material collected from a depth of 6-8 cm on the rim of the Shorty crater during the Apollo 17 mission. This sample exhibits the characteristic 74220 composition, being almost entirely composed of volcanic orange glass spherules and fragments thereof (hence orange colour in Figure 4.3 a, Figure 4.3 b shows individual glasses and glass fragments), grain size is normally distributed about a 40 micron mean (Heiken et al., 1974). The glasses are often devitrified and contain olivine needles and ilmenite feathers (not directly seen in samples with BSE imaging in this work), which render them opaque, or black, yet they are compositionally identical to the pristine glasses (Haggerty, 1974; Heiken et al., 1974; Arndt and von Engelhardt, 1987). Based on $^{40}$Ar-$^{39}$Ar ages (Husain and Schaeffer 1973; Eberhardt. et al. 1975; Alexander et al. 1978; Huneke 1978), their crystallisation occurred simultaneously with the mare basalts, 3.6 Ga ago, a figure which does not drastically change with the recent revisions to the $^{40}$K decay constant (Renne et al., 2011). Cosmic ray exposure ages of the Apollo 17 volcanic orange glasses and soils have been reported as ~ 10 Ma by nuclear track aging (Kirsten et al. 1973; Fleischer and Hart, 1974; Crozaz 1978), 32 Ma by cosmogenic $^{38}$Ar production (Husain and Schaeffer, 1973), 27 Ma by cosmogenic $^{21}$Ne production (Hintenberger et al., 1974),

and 30 Ma by a parallel analysis of cosmogenic $^{38}Ar$ and $^{21}Ne$ (Kirsten et al., 1973). Burial depth is not explored in these studies beyond interpretations suggesting punctuated cosmic ray shielding and exposure since crystallisation. Combined cosmogenic noble gas production rates for similarly emplaced Apollo 17 samples suggest 74220 was excavated by the impact which formed the Shorty Crater around 19 Ma ago (Eugster et al., 1977, 1978; Bogard and Hirsch, 1978).

Apollo 17 glasses including those of 74220 feature a surficial coating of volatile elements (Zn, Pb, S, Cl, Hg, Ge, Au, Ir, Cu, Pb) condensed after eruption (Meyer et al., 1975; Butler and Meyer, 1976), and the soil has a general enrichment of volatile elements throughout (Meyer et al., 1975; Butler and Meyer, 1976). This soil features a low ferromagnetic resonance (FMR) surface exposure (maturity) index ($I_s$/FeO), a ratio of the coupling between an electromagnetic wave and the material it passes through to the FeO concentration, indicating the amount of $Fe^{2+}$ that remains unsegregated or converted to fine grained metal by micrometeorite bombardment at the lunar surface (Morris, 1976, 1978). The low FMR surface exposure index of 74220 soil ($I_s$/FeO = 1), is indicative of minimal surface exposure, or soil immaturity (Morris, 1978). The volcanic glasses also feature scant evidence of micrometeorite damage, another measure of pristinity (Delano, 1986; Zellner et al., 2009). The soil and glasses of 74220 are closely matched geochemically, suggesting minimal mixing with adjacent lunar regolith by gardening (Philpotts et al., 1974).

The glasses were grouped geochemically by refractory element analyses of Delano and Lindsley (1983) and Delano (1986), yet individual glass analyses exhibit some variability about these groups as in 15426 (Hughes et al., 1990). The orange volcanic glasses of 74220 are distinguished from impact glasses by a relative depletion in Ni and its siderophile analogue $Al_2O_3$ (due to the metal/silicate fractionation during planetary core-formation), a general enrichment in Ti, and the characteristically proportioned ratios of

MgO, $Al_2O_3$ and CaO (including the $MgO/Al_2O_3 > 1.25$ indicator) established by Delano (1986). Additionally, the optical basis for 74220 orange glass pristinity is defined by Delano (1986), and encompasses the intrasample homogeneity and clustering observed by Delano and Lindsley (1983) and Hughes et al. (1990).

The particular subsample used in this work is 74220,939, a loose collection of regolith from which particles exceeding one millimetre in diameter were removed by sieve prior to this work. Optical inspection of the sample before and during sorting confirmed the samples exhibited no significant deviations from most aspects of the previously published sample description. An optical and electron probe microanalysis description of the glasses contained in this particular subsample is presented in Section 4.4.1.

### 4.2.3. Sample selection and sorting

The Apollo 15 and 17 samples used in this work also contain impact-derived glasses, which are ubiquitous on the lunar surface, and often closely resemble volcanic glasses (Butler et al., 1971; Vaniman and Papike, 1977a, 1977b). Distinction of these impact glasses from the similarly sized volcanic glasses can require geochemical or petrologic evidence (as described in Sections 4.3.1 and 4.3.2). The distinction can be made by optical and geochemical methods developed by Delano and Livi (1981), Delano (1986), Zellner et al (2018), and Zellner (personal communication). Distinguishing the impact derived glasses from the volcanic glasses was of great importance to this work, as their complex noble gas composition (as exhibited in the Ar work of Zellner et al. 2009; Zellner 2019) could easily influence the interpretation of volcanic glasses if falsely identified. The following section describes the increasingly confident means of optical classification under microscope preceding geochemical confirmation by EPMA (Electron Probe MicroAnalysis) major element data (described in Section 4.5.1). While chemical analysis

by EPMA was ultimately employed to definitively determine an impact or volcanic origin for many glasses, the large number of candidate glasses in each sample, and time constraints, required a ‘shortlist’ of the most pristine to be selected for microprobe analysis. This shortlist of the best-preserved glasses most likely to be volcanic was populated by optical inspection according to the following criteria, an adapted version of the criteria of Delano (1986):

- *The glasses which exhibited the largest volume.*

  The larger mass also allows for a larger volume of noble gases, improving the signal to noise ratio, and reducing uncertainty. The longer diffusion paths of larger glass spherules mean they are more likely to retain trapped noble gases.

- *The glasses which most resembled the green/orange colouration observed in previous research, distinguishing them from the darker impact glasses.*

  The colours were the primary means of sorting volcanic glasses from the impact glasses. The impact glasses are often devitrified, resulting in their black or opaque appearance.

- *The glasses with the cleanest surfaces.*

  Pitted or damaged surfaces were often hard to distinguish from groups of glass spherules which had fused together, fused with regolith, or had not retained their original surfaces. Fusing and melting of glasses involve heating to temperatures which could mobilise noble gases, so distinguishing these examples for removal is important. Pitted or damaged glasses complicate attribution of noble gases to sample surfaces or interiors, as volumes and surface areas are hard to determine.

- *The least damaged glasses.*

  Similar to the previous criterion, this excludes glass spherules which may have lost material by gardening processes or micrometeorite bombardment. This condition also indirectly helped with colour and surface condition, as they were often obscured with the damaged spherules.

Samples 15426,189 and 74220,939 were decanted into individual petri dishes from their Teflon capped stainless steel containers; the contents were in the loose form explained in Sections 4.2.1 and 4.2.2, and shown in Figure 4.3. Each sample was then soaked in acetone and the petri dish swilled to roughly separate by size, similarly to gold panning. Soaking in acetone also served to wash away the finer surficial dust coating attached to the larger grains, revealing their surface colouration and damage. The larger grains were then removed by tweezers and sorted according to colour, size, and apparent pristinity under an optical microscope. This process was repeated until the remaining unpicked samples were too fragile for manual removal without some being crushed during picking. While the nature of this work fortunately favoured the largest glass spherules, it should be noted that there were significantly more glasses remaining in the regolith than were removed, but their picking would require a more delicate and efficient sorting method.

This sorting was particularly simple for 15426,189 due to the obvious colour difference between the impact and volcanic glasses, with the former appearing opaque and black, often without the need of an optical microscope. However, the orange volcanic glass spherules of Apollo 17 posed a minor problem at this stage as their opacity appeared to increase with volume, making them increasingly indistinguishable from the black impact glasses. This problem could be resolved with a more intense light source, ideally from

beneath the sample, however, individual inspection under a greater magnification was sufficient for this work.

Table 4.1 contains information on the samples selected for xenon analysis by this process. Sample volumes were determined by measuring multiple glass spherule diameters, calculating each spherule as an ellipsoid. All measurements were conducted by digital inspection of multiple two-dimensional images of each glass captured by optical microscope. Scales of sufficient precision to measure masses for individual glasses were not available for this work, so masses were estimated by subtracting the polished fraction of each glass as a spherical cap from the ellipsoid. Glass volumes can therefore be expected to feature large uncertainties due to compounded measurement uncertainties (initial volume and estimated fraction removed by polishing) and cubic scaling of the two-dimensional measurements used for the ellipsoid volume.

A small selection of glasses suspected to be of impact origin were also selected. These glasses did not satisfy the volcanic glass criteria. Some of these glasses were included in the EPMA analyses in order to confirm their chemical distinction from volcanic glasses. Once EPMA had confirmed the optical distinction of volcanic and impact glasses, further volcanic glasses were selected relying solely on optical characterisation. These were mostly used in the “multi-spherule” analyses (Table 4.1).

***Table 4.1*** *Volcanic glass spherule parameters measured before and after polishing.*

| Parent | Subsample | Analysed by EPMA | Sample volumes ($10^{-6}$ $cm^3$) | | Mass (µg) Post-polish | Diameter (mm) |
|---|---|---|---|---|---|---|
| | | | Original | Post-polish | | |
| 15426 | A | ✓ | 95.9 | 88 | 263.9 | 0.57 |
| | B | ✓ | 54.6 | 27.3 | 82 | 0.47 |
| | D | ✓ | 17.8 | 8.9 | 26.7 | 0.32 |
| | F | ✓ | 8.3 | 5.4 | 16.2 | 0.25 |
| | H | ✓ | 14.4 | 9.8 | 29.5 | 0.3 |
| | J | ✓ | 8.2 | 4.1 | 12.2 | 0.25 |
| | L | | 5.9 | - | 17.8 | 0.22 |
| | Z | | 11.7 | - | 35.1 | 0.28 |
| 15426 'Multi-spherule' | 1 | | 9.3 | - | 27.8 | 0.26 |
| | 2 | | 5.4 | - | 16.1 | 0.22 |
| | 3 | | 1.8 | - | 5.4 | 0.15 |
| | 4 | | 12.2 | - | 36.6 | 0.29 |
| | 5 | | 3.6 | - | 10.7 | 0.19 |
| | 6 | | 7.5 | - | 22.5 | 0.24 |
| | 7 | | 5.5 | - | 16.6 | 0.22 |
| | 8 | | 7.1 | - | 21.3 | 0.24 |
| | Total | | 52.4 | - | 157 | - |
| 74220 | A | ✓ | 6.6 | 2.9 | 8.7 | 0.23 |
| | C | ✓ | 8.2 | 6.7 | 20.1 | 0.25 |
| | D | ✓ | 23.1 | 22.9 | 68.8 | 0.35 |
| | F | ✓ | 63.5 | 62.9 | 188.6 | 0.49 |
| | H | ✓ | 3 | 1.5 | 4.5 | 0.18 |
| | I | ✓ | 9.7 | 5.7 | 17.1 | 0.26 |
| | X | | 4.6 | - | 13.8 | 0.21 |
| 74220 'Multi-spherule' | 1 | | 2 | - | 6 | 0.16 |
| | 2 | | 1.2 | - | 3.7 | 0.13 |
| | 3 | | 2.5 | - | 7.4 | 0.17 |
| | 4 | | 1.9 | - | 5.8 | 0.15 |
| | 5 | | 2.9 | - | 8.8 | 0.18 |
| | 6 | | 0.6 | - | 1.8 | 0.11 |
| | 7 | | 1.3 | - | 3.8 | 0.13 |
| | Total | | 12.4 | - | 37.2 | - |

*Masses correspond to estimates based on volume and an assumed density of 3 g/$cm^3$. Hyphens in post-polish column indicate the corresponding samples were not polished. Non-polished samples represent volcanic glasses purely identified by optical means (no tick in 'Analysed by EPMA' column). Diameter column corresponds to average diameters measured from often ellipsoidal glasses, so should only be used as a guide of sample size.*

## 4.3. Methodology

### 4.3.1. Sample preparation

Once each sample was picked and sorted by apparent origin, size and pristinity according to the optical methods explained in Section 4.2.3, they were prepared for geochemical evaluation with EPMA by mounting and polishing. Samples selected for probe analysis were individually cleaned in an ultrasonic bath of isopropanol to remove any residual dust from picking. Selecting a medium in which to mount the samples during their polishing presented a number of issues. This medium would have to be strong enough to hold the samples during polishing, stable in the probe's operating vacuum and electron beam, feature minimal heating, and allow for easy removal of the samples after probe work. The paradigm in the field of electron microprobe work is to use epoxy, which satisfies all criteria but the removal from the sample, as previous attempts have caused significant hydrocarbon contamination within RELAX and other instruments (Cohen et al., 2005; Cohen, 2013). The use of Crystalbond 503 (Delano et al., 2007; Zellner et al., 2009; Gombosi et al., 2015; Zellner and Delano, 2015) has precedence in lunar glass work, but the heating during mounting introduced the risk of liberating volatiles, including xenon, and the material's stability when subjected to an electron beam was questionable (Geller and Engle, 2002). Superglue was selected due to its room temperature mounting procedure, its adequate stability when briefly subjected to an electron beam in a vacuum, and its ease of sample removal due to its solubility in acetone. Testing of different varieties of superglue discovered that the viscosity, curing time, and tendency to avoid forming bubbles favoured the use of Pattex "Sekundenkleber Flüssig Matic" superglue, which would be the exclusive choice for mounting in all following work.

The common EPMA mounting and polishing procedure (detailed by Brown and Gooding, of the Smithsonian National Museum of Natural History, SNMNH) was partially adapted for this work after practice with terrestrial analogues of olivine. The samples were mounted inside acrylic pipes with an outer diameter of 0.5 mm, cut to 2 mm, the same length as the depth of the brass mount used to hold samples for analysis in EPMA. The pipes were placed on double sided sticky-tape, sample side down, then backfilled with superglue from the open top of the cylinder. Aside from a gentle press applied to the sample to ensure its adherence to the tape, and the removal of bubbles from the setting superglue, the tubes were left to harden for 48 hours. The hardened samples were then slotted into a brass mount and polished using fine (600 grit) sand paper to remove the glue coating, then sequentially finer grades of polish with diamond paste (6 µm, 3 µm, then 1 µm), lapping paper, and Microid diamond compound extender. The individually mounted cylinders would prove particularly useful during this process, as the range of sample sizes (0.11 mm < 0.57 mm in diameter) meant extra care had to be taken to ensure some of the samples were not completely consumed by the polishing before others were ready. This was achieved by temporary removal of acrylic cylinders containing glasses with a more developed polish. Preserving as much sample volume as possible was particularly important given the volume correlation of most xenon components and the samples being likely to feature low xenon concentrations. After sufficient polishing, the samples were carbon coated for probe analysis.

Backscatter images of all glasses were taken prior to EPMA analysis within the JEOL 8530 at The University of Manchester, revealing a homogeneous structure in all glasses apart from one glass of 15426 (pictured and explained in Figure 4.2). The backscatter images also provided information on the polish quality and areas of each glass most appropriate for spot analysis by EPMA.

After EPMA analysis, the samples were polished to remove the carbon coating and taken from the brass mounts. Samples were then plucked from their superglue housing and subjected to a cleaning regime in order to remove as much superglue as possible, a likely source of hydrocarbons and atmospheric xenon which would affect the RELAX analysis. Each glass spherule was roughly cleaned of large pieces of superglue in a shallow acetone bath before being transferred to a beaker containing 10 cl of acetone. The beaker was then placed in an ultrasonic bath for 5 minutes, after which the glass spherule was transferred to another beaker containing a fresh 10 cl of acetone which was ultrasonically bathed for another five minutes. This cycle was repeated four times for each glass spherule, and followed up with inspection under optical microscope to confirm removal of superglue, which turned cloudy after acetone exposure.

### 4.3.2. Electron Probe MicroAnalysis (EPMA)

Electron Probe MicroAnalysis (EPMA) is a technique in which sample material is irradiated by an electron beam which temporarily excites atoms in the sample to higher energy electron configurations. These decay to the ground states, emitting X-ray photons of wavelengths characteristic of their corresponding elements. The electron beam interacts with the sample surface and subsurface in two ways. The electrons interact with the material inelastically, producing the element specific X-rays and secondary electrons. The electrons also scatter elastically to produce an excited volume in the sample material and back-scattered electrons useful for imaging (as in Figure 4.2). This excited volume occupies an area extending into the sample subsurface to a depth closely related to electron beam energy and sample density; modelling by Goldstein et al. (2003) shows this depth is typically a couple of microns. This area is wider at depth than the incident electron beam as some of the electrons scatter outwards. X-rays may be produced by inelastic interactions from anywhere within this volume.

Within wavelength dispersive spectrometers (WDS), crystals are selected to diffract particular wavelengths of the produced X-rays into detectors which produce a signal proportional to the intensity of X-rays specific to an element, many of these spectrometers can be employed simultaneously. The sample signal is then compared to an equivalent signal taken from a standard with a known composition. This comparison allows a relative concentration of the target element to be calculated.

The X-rays detected by the spectrometers within the EPMA are not representative of the total amount of X-rays produced by inelastic interactions. X-rays are emitted isotropically from excited atoms, and some are reabsorbed before they escape the sample. The relationship between the detected X-rays, the X-rays which do not reach the detector, and the subsequent concentration of species required to produce the X-rays is calculated according to a model which assumes the sample surface is horizontal. Samples with uneven surfaces have different excitation volumes and distances over which X-rays could be absorbed, so produce X-ray signals which do not correspond to the model. In the case of a chemically homogenous sample with an uneven surface, EPMA with multiple spot analyses may produce different concentrations for each spot due to their differing topography and excitation volumes, increasing the error associated with the concentration (Geller and Engle, 2002). The flatness of a sample prepared for EPMA is subsequently important for the reliability of the results. Multiple stages of polishing (as described in Section 4.4.1) are required to produce a polish sufficiently flat for reproducible EPMA data.

The selection of superglue as a mounting material would introduce some flatness problems which only became apparent after topographical mapping of the polished surfaces in the probe. Some of the samples protruded out of the polished plane of superglue and featured rounded surfaces unsuitable for EPMA analysis. Individual mounting of the

samples in acrylic tubes allowed remedial repolishing of the problematic samples to be conducted while other samples were being analysed, however, these repolished samples returned mixed results (see 4.5.1).

Standard selection and instrument settings attempted to replicate those of Delano et al. (2007), within the constraints of the available probe's features and post-EPMA noble gas analyses. Quantitative wavelength dispersive X-ray chemical analyses were performed using the JEOL 8530 at The University of Manchester at 15 keV, 30 nA, and a beam diameter of 15 µm for 50 seconds on Si, Ti, Al, Ca, Fe, Mn, Mg, K, Na, and Ba, and 100 seconds on $Cr_2O_3$. These species were detected by three analysing crystals, Mg and Al by TAP, Fe, Cr and Mn by LIFL, and K, Ca, Ti, Ba, and Si by PETL. The selection of Si, Ti, Al, Ca, Fe, Mn, Mg, K, and Na was in line with previous analyses of lunar volcanic glasses apart from Ba. The instrument was loaded with reference standards to act as analogues of the sample chemistry and primary standards to provide a high signal intensity for tuning the instrument. Off-peak measurements were taken throughout analyses to determine a background signal, subtracted from the oxide weights presented herein. The reference standards were volcanic glasses A-99 and VG-2 (as in Delano et al. 2007), whose measurements bracketed each sample analysis (results are presented in Appendix 4A.1-4). No internal working standards were implemented in these analyses, with the implications discussed in Section 4.5.1.

With small samples, EPMA spot analyses beside grain boundaries or the edges of samples, the excitation volume may extend into the surrounding material. In these cases, the emitted X-rays correspond to all enveloped materials. A proportion of the detected X-rays are therefore produced by the additional material. Given the small size of the samples analysed in this work, EPMA spots were chosen towards the inside of the available polished surfaces, so that the excited volume did not extend beyond the glass. The poor

polish quality made this impossible in some of the glasses, where the spots were restricted to the areas featuring the best quality polish. The implications for this decision are explored in Section 4.4.1.

Irradiating samples with an electron beam current exceeding 4 nA has been proven to mobilise volatile species such as OH in apatites (Barnes et al., 2013). The 30 nA current electron beam used in this work may therefore be capable of mobilising other volatile elements, such as xenon. However, other lunar regolith glass studies have conducted EPMA major element measurements with currents exceeding the 4 nA current capable of mobilising OH prior to noble gas analysis, and returned noble gas data for He, Ne, Ar after < 12 nA electron beam irradiation (Füri et al., 2014), and $^{40}$Ar-$^{39}$Ar ages after 50 nA electron beam irradiation (Zellner et al., 2009). Notably, cosmogenic signatures produced in the lunar surface were retained in both of these cases. Xenon should be less susceptible to mobilisation due to its larger atomic radius, so mobilisation by electron beam is expected to be less significant than He, Ne, and Ar.

### 4.3.3. Refrigerator Enhanced Laser Analyser for Xenon (RELAX)

RELAX is a time of flight mass spectrometer specifically designed for the analysis of samples containing low abundances of xenon atoms (Gilmour et al., 1994; Crowther et al., 2008), and is described in more detail in Section 2.1. For this work RELAX measured gases extracted by stepped heating in a procedure detailed below.

After the spherules were removed from the EPMA brass mount and cleaned with acetone to remove the superglue, they were mounted individually in twelve holes (2 mm in diameter and depth) drilled in two aluminium disks. Each disk was analysed separately within RELAX according to the following procedure. The sample disk was placed in a

sealed sample port with a copper gasket and pumped down to $10^{-5}$ mbar. The sample port and vacuum system to the pumps was then subjected to baking by lamp and heating strips for 48 hours at < 150 °C to remove volatiles adsorbed while this section of the instrument and sample were exposed to atmosphere. Pumping down to maintain and improve the vacuum was conducted throughout this baking process by turbomolecular and ion pump. Once pressure stabilised at ~ $10^{-9}$ mbar the instrument was tuned and calibrated according to a known volume aliquot of air, and a blank. Air and blank measurements would then sandwich sample analyses by being conducted at the start and end of analyses, and after each four heating step measurements. Blank measurements in which timing and volumes mirrored sample procedures (excluding gas extraction) were conducted alongside sample analyses. Sample gas extraction was achieved by step heating of samples by subjection to an infrared Fiber laser shone through the sample port window.

Methods by which actual temperatures of heating steps employed during sample gas extraction, such as pyrometric calibrations of the sample, or thermostat-controlled furnaces, were not available. Temperatures of heating steps are most closely approximated by power, which is controlled by changing the duty cycle of the Fiber laser. The duty cycle effectively varies the fraction of each 10 kHz cycle in which laser light is output, up to a duty cycle of 100% (corresponding to a continuous wave), after which the input power is varied directly. For all heating steps, the sample is illuminated for 30 seconds. Two to eight heating steps were applied to each sample, featuring approximate powers of ~ 0.17 W up to continuous illumination roughly equivalent to 17 W. Power was varied step-by-step based on the gas released by the previous power, and the expected behaviour based on similarly sized volcanic glasses. Heating steps were generally stopped when the sample was observed to glow and melt. All contained gases are expected to have been released by the time the sample melts, which was usually achieved under the subjection of an 8 W beam for these samples.

One EPMA-confirmed impact glass, 74220,939 “G” was included in the xenon analyses under the working assumption that it experienced a roughly similar history of residence on the lunar surface compared to the volcanic glasses. This impact glass was intended to provide a “control”, of a sample subject to similar surface conditions to the volcanic glasses, such as SW-Xe implantation and cosmogenic xenon production, without the original lunar interior xenon. Subtracting the impact glasses “control” xenon composition from the compositions contained in the volcanic glasses would highlight the compositional difference between the two glass categories, and potentially help identify a component only present in the volcanic glass, ideally an indigenous lunar interior composition. Experimental time constraints did not allow for more xenon measurements of impact glasses to constitute a more robust control.

## 4.4. Results

### 4.4.1. Major element data

Table 4.2 contains the results of the oxide weight percentages gathered by the electron microprobe for ten glasses retrieved from 15426,189 and nine from 74220,939. The number of analyses column indicates the number of spots from which data were gathered on the polished surface of each glass. The numbers one and two beside subsamples C and D of 15426,189 indicate the data gathered before and after repolishing. Note that the major element data totals were not normalised in order to exhibit the range of totals, which does not affect the ratios used in the following major element plots.

Figure 4.4 shows a plot of average $MgO/Al_2O_3$ and MgO/CaO data gathered by the EPMA analyses of each individual glass of 15426,189, alongside other literature values for volcanic green glasses of Apollo 15 and impact-derived materials. Of the twelve analyses shown in Figure 4.4, two glasses (shown as green diamonds) plot amongst the group of materials of impact origin (shown as black diamonds), these glasses were members of the group which did not fulfil the pristine volcanic glass criteria of Section 4.2.3. The glasses which plotted in the top right of Figure 4.4 expressed the indicative $MgO/Al_2O_3 > 1.25$, and low abundance of the regolith-correlated CaO, characteristic of volcanic glasses. The seemingly volcanic glasses also plot amongst previously reported values for groups of Apollo 15 volcanic glasses (Delano, 1986; Galbreath et al., 1990; Steele et al., 1992; Shearer and Papike, 1993). However, attempts to place the glasses of 15426 amongst the sub-groups of green glasses defined in previous work (Steele et al., 1992; Shearer and Papike, 1993) are difficult, as poor EPMA precision leave them scattered around and amongst the reported groups (plotted as a contiguous group in Figure 4.4, as described by Delano 1986).

Figure 4.5 shows a plot of average $MgO/Al_2O_3$ and MgO/CaO data gathered by EPMA analyses of each individual glass of 74220,939 against other literature values for volcanic orange glasses of Apollo 17 and impact-derived Apollo 17 materials. Of the nine analysed glasses exhibited in Figure 4.5, two (shown as orange diamonds) plot amongst the group of materials of impact origin (shown as black diamonds), with the previously defined characteristic enrichments in Ca and an Al/Mg value lower than 1.25. As with 15426, the discovery of the impact glasses was not a surprise given their partial fulfilment of the pristine selection criteria (Section 4.2.3).

The orange 74220 glasses in this work express similarly low-Ti abundances to the VLT (II) group of orange 74220 glasses as elaborated in Delano and Lindsley (1983) and expressed by Figure 4.6, yet plot closer to the Orange I and II groups of Delano and Lindsey (1983), and the 74220 type of Shearer et al. (1991) for the other, more abundant and reliable EPMA measurements (Figures 4.5 and 4.7). While the presented data appear inconclusive with regards to which group the orange glasses of 74220 belong to, the fact VLT glasses belong to a lunar breccia with no obvious relationship to 74220 suggest their similarity results from analytical error.

Many glasses exhibit low totals (such as 15426 “F” and others ~ 90% shown in Table 4.2), scatter around the expected concentrations (as in Figure 4.4), and sometimes group significantly further away from literature values (as in Figure 4.6 and Figure 4.7). These results are indicative of poor sample preparation for EPMA analysis, as elaborated in Section 4.3.2, and discussed in Section 4.5.1. These data are not sufficiently precise to determine the compositional groups the glasses belong to, or serve as reference data. However, the primary objective of collecting these data was achieved, as exhibited in Figure 4.4 and Figure 4.5, in the distinction of the volcanic and impact origin of the glasses using oxide ratios.

Figure 4.8 contains a comparison of the two volcanic glasses of 15426 which were analysed twice by EPMA, punctuated by removal and polishing to reveal a fresh surface to the instrument for the second analysis.

The standard data obtained during the EPMA sessions were compared on an element by element basis to the work conducted by Delano et al. (2007) and the data reported by Smithsonian Institution of The National Museum of Natural History (SNMNH) (Jarosewich, 2002) in Appendix figures 4A.1 to 4A.4. The standard EPMA data obtained in this work are consistent with the values expected from the literature they were being compared to (Jarosewich, 2002; Delano et al., 2007), and exhibited no apparent drift or evidence of inaccurate calibration. This observation precludes EPMA instrument effects as the cause of variation in the volcanic glass sample EPMA data between repeat analyses.

***Table 4.2*** *EPMA data gathered for glass spherules of 15426,189 and 74220,939.*

| Sample | Subsample | Number of analyses | Oxide weight % | | | | | | | | | | | |
|---|---|---|---|---|---|---|---|---|---|---|---|---|---|---|
| | | | $SiO_2$ | $TiO_2$ | $Al_2O_3$ | $Cr_2O_3$ | FeO | MnO | MgO | CaO | $Na_2O$ | $K_2O$ | BaO | TOTAL |
| 15,426,189 | A | 8 | 38.4 (0.24) | 8.89 (0.03) | 5.34 (0.03) | 0.67 (0.01) | 21.5 (0.13) | 0.28 (0.00) | 14.8 (0.05) | 6.93 (0.01) | 0.37 (0.00) | 0.06 (0.00) | 0.00 (0.00) | 97.3 (0.29) |
| | B | 10 | 42.3 (0.16) | 0.36 (0.00) | 6.53 (0.06) | 0.45 (0.00) | 16.1 (0.23) | 0.22 (0.01) | 16.6 (0.08) | 7.17 (0.03) | 0.10 (0.00) | 0.01 (0.00) | 0.00 (0.00) | 90.0 (0.39) |
| | C - 1 | 20 | 39.4 (0.36) | 9.14 (0.03) | 5.27 (0.08) | 0.70 (0.01) | 22.2 (0.19) | 0.27 (0.00) | 14.3 (0.24) | 7.12 (0.02) | 0.32 (0.01) | 0.05 (0.00) | 0.01 (0.00) | 98.9 (0.39) |
| | C - 2 | 10 | 43.7 (0.09) | 0.36 (0.00) | 7.11 (0.08) | 0.50 (0.01) | 17.6 (0.13) | 0.23 (0.01) | 17.0 (0.17) | 7.62 (0.02) | 0.12 (0.00) | 0.00 (0.00) | 0.00 (0.00) | 94.4 (0.29) |
| | D - 1 | 8 | 38.7 (0.45) | 8.74 (0.15) | 5.23 (0.08) | 0.65 (0.02) | 20.1 (0.50) | 0.25 (0.01) | 13.4 (0.40) | 6.87 (0.08) | 0.36 (0.01) | 0.06 (0.00) | 0.00 (0.00) | 94.5 (1.05) |
| | D - 2 | 10 | 43.9 (0.32) | 0.38 (0.00) | 7.30 (0.10) | 0.52 (0.01) | 19.0 (0.08) | 0.25 (0.01) | 17.6 (0.28) | 7.90 (0.04) | 0.14 (0.01) | 0.00 (0.00) | 0.00 (0.00) | 97.0 (0.46) |
| | E* | 10 | 38.6 (0.07) | 4.97 (0.03) | 8.60 (0.03) | 0.28 (0.01) | 20.2 (0.16) | 0.23 (0.01) | 8.21 (0.05) | 8.40 (0.04) | 0.45 (0.01) | 0.10 (0.00) | 0.01 (0.00) | 90.2 (0.35) |
| | F | 10 | 39.7 (0.37) | 0.32 (0.00) | 6.82 (0.16) | 0.40 (0.01) | 13.9 (0.28) | 0.18 (0.01) | 17.2 (0.47) | 6.25 (0.12) | 0.13 (0.01) | 0.01 (0.00) | 0.00 (0.00) | 84.9 (0.72) |
| | G* | 10 | 43.2 (0.22) | 0.71 (0.00) | 20.6 (0.13) | 0.16 (0.01) | 6.81 (0.05) | 0.08 (0.00) | 8.35 (0.04) | 11.2 (0.08) | 0.27 (0.01) | 0.10 (0.01) | 0.02 (0.00) | 91.6 (0.48) |
| | H | 10 | 44.3 (0.23) | 0.37 (0.00) | 7.53 (0.05) | 0.57 (0.01) | 19.7 (0.08) | 0.25 (0.01) | 17.3 (0.07) | 8.13 (0.01) | 0.10 (0.00) | 0.00 (0.00) | 0.00 (0.00) | 98.4 (0.26) |
| | I | 10 | 38.7 (0.81) | 9.27 (0.31) | 5.72 (0.37) | 0.62 (0.02) | 20.5 (0.46) | 0.26 (0.00) | 12.6 (1.03) | 7.61 (0.56) | 0.33 (0.05) | 0.05 (0.00) | 0.01 (0.00) | 95.8 (0.87) |
| | J | 20 | 38.6 (0.20) | 8.84 (0.03) | 5.36 (0.03) | 0.67 (0.01) | 21.6 (0.15) | 0.27 (0.00) | 14.7 (0.10) | 6.92 (0.02) | 0.32 (0.01) | 0.05 (0.00) | 0.00 (0.01) | 97.6 (0.43) |
| 74,220,939 | A | 8 | 45.3 (0.32) | 0.42 (0.00) | 6.91 (0.02) | 0.54 (0.01) | 19.9 (0.15) | 0.25 (0.01) | 17.0 (0.06) | 8.06 (0.03) | 0.12 (0.00) | 0.01 (0.00) | 0.00 (0.00) | 98.8 (0.50) |
| | B | 20 | 46.1 (0.33) | 0.42 (0.00) | 6.84 (0.04) | 0.54 (0.01) | 19.9 (0.09) | 0.26 (0.00) | 17.1 (0.11) | 8.07 (0.01) | 0.11 (0.01) | 0.01 (0.00) | 0.00 (0.00) | 99.6 (0.42) |
| | C | 10 | 45.4 (0.34) | 0.38 (0.00) | 6.85 (0.02) | 0.52 (0.01) | 18.9 (0.08) | 0.24 (0.00) | 16.5 (0.08) | 7.93 (0.02) | 0.12 (0.00) | 0.00 (0.00) | 0.00 (0.00) | 96.9 (0.32) |
| | D | 20 | 45.3 (0.38) | 0.39 (0.00) | 6.91 (0.03) | 0.54 (0.01) | 19.6 (0.11) | 0.25 (0.00) | 16.8 (0.08) | 8.14 (0.03) | 0.12 (0.01) | 0.00 (0.00) | 0.00 (0.00) | 98.2 (0.47) |
| | E* | 20 | 41.6 (0.31) | 5.56 (0.02) | 8.39 (0.07) | 0.32 (0.01) | 23.0 (0.16) | 0.27 (0.01) | 8.10 (0.06) | 9.21 (0.02) | 0.44 (0.02) | 0.11 (0.00) | 0.01 (0.00) | 97.1 (0.54) |
| | F | 10 | 44.2 (0.50) | 0.41 (0.00) | 6.99 (0.05) | 0.51 (0.02) | 18.6 (0.15) | 0.24 (0.00) | 17.7 (0.10) | 7.58 (0.04) | 0.12 (0.00) | 0.01 (0.00) | 0.00 (0.01) | 96.5 (0.81) |
| | G* | 20 | 47.5 (0.37) | 0.86 (0.01) | 20.6 (0.21) | 0.19 (0.00) | 8.32 (0.11) | 0.10 (0.01) | 8.36 (0.04) | 12.9 (0.04) | 0.29 (0.04) | 0.09 (0.03) | 0.03 (0.00) | 99.4 (0.40) |
| | H | 20 | 45.4 (0.65) | 0.37 (0.00) | 7.03 (0.06) | 0.54 (0.01) | 19.2 (0.19) | 0.25 (0.01) | 16.5 (0.13) | 8.17 (0.05) | 0.11 (0.01) | 0.00 (0.00) | 0.00 (0.00) | 97.8 (0.90) |
| | I | 10 | 45.2 (0.34) | 0.41 (0.00) | 6.86 (0.06) | 0.53 (0.01) | 19.7 (0.14) | 0.25 (0.00) | 17.7 (0.11) | 7.91 (0.01) | 0.10 (0.00) | 0.01 (0.00) | 0.00 (0.00) | 98.8 (0.45) |

*Analysis by the JEOL 8530 at the University of Manchester. Letters denote individual spherules. Asterisks denote spherules of impact origin, all other samples are of volcanic origin. Numbers after letters denote multiple analyses after repolishing. Parentheses denote standard errors.*

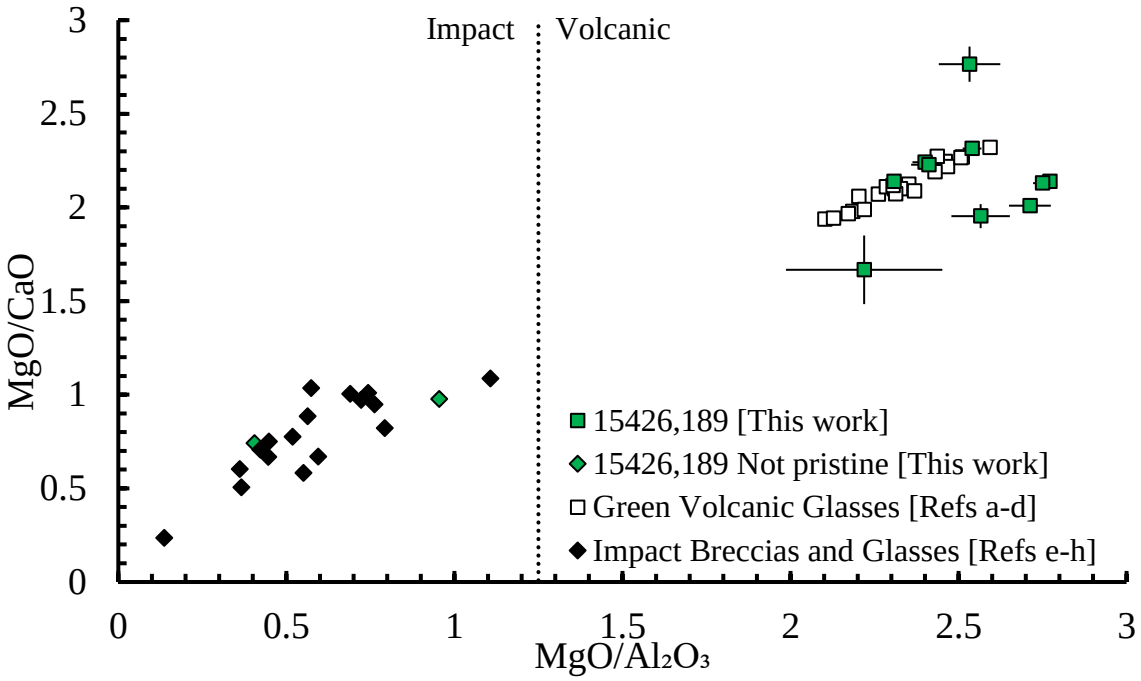


***Figure 4.4*** *MgO/CaO and MgO/$Al_2O_3$ plot of pristine 15426 glasses picked and polished for this work (green squares), glasses which did not satisfy the pristine criteria of Section 4.3.3 (green diamonds), and literature values for volcanic glasses (white squares) and impact breccias and glasses (black diamonds). References: a (Galbreath et al., 1990) b (Shearer and Papike, 1993) c (Steele et al., 1992) d (Delano, 1986) e (Zellner et al., 2009) f (Korotev et al., 2009) g (Morgan et al., 1973) h (Karouji et al., 2006). Vertical dashed line denotes location of impact/volcanic dichotomy of Delano (1986). 1σ errors.*

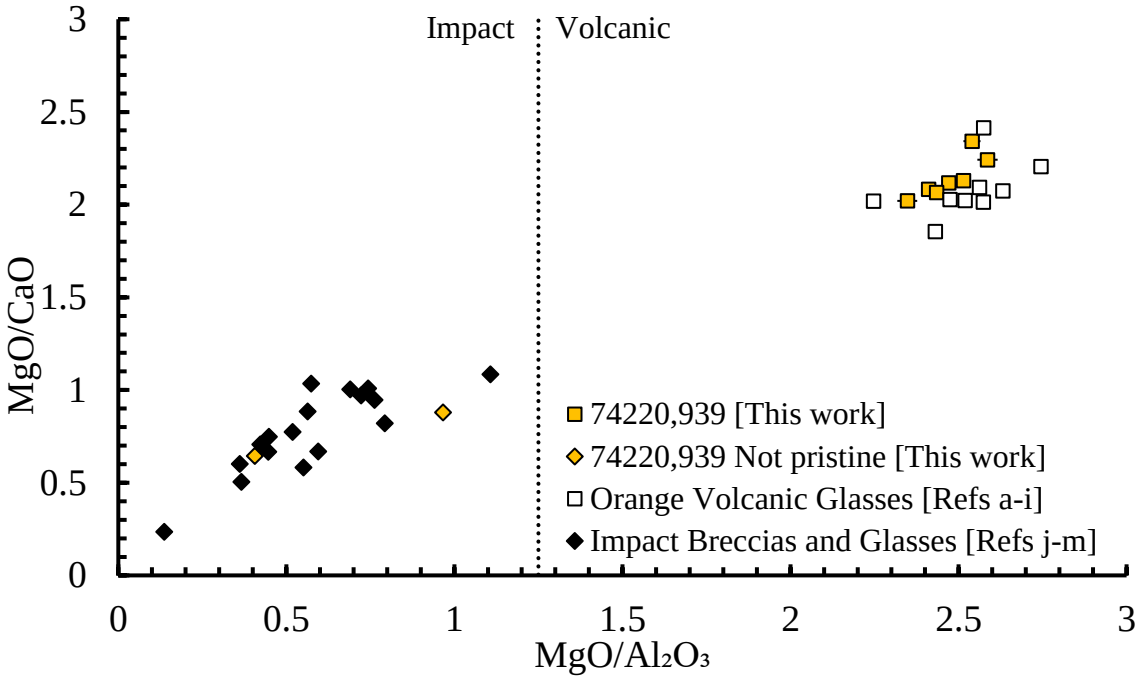


***Figure 4.5*** *MgO/CaO and MgO/$Al_2O_3$ plot of pristine 74220 glasses picked and polished for this work (orange squares), glasses which did not satisfy the pristine criteria of Section 4.3.3 (orange diamonds), and literature values for 74220 volcanic glasses (white squares) and impact breccias and glasses (black diamonds). References: a (Delano and Livi, 1981) b (Reid et al., 1973) c (Prinz et al., 1973) d (Carter et al., 1973) e (Glass, 1976) f (Roedder and Weiblen, 1973) g (Warner et al., 1979) h (Mao et al., 1973) i (Heiken et al., 1974) j (Zellner et al., 2009) k (Korotev et al., 2009) l (Morgan et al., 1973) m (Karouji et al., 2006). Vertical dashed line denotes location of impact/volcanic dichotomy of Delano (1986). 1σ Errors.*

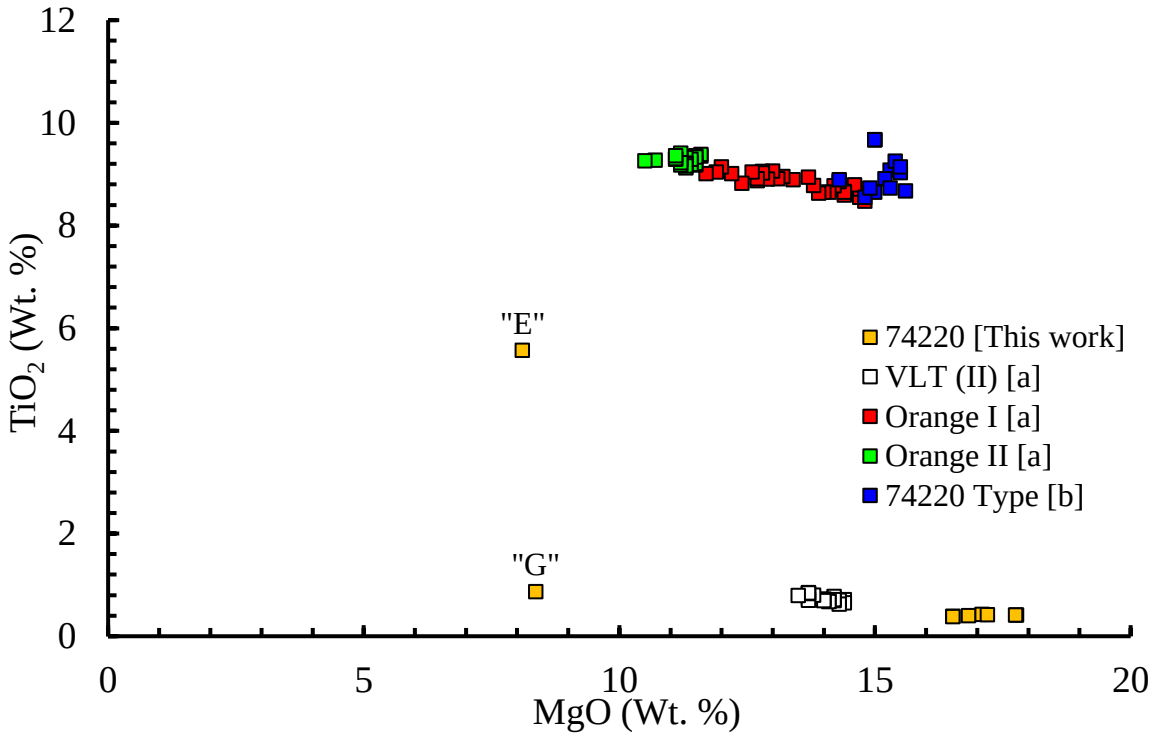


***Figure 4.6*** *MgO Weight % and $TiO_2$ Weight % plot of 74220,939 glasses characterised by this work (orange squares) and literature values for compositional groups: 'VLT (II)' (white squares), 'Orange I' (red squares), 'Orange II' (green squares), and '74220 Type' (blue squares). References: [a] Delano and Lindsley (1983) [b] Shearer et al. (1991). Note the two impact glasses ("E" and "G") of this work depleted in MgO relative to all orange glasses. Error bars representing 1σ are too small to be seen.*

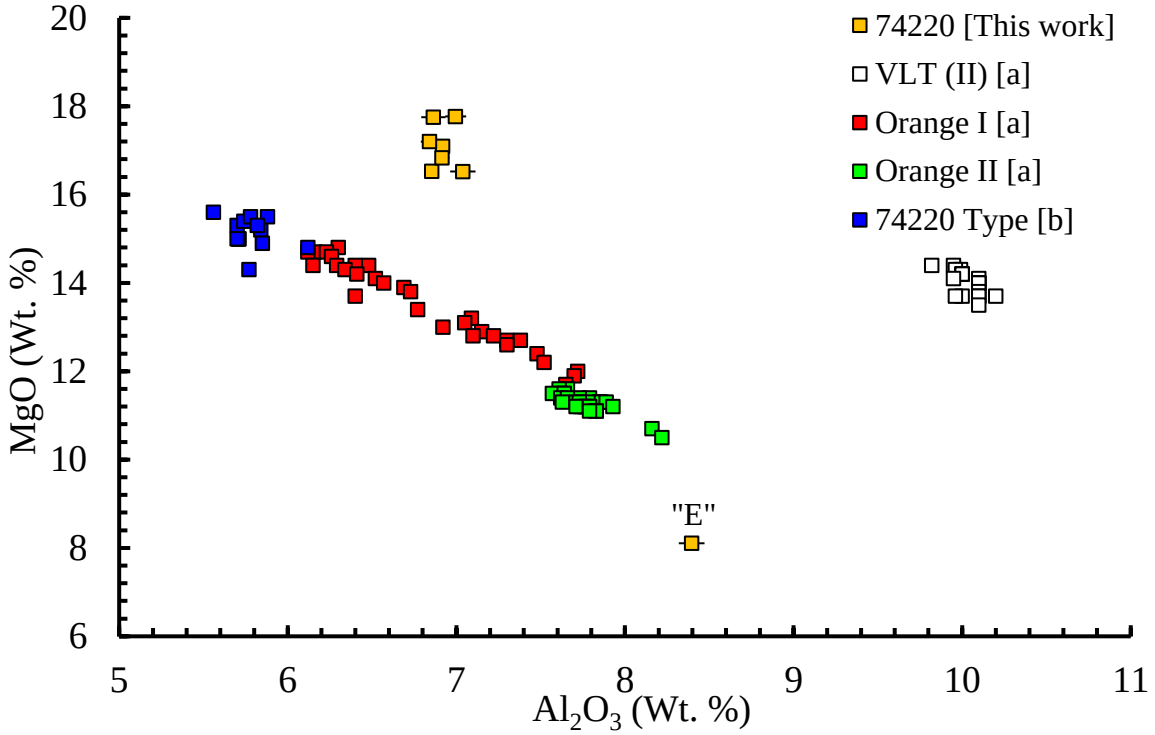


***Figure 4.7*** *$Al_2O_3$ Weight % and MgO Weight % plot of 74220,939 glasses characterised by this work (orange squares) compared to literature values for compositional groups: 'VLT (II)' (white squares), 'Orange I' (red squares), 'Orange II' (green squares), and '74220 Type' (blue squares). References: [a] Delano and Lindsley (1983) [b] Shearer et al. (1991). The impact glasses of this work are depleted in MgO relative to all orange glasses ("E" is plotted, and the other impact glass "G" plots to the right of the displayed scale). Error bars representing 1σ are too small to be seen.*

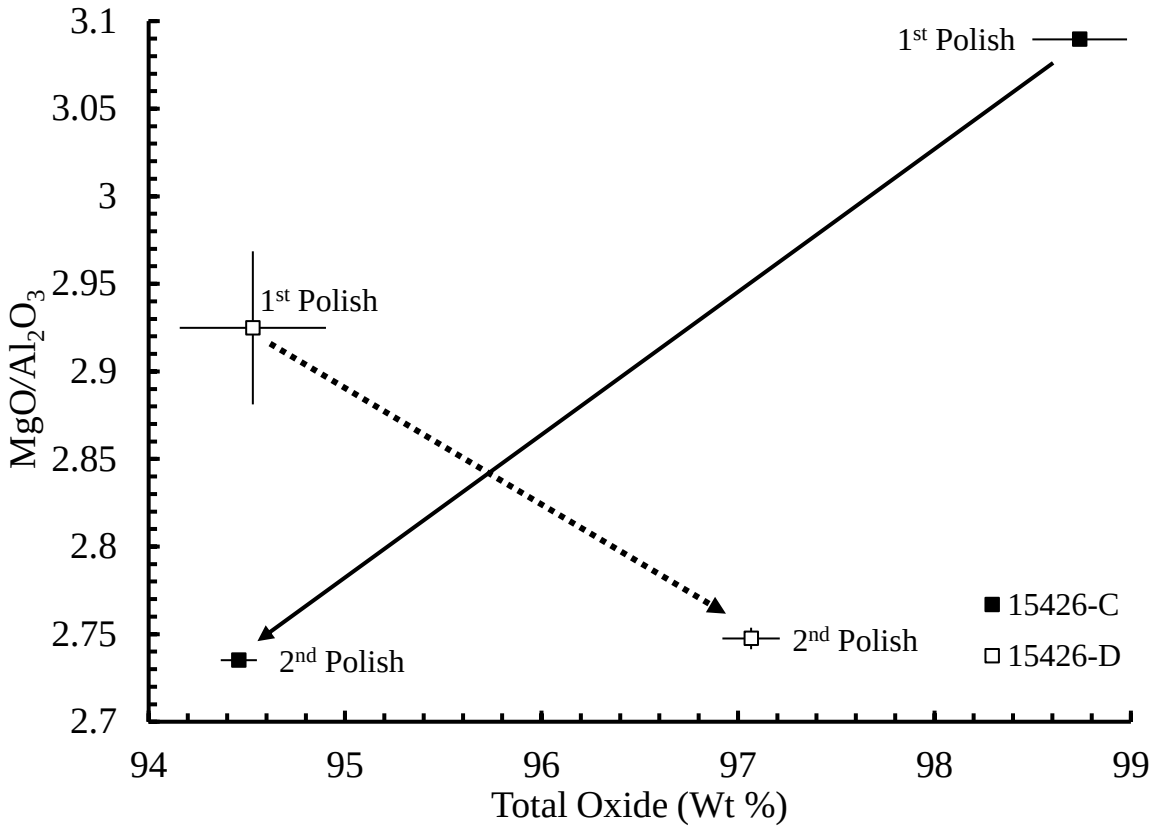


***Figure 4.8*** *EPMA data for repeat analyses of 15426,189 subsamples C (black squares) and D (white squares), arrows point towards later analyses of the same samples after extraction and repolishing. $MgO/Al_2O_3$ (ordinate), Total Oxide weight percent (abscissa). Note that oxide totals (usually a measure of better quality EPMA data) did not reliably improve after removal and a second polish. Error bars represent 1σ.*

### 4.4.2. Xenology

The glasses are assumed to contain a number of xenon compositions attributable to extant or extinct reservoirs or processes (Table 4.3 and Table 4.4), based on findings of previous work, our understanding of the conditions on the lunar surface, and the treatment of the samples prior to analysis. The following section describes the techniques, expectations, and validations to be employed in the xenon isotopic interpretation of the Apollo 15 and 17 glasses analysed in this work.

Searching for an unknown composition of dubious existence is obviously difficult to prepare for, but we can make a number of assumptions based on what we find in the xenon reservoirs of the Earth, its primordial compositions, and the overall composition of Solar System xenon. Xenon ultimately derived from the solar nebula dominates the Solar System and is most likely the ultimate progenitor of terrestrial reservoirs, including the Earth-Moon system. It is therefore reasonable to assume a "trapped" indigenous lunar xenon composition would be similar to this composition, for which solar wind is a suitable approximation. This "trapped" xenon would be most easily recognised by a composition dominated by $^{132}$Xe, the xenon isotope dominant in most of these reservoirs.

Discerning the exact origin of a component resembling "trapped" xenon requires further isotopes to be considered, this can be achieved by delta plots exhibiting permille deviations of each isotope from expected compositions, three isotope plots, or software capable of pan-isotopic investigation. In this work, a combination of all techniques will be employed with the assumption that a hypothetical indigenous lunar xenon composition most likely resembles the "trapped" compositions of the Solar System, and its determination requires confident deconvolution from other sources of xenon.

The volcanic and impact glasses of both Apollo 15 and 17 may contain xenon derived from Galactic Cosmic Ray (GCR) spallation with REEs, neutron capture by $^{130}$Ba, and fission products of $^{235\text{-}238}$U, $^{244}$Pu, and other extinct radionuclides. Fission and cosmogenic (GCR) xenon, being directly produced by atom scale decays or interactions, is correlated with the parent chemicals contained in a sample. Given the presence of these parent elements and chemical homogeneity of each volcanic glass (confirmed by backscatter observation), the distribution of fission and cosmogenic xenon are assumed to be equally homogeneous. Additionally, fission-derived xenon ($^{235}$U, $^{238}$U, and, $^{244}$Pu) attributed to a radionuclide whose period of activity has been constrained could elucidate the timing of glass formation.

***Table 4.3*** *Xenon isotopes and their production by radiogenic and cosmogenic processes.*

| Process | Parent | $^{124}$Xe | $^{126}$Xe | $^{128}$Xe | $^{129}$Xe | $^{130}$Xe | $^{131}$Xe | $^{132}$Xe | $^{134}$Xe | $^{136}$Xe |
|---|---|---|---|---|---|---|---|---|---|---|
| $\beta^-$ decay | $^{129}$I | | | | ✓ | | | | | |
| | $^{130}$Te | | | | | ✓ | | | | |
| $2\beta^+$ decay* | $^{132}$Ba | | | | | | | ✓ | | |
| Spontaneous Fission | $^{238}$U | | | | ✓ | | ✓ | ✓ | ✓ | ✓ |
| | $^{244}$Pu | | | | ✓ | | ✓ | ✓ | ✓ | ✓ |
| Slow Neutron Capture | $^{235}$U | | | | | | ✓ | ✓ | ✓ | ✓ |
| | Ba | | | | | | ✓ | | | |
| GCR Spallation | REE | ✓ | ✓ | ✓ | ✓ | ✓ | ✓ | ✓ | | |
| | $^{130}$Ba | ✓ | ✓ | ✓ | ✓ | ✓ | ✓ | ✓ | ✓ | |

*Ticks indicate a particular isotope is produced in the process it shares a row with. Note that this table does not consider the relative production rates for processes producing more than one isotope. Exhibited processes are those which may have influenced the xenon composition of the glasses analysed in this work. *Double beta decay ($2\beta^+$) is rare.*

***Table 4.4*** *Table containing common xenon reservoirs and their isotopic compositions.*

| Xenon Reservoirs | | Xenon Isotopic Compositions Normalised to $^{132}Xe \equiv 100$ | | | | | | | | | | | | | | | | Reference |
|---|---|---|---|---|---|---|---|---|---|---|---|---|---|---|---|---|---|---|
| | | 124 | | 126 | | 128 | | 129 | | 130 | | 131 | | 134 | | 136 | | |
| Planetary | Earth Atmosphere | 0.3537 | - | 0.33 | - | 7.14 | - | 98.32 | - | 15.14 | - | 78.90 | - | 38.79 | - | 32.94 | - | n/a |
| | Solar Wind | 0.482 | (0.005) | 0.422 | (0.0066) | 8.412 | (0.0216) | 8.412 | (0.0216) | 16.494 | (0.0272) | 82.632 | (0.2403) | 36.978 | (0.1026) | 29.985 | (0.0825) | a |
| Cosmogenic | Ba Spallation | 51.7 | (16.2) | 95.0 | (29.8) | 153.9 | (48.3) | 151.9 | (60.9) | 118.5 | (37.3) | 414.1 | (129.9) | 6.6 | (2.4) | - | - | b |
| | REE Spallation | 1283.3 | (1497.4) | 1666.7 | (1944.4) | 2033.3 | (2372.7) | 2666.7 | (3181.7) | 66.7 | (169) | 2733.3 | (3213.9) | 0.0 | (0) | - | - | b |
| Radiogenic | $^{235}U$ Fission | - | - | - | - | - | - | - | - | - | - | 67.6 | (1.1) | 183.0 | (2.1) | 148.8 | (1.3) | c |
| | $^{238}U$ Fission | - | - | - | - | - | - | 0.1 | (0) | - | - | 14.4 | (0.1) | 143.5 | (0.3) | 173.3 | (0.3) | d |
| | $^{244}Pu$ Fission | - | - | - | - | - | - | 5.4 | (6.2) | - | - | 27.8 | (2.4) | 106.1 | (3.7) | 113.0 | (3.8) | c |

*Isotopes given as ratios to $^{132}Xe \equiv 1$. Parentheses contain standard deviation. Hyphens denote the lack of an isotope being produced or contained in the corresponding reservoir. Hyphens for air composition are not included due to the derivation of all other ratios from Earth's current atmosphere as a constant. Refs: [a] (Meshik et al., 2019) [b] (Hohenberg et al., 1981) [c] (Ozima and Podosek, 1999) [d] (Ragettli et al., 1994).*

Of the 17 spherules characterised as volcanic by the probe data, a total of 15 were chosen to be analysed by stepped heating in the RELAX spectrometer, eight from 15426,189 and seven from 74220,939. Two spherules from 15426,189 ("L" and "Z") and two spherules from 74220,989 ("H" and "X") which were not characterised by EPMA were also selected for noble gas analysis after classification as volcanic by purely optical means (described in Section 4.2.3). Additionally, two groups of optically classified volcanic spherules, one containing eight spherules from 15426,189 and the other seven spherules from 74220,939, were also included to each be analysed en masse as "multi-spherule" representatives of the volcanic glasses in their respective samples. The optically classified glasses which were not exposed to an electron beam may also serve as controls to identify and quantify xenon mobilisation (as discussed in Section 4.3.2). One impact glass identified by EPMA within the sample 74220,939 was also included (for reasons explored in Section 4.3.3). The finalised dataset discard measurements where the signal did not exceed three standard errors above the typical blank in order to ensure the reported signals can be confidently attributed to xenon released from the samples. The procedural blank of the following data is atmospheric xenon containing 3000 atoms of $^{132}$Xe. Signal in atoms of each isotope confidently above blank for each heating step, and the heating step parameters, are reported in Appendix 4A.5 and 4A.6.

Interior and surface-correlated xenon components are important to distinguish in lunar volcanic glasses given the differing reservoirs they may sample (outlined in Section 4.2). The surfaces of the volcanic glasses are more likely to contain xenon from solar wind implantation and potentially the adsorption of a transient lunar atmosphere, whereas the interiors of the glasses are more likely to contain xenon from their lunar mantle source alongside cosmogenic xenon. Differentiation between the internal or surficial source of sample gas is made difficult by compositional similarities between xenon components and the problems with discretely extracting components as a function of sample depth. While

surficial Xe components are expected to be released at low temperature steps and interior components at higher temperatures, separating the gases within the sample between greater numbers of analyses can compromise precision. Volumes of xenon greatly exceeding the ideal amount of roughly $2.5 \times 10^5$ atoms $^{132}Xe$ results in instrument fractionation due to detector saturation (elucidated in Section 2.3.2). Too little xenon results in a lower signal to noise ratio and worse precision. There are two approaches to determining whether a component is surface or volume correlated:

- *Assume that higher temperature steps release xenon components from increasingly deeper within the sample.*

  Lower temperature steps release more surface correlated xenon, and higher temperature steps release more volume correlated xenon.

- *Use the size distribution of glasses to determine any compositional dependency on the ratio of surface area to volume.*

Even with a full appreciation of the temperature profile of a sample, which is unknown in these analyses, diffusion of xenon from a sample is also dependent upon the crystal structure, and fractures or vesicles which could act as conduits for deeper gases. A simplified model of the relationship between surface area and volume is much more easily constrained and applicable. This approach is mostly reliant upon how precisely the volume of each sample can be determined, as discussed in Section 4.2.3.

The cautionary approach to stepped heating was chosen to spread the surface and interior correlated xenon between more releases, and as a precaution against the large expected volumes of xenon described in Section 4.2. Each glass released a significant signal over blank in at least one step, and for some this significant release was split over two or three steps. The heating steps with releases which did not confidently exceed blank

may have contained lost sample gas, but are relatively insignificant compared to the total xenon released from each glass, and would not have significantly changed the data. The decreased precision from splitting the larger gas releases over multiple steps compared to one large release is only a problem in the few glasses whose total releases barely exceeded the RELAX detection limit, and an equivalently aggressive approach to stepped heating would have replaced this problem with large volume gas analysis problems (detailed in Section 2.3.2).

Table 4.5 shows that the volume of xenon released and measured from each glass spherule was inconsistent between spherules belonging to the same Apollo subsample. The average concentration of $^{132}$Xe was $1.1 \times 10^{-10}$ cm$^3$ STP g$^{-1}$ and $2.5 \times 10^{-10}$ cm$^3$ STP g$^{-1}$ for the volcanic glasses of 15426,189 and 74220,939, respectively. These concentrations are blow or close to the lower estimates provided in Section 4.2 ($^{132}$Xe of $2 \times 10^{-10}$ cm$^3$ STP g$^{-1}$ < $7 \times 10^{-10}$ cm$^3$ STP g$^{-1}$) using the 74220 glass data of Kirsten et al. (1973). However, the dominant isotope in all but two of the glasses was $^{131}$Xe. The relative depletion in $^{132}$Xe compared to many of the other isotopes which are typically less abundant than $^{132}$Xe in "trapped" xenon reservoirs (as shown by ratios of Table 4.5), and the fact these isotopes often greatly exceeded the blank (as in Table 4.5), suggests non-trapped xenon compositions are dominant within most of the volcanic glasses of 15426 and 74220.

The purely optically classified individual glasses "L" and "Z" of 15426, "H" and "X" of 74220, and both multi-spherule samples contained lower average concentrations of $^{132}$Xe ($5.1 \times 10^{-11}$ cm$^3$ STP g$^{-1}$ and $6.2 \times 10^{-12}$ cm$^3$ STP g$^{-1}$, for 15246 and 74220, respectively) to the EPMA classified glasses ($1.4 \times 10^{-10}$ cm$^3$ STP g$^{-1}$ and $3.9 \times 10^{-10}$ cm$^3$ STP g$^{-1}$, for 15426 and 74220, respectively). Concentrations of $^{131}$Xe in the optically classified glasses were similarly depleted relative to the EPMA classified

glasses, with averages of $8.2 \times 10^{-11}$ $cm^3$ STP $g^{-1}$ and $1.3 \times 10^{-11}$ $cm^3$ STP $g^{-1}$ of $^{131}Xe$ in the optically classified glasses of 15426 and 74220, respectively, and $1.5 \times 10^{-10}$ $cm^3$ STP $g^{-1}$ and $3.2 \times 10^{-10}$ $cm^3$ STP $g^{-1}$ of $^{131}Xe$ in the EPMA classified glasses of 15425 and 74220, respectively.

Figure 4.9 shows that the heavy isotopes of xenon do not indicate the presence of fission xenon in volcanic glasses of 15426 or 74220, and ratios useful for this determination suffer from large uncertainties, especially in the volcanic glasses of 74220. This is consistent with the delta plot in Figure 4.10, which shows a heavy isotope depletion in the volcanic glasses relative to solar wind and $^{131}Xe$, which is itself relatively depleted in the heavy isotopes compared to fission products.

Table 4.5 and Figure 4.10 illustrate that most of the volcanic glasses of both Apollo 15 and 17 featured significant excesses in the light isotopes $^{124}Xe$, $^{126}Xe$ and $^{131}Xe$ relative to “trapped” components such as Q-Xe and solar wind; these suggest the presence of cosmogenic xenon (from spallation of Ba and REE, and neutron capture by $^{130}Ba$). This observation is consistent with the summed isotopic compositions reported in Table 4.5 which shows the heavy xenon isotope concentrations barely exceed the RELAX detection limit, and Figure 4.10 which shows the heavy isotopes are significantly depleted relative to solar wind and $^{131}Xe$. GCR spallation produces lighter xenon isotopes significantly more efficiently than heavy xenon isotopes up to $^{136}Xe$, which is produced in vanishingly small amounts by GCR spallation (as shown in Tables 4.3 and 4.4, and explored in Hohenberg et al. (1981)).

***Table 4.5*** *Xenon isotopic data for individual glass spherules of 15426,189 and 74220,939 normalised to $^{131}Xe \equiv 100$ as measured by RELAX.*

| Sample | Subsample | Heating Steps | $10^{-16}$ cc $^{131}$Xe STP | Xenon Isotopic Compositions Normalised to $^{131}Xe \equiv 100$ | | | | | | | | | | | | | | | |
|---|---|---|---|---|---|---|---|---|---|---|---|---|---|---|---|---|---|---|---|
| | | | | 124 | | 126 | | 128 | | 129 | | 130 | | 132 | | 134 | | 136 | |
| 15426,189 | A | 8 | 48 | 8.0 | (0.14) | 12.7 | (0.17) | 22.1 | (0.17) | 29.0 | (0.28) | 15.9 | (0.14) | 21.6 | (0.25) | 7.5 | (0.14) | 4.4 | (0.12) |
| | B | 4 | 560 | 0.9 | (0.05) | 0.9 | (0.02) | 10.2 | (0.04) | 123.7 | (0.17) | 20.2 | (0.05) | 117.6 | (0.16) | 44.2 | (0.08) | 35.3 | (0.07) |
| | D | 7 | 7.3 | 5.1 | (0.6) | 4.4 | (0.51) | 8.0 | (0.87) | 90.4 | (2.19) | 18.3 | (0.78) | 86.1 | (2.16) | 36.8 | (1.23) | 36.4 | (1.16) |
| | F | 3 | 2.8 | 7.8 | (1.57) | 12.8 | (1.76) | 25.2 | (2.09) | 34.4 | (4.18) | 16.6 | (2.08) | 21.6 | (3.85) | 5.5 | (2.21) | 6.5 | (2.03) |
| | H | 7 | 19 | 5.7 | (0.23) | 10.5 | (0.21) | 18.4 | (0.37) | 31.3 | (0.61) | 13.7 | (0.28) | 25.5 | (0.6) | 8.6 | (0.35) | 6.7 | (0.3) |
| | J | 7 | 12 | 6.0 | (0.28) | 10.3 | (0.32) | 18.0 | (0.5) | 24.4 | (0.86) | 14.3 | (0.42) | 17.9 | (0.84) | 6.3 | (0.49) | 5.6 | (0.43) |
| | L* | 7 | 8.6 | 6.5 | (0.37) | 10.7 | (0.39) | 16.2 | (0.65) | 32.4 | (1.28) | 14.0 | (0.56) | 25.7 | (1.23) | 11.3 | (0.7) | 7.3 | (0.6) |
| | Z* | 6 | 33 | 4.7 | (0.13) | 7.6 | (0.14) | 15.9 | (0.2) | 61.2 | (0.51) | 16.2 | (0.21) | 54.0 | (0.48) | 19.8 | (0.27) | 16.1 | (0.24) |
| | Multi-spherule* | 7 | 160 | 3.0 | (0.03) | 3.9 | (0.06) | 13.1 | (0.06) | 94.7 | (0.23) | 17.9 | (0.08) | 86.1 | (0.22) | 31.5 | (0.11) | 25.6 | (0.1) |
| 74220,939 | A | 2 | 130 | 0.7 | (0.05) | 0.7 | (0.05) | 9.1 | (0.1) | 123.3 | (0.84) | 19.0 | (0.24) | 126.0 | (0.83) | 49.1 | (0.43) | 40.8 | (0.38) |
| | C | 6 | 270 | 7.3 | (1.24) | 15.7 | (1.49) | 22.0 | (3.37) | 42.8 | (4.7) | 32.0 | (2.24) | 51.4 | (4.98) | 22.3 | (3.09) | 7.8 | (2.47) |
| | D | 6 | 13 | 9.4 | (0.33) | 12.5 | (0.39) | 28.2 | (0.54) | 54.1 | (0.93) | 18.0 | (0.46) | 50.4 | (0.92) | 19.2 | (0.53) | 12.8 | (0.48) |
| | F | 6 | 2.4 | 9.5 | (1.43) | 21.6 | (1.51) | 39.9 | (2.66) | 23.4 | (4.62) | 23.1 | (2.01) | 23.2 | (4.16) | 11.5 | (2.56) | 9.4 | (2.22) |
| | H* | 6 | 6.7 | 14.4 | (3.62) | 19.7 | (4.15) | 331.8 | (37.53) | 68.6 | (15.61) | 27.7 | (6.46) | 63.9 | (17.1) | 108.7 | (14.63) | 32.0 | (8.09) |
| | I | 7 | 0.8 | 12.1 | (1.07) | 24.4 | (1.23) | 33.3 | (1.71) | 44.0 | (2.96) | 23.0 | (1.32) | 27.8 | (2.7) | 15.0 | (1.56) | 10.6 | (1.45) |
| | X* | 5 | 3.8 | 11.2 | (2.46) | 18.2 | (2.39) | 13.8 | (3.79) | 33.8 | (7.71) | 42.9 | (3.97) | 26.7 | (7.57) | 13.4 | (4.25) | 19.2 | (4.1) |
| | Multi-spherule* | 7 | 1.4 | 11.8 | (0.9) | 18.4 | (0.85) | 25.2 | (1.33) | 61.5 | (2.77) | 20.3 | (1.14) | 47.2 | (2.57) | 12.5 | (1.36) | 15.6 | (1.28) |
| Impact | G | 7 | 4.4 | 9.3 | (0.67) | 21.7 | (0.83) | 33.8 | (1) | 38.5 | (1.75) | 24.0 | (0.78) | 24.8 | (1.58) | 8.1 | (0.91) | 6.9 | (0.81) |
| RELAX Detection Limit | | | 2.8 | 2.23 | - | 1.74 | - | 28.92 | - | 130.05 | - | 19.22 | - | 129.94 | - | 48.75 | - | 38.65 | - |

*All data are blank corrected. Asterisks denote samples characterised by purely optical means. "Multi-spherule" samples refer to collections of 8 and 7 spherules for the Apollo 15 and 17 samples respectively. Errors in parentheses refer to one σ instrumental counting errors propagated through the normalisation equations. The included impact glass was picked from the 74220,939 sample, all other subsamples are volcanic glasses. RELAX detection limit is concentration and composition of procedural plank plus three standard errors.*

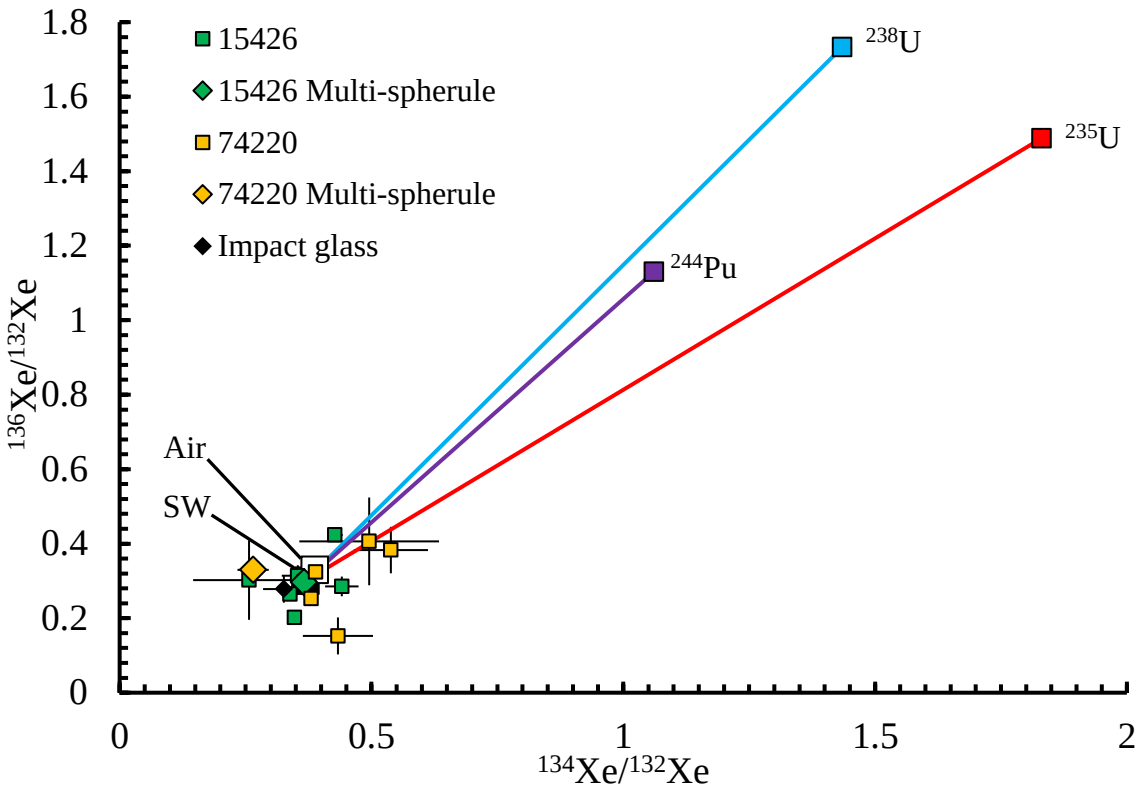


***Figure 4.9*** *Three isotope plot of $^{134}Xe/^{132}Xe$ and $^{136}Xe/^{132}Xe$ for total xenon released from individual glasses of 15426 (green squares), and 74220 (orange squares). Other points: 'multi-spherule' glasses simultaneously analysed in 15426 (green diamond) and 74220 (orange diamond), impact glass of 74220 (black diamond). End members: solar wind (black square), Earth atmosphere (white square). Fission products of $^{235}U$ (red), $^{238}U$ (light blue), and $^{244}Pu$ (purple), plotted with mixing lines from SW. 1σ errors.*

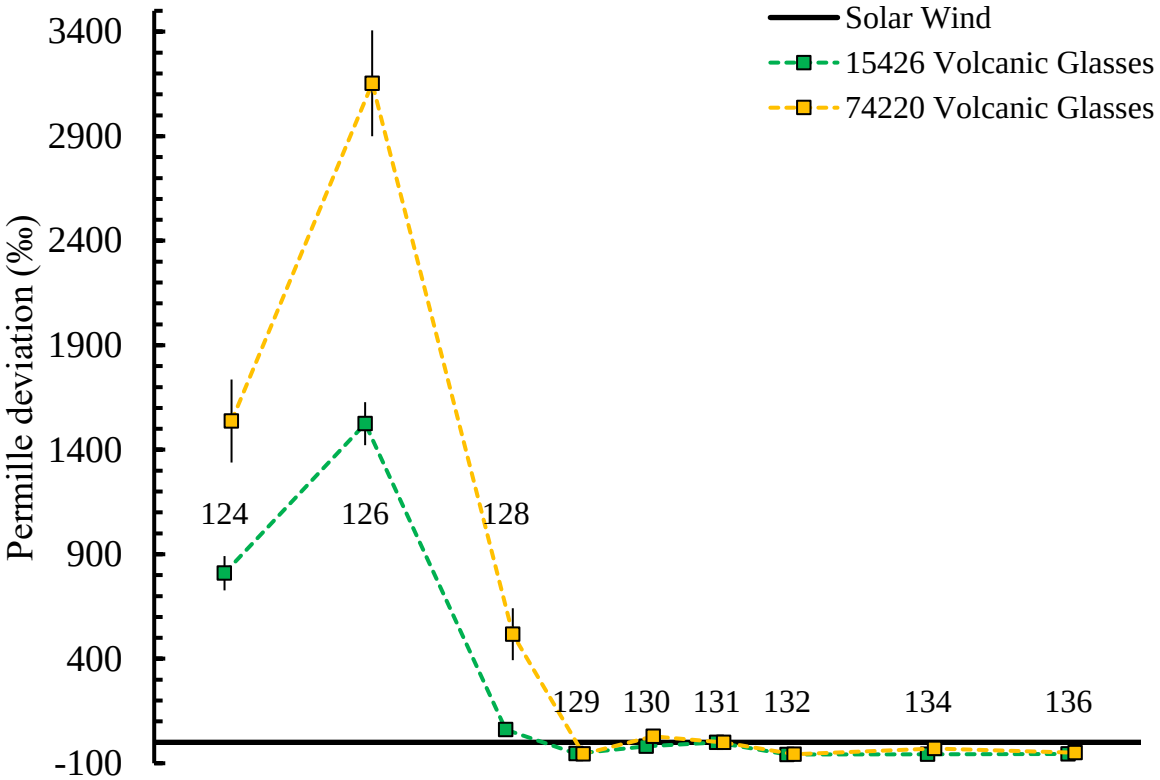


***Figure 4.10*** *Delta plot of average xenon compositions for volcanic glasses of 15426 (green squares/line) and 74220 (orange squares/line) showing permille deviations of isotopic ratios from solar wind (Meshik et al., 2014). Data are normalised to $^{131}Xe$ due to its abundance and subsequent reduction in error propagation. 1σ errors.*

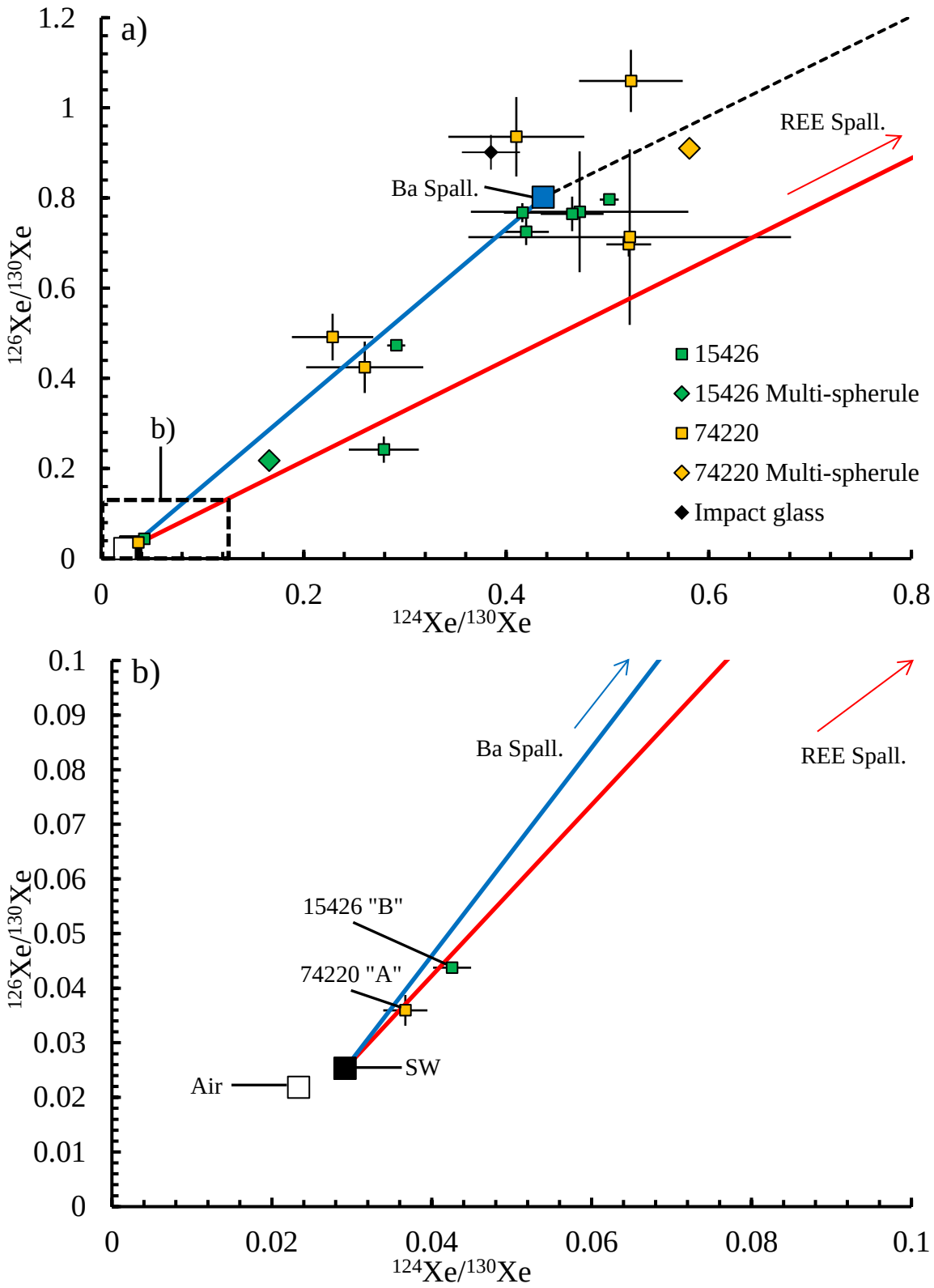


***Figure 4.11*** *Three-isotope plots of $^{124}Xe/^{130}Xe$ (abscissa) and $^{126}Xe/^{130}Xe$ (ordinate) for total xenon released from individual glasses of 15426 (green squares), and 74220 (orange squares). Inset b) focuses on "trapped" gas-rich glasses 15426 "B" and 74220 "A" by expanding dashed box labelled "b)" in figure a). Other points: 'multi-spherule' collections of glasses simultaneously analysed in 15426,189 (green diamond) and 74220,939 (orange diamond), the impact glass of 74220 (black diamond) and potential end members: solar wind (black square), Earth's atmosphere (white square), and spallation components for Ba (blue square and mixing line from SW) and REE (red mixing line from SW, end member composition plots outside range of figure, $^{124}Xe/^{130}Xe$ = 22, $^{126}Xe/^{130}Xe$ = 25). Dashed black line indicates mixing line between Ba and REE end members. Error bars represent 1σ.*

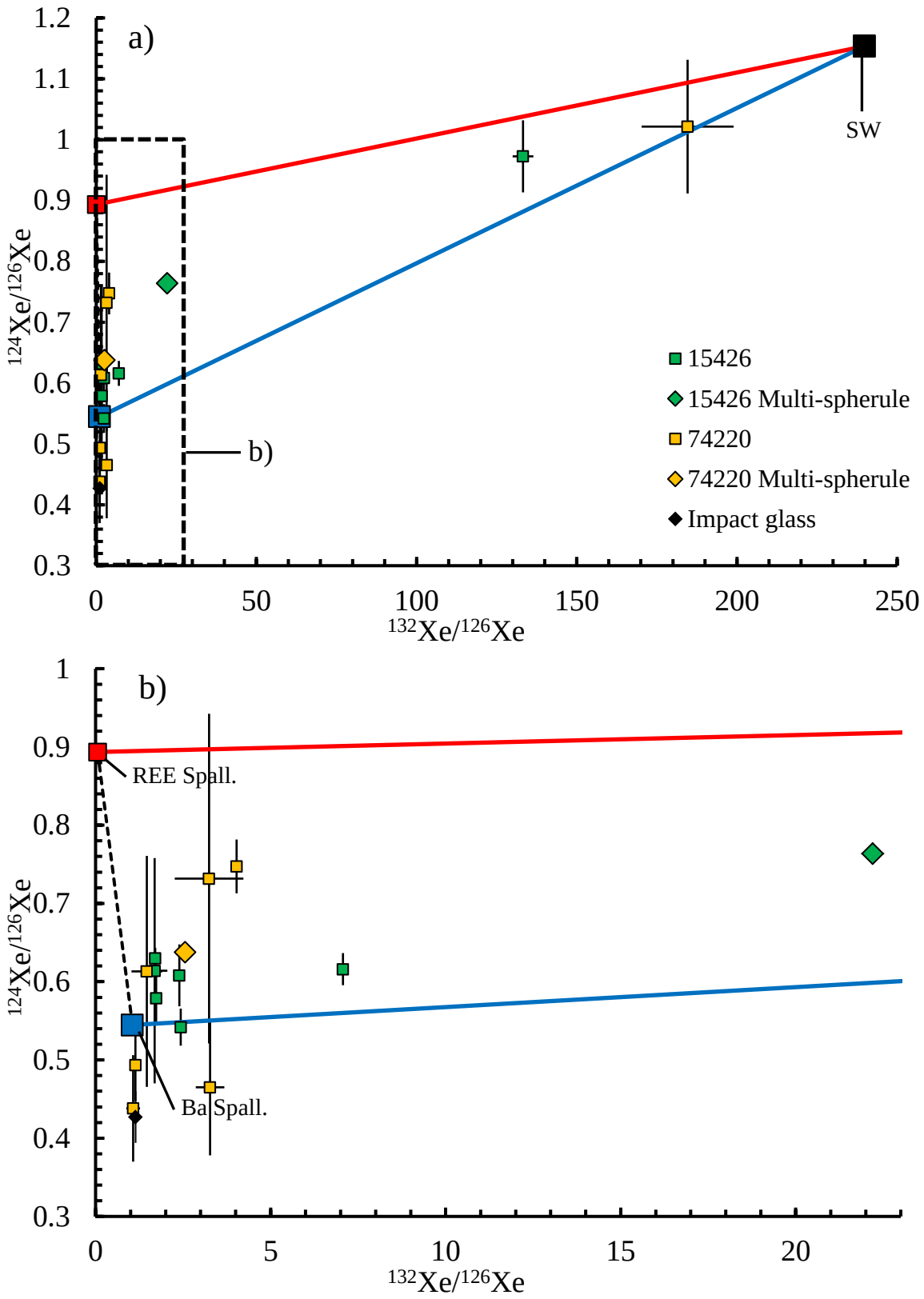


***Figure 4.12*** *Three-isotope plots of $^{132}Xe/^{126}Xe$ (abscissa) and $^{124}Xe/^{126}Xe$ (ordinate) for total xenon released from individual glasses of 15426 (green squares), and 74220 (orange squares). Inset b) focuses on glasses rich in spallation components by expanding dashed box labelled "b)" in figure a). Other points: 'multi-spherule' collections of glasses simultaneously analysed in 15426,189 (green diamond) and 74220,939 (orange diamond), the impact glass of 74220 (black diamond) and potential end members: solar wind (black square), and spallation components for Ba (blue square and mixing line from SW) and REE (red mixing line from SW. Dashed black line indicates mixing line between Ba and REE end members. Error bars represent 1σ.*

Figure 4.11 is a three-isotope plot of the volcanic glasses of Apollo 15 and 17 distinguishing the REE or Ba origin of a GCR spallation component (Hohenberg et al., 1981). The isotopes $^{124}$Xe and $^{126}$Xe are produced in characteristic proportions in each spallation component (as illustrated in Table 4.4 and Hohenberg et al., 1981). The choice of denominator in these plots is based upon its signal (larger abundance generally resulting in lower uncertainties) and provenance within the xenon reservoirs and compositions in question. In this case, $^{130}$Xe is selected as its combination with the more abundantly produced cosmogenic isotopes ($^{124}$Xe and $^{126}$Xe) provides a clear distinction between the two spallation components, with minimal interference from depth dependent isotopic effects.

Figure 4.11 and Figure 4.12 exhibit the xenon isotopic compositions indicative of spallation components for the volcanic glasses of 15426 and 74220. The releases generally lie on a mixing line between "trapped" xenon (solar wind and/or Earth atmosphere) and cosmogenic isotopes more closely resembling GCR spallation of Ba instead of REE. Most of the volcanic glasses of both 15426 and 74220 contain xenon dominated or solely composed of the Ba spallation component, as shown by their proximity to the 'pure' Ba spallation composition. Many of the 74220 glasses (and a couple of the 15426 glasses) plot multiple standard deviations aware from the pure Ba spallation end member, or the mixing lines between Ba spallation and solar wind. These compositions are unlikely to indicate a minor contribution from REE spallation due to it featuring significantly higher ratios of $^{126}$Xe/$^{130}$Xe = 22 and $^{126}$Xe/$^{130}$Xe = 25, and $^{124/126}$Xe as shown in Figure 4.12. The scatter could be the product of the different production rates of certain isotopes at different shielding depths, as shown in Figure 4.13, Figure 4.16, and Figure 4.17. Despite the scatter, the glasses of both 15426 and 74220 clearly illustrate the GCR spallation is most likely to be Ba-derived.

Excesses in $^{124}$Xe, $^{126}$Xe, and $^{131}$Xe, and the apparent dominance of a Ba spallation composition in Figure 4.10, Figure 4.11, Figure 4.12, and Table 4.5 indicate a significant cosmogenic contribution to the xenon composition. Figure 4.13 includes the burial depth sensitive isotope $^{131}$Xe in a three-isotope plot, whose excess is potentially indicative of burial depth. $^{131}$Xe is produced by primary interactions of target elements with GCRs and also secondary neutron capture by $^{130}$Ba. Secondary neutron capture varies as a function of depth due to its reliance upon GCR sputtering of shallower atoms creating a shower of liberated neutrons. For atoms at the surface, there is a relatively tiny density of atoms above them to provide a source of sputtered neutrons, so the neutron flux is significantly lower. The secondary neutron production and capture (and by extension its role in $^{131}$Xe production) increases with depth from the surface and then tails off at greater depths (as shown in Figure 4.16). This depth-dependent production rate of $^{131}$Xe, by comparison to the primary GCR-produced $^{126}$Xe (which Figure 4.16 exhibits a simple decay in production rate with depth), can be exploited to determine a 'shielding depth' indicating the depth at which the production rate of $^{131}$Xe/$^{126}$Xe matches the observed ratio (as in Figure 4.17) (Eberhardt et al., 1971; Hohenberg et al., 1981), elucidated in Section 4.4.3.

Figure 4.13 illustrates an excess of $^{131}$Xe exhibited by many of the volcanic glasses of 15426 plotting below the mixing line between SW and Ba spallation on the surface (denoted by "surface" at end of black arrow). The identical plot for the volcanic glasses of 74220 shows their residence on the mixing line between primary GCR spallation products of Ba and solar wind, with no apparent excess in $^{131}$Xe. Figures 4.9 and 4.13 also exhibit one of the volcanic glasses of 74220 containing xenon resembling Earth's atmospheric composition. Given the similar composition and therefore location of SW and Earth's atmospheric xenon on the $^{124}$Xe/$^{131}$Xe and $^{132}$Xe/$^{131}$Xe plots, the other samples may just as easily reside on a mixing line between Ba spallation and a "normal" composition resembling Earth's atmosphere instead of SW.

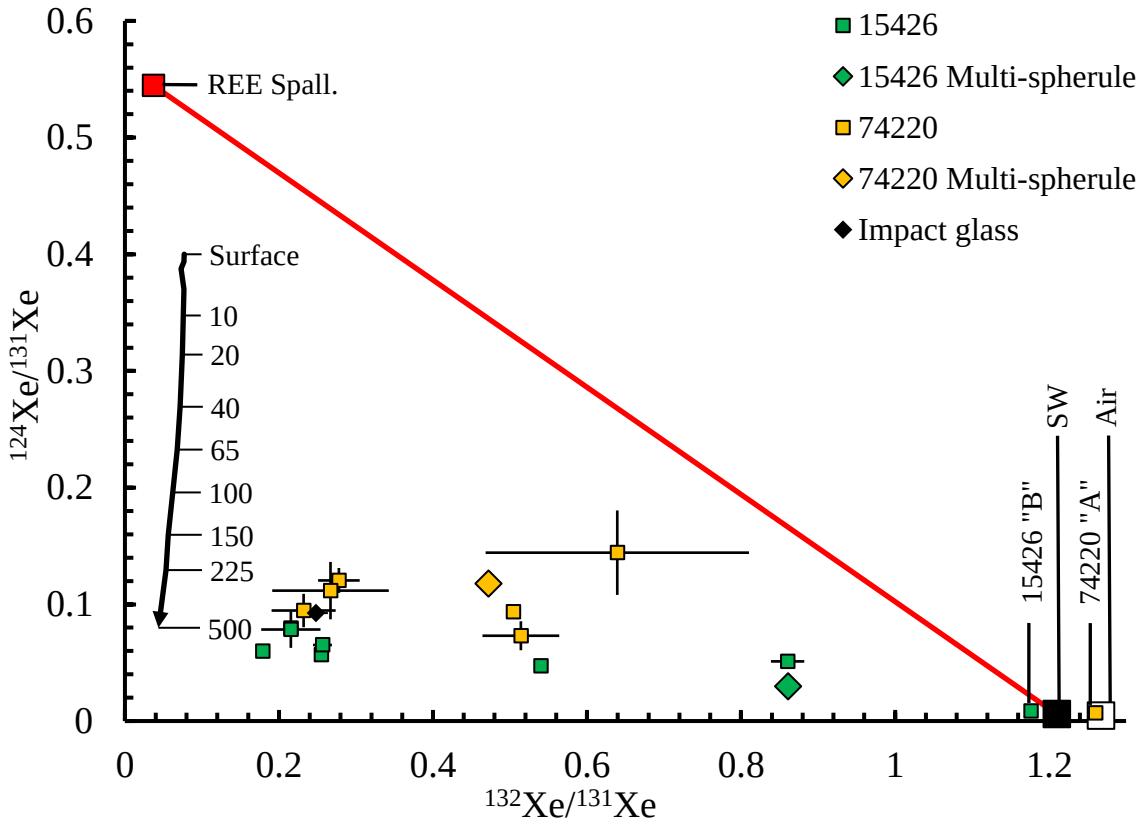


***Figure 4.13*** *Three-isotope plot of $^{124}Xe/^{131}Xe$ and $^{132}Xe/^{131}Xe$ for total xenon released from individual glasses of 15426 (green squares), and 74220 (orange squares). Ba spallation plotted as arrow to show isotopic composition dependence upon burial depth (in g/cm$^2$, labelled on figure). Other points: 'multi-spherule' collections of glasses simultaneously analysed for 15426 (green diamond) and 74220 (orange diamond), the impact glass (black diamond). Potential end members: solar wind (black square), Earth's atmosphere (white square), REE spallation (red square and mixing line from SW). 1σ error bars plotted for all points, most are too small to be seen at this scale.*

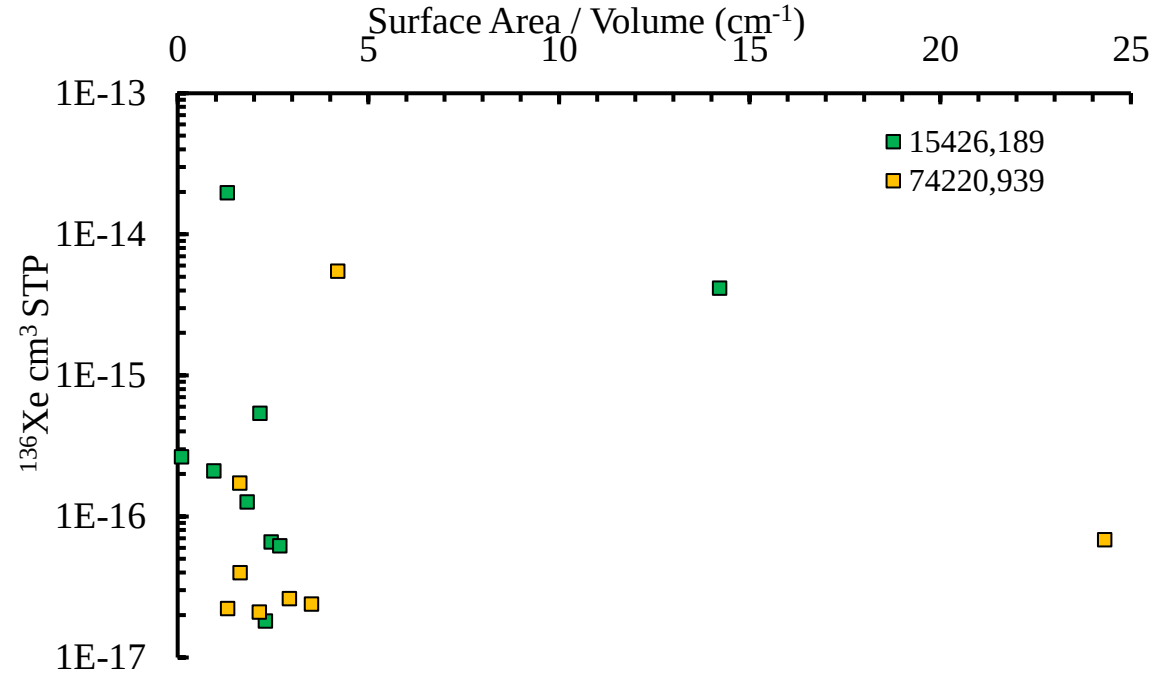


***Figure 4.14*** *Total $^{136}Xe$ xenon atoms (logarithmically plotted in number of atoms as ordinate) and surface area to volume ratio (as $cm^{-1}$ as abscissa, corrected for volume and surface area lost to polishing) in volcanic glasses of 15426 (green squares) and 74220 (orange squares). Errors (not plotted) are discussed in section 4.2.3.*

Figure 4.14 compares the total number of $^{136}Xe$ atoms confidently exceeding the blank extracted from each volcanic glass along with the respective surface area to volume ratio. $^{136}Xe$ is not produced by GCR spallation or secondary neutron capture, and does not appear to be present as the product of fission in these samples, so is assumed as a proxy for solar wind. Given the implantation of solar wind xenon is expected to be strongly surface-correlated, its concentration should express a positive correlation with an increased surface area/volume ratio. The data presented in this work generally plot within the same region of the chart, mainly due to the selection method favouring glasses of similar sizes, so no clear correlation is observed.

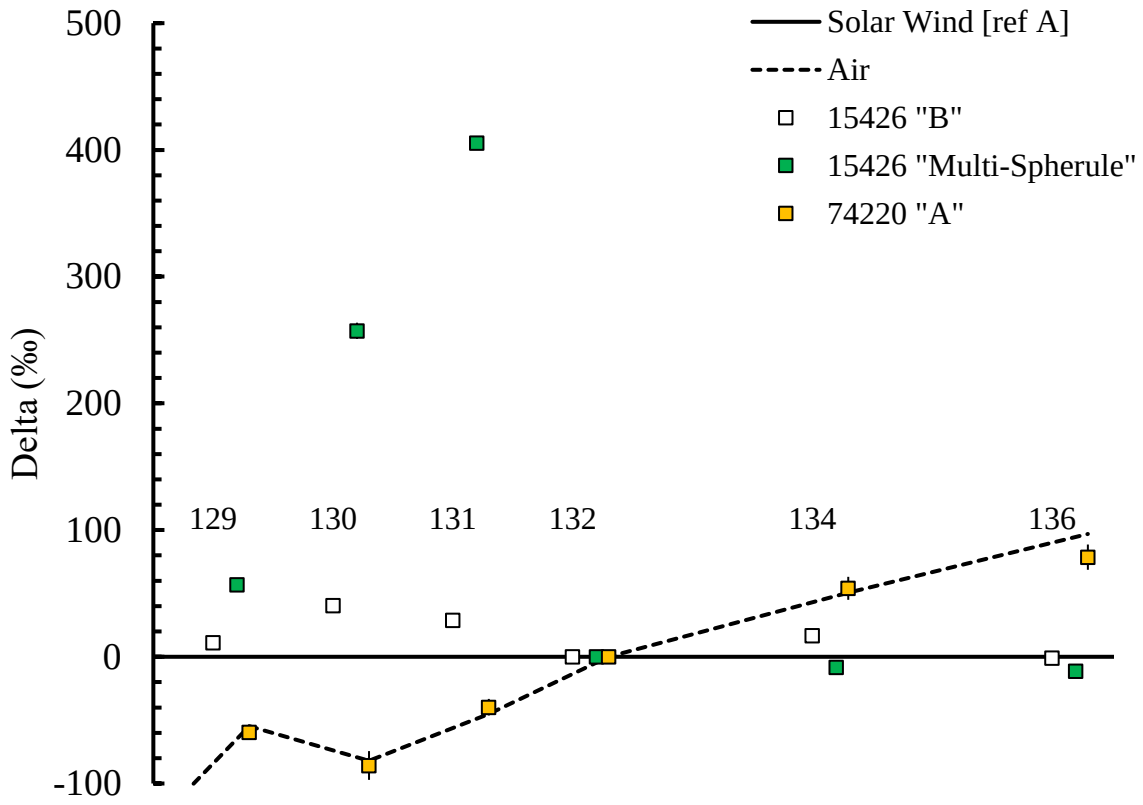


***Figure 4.15*** *Delta plot of xenon isotopes in glasses (15426 "B" – white squares, 15426 "Multi-Spherule" – green squares, and 74220 "A" – orange squares) containing most "trapped" xenon compositions with respect to solar wind (black line, abscissa). Permille deviations of air (dotted black line) from solar wind are also plotted for reference. Note the large excesses in isotopes sensitive to cosmogenic production for 15426 "Multi-Spherule".*

Some of the glasses appeared to contain a trapped component, roughly indicated by the $^{132}$Xe signal being multiple factors above the blank. These samples, 15426 “B”, 15426 “multi-spherule”, and 74220 “A”, are the ones which plotted closer to the trapped components in most of the figures (although notably in Figure 4.11 and Figure 4.13). Figure 4.15 shows a delta plot of the xenon isotopes measured from these samples as permille deviations from solar wind xenon, along with the deviation of Earth’s atmospheric xenon from solar. Light isotopes $^{124}$Xe, $^{126}$Xe, and $^{128}$Xe are excluded due to their significant cosmogenic excesses (illustrated in the other delta plot in Figure 4.10). Even in these samples, which constitute the highest concentrations of “trapped” xenon, the composition is clearly affected by cosmogenically produced isotopes, as illustrated in the excesses of $^{129}$Xe, $^{130}$Xe, $^{131}$Xe, and the lighter isotopes (not plotted), for the 15426 “B” and “multi-spherule” glasses at least.

The heavy isotopes which are significantly less affected by cosmogenic production plot close to solar wind for 15426 “B” and “multi-spherule” and atmospheric xenon for 74220 “A”. In Figure 4.15 the 74220 “A” glass xenon composition appears to very closely match the composition of Earth’s atmospheric xenon for all plotted isotopes, even those sensitive to cosmogenic production. Possible explanations for this composition are considered in Section 4.5.2.

### 4.4.3. Exposure age

The positive identification of cosmogenic xenon allows determination of galactic cosmic ray exposure histories of both sets of glasses. The exposure age calculations were made in accordance with the work of Hohenberg et al. (1981), defined as follows:

$$Exposure\ age\ (Ma) = \frac{^{126}Xe_{Spall}}{P_B([Ba] + P_R/P_B[La + Ce + Nd])}$$

***Equation 4.1*** *Cosmic ray exposure age calculation according to Hohenberg et al. (1981), where $^{126}Xe_{Spall}$ is the amount (in $cm^3$ STP $g^{-1}$) of $^{126}Xe$ attributable to spallation of Ba, La, Ce, and Nd (in g/g concentration). $P_R$ and $P_B$ are production rates of REE and Ba, respectively, explained in more detail in the original publication.*

The green lunar glasses of Apollo 15 typically exhibit rare Earth element abundances enriched by a factor of 4.5 compared to chondritic, yet have similar relative abundances to chondrites excluding europium, which is depleted (Ridley et al., 1973; Chou et al., 1975; Delano, 1986; Galbreath et al., 1990). Apollo 17 glasses also exhibit a similarly enriched chondritic relative abundance of rare Earth elements (Philpotts et al., 1974; Hughes et al., 1990). The present work did not include measuring the abundances of rare Earth elements (REE), yet the EPMA data and visual categorisation is sufficient to suggest green and orange glasses belong to the same suite of volcanic glasses which exhibit such reproducible REE abundances in previous works. The weighted 70 spherule average rare Earth element abundances of Galbreath et al. (1990) are assumed for our Apollo 15 green glasses, and a weighted average for 60 µg of orange glasses of 74220 reported by Hughes et al. (1990). This work takes a similar approach to Ba in each sample, for which EPMA is insufficiently precise for use in the cosmic ray exposure age calculation.

Spallation target elements of concern to xenon analysis (Ba, La, Ce, and Nd) assumed for this work are presented in Table 4.6, as measured by previous volcanic glass ion microprobe work.

***Table 4.6*** *Measured/Published oxide data and inferred spallation element concentrations.*

| Oxides & Elements | | Apollo 15 Green Glasses | | Apollo 17 Orange Glasses | |
|---|---|---|---|---|---|
| | | Ref [a] | This work | Ref [b] | This work |
| Oxides (wt. %) | $SiO_2$ | 45.6 | 43.0 | 39.1 | 46.2 |
| | $TiO_2$ | 0.42 | 4.94 | 9.1 | 0.4 |
| | $Al_2O_3$ | 7.5 | 6.6 | 6.2 | 7.1 |
| | FeO | 19.5 | 20.2 | 22.6 | 19.8 |
| | MnO | 0.29 | 0.26 | 0.28 | 0.26 |
| | MgO | 17.9 | 16.5 | 13.9 | 17.4 |
| | CaO | 8.3 | 7.6 | 7.8 | 8.1 |
| | $Na_2O$ | 0.15 | 0.25 | 0.44 | 0.12 |
| | $K_2O$ | n.d | 0.04 | 0.07 | 0.01 |
| Spallation Elements (ppm) | Ba | 13 | n.d | 99 | n.d |
| | La | 1.2 | n.m | 5.7 | n.m |
| | Ce | 3.1 | n.m | 16.6 | n.m |
| | Nd | 1.7 | n.m | 16.7 | n.m |

*Refs: [a] Galbreath et al. (1990), data is weighted average of 70 glasses [b] Hughes et al. (1990) data is weighted average of 60 µg of glasses. Oxide data all collected by EPMA, and spallation element data by ion probe [a], INAA [b], or attempted with EPMA for Ba in this work. n.d indicates 'not detected' and n.m 'not measured'. Spallation element data are assumed for the corresponding glasses of this work. Oxide data reported for this figure are normalised to total % ≡ 100 to more closely correspond to published data.*

A purely spallation-attributable count of atoms of $^{126}Xe$, 'spallation $^{126}Xe$', was determined under the assumption that the volcanic glasses represent a simple two-component mixture of solar wind and spallation xenon, on the assumption that all $^{136}Xe$ can be attributed to solar wind as it is barely produced by the interaction of galactic

cosmic rays with barium or REE. The subsequent values for purely spallogenic $^{126}Xe$ are presented in Table 4.7 along with the exposure ages without shielding.

2π large celestial body irradiation geometry corrections are applied to all of the production rates used in these calculations according to Hohenberg et al. (1978). This correction essentially models the lunar surface as plane of infinite thickness, and is frequently used in lunar surface GCR exposure modelling (Hohenberg et al., 1978; Leya et al., 2001; Fernandes et al., 2013; Mahajan, 2015). The resultant flux of GCR particles is reduced by a factor of 2π.

***Table 4.7*** *Exposure ages of 15426 and 74220 volcanic glasses with no shielding.*

| Sample | Subsample | Mass (μg) | Spall $^{126}Xe$ ($10^{-12}$ $cm^3$ STP/g) | Exposure Age (Ma) | Burial Depth (g/$cm^2$) |
|---|---|---|---|---|---|
| 15426,189 | A | 263.9 | 2.3 | 490 (49) | - |
| | B | 82 | 2.7 | 570 (67) | 405 |
| | D | 26.7 | 1.1 | 227 (37) | - |
| | F | 16.2 | 2.2 | 466 (77) | 318 |
| | H | 29.5 | 6.6 | 1407 (143) | 456 |
| | J | 12.2 | 9.9 | 2113 (221) | 490 |
| | L* | 17.8 | 5.1 | 1081 (114) | 425 |
| | Z* | 35.1 | 7.1 | 1508 (153) | 423 |
| | Multi-Spherule* | 157 | 3.6 | 777 (79) | 502 |
| 74220,939 | A | 8.7 | 1.8 | 51.6 (25) | - |
| | C | 20.1 | 2.1 | 60.3 (8) | 187 |
| | D | 68.8 | 2.4 | 70.1 (7) | 206 |
| | F | 188.6 | 0.3 | 7.8 (1) | 77 |
| | H* | 4.5 | 3.2 | 92 (19) | - |
| | I | 17.1 | 5.3 | 155 (17) | 45 |
| | X* | 13.8 | 1.8 | 51.1 (8) | 29 |
| | Multi-Spherule* | 37.2 | 2.1 | 62.3 (7) | 58 |

*Masses (μg), spallation derived $^{126}Xe$ concentration ($10^{-12}$ $cm^3$ STP $g^{-1}$), and exposure ages (in Ma) for individual volcanic glasses of 15426 and 74220, and 'multi-spherule' collections. All values corrected for 2π irradiation geometry. REE and Ba data used in calculation were inferred from Table 4.6, and the production rates of Hohenberg et al. (1981). Errors in parentheses indicate one standard deviation. Burial depths inferred from $^{131}Xe/^{126}Xe$ production rates with changing depth from Hohenberg et al. (1978). Missing values correspond to ratios or depths for which the data are not reliable.*

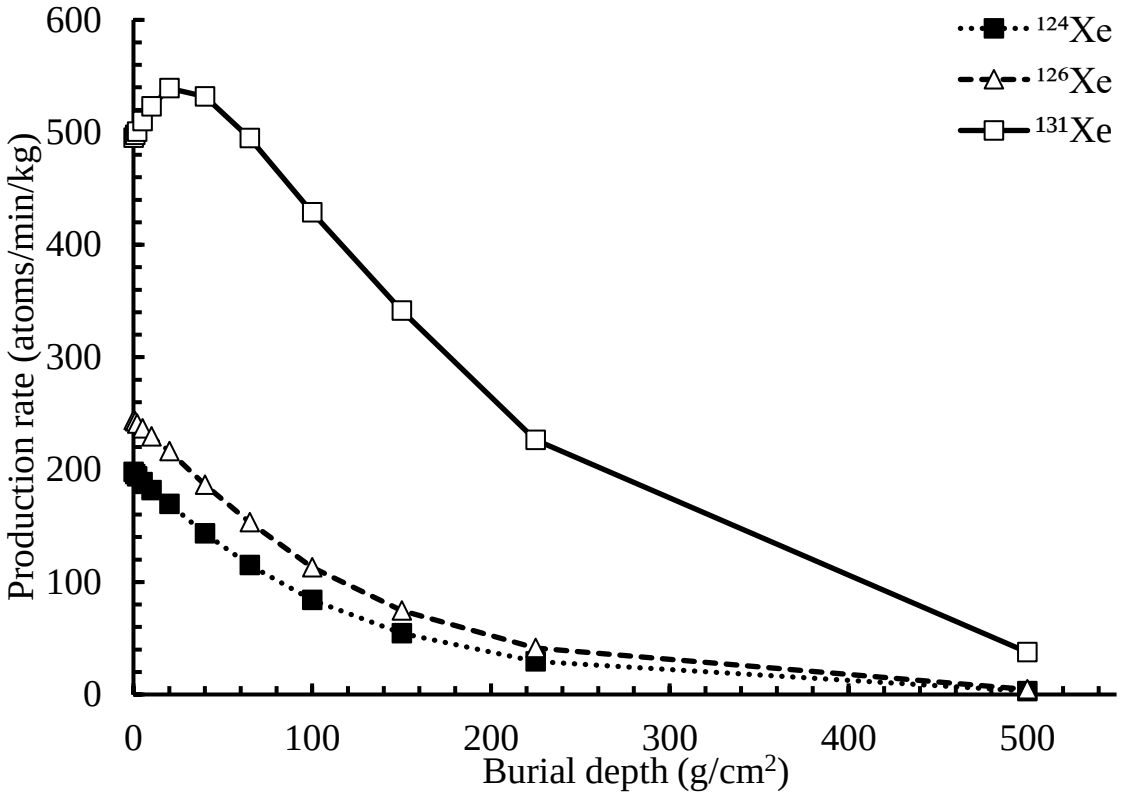


***Figure 4.16*** *GCR and secondary neutron production rates of xenon isotopes of amus 124 (black squares/dotted line), 126 (open triangles/dashed line), and 131 (open squares/solid line) in atoms/min/kg relative to burial depth in g/cm$^2$ from Hohenberg et al. (1978).*

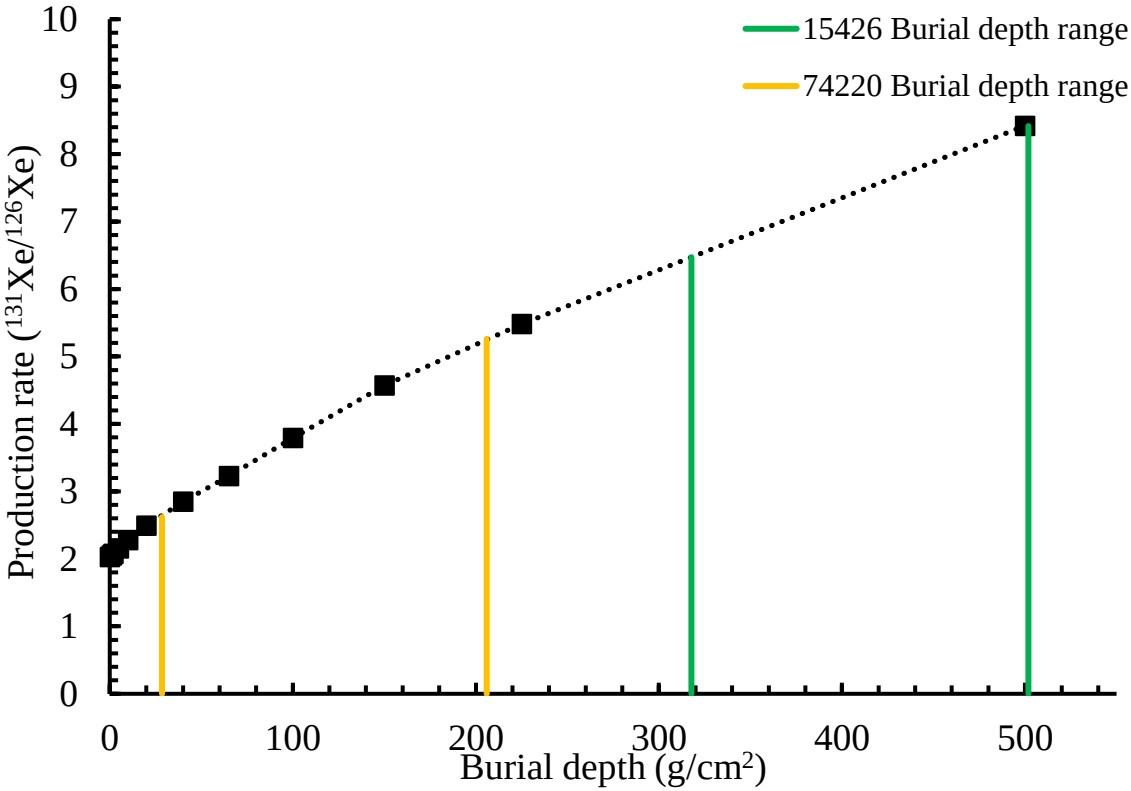


***Figure 4.17*** *Cosmogenic xenon measured in volcanic glasses of 15426 and 74220 plotted on curve of $^{131}Xe/^{126}Xe$ production rate ratio (ordinate) as a function of burial depth (abscissa, in g/cm$^2$). Burial depth ranges for measured glasses of 15426 (between two green lines) and 74220 (between two orange lines) are shown by lines indicating the maximum and minimum measured values. Modelled data (black squares/dotted line) adapted from Hohenberg et al. (1978). Glass-specific data are presented in Table 4.7.*

Table 4.7 also contains the calculated shielding/burial depths for cosmogenic isotope production inferred from modelled production rates of $^{131}Xe/^{126}Xe$ as a function of depth. Apollo 15 glasses tend to cluster around 400 g/cm$^2$ ($\sigma$ = 56). Apollo 17 glasses exhibit a much more variable shielding depth, with some glasses containing cosmogenic compositions corresponding to no shielding, and others ~ 200 g/cm$^2$.

***Table 4.8*** *Solar wind exposure ages relative to GCR exposure ages and calculated shielding depths for two samples with assumed solar wind xenon composition.*

| Sample | GCR exposure age (Myr) | SW exposure age using $^{132}Xe$ (Myr) | SW exposure age using $^{136}Xe$ (Myr) | Calculated shielding depth (g/cm$^2$) |
|---|---|---|---|---|
| 15426 "B" | 570 | $2.02 \times 10^{-4}$ | $2.04 \times 10^{-4}$ | 407 |
| 15426 "Multi-spherule" | 777 | $2.93 \times 10^{-6}$ | $2.93 \times 10^{-6}$ | 500 |

*Fluxes of solar wind $^{132}Xe$ and $^{136}Xe$ are taken from Crowther and Gilmour (2013)*

A different type of surface exposure can be determined using the flux of solar wind particles to the lunar surface. Assuming all $^{132}Xe$ in the glasses with the most "trapped" xenon compositions (15426 "B" and 15426 "Multi-spherule") is attributable to solar wind (excluding 74220 "A", which resembles Earth's atmospheric composition), Table 4.8 contains the corresponding surface exposure ages. These ages were calculated according to the glass cross sections and the solar wind particle flux of Crowther and Gilmour (2013). Ages considering the flux of solar wind $^{136}Xe$ are also included to further discount the contribution from cosmogenic sources (which are clearly also present in 15426 "multi-spherule", as shown in the lighter isotopes of Figure 4.15). The solar wind exposure ages are significantly lower than the cosmogenic exposure ages, suggesting their residence on the surface was brief, or the samples have lost solar wind xenon somehow. Shielding depths are consistent with the glasses having resided at depth while their cosmogenic xenon was produced.

## 4.5. Discussion

### 4.5.1. EPMA data

Despite the precision of the microprobe data being insufficient for confident grouping of the volcanic glasses of Apollo 15 or 17, the combined geochemical and optical data gathered for the analysed samples allowed us to confidently identify the volcanic or impact origin of the analysed spherules according to the criteria detailed in Section 4.2.3 and the data presented in Section 4.4.1.

The variable oxide totals (> 84.9%) of the EPMA data reported in this work would be concerning if these data were to be used in isolation, and may be attributed to any combination of a number of factors. The fact that beam parameters and the choice of elements to measure in this work was based on previous major element analyses of impact and volcanic glasses of similar sizes and provenance (Delano, 1986; Galbreath et al., 1990; Hughes et al., 1990; Zellner et al., 2002, 2009; Delano et al., 2007) which provided near 100% totals suggests the < 100% total percentages of this work are not likely to represent an element which was not measured.

The poor totals of some of the glasses may be due to excitation of the superglue below the surface of the samples, a consequence of poor polish limiting spot analyses to areas where the sample was especially thin or close to the sample and superglue boundary. If we assume the maximum modelled electron beam penetration depth of Goldstein et al. (2003) as about ten microns, and the smallest diameter glass analysed by EPMA in this work (“H” of 74220 in Table 4.1) as 1.8 mm (or 1800 microns), the sample is significantly thicker than the beam can penetrate. Even if we assume the sample were two orders of magnitude less thick at the edge of the sample, the maximum electron penetration depth

would still not exceed the sample thickness. This is despite our samples featuring a higher target density (basaltic glass compared to their carbon) and lower beam energy (15 KeV compared to their 20 KeV) than the maximum penetration depth of Goldstein et al. (2003). Additionally, the majority of X-rays are still produced at smaller depths than the maximum electron penetration range, and this phenomenon is not observed in any of the existing probe literature on equally small volcanic glasses.

The most likely cause of the poor oxide totals is that the samples were not sufficiently flat for probe analysis. Movement of the samples within the superglue during polishing, presumably due to its softness relative to epoxy (upon which the polishing techniques are usually employed), was suspected during sample preparation and confirmed with the probe's topographic electron microscope setting. Some samples were polished a second time, with a greater attention to improved polishing technique and higher standards of completion, in an attempt to improve the flatness of the surface onto which the EPMA electron beam would be incident. Comparing the analyses of the particularly rounded samples (15426, "C" and "D") from which data were extracted before and after repolishing reveals that the totals barely improved (~ 2.5% in the case of 15426 "D") or worsened (~ 4.5% in the case of 15426 "C"). Some of this fluctuation is presumably a consequence of internal heterogeneity within each sample, and potentially the mobilisation of the more volatile elements under prolonged electron beam incidence. However, the poor totals of the remaining and repolished samples indicate a broader material issue with the use of superglue in sample preparation, and should be considered by those interested in using a similar mounting medium. Unfortunately, repeat backscatter images of repolished samples were not taken, so evidence that repolishing changed the quality of the polish is only available indirectly as total oxide totals.

A relatively insignificant degree of oxide total variability can be attributed to instrumental flux, as exhibited by the standards during the two periods of analysis. For example, A99 featured an average total of 99.1% ± 0.51%, and VG2 an average total of 99.2% ± 0.72%. These data are clearly of a better quality to the Apollo glass sample analyses, as is to be expected of standards whose flatness and homogeneity are relied upon. It would be reasonable to assume that similarly orthodox preparation of Apollo 15 and 17 volcanic glass candidates could have returned similarly precise oxide totals, allowing the glasses to be attributed to specific compositional groups. However, without multiple analyses, such a pursuit assumes the glasses within each sample are of consistent provenance. Any meaningful major element classification would have required similarly large and pristine glasses to those earmarked for xenon analysis, which would then be made unsuitable for xenon measurement in RELAX, thus detracting from the focus of this work.

### 4.5.2. Xenon data

Attempts to optimise gas release and beam power from sample to sample in this work were not successful, as cautious stepped heating actually resulted in unnecessary separation of aliquots of gas which could have been analysed singularly with no analytical repercussions (e.g., reduced relative blank contribution and a lowered risk of saturation, explored in Section 2.3.2). The data are subsequently spread out between more heating steps than was desired, as resolving an interior and surficial component was given precedence over the statistical benefits of a larger signal/noise ratio at the risk of saturation. The xenon contained in the glasses is subsequently best considered in terms of the total atoms of each isotope measured in each heating step which confidently exceeded the blank. This technique rendered the typical method of deconvolution of interior and exterior xenon by power impossible, so it instead had to rely upon geometrical

relationships (surface area vs volume, with its own set of uncertainties outlined in Section 4.2.3 and employed in Section 4.4.3).

The possible mobilisation of xenon by electron beam exposure in the samples characterised by EPMA (explained in Section 4.3.2) should be evident as a decreased xenon concentration when compared to the optically classified glasses, but no effect is observed. The optically classified glasses actually contain lower average concentrations of $^{131}$Xe and $^{132}$Xe in both 15426 and 74420, when compared to the EPMA classified glasses. These results confirm that xenon mobilisation by electron beam exposure in lunar volcanic glasses is negligible in this application, but such an effect could be more apparent in samples featuring a more consistent distribution of xenon concentrations.

The large isotopic excesses of $^{124}$Xe, $^{126}$Xe, and $^{131}$Xe in all but two of the volcanic glasses (subsamples ‘A’ and ‘B’ of 74220), and most of the three-isotopic plots suggest the dominant presence of a cosmogenic xenon composition over any known “trapped” composition or fission. Determination of the nature of a contained “trapped” or fission xenon composition was especially difficult given the low concentrations of xenon isotopes outside of those directly attributable to spallation. The heavy isotopes suffered from a poor enough resolution that their origin, or existence is hard to justify in the volcanic glasses analysed in these samples. Attempts to deconvolute the mixtures by using the Automaton program also suffered from these low concentrations and spallation dominance. Use of the isotopes featuring better precision for the modelling, $^{124}$Xe, $^{126}$Xe, and $^{131}$Xe, were so dominated by spallation that the solutions struggled to resolve any other components.

The three most “trapped” xenon-rich volcanic glasses, “B” and “multi-spherule” of 15426, and “A” of 74220 are outliers amongst their fellow volcanic glasses, which are too depleted in isotopes useful for “trapped” xenon determination to provide any bearing on

the nature or even presence of a trapped, “trapped” composition. The “trapped” xenon-rich glasses (15426 “B”, and 15426 “Multi-spherule”) plot close to solar wind xenon, as would be expected of materials which once resided on the lunar surface. The xenon in glass “A” of 74220 closely resembling Earth’s atmospheric composition is unique within these data. It is unlikely that this could be an indigenous composition to the moon, given the unique mixture and fractionation it is the product of (discussed in depth in Chapter 3), and the fact no other glasses share similar compositions. It is most likely a consequence of the incomplete removal of superglue.

The volcanic glasses of 15426 and 74220 analysed in this work do not contain evidence of trapped xenon resembling fission products or an obvious indigenous lunar xenon composition from the lunar interior or transient atmosphere. The volcanic glasses in this work share similarities with other bulk samples containing fission xenon excesses collected near Shorty crater (Eugster, 1985), and fission argon excesses in lunar meteorites of similar age (Fernandes et al., 2004). The glasses were also all erupted in a volatile-rich environment, in gas-charged eruptions (Heiken et al., 1974; Meyer et al., 1975; Delano, 1986), into a temporal atmosphere the glasses are likely to have quenched within (Needham and Kring, 2017; Saxena et al., 2017; Hui et al., 2018), and feature volatiles trapped within and sublimed onto their surfaces (Heiken et al., 1974; Delano and Lindsley, 1983; Barraclough and Marti, 1985). One may expect to find an indigenous xenon composition dissolved within the melt precursor to the glasses, trapped within vesicles, or adsorbed and trapped within the volatiles on the surface of the glasses. Given these criteria, why is there no evidence of a retained indigenous xenon signature from either the lunar interior or transient atmosphere in the volcanic glasses?

A scenario in which there was no xenon dissolved in the melt precursor to the glasses, or within the transient atmosphere the glasses quenched within, is unlikely given

the volatiles (including light noble gases) present in the vesicles within the glasses and quenched onto the glass surfaces (Heiken et al., 1974; Delano and Lindsley, 1983; Barraclough and Marti, 1985), and the fission excesses in xenon and argon samples of similar provenance (Eugster, 1985; Fernandes et al., 2004). If the melt from which the glasses originated, or the temporal atmosphere produced by the eruptions did not contain xenon, the processes which caused it would have to selectively remove xenon and not the other volatiles.

Assuming an indigenous xenon component was present in the melt precursor to the glasses, or within the transient atmosphere in which the glasses quenched, could this xenon have diffused out of the glasses after eruption? There is a lack of petrologic evidence in the glasses suggesting significant heating or shock since eruption (Delano, 1986), and volatiles on the glass surfaces and within vesicles (Meyer et al., 1975; Butler and Meyer, 1976), including lighter noble gases (Barraclough and Marti, 1985), are unlikely to have been retained in conditions which could remove trapped xenon. This scenario also contradicts the presence of trapped spallation xenon in the glasses, which proves that the glasses do not quantitatively lose xenon while exposed to the near-surface environment. Assuming an indigenous xenon component was purely retained within the surface coating, not the vesicles or homogenously distributed within the glasses like spallation xenon, we could suppose a gentle post-eruptive process which purely removed surface-correlated xenon, this would help explain the lack of solar wind xenon in many of the glasses. However, I can think of no reasonable explanation for why this process would not have not affected the other surface-correlated volatiles, and why the temporal atmospheric volatiles would be preserved within the vesicles and the glass surfaces yet xenon would remain purely surface-correlated.

Assuming an indigenous xenon composition was dissolved within the melt which produced the glasses and present in the temporal atmosphere the glasses were erupted and quenched within, and assuming the post-eruption near-surface processes did not remove a trapped component, could processes during eruption have removed a detectable indigenous xenon component? As proven in this work, heating the volcanic glasses to temperatures sufficient to melt them leads to loss of xenon. The volcanic glasses were erupted as liquid droplets of a volatile-rich melt into a local elevated gas pressure, and quenched rapidly, such that ambient volatiles in the surrounding atmosphere were condensed onto the glass surfaces and within vesicles in the glasses (Heiken et al., 1974; Meyer et al., 1975; Delano and Lindsley, 1983; Barraclough and Marti, 1985; Needham and Kring, 2017; Hui et al., 2018). A process similar to stepped heating, in which volatiles including xenon are removed from the melted glasses, would have to have occurred within the brief period prior to quenching, which may explain the evidence for the abundance of gaseous volatiles during eruption.

It is possible to estimate the amount of indigenous xenon we could expect to be dissolved in the glasses if we estimate the partial pressure of the xenon in the temporal atmosphere, assume the glasses were quenched when in equilibrium with the ambient gas at eruption, and use appropriate xenon solubility calculations for similar silicate melts. Estimating the maximum pressure of the gas the glasses were erupted into and quenched within is complicated by the fact that the temporal atmosphere was maintained by these eruptions, so the local pressure at their formation is likely to be much higher than the average, the best estimate for the global average atmospheric pressure is ~ 0.01 bar, calculated using volatile concentrations from Apollo 15 and 17 volcanic glasses and estimates of the mass of erupted lava (Needham and Kring, 2017). An ancient or modern lunar volume mixing ratio of xenon is not available, and the modern mixing ratio would likely be different to the temporal atmosphere at ~ 3.5 Ga due to the changing rate and

nature of atmospheric loss, the proximity to volatile-rich volcanism, and a difference in surface conditions, such as the possibility of xenon sinks on the colder areas of the lunar surface (Bar-Nun et al., 1987; Laufer et al., 1987; Needham and Kring, 2017; Curran et al., 2020). A volume mixing ratio must therefore be inferred from a gas reservoir containing xenon of similar provenance, such as Earth's atmosphere, or solar wind. Assuming the volume mixing ratio of xenon in the ancient lunar atmosphere resembled Earth's modern atmosphere, the maximum partial pressure of xenon in the temporal lunar atmosphere may have peaked at around $8.7 \times 10^{-10}$ bar (Porcelli and Ballentine, 2002; Wieler, 2002). Using this partial pressure and assuming a xenon solubility from silicate melt with the closest equivalent density ($\sim 0.9 \times 10^{-5}$ $cm^3$ STP $g^{-1}$ $a^{-1}$) (Lux, 1987), the equilibrium concentration of xenon is $\sim 7 \times 10^{-5}$ $cm^3$ STP $g^{-1}$, which corresponds to a concentration up to two orders of magnitude lower than the detection limit of RELAX ($3.5 \times 10^{-17}$ $cm^3$ STP) for the masses of the volcanic glasses of Apollo 15 and 17. This does not account for the xenon contained in the vesicles, which may have been more easily quantified if more backscatter images were taken of the polished glasses, nor does it account for the xenon in the volatile-rich rims of the glasses, but these sources would need to account for a xenon concentration increase of two orders of magnitude for this hypothetical indigenous xenon to be detected by RELAX. However, an estimated concentration of xenon using this method, even including estimates of vesicle and volatile-rich rim contributions, is of questionable reliability given the significant assumptions and equivalencies its calculation requires.

Given that no indigenous xenon was observed in the volcanic glass analyses, what constraints can this place on the partial pressure of xenon in a transient atmosphere during eruption? Assuming the glasses were quenched when in equilibrium with the ambient xenon upon eruption, and have since retained their dissolved xenon (approximated by an equivalent xenon solubility $\sim 0.9 \times 10^{-5}$ $cm^3$ STP $g^{-1}$ $a^{-1}$), the masses of the heaviest

glasses and the detection limit of RELAX can be used to estimate the maximum partial pressure of ambient xenon upon eruption (Lux, 1987). In this scenario, the partial pressure of xenon in the transient atmosphere is up to $2.47 \times 10^{-8}$ bar, although this excludes the xenon contained within vesicles and volatile rims, and these contributions would lower the estimate.

The glasses appear to have resided underneath the lunar surface according to the relative production rates of cosmogenic isotopes with depth. The lack of solar wind xenon, of which only a few of the volcanic glasses contained any trace of, adds weight to the idea that the glasses were not exposed at the surface for the majority of their existence. Either that, or the glasses have since degassed the solar wind xenon and fission once contained within, however, this also contradicts the volatile presence on the spherule surfaces and within the spherules, and the retention of cosmogenic xenon.

The spallation xenon composition can be almost exclusively attributed to that expected from Ba spallation by GCR interaction, as opposed to REE spallation. This is interesting given the apparently higher production rates of xenon isotopes from REE relative to Ba (~ 6 for $^{131}$Xe from Hohenberg et al. 1978), but consistent with the relative enrichment in Ba to REE exhibited in the volcanic glasses.

Exposure ages within the volcanic glasses of 15426 expressed a large range of exposure ages (227 Ma < 2113 Ma, average ~ 982 Ma), whose average roughly coincided with the “multi-spherule” glass exposure age of 777 Ma, which can reasonably be assumed to feature a similarly varied exposure age from glass to glass. The number of glasses measured does not allow us to confidently suggest exposure ages are normally distributed around this mean, or express a bimodal distribution between two possible groups (~ 440 Ma for A, B, D, and F, and ~ 1530 Ma for H, J, L, and Z).

The volcanic glasses of 15426 all feature crystallisation ages significantly older than these exposure ages, so another process must explain the lack of much of the spallation derived $^{126}$Xe. The glasses were apparently erupted onto the lunar surface after quenching, and were definitely collected from the surface during the Apollo 15 mission, yet cannot have resided on the lunar surface for the intervening period unless significant diffusive loss of $^{126}$Xe occurred. However, such a diffusive loss is inconsistent with the other isotopes of xenon produced by spallation (all except $^{134}$Xe and $^{136}$Xe), which do not exhibit evidence of mass dependent fractionation, and are very close in resemblance to unfractionated spallation of Ba (apart from $^{131}$Xe excess). Another alternative is that the glasses were buried after eruption, and exhumed before collection, such that the glasses were only ever exposed to GCRs for around 440 Ma < 1530 Ma, and completely shielded for the remaining ~ 2 Ga < 3 Ga. The processes which could have buried and exhumed the glasses are most likely those of impact cratering or moon quakes, considering the scale (using regolith density estimates of Kring, (2006), 1.6 g/cm$^3$ < 2.3 g/cm$^3$, between 220 cm < 310 cm deep) of burial required for complete shielding. Burial beneath a warm ejecta blanket from a nearby impact may explain the apparent lack of indigenous noble gases, although it would need to be cool enough to not melt the glasses. The glasses also retain their original shapes and exhibit no evidence of shock, features which you would expect if they were in close proximity to impacts. A low-energy and distant impact event satisfies these criteria, as does some form of moonquake-derived mass waste.

These results are higher than the varied exposure ages (< 400 Ma) for the volcanic glasses of Apollo 15 reported previously by light noble gas work (Huneke et al., 1973; Lakatos et al., 1973; Spangler et al., 1984; Füri et al., 2018). This is most likely the result of diffusive loss of the lighter daughter isotopes of these noble gases compared to xenon, leading to underestimates on the exposure ages of light noble gas studies. Alternatively, the

glasses of this work could be more representative of the total range of exposure histories experienced by the volcanic glasses of 15426.

The shielding depth calculations for the volcanic glasses of 15426 add a caveat to the simple model of complete GCR shielding in between exposures, in that they appear to exhibit evidence of accruing spallation xenon at depths where $^{131}Xe/^{126}Xe$ production is significantly different to surface conditions. The data actually place the volcanic glasses of 15426 at the very edge of GCR penetration, ~ 400 g/cm$^2$. Residence around this area could explain the improbability of glasses with drastically different exposure histories ending up within such close proximity when they were collected. In this boundary zone some glasses could lie outside the reach of GCRs, while others remain within reach of GCRs. However, GCR penetration continuously decreases with depth (as shown in Figure 4.16) (Hohenberg et al., 1978), so this boundary zone does not represent an abrupt end to GCR flux. Defining an exact range of depths required to exceed this boundary zone and produce such an effect is probably beyond the precision of the GCR penetration model of Hohenberg et al. (1978) used in this work, but if we suggest the proximity of the glasses upon collection was roughly 2 cm, and use the highest regolith density (2.3 g/cm$^3$) of Kring, (2006), the glasses were separated by up to 5.6 g/cm$^2$ of shielding material. Figure 4.16 illustrates the insignificance of such a small change in burial depth on production rates of xenon isotopes, even with the generous conditions of this scenario where the displacement is assumed to be parallel to GCR flux and the higher estimate of regolith density is used. The crystallisation age/exposure age discrepancy still requires predominant residence outside the reach of GCRs, but sometime within the outer depths of GCR penetration is consistent with shielding depth calculations and such varied exposure ages.

The exposure ages for the volcanic glasses of 74220 were more consistently grouped around 70 Ma ($\sigma$ = 45), a figure consistent with the multi-spherule calculation of

62 Ma. These are significant and consistently lower exposure ages compared to their crystallisation ages (~ 3.5 Ga), so the exposure history is most likely one of burial for the majority of the existence of the volcanic glasses, and exhumation before collection by Apollo 17 astronauts. Such a model is consistent with the apparent lack of any solar wind in the glasses of 74220, indicating minimal, if any surface exposure. Shielding depth calculations confuse this model slightly, in that they are either consistent with GCR exposure with basically no shielding, or GCR exposure at shielding depths of 80 g/cm$^2$ < 200 g/cm$^2$. Other volcanic glasses of 74220 featured $^{131}Xe/^{126}Xe$ ratios which did not allow shielding depth calculations. These values are not drastically dissimilar to the 30 g/cm$^2$ shielding depth calculation for the orange soils of 74220 by Eugster at al. (1977), which used the same 2π irradiation geometry correction and assumed chondritic abundances of the target elements which produced cosmogenic Ne, ultimately affecting the $^{21}Ne/^{22}Ne$ ratio. Leya et al. (2001) has since revised the cosmogenic neon production rate with depth, but suggests shallow depths such as these are still correct within 10%. The deposition/deep burial/exhumation model is consistent with the existing models of GCR exposure prior to burial, then exhumation by formation of the Shorty Crater 17 Ma ago (Eugster et al., 1982; Eugster, 1985). Although a lack of solar wind suggests the glasses were shielded from the lunar surface almost immediately after eruption, presumably by gardening.

Despite the unexpected lack of a solar wind compositional dominance, the question of surficial implantation or inward diffusion of solar wind into the volcanic glasses, as suggested by Füri et al. (2018) (for helium, neon, and argon), could be extended to xenon by these data. Implanted solar wind xenon has been experimentally shown and modelled to be surface-correlated, residing within a depth on the scale of tens of nanometres (Heber, 2002; Wieler et al., 2007; Mohapatra et al., 2011). An inwardly diffused component which has reached an equilibrium of homogeneous distribution within a sample can be expected

to be volume-correlated. The comparison of $^{136}Xe$ concentration as a solar wind proxy to the surface area to volume ratio of the volcanic glasses exhibited no clear correlation, suggesting solar wind may well be inwardly diffused in the volcanic glasses of 15426 and 74220. It is worth noting the sample sizes analysed in this work were not tailored for a surface area to volume ratio, and were roughly similar volumes, so a correlation would be less apparent than a sample tailored to feature a larger range of sizes. Additionally, the low concentration and relatively high uncertainty of $^{136}Xe$ is not useful for meaningful interpretation of these data, especially given the imperfect use of $^{136}Xe$ as a proxy for solar wind.

The inclusion of the single impact glass in the xenon measurements to act as a control composition to be subtracted from the volcanic glass xenon was not practical given the range of compositions, and subsequently varied interpretations, of individual volcanic glasses within 15426 and 74220. The impact glasses are also ubiquitous and varied in their provenance (Delano, 1986; Zellner et al., 2002; Delano et al., 2007; Gombosi et al., 2015; Zellner and Delano, 2015), and may therefore be expected to contain more heterogeneous xenon compositions than the volcanic glasses, so one single impact glass was unlikely to comprise a reliable control.

### 4.6. Conclusions

The volcanic glasses of 15426 and 74220 analysed in this work contain xenon compositions most closely resembling a mixture of galactic cosmic ray products and solar wind, and do not contain xenon in concentrations large enough for resolution of an indigenous noble gas composition. The exposure histories of both volcanic glass samples indicate a history in which they mostly resided at depths beyond the reach of GCRs, then exposure not long before collection. Shielding depths suggest the volcanic glasses of 15426 resided at the edge of GCR penetration, whereas the volcanic glasses of 74220 appear to have been almost completely shielded from GCRs in between their eruption and exhumation.

The inconclusive and heterogeneous xenon composition and concentration contained in the volcanic glasses did not allow us to discern a significant difference between the impact and volcanic glasses, as had been initially proposed. This proposal ignored the complex history of the impact glasses, whose xenon compositions are potentially influenced by timing and nature of impactor and location, and the duration and nature of surface exposure or burial. That is to say nothing of the inconsistencies expressed by the volcanic glasses. For future research which may be interested in using impact glasses as a proxy for the non-volcanic noble gas content of the soil, the volume of xenon needs to be significantly more than was measured in this work. In practical terms, this requires a larger sample or a more sensitive instrument. However, the significant difference between provenance of the volcanic and impact glasses, and various factors such as crystallisation age, composition and its bearing on noble gas diffusion or creation from decay and spallation, and minor differences in shielding history producing vastly different compositions, make use of impact glasses as controls unlikely to be helpful.

This work provides an interesting insight into the volcanic glasses of 15426 and 74220, but is not a conclusive end of the indigenous lunar noble gas hunt within the pristine volcanic glasses. The problems with polishing, weight determination (for spallation calculations), and volume/surface area resolution, could all be solved by the use of larger samples. Larger spherules may also contain larger volumes of gas for analyses, thus improving the signal of sample xenon relative to blank signal, and reducing uncertainties, although no correlation between sample size and extracted xenon concentration was evident in this work. Additionally, the volume of a spherule is proportional to its ability to retain trapped noble gases, as the rate of diffusion is partially controlled by the distance the xenon has to diffuse to leave a material. Arguments for the volcanic glasses losing their trapped xenon content due to post-eruption, near-surface processes, such as heat fluctuations during day/night cycles, would be less plausible if larger glasses are analysed, although such a situation is already unlikely given the retention of spallation xenon and presence of volatiles on the surfaces and within vesicles in the glasses (Meyer et al., 1975; Butler and Meyer, 1976; Barraclough and Marti, 1985). Estimating an ideal volcanic glass sample volume which could have retained indigenous xenon requires tenuous assumptions of partial pressures and temperatures surrounding the glasses after eruption, figures which are too poorly constrained to provide a helpful figure.

However, even in the case of a large enough sample for total and precise xenon component deconvolution, attributing any of it to what is essentially an unknown reservoir is problematic. Indigenous lunar xenon could resemble any combination of known reservoirs. Such a sample of a larger volcanic glass spherule would presumably contain larger concentrations of many of the components which would need deconvolution. An ideal sample would be sourced from deeper in the Moon, beyond the reach of GCR penetration and solar wind, where it is sufficiently shielded from solar wind and cosmic rays.

## 5. Towards noble gas analysis of Stardust samples with closed-system etching

### 5.1. Introduction

The majority of noble gas studies of 81P/Wild 2 samples collected by Stardust have focussed on the light noble gases. Stardust samples with melted aerogel and terminal particles contain neon resembling the component contained in phase Q ($10.1 < {}^{20}Ne/{}^{22}Ne < 10.7$, $2.78 < {}^{21}Ne/{}^{22}Ne < 2.94$), yet elemental ratios of $1 < {}^{4}He/{}^{20}Ne < 20$ incompatible with phase Q (${}^{4}He/{}^{20}Ne = 110 \pm 30$) or solar wind ($520 < {}^{4}He/{}^{20}Ne < 670$) (Busemann et al., 2000; Marty et al., 2008; Palma et al., 2009; Palma et al., 2013). Helium compositions in these samples have been reported as $2.47 \pm 0.34 \times 10^{-4} < {}^{3}He/{}^{4}He < 2.92 \pm 0.26 \times 10^{-4}$, intermediate between solar wind (${}^{3}He/{}^{4}He = 4.44 \pm 0.10 \times 10^{-4}$) and phase Q (${}^{3}He/{}^{4}He = 1.45 \pm 0.15 \times 10^{-4}$) (Busemann et al., 2000; Marty et al., 2008). Stardust aerogel sections which featured no observable tracks or particles were found to have trace helium and neon resembling the composition of solar wind (${}^{20}Ne/{}^{22}Ne = 13.9 \pm 0.08$, ${}^{21}Ne/{}^{22}Ne = 3.35 \pm 0.07 \times 10^{-2}$) within large uncertainties (Palma et al., 2010, 2012).

Whether the compositions and behaviours of light noble gases in Stardust samples can be extended to heavy noble gases is unclear. The elemental ratios of helium and neon in Stardust samples are inconsistent with the compositions suggested by their individual isotopic ratios (Marty et al., 2008), and heavy noble gases are more chemically distinct. Mohapatra et al. (2013) modelled expected abundances of implanted heavy noble gases in Stardust aerogel without tracks or particles and compared it to measurements, finding measured concentrations of Ar and Kr to be depleted relative to Xe. These cases suggest that the isotopic composition of the xenon contained in 81P/Wild 2 cannot be reliably inferred from other noble gases, and must be measured directly.

Mohapatra et al. (2013) comprises the only measurement of xenon collected from 81P/Wild 2 by Stardust. The study measured xenon contained an aerogel tile containing no terminal particles or tracks; one sample was from the surface of the tile exposed to 81P/Wild 2, another was from the rear of the same tile. They reported a factor of fifty enrichment in $^{132}$Xe in the comet-facing tile, suggesting the possibility of 81P-Xe being implanted in the surface of the exposed aerogel, or the structure of the comet-facing aerogel being more prone to adsorption of a large atmospheric xenon composition. An isotopic composition of the surface-correlated xenon was not provided apart from its resemblance to mass fractionated atmospheric xenon with a heavy isotope enrichment. The closest equivalent to heavy noble gas measurements of the solid material from comets sampled in the track walls and terminal particles of 81P/Wild 2 are interplanetary dust particles (IDPs) of probable cometary descent, in which upper limits on concentrations have been calculated alongside elemental ratios resembling fractionated solar wind (Kehm et al., 2002, 2009; Busemann et al., 2010).

The disparity between the lack of 81P-Xe measurements and the importance of another cometary xenon composition reflects the difficulty of constraining 81P-Xe, principally due to the nature of sample collection by Stardust. Samples collected by Stardust are mostly heated by shock upon impact and friction during deceleration, possibly beyond the temperature ranges within which trapped xenon is retained in solids. This heating is responsible for effects ranging from the incorporation of aerogel-derived crusts, to the evaporation and disintegration of a number of the less cohesive particles (Burchell et al., 2008; Leroux et al., 2008; Roskosz et al., 2008; Leroux, 2012). Simulations of Stardust sample collection found that temperature-sensitive materials (which melt at ~ 600 °C) over a micron in size could be captured with minimal thermal alteration, except for particle surfaces, which are subjected to extremely high thermal gradients and ablation (over 2000 K at molten aerogel contact) (Brownlee et al., 2006; Roskosz et al., 2008). The

removal of surficial material from the particles may influence the isotopic composition of the particle (as in solar wind's depth dependence in lunar regoliths) (Meshik et al., 2014), as lighter isotopes are generally implanted closer to the surface than the heavier isotopes with more energy. For particles which were smaller than a micron thermal inertia was unable to insulate the grain from extensive heating (Brownlee et al., 2006).

Interplanetary dust particles and micrometeorites (which are typically over 1 μm) in diameter are supposed to have had similar levels of heating to Stardust samples during atmospheric entry (< 600 °C) (Nier and Schlutter, 1993), yet still retain heavy and light noble gas components (Kehm et al., 2009; R. L. Palma et al., 2013). Light noble gases trapped in track walls imply that lost internal components could be re-trapped in the molten aerogel while it solidifies (Marty et al., 2008; Palma et al., 2009, 2010, 2012), the same may be true of the heavy noble gases. It follows that analyses of tracks featuring no terminal particles could still be useful in determining 'trapped' xenon content in destroyed dust particles (Marty et al., 2008; Roskosz et al., 2008), although care would have to be taken to discern it from a potential implanted component (Mohapatra et al., 2011), and the inevitable atmospheric component.

The following sections describe the development of a procedure for the analysis of noble gases contained within 81/Wild 2 samples collected by the Stardust spacecraft with CSSE and RELAX.

### 5.2. Characterising Stardust xenon conventionally

Stardust employed silica aerogel due to its physical properties being well suited to the collection and deceleration of solid cometary materials with minimal thermal modification, however, this material introduces a significant problem for noble gas extraction. Typical noble gas extraction techniques heat samples to release adsorbed and trapped gases, subjecting samples to increasingly higher temperatures in order to liberate gases from more thermally resilient phases and/or locations.

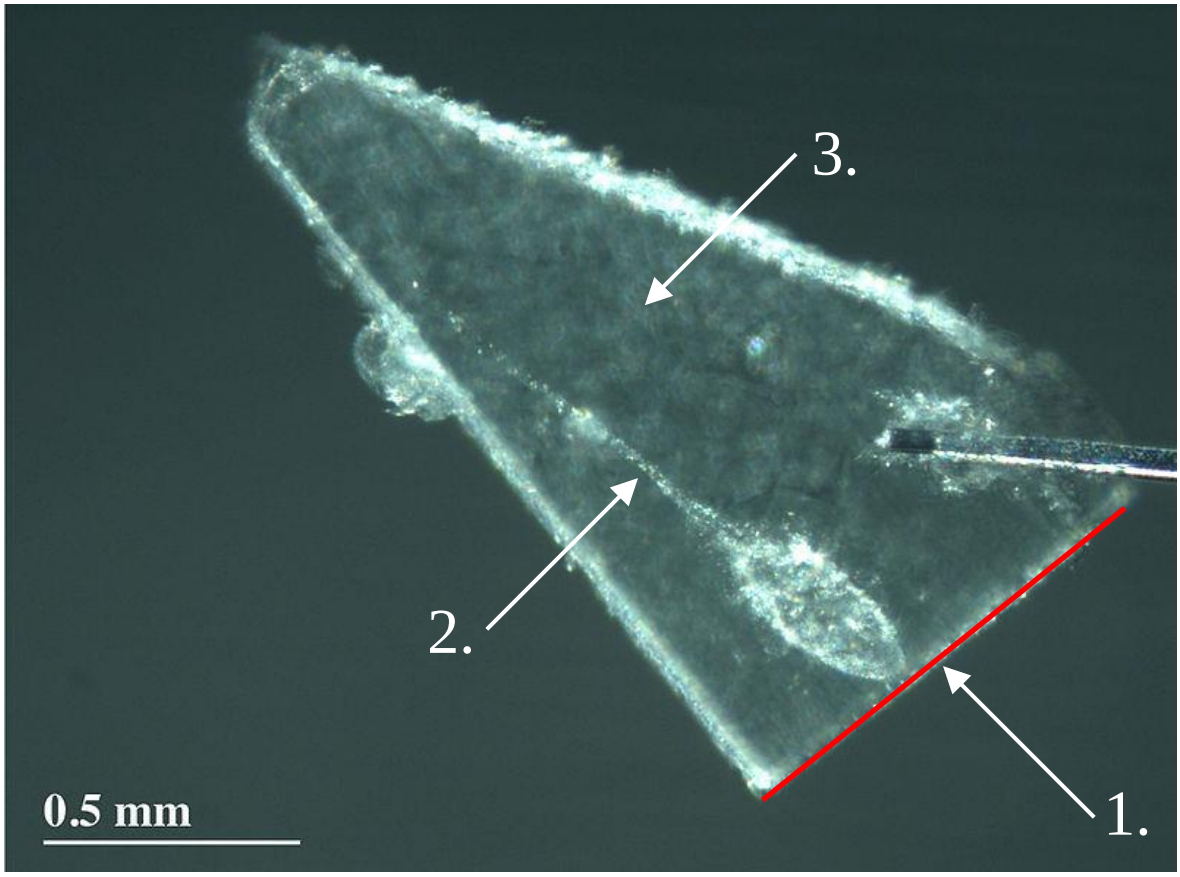


***Figure 5.1*** *Annotated Stardust aerogel 'keystone' featuring particle track (labelled 3.). Numbers illustrate materials likely to contain different noble gas compositions; 1. Aerogel surface (red border) – potentially containing implanted cometary xenon (only on face which particles were incident, indicated by red line), 2. Aerogel interior – containing terrestrial atmospheric xenon from manufacture and sample curation, 3. Particle tracks and terminal particle – containing xenon from terminal particle mixed with resolidified aerogel in track walls. Image adapted from NASA/JPL.*

As described in Section 1.4.2, aerogel is an amorphous and ultra-porous gel of silica ($SiO_2$) with an extremely large surface area (between 500 $m^2/g$ < 1500 $m^2/g$) (Pierre and Pajonk, 2002; Tsou et al., 2003, 2004; Pan et al., 2017; Feng et al., 2018). Any surface of a solid is a potential site onto which any volatile may adsorb, including xenon. Stardust aerogel may therefore be expected to contain a large volume of adsorbed gases, presumably of Earth's atmospheric composition from its manufacture and post-flight curation on Earth ("1." and "2." of Figure 5.1). Terminal particles and their tracks contained smeared trails of melted and re-solidified aerogel mixed with particle material, or even complete mixtures of aerogel and sample material without terminal particles ("3." of Figure 5.1).

Predicting which of these structures and compositions would be targeted by the application of uniform heating steps of increasing temperature is extremely difficult. Low temperatures may release atmospheric xenon adsorbed onto the aerogel along with implanted surficial aerogel. Deconvolving any composition, and especially an unknown one, from such a large volume of adsorbed atmospheric xenon would be challenging. Higher temperatures intended to target terminal particles or noble gases trapped in the particle tracks can expect to simultaneously release the xenon trapped in the similarly $SiO_2$-dominated aerogel, and the trapped atmospheric xenon incorporated into the particle tracks during capture. Deconvolution of these components would result in large uncertainties. With what certainty can the extracted xenon be attributed to a particular material? Was the extraction complete, or is the composition isotopically fractionated, or depth-correlated? How much of the released gases can be attributed to terrestrial atmospheric xenon contained in the aerogel, and was this component fractionated? Should the heating steps increase the temperature aggressively at the risk of instrument saturation, or conservatively at the risk of 'diluting' the sample xenon?

Additionally, uniform heating is not guaranteed in the stepped heating method employed in RELAX, which uses an infrared laser where power and duty cycle of the laser provides a rough control on temperature (described in Section 4.3.3). This method may heterogeneously heat the sample according to laser foci, laser illumination from one side of the sample, how efficiently the laser transfers heat to the sample, and the conduction of heat away from the sample by surfaces in contact with the sample holder. Uniform heating is achieved in crucible gas extraction, where an entire sample chamber is heated, although this is typically at the expense of increased blank from degassing of the heated vacuum chamber material.

### 5.3. Closed-System Stepped Etching (CSSE) for Stardust

This work aims to develop the analytical procedures and experimental feasibility of measuring xenon contained in Stardust samples by in vacuo etching. The following sections describe a collaboration with ETH Zürich in which parallel experiments were conducted with in vacuo etching of aerogel with RELAX (O'Mara et al., 2014), and in vacuo etching of a Stardust sample analogue with a conventional mass spectrometer (Will et al., 2017). In vacuo closed-system stepped etching is essentially a means of extracting gases by controlled exposure to acid vapour (explained in more detail in Section 2.2). Samples are exposed to acid vapour "etching steps" of increasing duration, temperature, and different acids which can target specific volumes, materials and locations within a sample. In vacuo closed-system stepped etching could separately extract discrete noble gas components contained within a Stardust sample with a spatial and compositional resolution which stepped heating is incapable of.

In practice, the CSSE approach (Weiler et al., 1986; O'Mara et al., 2014; Will et al., 2017) to Stardust analysis assessed in this work attempts to exploit the differences in chemical lability of each noble gas host phase chemistry and physical structure. The theory proceeds as follows:

1. Initial etching steps using concentrated hydrofluoric acid (HF, ~ 99%) of minimal vapour pressure will preferentially etch the first siliceous material they come into contact with. In the case of Stardust samples, this is dominated by the aerogel's surface and ultraporous structure, within which the major source of atmospheric contamination is contained ('1' and mostly '2' of Figure 5.1). Ideally, the xenon released in these initial etching steps will be almost entirely composed of the aerogel-xenon, and a relatively negligible amount of the xenon contained within the tracks and terminal

particles. This is due to the enormous disparity in surface area which the acid can react with. The immediacy of the outer ‘surface’ of the aerogel keystone (‘1’ and ‘2’ of Figure 5.1) compared to the tracks and terminal particles also contributes to its preferential etching. Carefully controlling the partial pressure of HF in these initial steps should allow the measurement of released xenon to determine the point at which a non-terrestrial xenon composition is observed, marking the transition to etching of something other than the aerogel. An additional feature of this approach is the possible ability to determine a surface implanted cometary xenon composition within the outer surfaces of the aerogel (the red line facing white arrow on Figure 5.1), such a composition would presumably be contained in the first, most gentle of etches, and could be deconvoluted from terrestrial xenon (released from the equally available remainder of the red line in Figure 5.1).

2. Etching of non-aerogel materials by later acid vapour steps. The surface area of the non-aerogel materials such as resolidified particle tracks and terminal particles is significant relative to the remaining aerogel. The xenon released during this phase will proceed in order of the host phases most susceptible to the chemical etching. The remaining silica-based materials such as the track walls and then the outer surfaces of terminal particles are most likely to be the targets of these etching steps due to their immediacy of surface area available to the acid vapour and potential chemical resilience relative to the actual terminal particles with their more crystalline silica structure.

3. Increasingly vigorous etching of the more resilient phases susceptible to HF vapour exposure, sequentially releasing xenon from the toughest areas of particle tracks, then outer areas of terminal particles, then different phases within the particle itself.

Ultimately concluding with the entire HF-susceptible portion of the sample being destroyed, and its contained xenon analysed.

4. Replacement of the HF with nitric acid ($HNO_3$) for the etching of HF-resistant organic compounds potentially contained within the collected cometary material. This step is particularly important for noble gas geochemistry due to the organic nature of the host phase for phase Q xenon (Q-Xe) literally being defined by its HF-resilience (Lewis et al., 1975).

This model of orderly procession of host phase etching and uniquely attributable xenon compositions is idealised, but even partial fulfilment of the theory, such as the selective removal of terrestrial-xenon contaminated aerogel from a Stardust keystone, would be worthy of CSSE employment over stepped heating.

It is also worth noting the potential for adsorption of released gases on the newly exposed etching surfaces of a sample, as is observed in experiments which crushed (Schwenzer et al., 2012) and etched (Ott, 2008) Martian meteorites. The tightly bound nature of the adsorbed xenon in the etching experiment of Ott (2014), mostly released at high stepped heating temperatures (1800 °C), should be irrelevant in CSSE, as xenon is released by destruction of the binding sites by etching. Such an effect on etched samples could make separate distinction of xenon components difficult, as the previously analysed gases would be adsorbed onto the surfaces which are to be etched in the subsequent step. However, should this effect be observed, the xenon isotopic composition would still plot on a mixing line between the etched compositions. Also, a cautionary approach to stepped etching, as is employed in this work to protect the mass spectrometer, increases the number of etching steps for any given sample volume, thus reducing the adsorbed gases from the previous step, and mostly confining their measurement to etches of similar host phases.

Even without this phenomenon, a gradual evolution of the gases etched from sample material is likely, as the acid is exposed to the entire sample surface, and even with controls on partial pressure, temperature and duration, some etching of all the sample material susceptible to the chosen acid is expected.

### 5.3.1. Contamination

This approach to sample analysis is rare in comparison to stepped heating due to the goldsmithing required for construction of the apparatus, and the harsh chemicals required for dissolution of mostly inorganic Solar System materials. In most mass spectrometers every attempt is made to remove active ions from gases extracted from samples as they can damage components and persist in the instrument volumes, hence why RELAX (Crowther et al., 2008) and CSSE (Weiler et al., 1986; Signer et al., 1991) are frequently employed with multiple gettering stages prior to sample gas analysis. In the etching of this work, the principal active ion is fluorine from the hydrofluoric acid, and the principal component which may be damaged is the microchannel plates used for ion detection due to their large surface areas. In many mass spectrometers, the means of ionisation is non-discriminatory, so fluorine can be ionised and mobilised every time the instrument is operated (Signer et al., 1991).

The RELAX mass spectrometer and CSSE are uniquely complimentary in that the resonance ionisation source selectively ionises xenon, and does not liberate fluorine ions from hydrofluoric acid. So should the HF be incompletely neutralised before entering the ionisation volume, its subsequent effect would be minimal. However, the use of CSSE with instruments more susceptible to fluorine contamination is possible due to the multiple gas treatment modules an aliquot of sample gas is exposed to before analysis (detailed in Section 2.2.1).

### 5.4. Stardust analogue

The novel and destructive analytical approach of this work and the high value of returned 81P/Wild 2 material made proof of concept with an analogue of Stardust material advisable. This analogue required particular properties in order to prove the suitability of the etching approach in the extraction of discrete noble gases from a Stardust sample:

1. The analogue would have to be composed of roughly equivalent materials to those expected to be present in Stardust samples.

2. These materials would need uniquely attributable noble gas compositions, whose deconvolution could be determined with precision in order to test whether the approach separated xenon components from the different phases.

Stardust analogue equivalency to real Stardust material was important given the novel approach, as its behaviour would set precedence for how a real Stardust etch would proceed. The distinct noble gas composition need only be distinct between materials to assess which combination or individual component xenon was being extracted from.

The analogue material was first analysed individually by stepped heating to precisely determine the xenon composition each contained, and then analysed en masse by CSSE. The nature of the gases characterised using the CSSE apparatus and acid switching technique was then compared to the ‘pure’ individual component compositions determined by the parallel stepped heating experiments. This comparison intended to assess the capabilities of CSSE as a technique for the effective separation of noble gas components contained in the discrete host phases of a Stardust sample.

The analysed sample material was not implanted into aerogel at high velocities like the Stardust material it was chosen to represent. This has implications for the composition, the chemical structure, and the siting of the noble gases, which are entirely confined to the respective phases, and not trapped in resolidified aerogel tracks or fused combinations of terminal particle and aerogel. In this work the aim was to demonstrate in principle that CSSE could separate xenon released from aerogel, from silicate grains, and from organics. The poorly characterised effects of artificial implantation on xenon budgets would have made it hard to draw firm conclusions about the efficacy of the technique.

### 5.4.1. Aerogel

Unflown aerogel was selected for inclusion in the stepped etching experiments. In direct comparison to the flown Stardust aerogel, this aerogel did not feature particle tracks or surfaces exposed to high velocity particles and noble gas atoms. The structural and chemical equivalency is therefore not representative of the areas surrounding the incident particles of collected Stardust materials, but is very closely matched to the remainder of the aerogel with its adsorbed atmospheric xenon composition. Implanted cometary xenon is not accounted for in this analogue.

### 5.4.2. “Q” Vigarano II

The organic residue rich in phase Q from HCl/HF digestion of the carbonaceous chondrite Vigarano II was chosen to represent a potential organic component in returned 81P/Wild 2 material (Lewis et al., 1975). More specifically, the sample used in this work is that characterised by Busemann et al. (2000), following the sample preparation technique of Lewis et al. (1975) and Alaerts et al. (1979). This organic residue is rich in Q gases including Q-Xe, which almost exclusively comprises its xenon content. Q-Xe is a mixture

of fractionated solar wind xenon, Xe-HL, and to a lesser extent $^{129}$Xe from $^{129}$I decay, whose proportions vary from sample to sample (Huss and Lewis, 1994; Busemann et al., 2000; Crowther and Gilmour, 2013).

In direct comparison to its Stardust collected, 81P/Wild 2 equivalent, "Q" Vigarano II differs in that it has not endured high velocity impact upon collection, this process is known to drastically alter organics in returned Stardust material, in which they are often destroyed (Sandford et al., 2006). As a result, it is hard to point to organic equivalents within 81P/Wild 2, although the ubiquity of phase Q within primitive chondrites, and the similarly primitive constituents of 81P/Wild 2 (Brownlee et al., 2006; Zolensky et al., 2006; Ciesla, 2007; Floss et al., 2013), suggests it presence is not implausible.

The digested phase Q-rich organic residue was selected instead of Vigarano II with phase Q in situ to allow for the greatest possible distinction of materials liberated by HF and $HNO_3$. Purely using undigested Vigarano II could introduce the possibility of partially digesting some of the contained phase Q susceptible to HF etching, or Q-Xe contained in the silicate phases (as observed in HF etching of CI chondrite Ivuna by Riebe et al. (2017)). The xenon contained in the silicate phases of Vigarano II is unlikely to feature as high or uniform a concentration of xenon as in PCA 02007 too, making proof of discrete etching more complicated.

### 5.4.3. PCA 02007

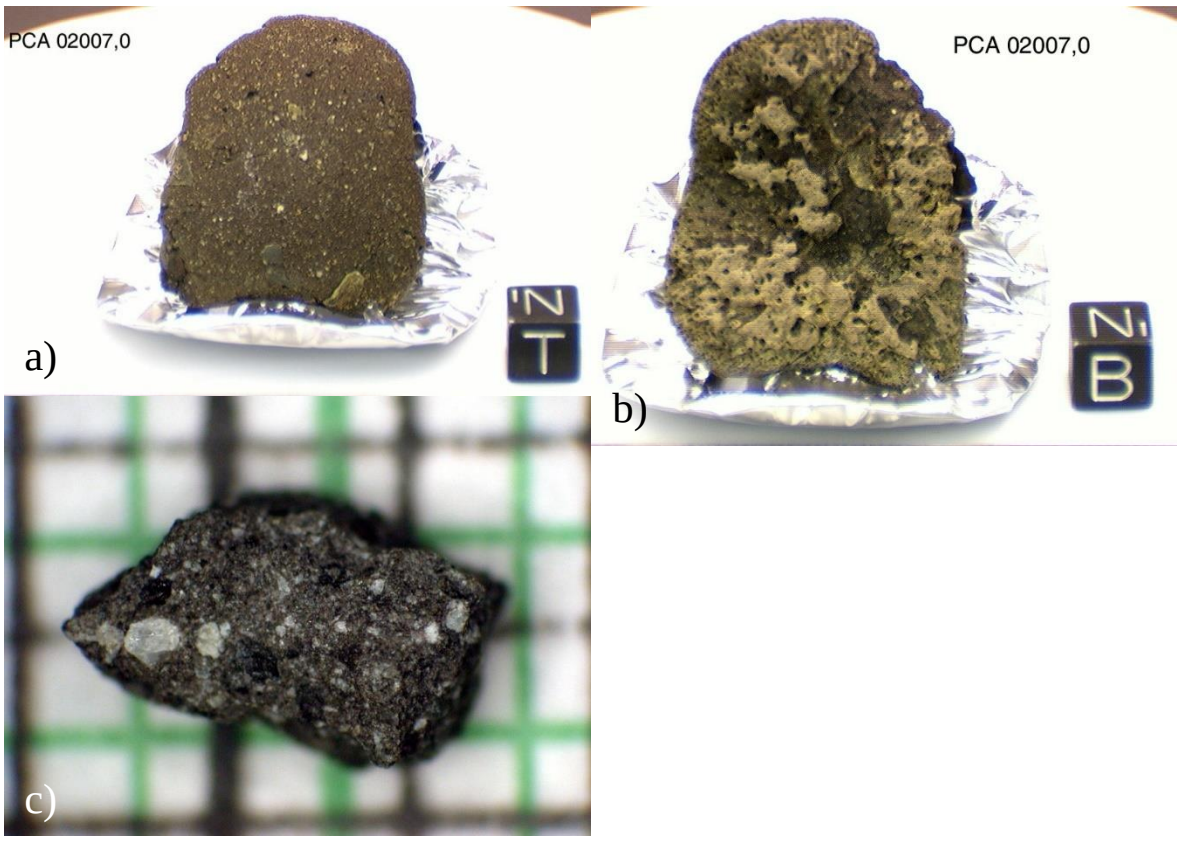


***Figure 5.2*** *Various PCA 02007 images. Source: top row: NASA, bottom left: Ryan Zeigler*
*a) Entire sample exhibiting various clasts of constituent regolith materials fused together. 1 $cm^3$.cube for scale.*
*b) Ropy textured exterior featuring "frothy" vesicular fusion crust.*
*c) Smaller fragment illustrating brecciated fragments cemented within dark matrix. Field of view ~ 6 mm wide.*

A lunar regolith breccia meteorite found in the Pecora Escarpment in Antarctica, PCA 02007 (Russell et al., 2004; Taylor et al., 2004; Righter, 2013; Gross et al., 2017), was selected to represent an equivalent of a silicate component contained in 81P/Wild 2 material returned by Stardust. This sample was initially selected mainly due to the expectation of it containing a high and homogenous concentration of solar wind xenon (SW-Xe) (confirmed subsequently by Will et al. (2016)), given its composition of fused materials exposed on the lunar surface. Xenon of solar wind composition was ideal in its easy distinction from the xenon contained in the organic "Q" Vigarano II residue (Q-Xe) and aerogel (Earth's atmosphere).

The non-volatile composition of PCA 02007 is not a perfect equivalent of the silicates recovered from Stardust material, although a representative sample is impractical given the range of compositions measured in silicates collected from 81P/Wild 2 by the Stardust mission (Zolensky et al., 2006). Chondritic material with a well-defined and homogenous noble gas composition could have satisfied the sample selection criteria and possibly better represents the primitive nature of 81P/Wild 2 silicates. However, such material is typically rich in Q-Xe, so a signal corresponding to that composition could correspond to etching of either the chondritic sample or the organic residue of Vigarano II. Lunar regolith breccias have been subjected to significant heating and shock from geological processes and impacts, so are unlikely to contain any organic materials which may be etched in parallel with the selected organic phase. An irradiated material would have a xenon composition more easily distinguished from Q-Xe, but would introduce an unnecessary safety risk.

PCA 02007 is also expected to have a high concentration of solar wind xenon, an expectation which would be confirmed by conventional measurement prior to stepped etching. A high concentration of xenon allows less vigorous etches of less sample material to produce identifiable signals. PCA 02007 is also expected to feature a homogenously distributed concentration of solar wind xenon due to it being composed of fused materials which were exposed to solar wind on the lunar surface. This feature is especially important in stepped etching due to its preferential etching of sample surfaces, PCA 02007 should be a roughly constant source of solar wind xenon until entirely etched.

### 5.4.4. Stepped heating data

One milligram of PCA 02007 and HF/HCl resistant Vigarano II residue was provided by H. Busemann of ETH Zurich, of which roughly 10 µg was separated from each sample and decanted into individual holes (5 mm diameter) within a Mo sample holder (cylinder 2 cm deep, 3.5 cm diameter). The Mo sample holder was then mounted within the RELAX mass spectrometer, and subjected to turbomolecular pumping down to $10^{-7}$ mbar during baking (at < 200 $^{o}$C) by heating lamp through the sample port window and heating strips elsewhere on the vacuum container for 24 hours. The vacuum was then reduced to ~ $1 \times 10^{-9}$ mbar by ion pump, at which pressure the instrument would remain for the following analyses.

Analyses were punctuated by calibrations using a known volume of atmospheric xenon to maintain instrument precision, and 'blank' measurements of the ambient signal not attributable to sample xenon. Analogue material was loaded in generous quantities in order to ensure a strong signal, and in preparation for large expected concentrations from the stepped etching experiment. Analyses of each sample lasted roughly three days, over which period no significant instrument drift occurred in calibrations or blanks.

Heating steps extracted xenon up to the final step in both analyses, so both samples are likely to contain more xenon than is presented in this work. Non-continuation of stepped heating until completion was enacted due to the consistency of the xenon compositions extracted from each sample, the lack of any compositional trends with increasing heating step temperature, and time constraints due to the large quantity of loaded sample material. Those observations, along with the existing data suggesting constant compositions of xenon in both analogue materials (Busemann et al., 2000; Will et al., 2017), suggest deviation from the reported compositions in this work are unlikely.

***Table 5.1*** *Average xenon isotopic compositions of PCA 02007 and "Q" Vigarano II with respect to potential end members.*

| End Members and Samples | | References | Xenon Isotopic Compositions Normalised to $^{132}Xe \equiv 100$ | | | | | | | | | | | | | | | |
|---|---|---|---|---|---|---|---|---|---|---|---|---|---|---|---|---|---|---|
| | | | 124 | | 126 | | 128 | | 129 | | 130 | | 131 | | 134 | | 136 | |
| *Sample* | *PCA 02007* | *this work* | 0.506 | (0.04) | 0.454 | (0.04) | 8.098 | (0.31) | 104.37 | (0.66) | 17.06 | (0.4) | 82.69 | (0.58) | 36.30 | (0.58) | 29.43 | (0.49) |
| | *"Q" Vigarano II* | | 0.48 | (0.03) | 0.419 | (0.02) | 9.021 | (1.72) | 110.14 | (4.03) | 15.35 | (0.3) | 82.06 | (0.79) | 38.48 | (0.5) | 32.05 | (0.5) |
| *Planetary* | *Solar Wind* | *a* | 0.482 | (0.005) | 0.422 | (0.007) | 8.41 | (0.022) | 8.41 | (0.02) | 16.49 | (0.03) | 82.63 | (0.24) | 36.98 | (0.1) | 29.99 | (0.08) |
| | *Q* | *b* | 0.455 | (0.002) | 0.406 | (0.002) | 8.22 | (0.02) | 104.2 | (0.2) | 16.19 | (0.03) | 81.85 | (0.08) | 37.80 | (0.11) | 31.64 | (0.08) |
| | *HL* | | 0.833 | (0.009) | 0.564 | (0.008) | 9.05 | (0.06) | 105.6 | (0.2) | 15.42 | (0.03) | 84.57 | (0.13) | 63.56 | (0.13) | 69.91 | ≡ 0 |
| *Fission* | $^{235}U$ | *c* | - | - | - | - | - | - | - | - | - | - | 67.6 | (1.1) | 183.0 | (2.1) | 148.8 | (1.3) |
| | $^{238}U$ | *d* | - | - | - | - | - | - | 0.1 | (0) | - | - | 14.4 | (0.1) | 143.5 | (0.3) | 173.3 | (0.3) |
| | $^{244}Pu$ | *c* | - | - | - | - | - | - | 5.4 | (6.2) | - | - | 27.8 | (2.4) | 106.1 | (3.7) | 113.0 | (3.8) |
| | $^{129}I$ | *e* | - | - | - | - | - | - | 100.0 | (0) | - | - | - | - | - | - | - | - |
| *Cosmogenic* | *Ba* | *f* | 51.7 | (16.2) | 95.0 | (29.8) | 153.9 | (48.3) | 151.9 | (60.9) | 118.5 | (37.3) | 414.1 | (129.9) | 6.6 | (2.4) | - | - |
| | *REE* | | 1283.3 | (1497.4) | 1666.7 | (1944.4) | 2033.3 | (2372.7) | 2666.7 | (3181.7) | 66.7 | (169) | 2733.3 | (3213.9) | 0.0 | (0) | - | - |

*Average Ratios normalised to $^{132}Xe \equiv 100$. Uncertainties contained within parentheses correspond to standard deviations. References:*
*[a] Meshik et al. (2014) [b] Busemann et al. (2000) [c] Podosek and Ozima (2000) [d] Jeffery and Reynolds (1961) [e] Hohenberg et al. (1981).*

#### 5.4.4.1. PCA 02007 xenon

The results for the stepped heating of PCA 02007 are presented in Table 5.1, Figure 5.3, Figure 5.4, Figure 5.5, and Figure 5.6. Up to ~ 10 µg of sample material was analysed, although not to completion, weight precision was limited at this value due to the scale used. Figure 5.3 shows a tight compositional grouping around that of solar wind, apart from an apparent excess in the lighter isotope $^{124}$Xe, and a depletion in $^{136}$Xe. Such depletions are indicative of fractionation of a solar composition in which the lighter xenon isotopes are enriched relative to the heavier xenon isotopes. Figure 5.4 takes a closer look at the isotopes produced by cosmogenic processes, galactic cosmic ray spallation products of Ba and REE. The PCA 02007 data appear to cluster around solar wind once again, although some of the less precise analyses may contain a minor contribution from either cosmogenic source. Figure 5.6 includes the compositions produced by fission of $^{235}$U, $^{238}$U, and $^{244}$Pu. Figure 5.6 a) shows that the gas released in the PCA 02007 heating steps consistently plotted far from all fission products, and do not appear to reside upon any fission product mixing lines from their prevailing SW composition. Inset b) of Figure 5.6 focuses on the cluster of stepped heating releases around SW, showing that they feature correlated depletions in $^{134}$Xe and $^{136}$Xe relative to SW, consistent with fractionated solar wind.

The xenon released from stepped heating of PCA 02007 is consistent with almost pure, fractionated solar wind, in which light and heavy isotopes of xenon are enriched and depleted respectively. Figure 5.5 illustrates this composition in a delta plot relative to solar wind xenon. The source of this fractionation is most likely a combination of the large volumes of xenon released in some of the heating steps, and an already fractionated composition of solar wind xenon within the sample, as in Will et al. (2017). The stepped

etching data of Will et al. (2017) PCA 02007 are not available to be plotted alongside the stepped heating data presented here.

The excess in $^{130}$Xe exhibited in Figure 5.5 could be an artefact from the tail bleed phenomenon discussed in Section 2.3.2.2, where resolving individual peak areas from one another is difficult due to large releases (all stepped heating data presented in Table 5A.1 of Appendix). A minor contribution from cosmogenic sources is also possible (as exhibited in Figure 5.4), although deconvolution of this composition from fractionated solar wind is problematic, given they both feature significant excesses in the light isotopes, and the amount of spallation derived xenon is minor relative to the fractionated solar wind signal.

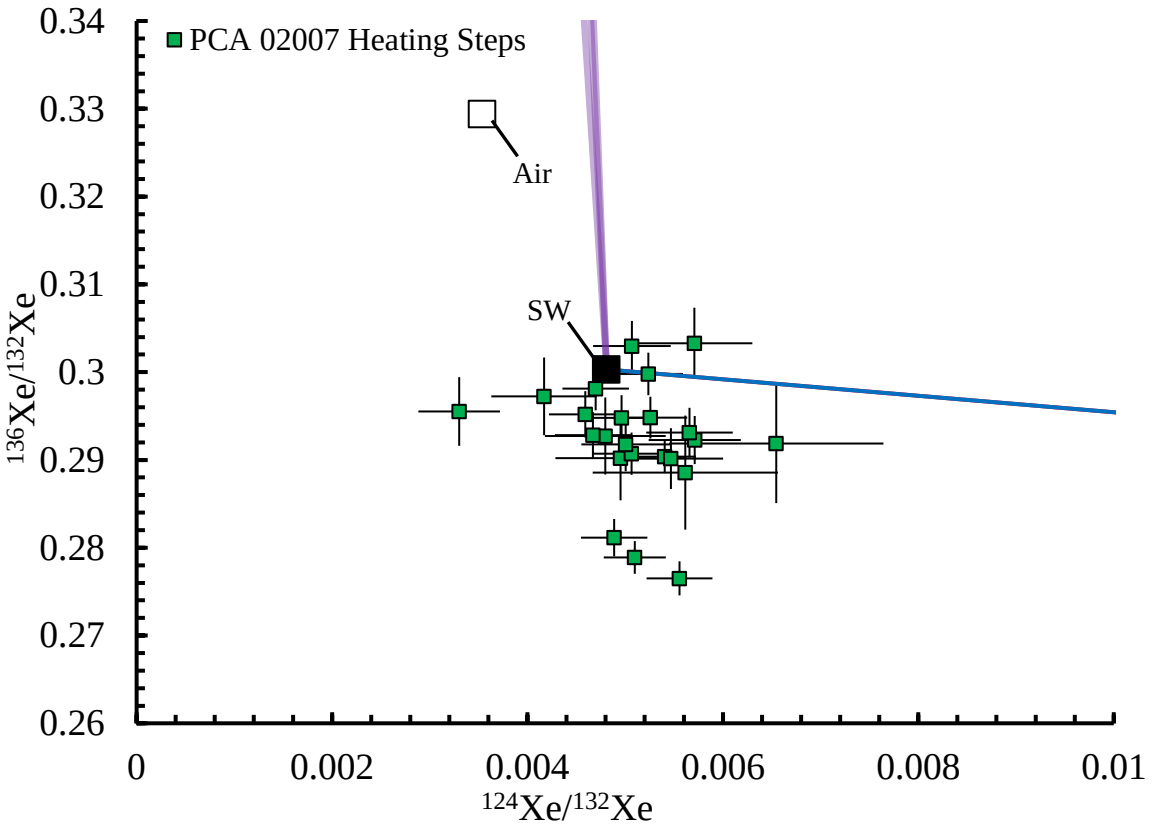


***Figure 5.3*** *Three isotope plot of $^{124}Xe/^{132}Xe$ (abscissa) and $^{136}Xe/^{132}Xe$ (ordinate) for xenon released in heating steps from PCA 02007 (green square indicates one heating step). End members: solar wind ("SW", black square), Earth's atmosphere ("Air", white square) also plotted. Spallation contributions are plotted as mixing lines from SW for Ba (blue line) and REE (red line). Fission contributions are plotted as a singular mixing line from SW to $^{235}U$, $^{238}U$, and $^{244}Pu$ (purple line). Error bars represent 1σ. End member data are taken from Table 5.1.*

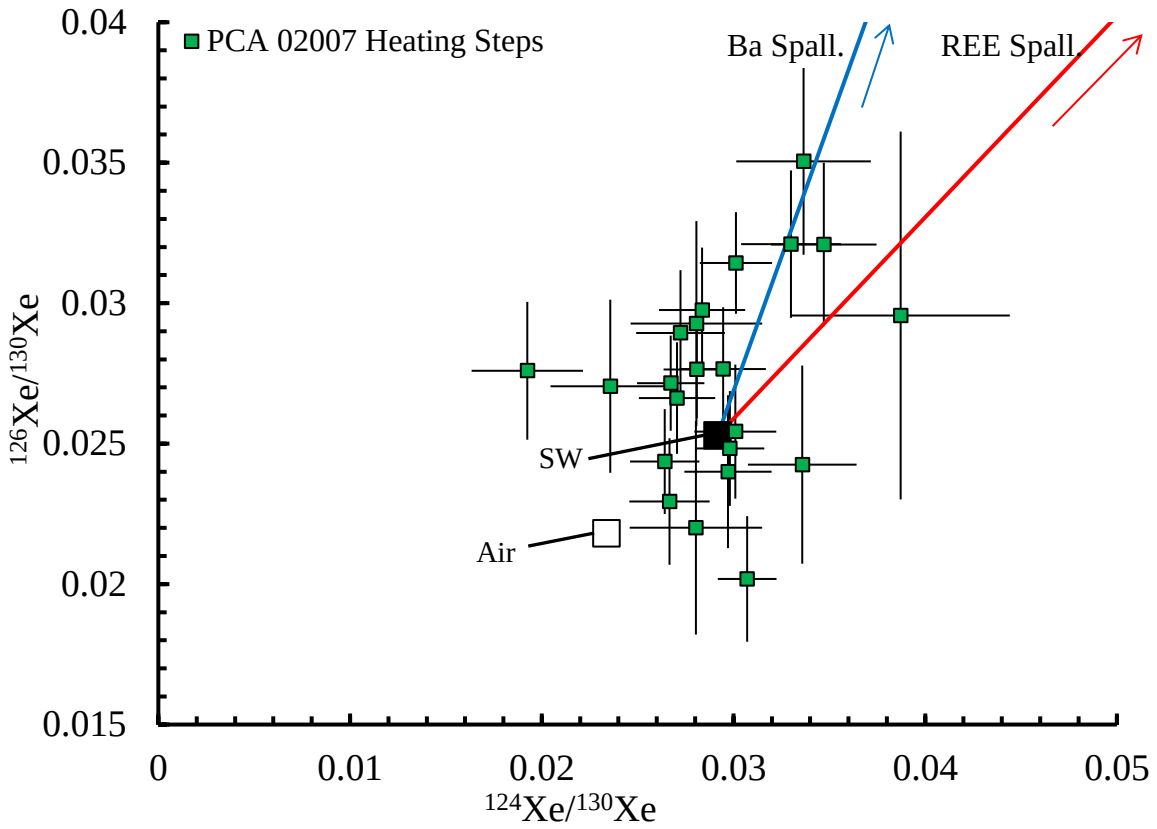


***Figure 5.4*** *Three isotope plot of $^{124}Xe/^{130}Xe$ (abscissa) and $^{126}Xe/^{130}Xe$ (ordinate) for xenon released in heating steps from PCA 02007 (green square indicates one heating step). End members: solar wind ("SW", black square), Earth's atmosphere ("Air", white square). Spallation contributions are plotted as mixing lines from SW for Ba (blue line) and REE (red line). Error bars represent 1σ. End member data are taken from Table 5.1.*

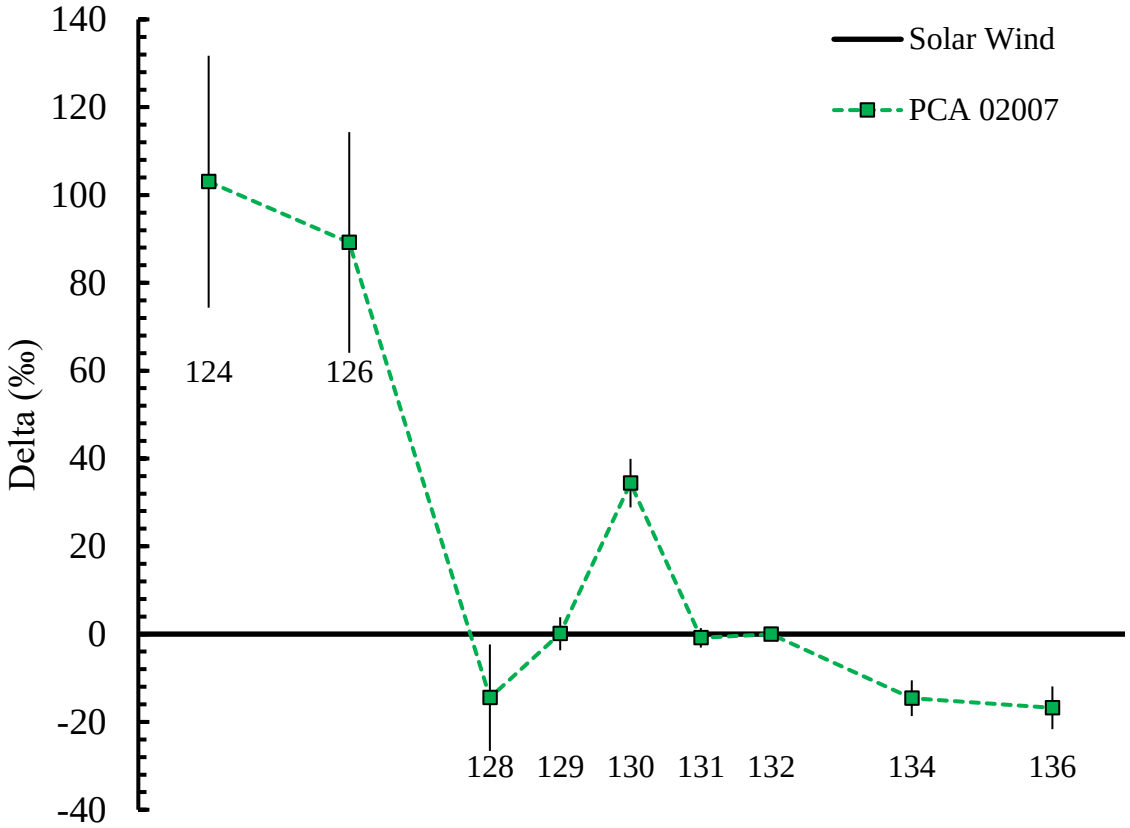


***Figure 5.5*** *Delta plot of average xenon isotopic composition of PCA 02007 as permille deviations from solar wind. Uncertainty represented as standard errors about the mean. Solar wind composition from Meshik et al. (2014).*

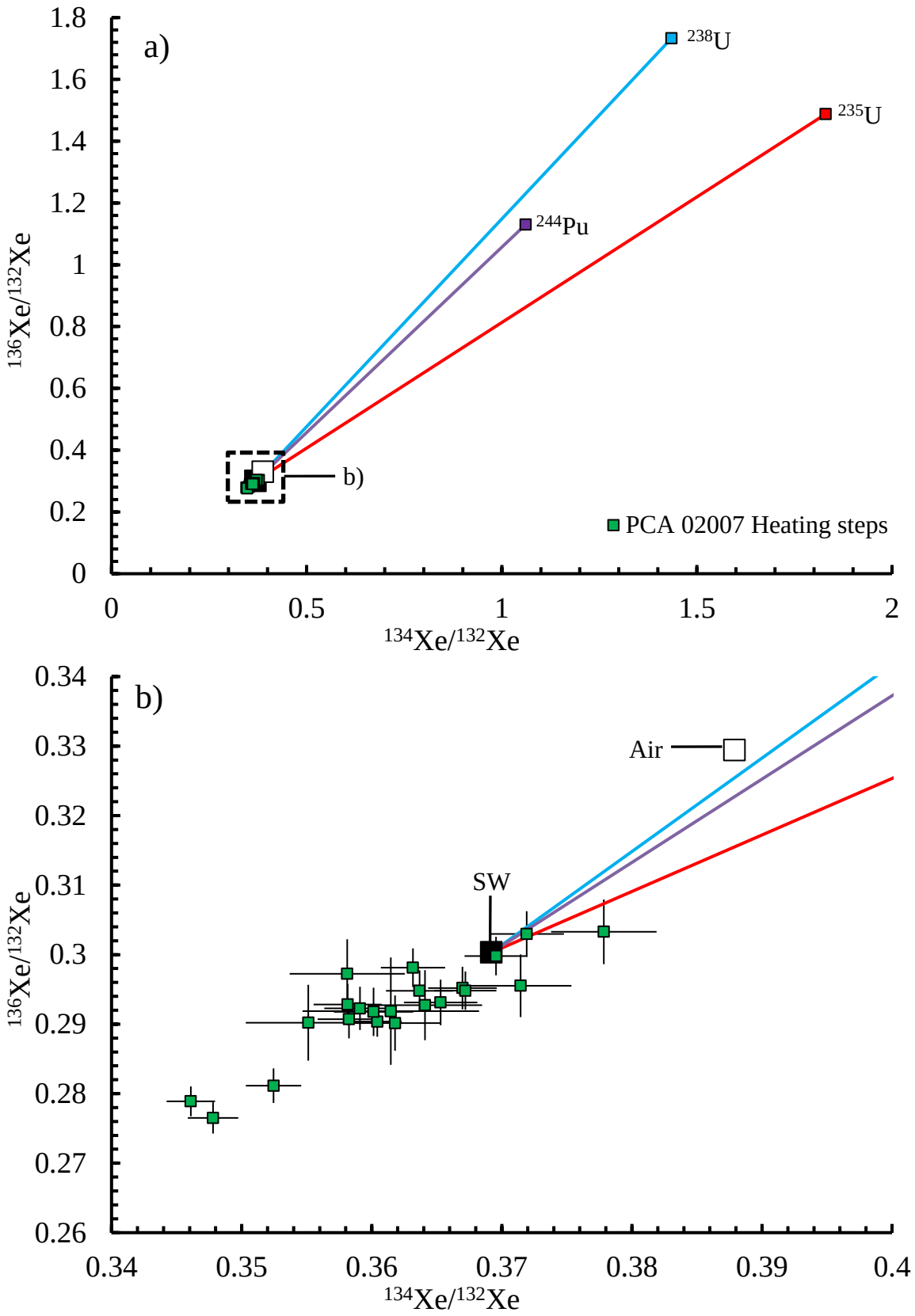


***Figure 5.6*** *Three isotope plots of $^{134}Xe/^{132}Xe$ (abscissa) and $^{136}Xe/^{132}Xe$ (ordinate) for xenon released in heating steps from PCA 02007 (green square indicates on heating step). Inset b) expands dashed box labelled "b)" in figure a). End members: solar wind ("SW", black square), Earth's atmosphere ("Air", white square) also plotted. Fission contributions are plotted as mixing lines from Q to $^{235}U$ (red line), $^{238}U$ (blue line), and $^{244}Pu$ (purple line). Error bars represent 1σ. End member data are taken from Table 5.1.*

#### 5.4.4.2. "Q" Vigarano II xenon

The results for the stepped heating of "Q" Vigarano II are presented in Table 5.1, Figure 5.7, Figure 5.8, Figure 5.9, and Figure 5.10. Up to ~ 10 µg of sample material was analysed, although not to completion, weight precision was limited at this value due to the scale used. Figure 5.7 shows a tight compositional group around the Q-Xe composition of Busemann et al. (2000), and a potential contribution from fission components ($^{235}$U, $^{238}$U, or $^{244}$Pu, combined on top plot of Figure 5.7 as broad purple line), or Xe-HL. A trend towards cosmogenic isotopes produced by spallation of Ba and/or REEs (Figure 5.7) may also be present. Figure 5.9 focuses on the isotopes most affected by cosmogenic processes such as spallation. The "Q" Vigarano II data cluster around Busemann et al. (2000) Q-Xe once again, and do not appear to contain any significant cosmogenic composition, as best illustrated by their composition being far from the end members of Ba or REE spallation in Figure 5.9 a). There does appear to be a minor enrichment in the $^{124}$Xe/$^{130}$Xe composition outside the expected mixing lines between cosmogenic and Q-Xe, most notably in Figure 5.9 b), possibly a consequence of fractionation before or during analysis, or the presence of a composition enriched in the lightest isotopes, such as Xe-HL. Figure 5.10 includes the heavier isotopes which are enriched in Xe-HL and produced by fission of $^{235}$U, $^{238}$U, and $^{244}$Pu with mixing lines from Q-Xe. Many of the heating steps of "Q" Vigarano II contained xenon which appears to be enriched in the heavier isotopes of xenon relative to Busemann et al. (2000) Q-Xe. This may indicate minor amounts of fission xenon, most likely from fission of $^{235}$U according to Figure 5.10 b).

"Q" Vigarano II xenon appears to feature a minor enrichment in heavy and light isotopes relative to Busemann et al. (2000) Q-Xe. The light isotope enrichment is unlikely to correspond to the presence of spallation products of Ba or REE, as the compositions do not reside upon a mixing line between Q-Xe and either component. Any such mixture

would be more obvious on the plots of Figure 5.9 due to dissimilarity of the spallation end members and Q-Xe. Similarly, the heavy isotope enrichment relative to Q-Xe is not easily attributed to fission products apart from $^{235}$U, whose minor contribution may be apparent in Figure 5.10 b), yet the compositions are still very far removed from the fission end members in Figure 5.10 a).

One possible explanation is minor enrichments in $^{124}$Xe relative to Q-Xe from fractionation either within the instrument or the xenon of "Q" Vigarano II, and a minor contribution of xenon from the fission products of $^{235}$U. However, fractionation would exhibit a complimentary enrichment in $^{126}$Xe, which is not observed in Figure 5.9 b). The delta plot of Figure 5.8 expresses a correlation in $^{124}$Xe and $^{126}$Xe excess relative to the Q-Xe defined in Busemann et al. (2000) used throughout this work, as would be expected with mass fractionation. Figure 5.8 also shows a consistent excess of $^{129}$Xe relative to Busemann et al. (2000) Q-Xe, potentially a result of the decay of $^{129}$I. This is consistent with the presence of the daughter isotopes of the similarly short-lived fissiogenic isotope $^{235}$U, which is to be expected of material from such a primitive meteorite, and is consistent with parallel analyses (Busemann et al., 2000; Will et al., 2017). "Q" Vigarano II xenon may also be explained by a composition of Q-Xe with larger contributions from $^{129}$I decay and Xe-HL than the Q-Xe defined in Busemann et al. (2000) used throughout this work, such as in Bekaert et al. (2019). Figure 5.8 compares "Q" Vigarano II xenon to Q-Xe from Busemann et al. (2000) and the Paris meteorite insoluble organic matter of Bekaert et al. (2019), showing a similar heavy isotopic enrichment to the Paris meteorite in "Q" Vigarano II, possibly from a similar H-Xe enrichment, but no enrichment in the light isotopes or $^{129}$Xe, and no $^{130}$Xe depletion. Despite the curious features of xenon in "Q" Vigarano II, the consistency of the extracted xenon composition in multiple steps, and its distinction from xenon as measured in PCA 02007, makes it suitable for the use as an analogue according to the criteria explained in Section 5.4.

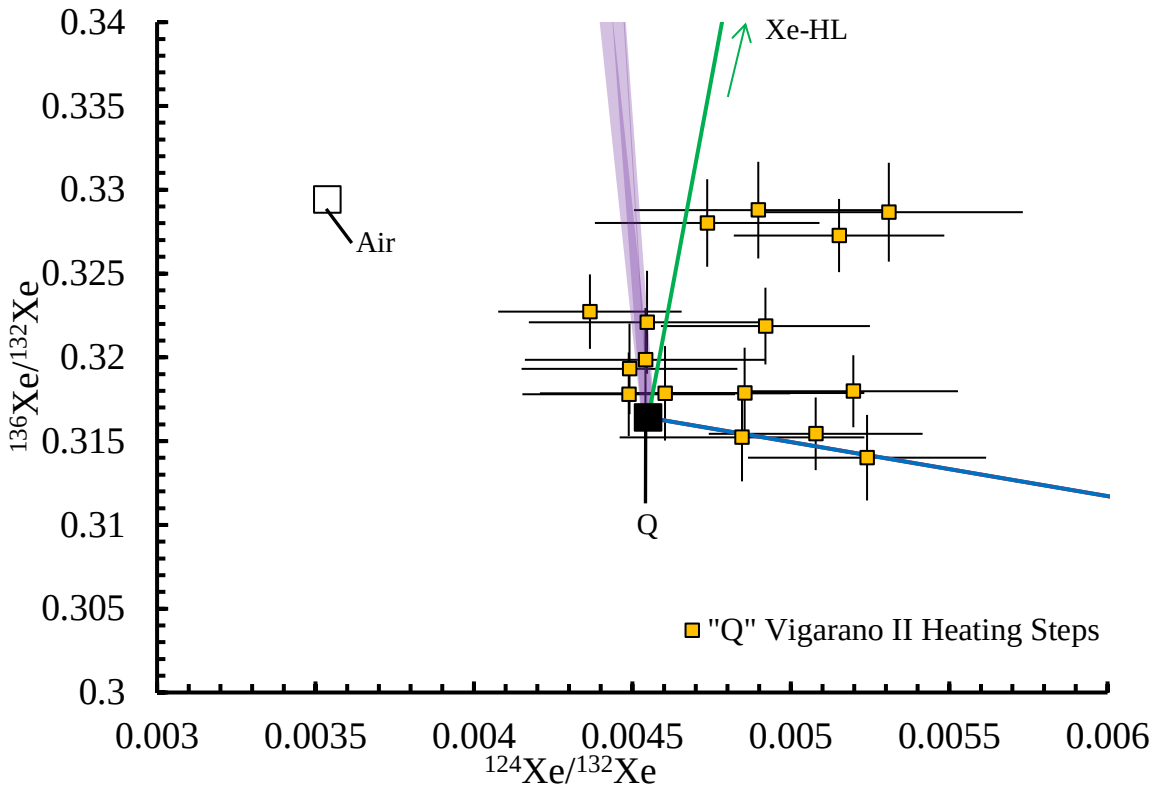


***Figure 5.7*** *Three isotope plot of $^{124}Xe/^{132}Xe$ and $^{136}Xe/^{132}Xe$ for xenon released in heating steps of "Q" Vigarano II (orange square for each heating step). End members: Q (black square), Earth's atmosphere ("Air", white square), Xe-HL (green line) are also plotted. Spallation contributions are plotted as mixing lines from Q for Ba (blue line) and REE (red line). Fission contributions are plotted as a singular mixing line (purple) from Q to $^{235}U$, $^{238}U$, and $^{244}Pu$. Error bars represent 1σ. End member data from Table 5.1.*

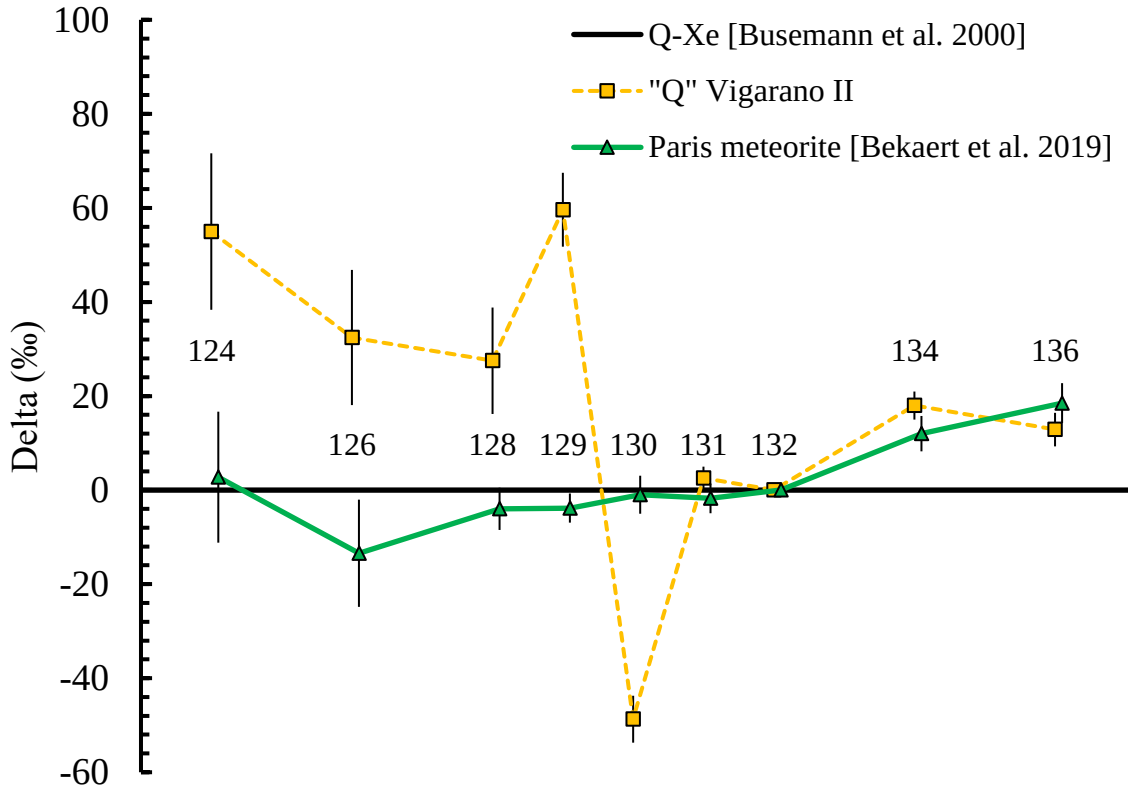


***Figure 5.8*** *Delta plot of average xenon isotopic composition of "Q" Vigarano II as permille deviations from Q-Xe. Uncertainty represented as standard errors about the mean. Q-Xe composition from Busemann et al. (2000), and insoluble organic matter from Paris meteorite (average of multiple samples) Bekaert et al. (2019).*

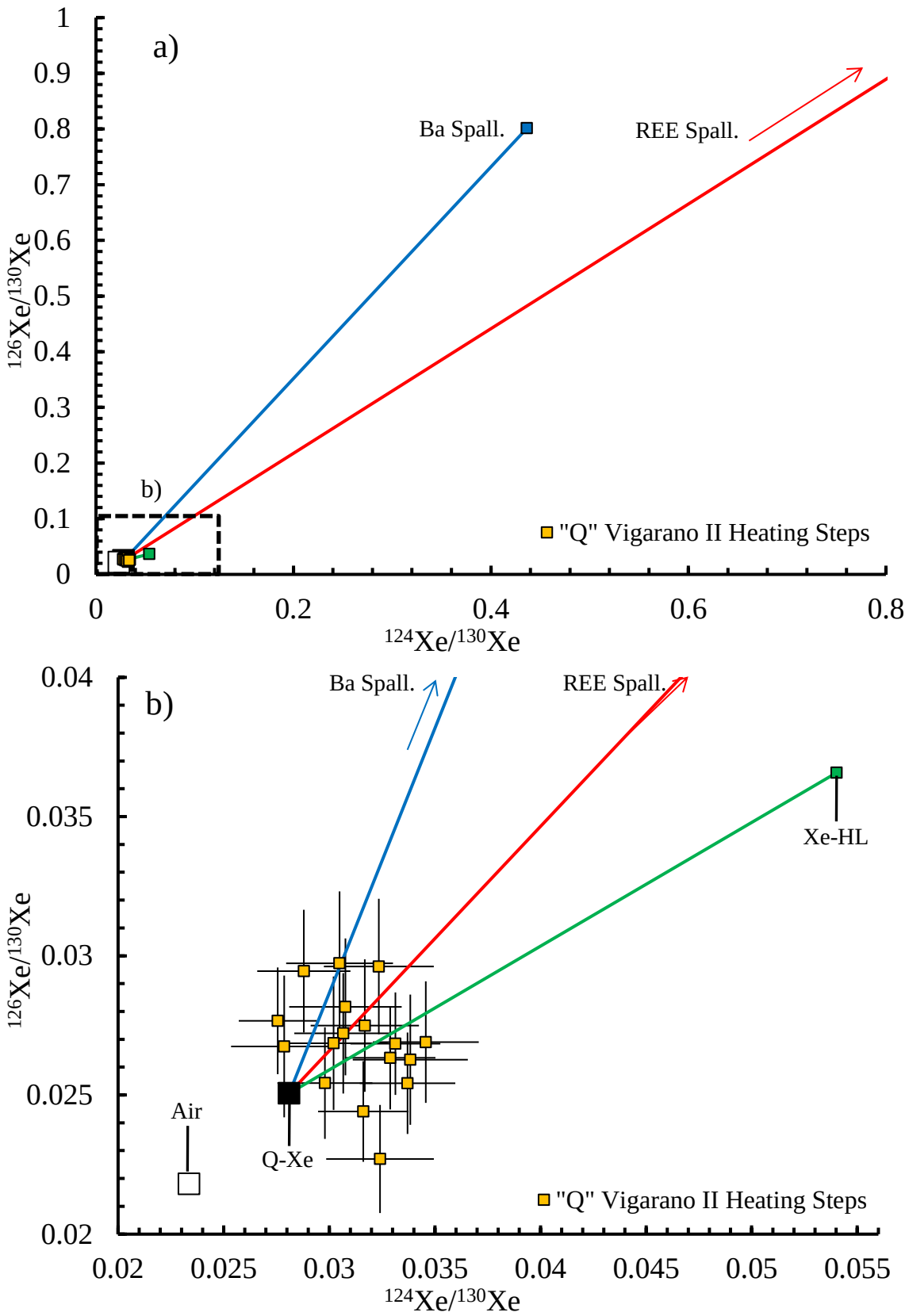


***Figure 5.9*** *Three isotope plots of $^{124}Xe/^{130}Xe$ (abscissa) and $^{126}Xe/^{130}Xe$ (ordinate) for xenon released in heating steps from "Q" Vigarano II (orange square indicates one heating step). End members: Q-Xe (black squares), Earth's atmosphere ("Air", white squares), and Xe-HL (green squares) are also plotted. Inset b) expands dashed box labelled "b)" in figure a). Xe-HL (green line) and spallation contributions are plotted as mixing lines from Q for Ba (blue line) and REE (red line, with composition, $^{124}Xe/^{130}Xe = 22$, $^{126}Xe/^{130}Xe = 25$, which plots outside range of figure). Error bars represent 1σ. End member data are taken from Table 5.1.*

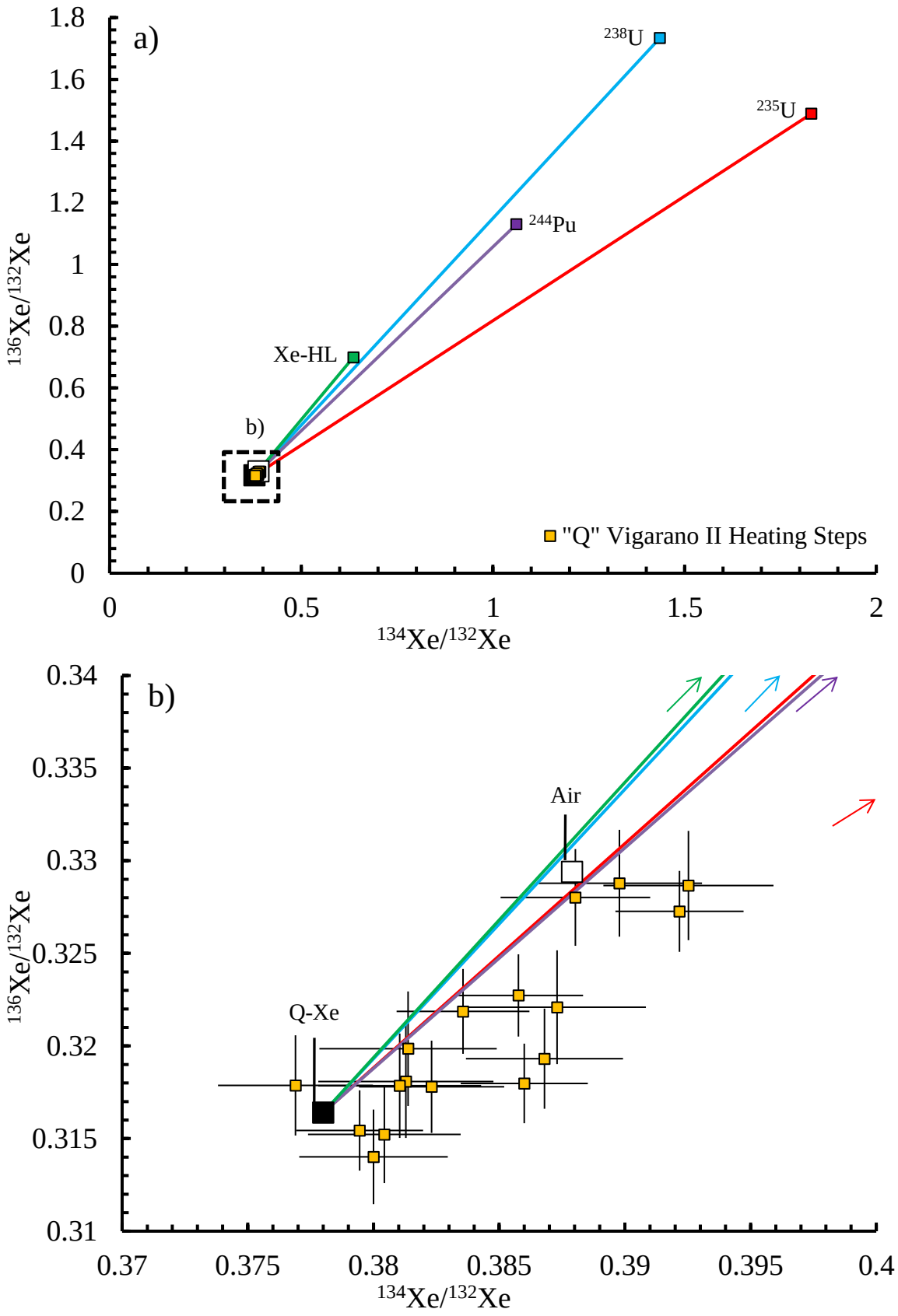


***Figure 5.10*** *Three isotope plots of $^{134}Xe/^{132}Xe$ (abscissa) and $^{136}Xe/^{132}Xe$ (ordinate) for xenon released in heating steps from "Q" Vigarano II (orange square indicates one heating step). Inset b) expands dashed box labelled "b)" in figure a). End members plotted: Q (black squares), Earth's atmosphere ("Air", white squares), and Xe-HL (green squares). Potential contributions are plotted as mixing lines from Q to $^{235}U$ (red line), $^{238}U$ (blue line), $^{244}Pu$ (purple line), as is Xe-HL (green line). Error bars represent 1σ. End member data are taken from Table 5.1*

## 5.5. Closed-system stepped etching of Stardust analogue with RELAX

### 5.5.1. Methodology

The Au sample finger was removed from the CSSE apparatus and cleaned by multiple cycles of injecting and evaporating deionised water and methanol using a syringe and heat lamp; cycles were repeated until there was no observed mass change. Once clean, aliquots of aerogel (of a volume equivalent to the previous aerogel CSSE/RELAX experiments of O'Mara et al. (2014)), then "Q" Vigarano II and PCA 02007 (in identical masses to those used in stepped heating, ~ 10 μg each) were separately prepared and transferred to the sample finger by tweezers and a foil funnel. The gold sample finger was them reattached to the CSSE apparatus with a replaced platinum gasket and thinner brass spacer to account for the spreading of the soft gold parts of the flange. Pumping and gentle baking (< 150 ℃) of the CSSE apparatus excluding the acid finger was then conducted for 48 hours until the pressure stabilised at ~ $10^{-8}$ mbar.

A first attempt at etching with CSSE and RELAX produced results which were indicative of no etching having occurred, with no sample etch releases exceeding the procedural blanks. The acid finger of the CSSE was subsequently removed and refilled with concentrated HF (~ 0.3 ml), before the beginning of the etching steps explained in the following sections. The time before fresh acid was introduced was used to replace the entire stainless-steel section of the etching apparatus to remove previous HF contamination and introduce fresh CaO for neutralisation of any residual HF in the etched sample gas. Blank accumulation tests on all of the gold/platinum valves after the rebuild confirmed their ability to seal themselves from pumping and open to release their accumulated blank.

Etching steps began with acid vapour exposures in which the sample was exposed to HF from the acid finger held at −70 ℃. These steps increased rapidly in duration from tens of seconds up to 80 minutes (in 6 increments, "−70 ℃ HF Vapour" of Table 5.2) due to the low quantities of released xenon. The next steps employed acid vapour etching at room temperature followed by condensation of the acid back into the acid finger, and yielded much more promising quantities of xenon. Twenty-nine of these steps were conducted with increasingly longer periods of room temperature acid vapour exposure (from one minute up to 120 hours). The final etch step consisted of distillation of the acid into the sample finger, followed by recondensation in the acid finger before analysis. Etching conditions and durations were based on the results of similar work (Wieler and Baur, 1994; Heber, 2002; Riebe et al., 2017), and personal correspondence with H. Busemann and P. Will of ETH Zürich during their parallel experiments.

The stepped heating analyses of the samples contained in the gold finger, plus the addition of aerogel containing a significant concentration of atmospheric xenon, suggested the etching steps would release large quantities of xenon. Steps were taken to reduce the amount of xenon allowed into RELAX by segregating the total sample gas volume and analysing a smaller aliquot of the treated sample gas (as described in Section 2.3.2). Depending upon the amount of xenon contained within this aliquot, the remainder of the sample gas would be admitted into the ion source or pumped away. As determining compositions was the primary purpose of this etching, and not concentrations within the etched sample, the removal of this "excess" gas did not affect the results. There were no grounds to conceive of a fractionation as a result of this aliquoting, and the sample gas was assumed to be homogeneously mixed. The effects of partial ionisation of the small aliquot test before introduction of the remaining sample gas was found to be minimal by testing with air calibrations.

Blanks and air calibrations were conducted throughout to mirror the timing and processes involved in sample gas treatment up to the mass spectrometer. All variations of blanks (outlined in Section 2.3.1) were conducted. Acid blanks via the detour were conducted four times throughout the entire etching process after large amounts of xenon were released. None of the acid blanks featured significant amounts of xenon.

The application of appropriate blanks during data reduction is a problem inherent in CSSE due to the inaccessibility of the sample volume during etching, and the impractical and imperfect recreation of procedural blanks that results from it. Blank gas accumulates at a constant rate from any given volume of the mass spectrometer and CSSE apparatus. The etching steps frequently varied in duration and exposure to specific volumes of the mass spectrometer or apparatus, for example, acid vapour etches accumulate atmospheric blank from the acid and sample finger during etching, whereas a wet etches distil the acid into the sample finger and seal the acid within, thus closing off the blank accumulation from the acid finger. In the case of acid finger blank accumulation, the accumulation rate cannot be quantified during sample analysis without exposing the sample to acid.

For the etching data in this work, a blank correction was made based on the 'procedural blank' approach described in Section 2.3.1.1, which effectively constrains the xenon accumulated during the gas treatment section of the CSSE apparatus and RELAX, without the sample finger (G1B of Figure 2.2 remains closed). This blank was measured before and after each etching step and subtracted from the etched sample xenon signal. The average figure for one of these procedural blanks was ~ $4.5 \times 10^{-16}$ $cm^3$ STP of $^{132}Xe$ (or ~ 12,000 $^{132}Xe$ atoms), this figure effectively represents a minimum blank applied to each etching step. However, the rate of accumulation of atmospheric blank was thoroughly tested before the acid and sample was loaded, and the rates are not expected to be

significant in sample releases confidently exceeding the applied blank (of which many etches achieved, as in Figure 5.11).

### 5.5.2. Results

The following section details the results of measuring the xenon released from the etching of the Stardust analogue (described in Section 5.4) within the CSSE apparatus attached to the RELAX mass spectrometer. Table 5.2 contains the xenon concentrations and isotopic compositions of released gases on a step-by-step basis, including details on the etching conditions. Figures 5.11 to 5.16 illustrate an investigation into the source of the released xenon through the amount and nature of xenon released in the steps.

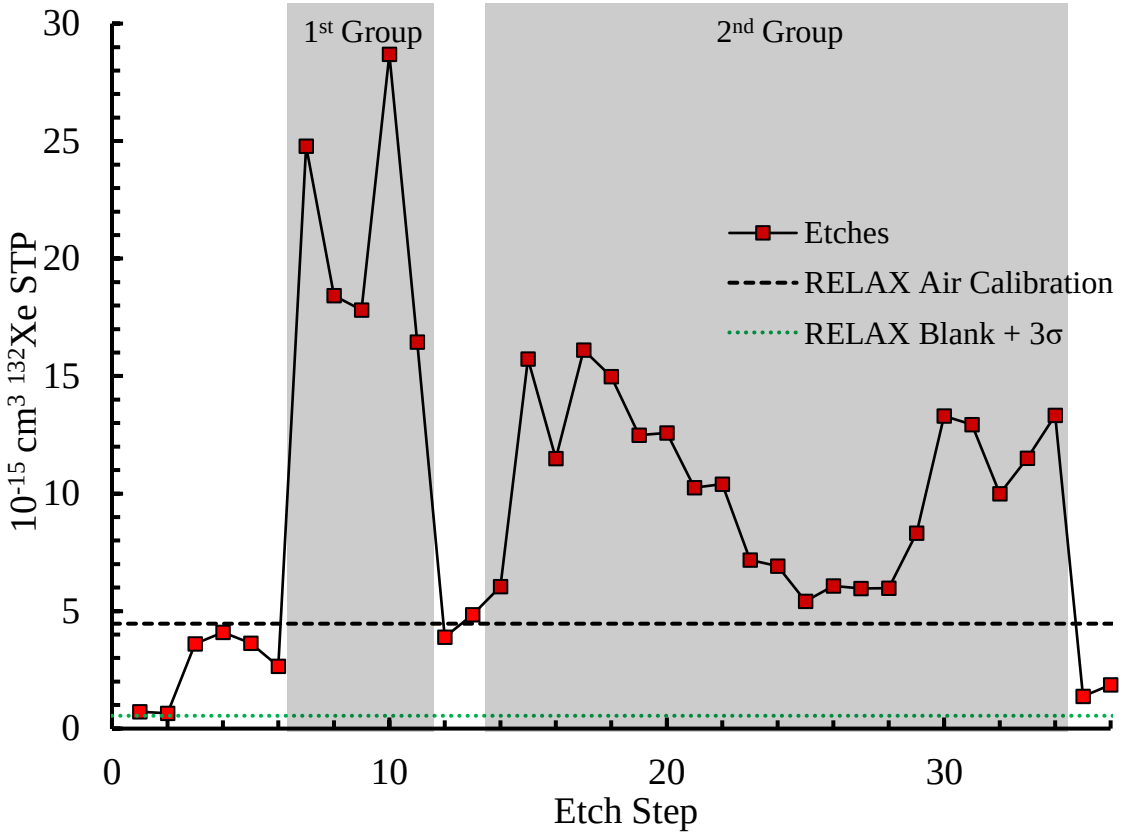


***Figure 5.11*** *Plot of total $^{132}Xe$ (in $10^{-15}$ $cm^3$ STP) released from sequential etch steps (red squares, connected in sequence by black line and abscissa). RELAX "Air Calibration" (black dashed line), and RELAX blank + 3σ (green dotted line) included for reference, and explained in Section 2.1.1. Etch data are not blank corrected. Grey shaded areas indicate groups of steps which most resembled PCA 02007 xenon (1st group) and air xenon (2nd group), as described in 5.2.2.*

Figure 5.12 and Figure 5.13 show a compositional dichotomy in the xenon released in the analogue etching steps, illustrating two distinct compositional groups corresponding to the etch steps before (1st Group) and after (2nd Group) the fifteenth etching step, when etching conditions were room temperature HF vapour exposures for an hour. This dichotomy is also expressed in the amount of gas released during etching, as shown in Figure 5.11, which shows a dip in the amount of gas released between the 1st and 2nd group, and a clear increase in the amount of gas released in either group compared to the blank. Figure 5.14 and Figure 5.15 show these compositional groups relative to the end members which may be expected during etching, air xenon from the aerogel, solar wind, and the previously measured PCA 02007 compositions. The etched releases of xenon which least resembled air belong to the 1st group and reside on a mixing line between solar wind/PCA 02007 and air xenon. The following etches which comprise the 2nd group are exclusively of compositions most closely resembling air-Xe. This result is contradictory to the expected order of etching, in which air xenon from aerogel were expected to release xenon first, and then more vigorous steps would trend towards solar wind and PCA 02007.

Table 5.2 and Figure 5.11 exhibit the amounts of gas extracted from the analogue etches in this work. These concentrations were significantly lower than was expected from the amount of sample included, and in many cases did not exceed the blank on the less abundant isotopes (as in the "n.d." of Table 5.2). The first six analogue etching steps conducted under HF acid vapour at −70°C in this work were comparable to the etching conditions of O'Mara et al. (2014), with what should have been an identical amount of aerogel, yet their etches released ~ $1.2 \times 10^{-11}$ $cm^3$ STP of $^{132}Xe$, whereas this work did not exceed the air calibration (~ $4 \times 10^{-15}$ $cm^3$ STP of $^{132}Xe$). In comparison to the stepped heating analyses, the total volume of gas released during all of the etching in this work did not exceed some of the larger heating steps. The first significant extractions of sample gas (exceeding the air calibration signal) occurred under room temperature acid vapour etches,

yet the concentration was still significantly lower than the etching steps of O'Mara et al. (2014). The significantly lower extractions of sample gas than was expected from the equivalent data of O'Mara et al (2014) suggested the etching was somehow inhibited. The subsequent etch steps increased the etching severity more rapidly than the first six etching steps, progressing to room temperature etches which increased according to the concentration of the previous step and similar etching experiment step progression (as discussed in Section 2.2.1) (Weiler et al., 1986; Heber, 2002; Riebe et al., 2017). As in previous experiments (Heber, 2002; O'Mara et al., 2014; Riebe et al., 2017), some etching conditions were repeated when the released xenon concentration was within an acceptable range. The quantity of released xenon never came close to the concentration of the previous aerogel etch of O'Mara et al. (2014), even in totality, with the total amount of $^{132}Xe$ analysed during these experiments being ~ $3.5 \times 10^{-13}$ $cm^3$ STP of $^{132}Xe$, an order of magnitude lower than some individual acid vapour etch steps of O'Mara et al. (2014).

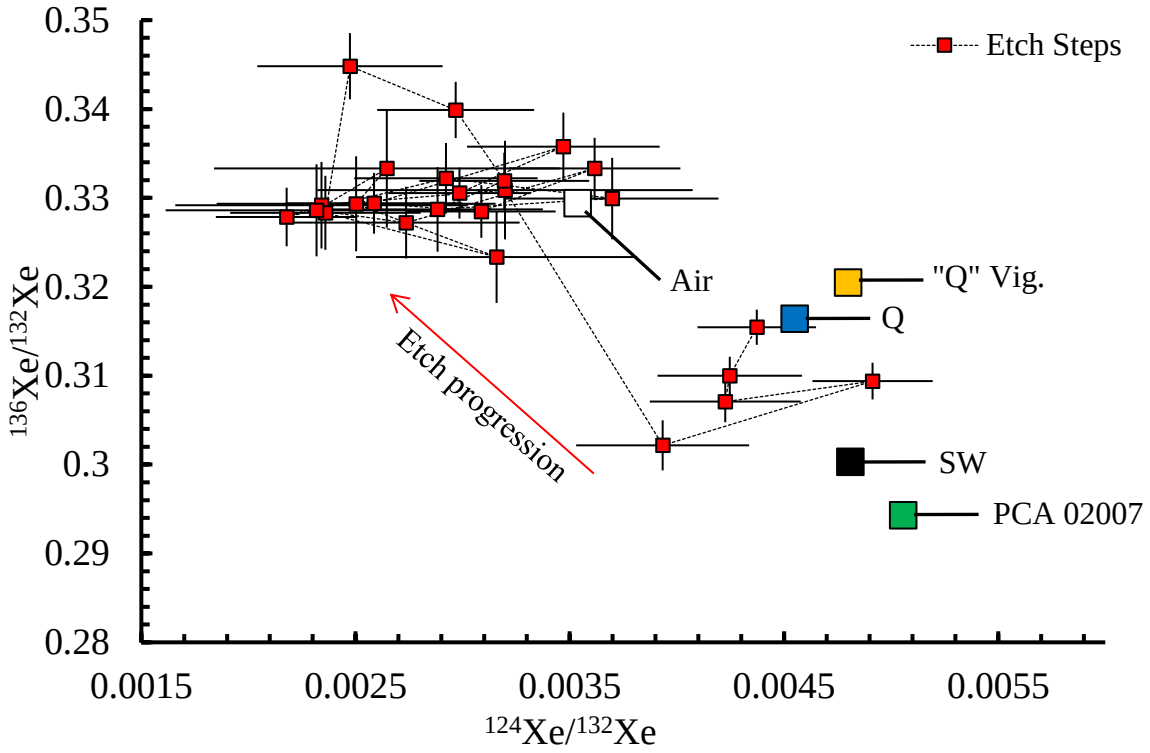


***Figure 5.12*** *$^{124}Xe/^{132}Xe$ and $^{136}Xe/^{132}Xe$ for xenon released in stepped etching of Stardust analogue (red square is one etching step, connected in sequence by dotted black line). Red arrow roughly indicates etch order. End members plotted as squares. Air/Aerogel (white), PCA 02007 (green), and "Q" Vigarano II (orange), plotted with literature values for; Q-Xe (blue), SW-Xe (black). Error bars are 1σ. Data from Table 5.1 (End members) and Table 5.2 (Etches). Etches not confidently in excess of RELAX blank are omitted.*

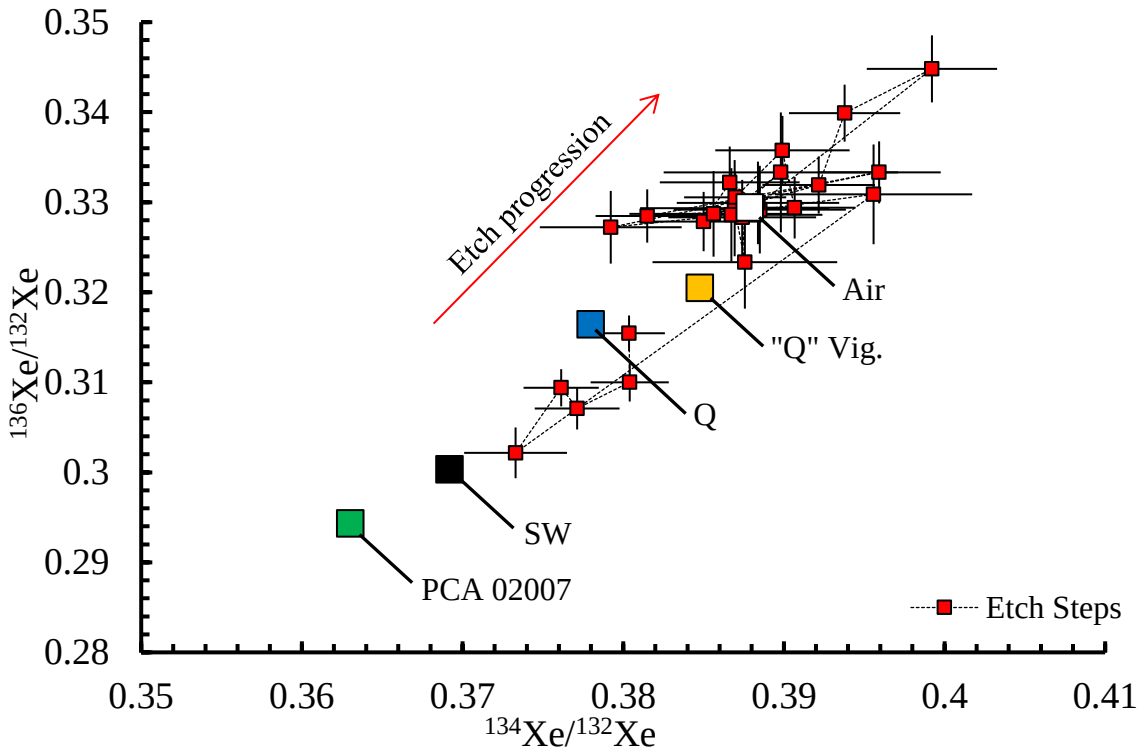


***Figure 5.13*** *$^{134}Xe/^{132}Xe$ and $^{136}Xe/^{132}Xe$ for xenon released in stepped etching of Stardust analogue (red square is one etching step, connected in sequence by dotted black line). Red arrow roughly indicates etch order. End members plotted as squares. Air/Aerogel (white), PCA 02007 (green), and "Q" Vigarano II (orange), plotted with literature values for; Q-Xe (blue), SW-Xe (black). Error bars are 1σ. Data from Table 5.1 (End members) and Table 5.2 (Etches). Etches not confidently in excess of RELAX blank are omitted.*

Figure 5.12 and Figure 5.13 show none of the etch steps extracting xenon resembling a pure PCA 02007 or solar wind xenon composition. Figure 5.14 and Figure 5.15 shows the 2nd group of etches extracted xenon which closely resembles the composition of air. None of the releases resembled Q-Xe or "Q" Vigarano II xenon compositions, as was expected with the HF etching.

The final two etch steps were conducted under significantly more severe etching conditions in order to etch all HF susceptible materials remaining within the CSSE apparatus. These are conditions resembling the most vigorous of etching steps of more resilient and larger samples analysed by CSSE elsewhere (Heber, 2002), conditions assumed to be severe enough for dissolving the smaller and more labile samples of this work. These last two etch steps extracted quantities of xenon which were not in excess of

RELAX's air calibration, in concentrations significantly lower than the preceding steps, so the etching was assumed to have stopped.

In total, the concentration of xenon resembling solar wind/PCA 02007 released during the etching was $1.1 \times 10^{-13}$ cm$^3$ STP of $^{132}$Xe. The stepped heating experiments extracted $6.8 \times 10^{-13}$ cm$^3$ STP of $^{132}$Xe before the experiment was stopped, so the total is most probably higher than that figure. The inconclusive results made proceeding with the $HNO_3$ etching of the organic phase "Q" Vigarano II of the Stardust analogue inadvisable before ascertaining whether the CSSE apparatus was functioning correctly.

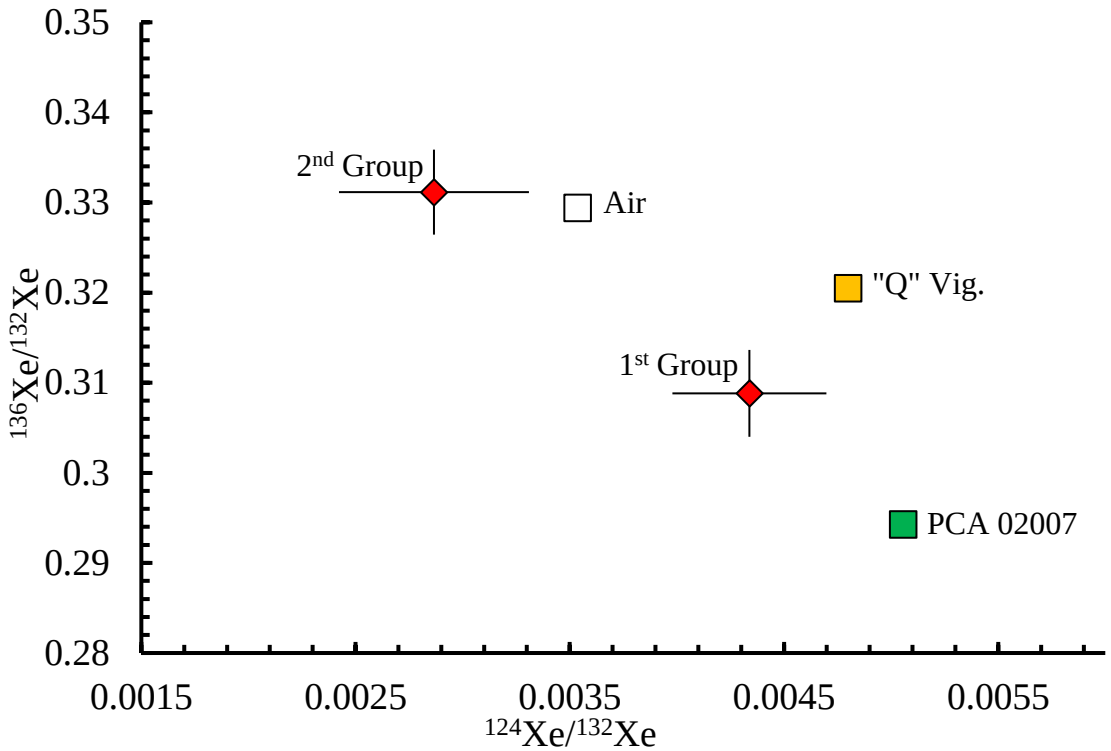


***Figure 5.14*** *Three isotope plot of $^{124}Xe/^{132}Xe$ (abscissa) and $^{136}Xe/^{132}Xe$ (ordinate) for xenon released in similarly composed groups of etching steps of Stardust analogue as described in Section 5.5 (red diamonds with sequence labelled). Expected analogue material end members as measured in this work; Air/Aerogel (white square), PCA 02007 (green square), and "Q" Vigarano II (orange square), are plotted as presented in Table 5.1 Etch data are presented in Table 5.2 Error bars represent 1σ.*

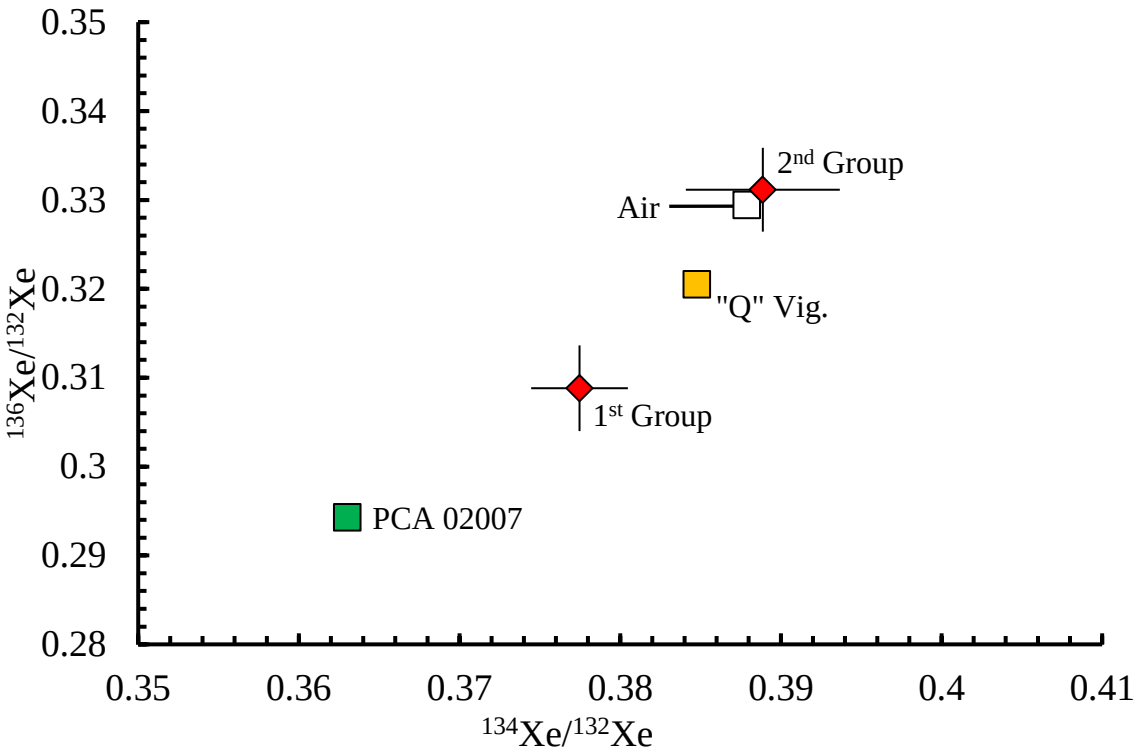


***Figure 5.15*** *Three isotope plot of $^{134}Xe/^{132}Xe$ (abscissa) and $^{136}Xe/^{132}Xe$ (ordinate) for xenon released in similarly composed groups of etching steps of Stardust analogue as described in Section 5.5 (red diamonds with sequence labelled). Expected analogue material end members as measured in this work; Air/Aerogel (white square), PCA 02007 (green square), and "Q" Vigarano II (orange square), are plotted as presented in Table 5.1 Etch data are presented in Table 5.2 Error bars represent 1σ.*

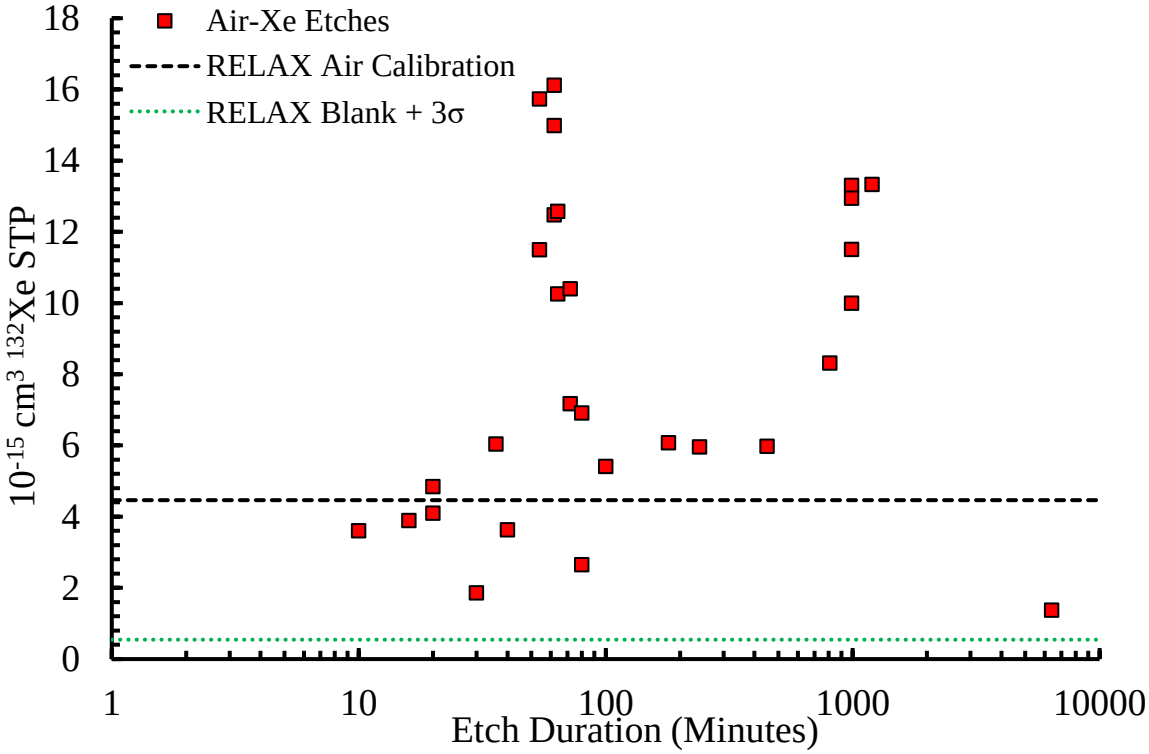


***Figure 5.16*** *Plot of etching step duration (abscissa, minutes) and extracted Stardust analogue $^{132}Xe$ (ordinate, in $10^{-15}$ $cm^3$ STP) released from sequential etch steps whose compositions resembled air-Xe (red squares). RELAX "Air Calibration" (black dashed line), and RELAX blank +3σ (green dotted line) included for reference, and explained in Section 2.1.1. Etch data are not blank corrected. Error bars are plotted on the figure but are small enough to be obscured by the data points.*

***Table 5.2*** *Xenon isotopic concentrations and compositions from stepped etching of Stardust analogue with CSSE and the RELAX mass spectrometer.*

| Etch Parameters | | Concentration | Xenon Isotopic Compositions Normalised to $^{132}Xe \equiv 100$ | | | | | | | | | | | | | | | |
|---|---|---|---|---|---|---|---|---|---|---|---|---|---|---|---|---|---|---|
| *Acid Condition* | *Duration* | $10^{-16}$ cm$^3$ $^{132}$Xe STP | 124 | | 126 | | 128 | | 129 | | 130 | | 131 | | 134 | | 136 | |
| *-70°C HF Vapour* | *10 sec.* | 3.95 | n.d. | | n.d. | | n.d. | | 88.42 | (6.14) | 11.91 | (1.91) | 81.96 | (5.67) | 40.50 | (3.65) | 35.09 | (n.d.) |
| | *30 sec.* | 3.23 | n.d. | | n.d. | | n.d. | | 98.81 | (7.56) | 16.34 | (2.4) | 81.25 | (6.5) | 39.30 | (4.21) | 38.64 | (n.d.) |
| | *10 min.* | 32.79 | n.d. | | n.d. | | 5.65 | (0.36) | 99.98 | (1.53) | 13.23 | (0.43) | 80.99 | (1.32) | 40.07 | (0.83) | 33.94 | (n.d.) |
| | *20 min.* | 37.69 | n.d. | | n.d. | | 5.98 | (0.33) | 99.36 | (1.41) | 14.10 | (0.41) | 79.37 | (1.2) | 39.36 | (0.77) | 33.70 | (n.d.) |
| | *40 min.* | 33.03 | n.d. | | n.d. | | 6.48 | (0.37) | 101.23 | (1.54) | 14.96 | (0.46) | 80.68 | (1.31) | 38.76 | (0.82) | 33.37 | (n.d.) |
| | *80 min.* | 23.26 | n.d. | | n.d. | | 5.50 | (0.46) | 100.53 | (1.82) | 14.81 | (0.54) | 78.93 | (1.53) | 39.35 | (0.98) | 32.23 | (n.d.) |
| *Room Temperature (21°C) HF Vapour* | *1 min.* | 244.57 | 0.44 | (0.03) | 0.40 | (0.02) | 8.19 | (0.09) | 104.44 | (0.44) | 16.89 | (0.15) | 82.27 | (0.37) | 38.04 | (0.22) | 31.54 | (n.d.) |
| | *2 min.* | 180.92 | 0.42 | (0.03) | 0.43 | (0.03) | 8.06 | (0.11) | 103.30 | (0.48) | 15.90 | (0.16) | 81.74 | (0.4) | 38.04 | (0.24) | 31.00 | (n.d.) |
| | *4 min.* | 174.88 | 0.42 | (0.04) | 0.38 | (0.04) | 8.35 | (0.12) | 103.37 | (0.51) | 15.94 | (0.18) | 81.22 | (0.43) | 37.71 | (0.26) | 30.71 | (n.d.) |
| | *8 min.* | 283.63 | 0.49 | (0.03) | 0.42 | (0.03) | 8.51 | (0.1) | 104.54 | (0.47) | 16.90 | (0.18) | 81.88 | (0.4) | 37.61 | (0.23) | 30.94 | (n.d.) |
| | *16 min.* | 161.21 | 0.39 | (0.04) | 0.42 | (0.04) | 8.53 | (0.14) | 104.46 | (0.64) | 16.81 | (0.2) | 82.08 | (0.53) | 37.33 | (0.32) | 30.22 | (n.d.) |
| | *16 min.* | 33.44 | 0.24 | (0.11) | 0.14 | (0.1) | 7.35 | (0.34) | 103.25 | (1.52) | 15.18 | (0.45) | 82.05 | (1.29) | 37.94 | (0.79) | 32.31 | (n.d.) |
| | *20 min.* | 42.96 | 0.32 | (0.09) | 0.22 | (0.08) | 7.46 | (0.26) | 104.28 | (1.17) | 14.57 | (0.34) | 82.45 | (0.99) | 39.56 | (0.61) | 33.09 | (n.d.) |
| | *36 min.* | 54.99 | 0.23 | (0.07) | 0.22 | (0.06) | 7.78 | (0.23) | 105.11 | (1.04) | 15.04 | (0.31) | 81.99 | (0.87) | 38.85 | (0.54) | 32.92 | (n.d.) |
| | *54 min.* | 151.86 | 0.22 | (0.03) | 0.25 | (0.03) | 7.40 | (0.14) | 101.84 | (0.69) | 16.14 | (0.24) | 79.41 | (0.58) | 38.50 | (0.36) | 32.79 | (n.d.) |
| | *54 min.* | 109.51 | 0.29 | (0.04) | 0.20 | (0.04) | 7.41 | (0.17) | 101.57 | (0.83) | 15.75 | (0.26) | 79.69 | (0.69) | 38.66 | (0.44) | 33.22 | (n.d.) |
| | *62 min.* | 155.70 | 0.37 | (0.05) | 0.28 | (0.04) | 7.41 | (0.2) | 102.46 | (0.96) | 15.62 | (0.3) | 80.02 | (0.81) | 38.84 | (0.51) | 32.99 | (n.d.) |
| | *62 min.* | 144.39 | 0.29 | (0.05) | 0.21 | (0.04) | 7.25 | (0.2) | 102.92 | (1.01) | 15.49 | (0.31) | 80.29 | (0.84) | 38.56 | (0.52) | 32.87 | (n.d.) |
| | *62 min.* | 119.36 | 0.32 | (0.04) | 0.28 | (0.04) | 7.57 | (0.14) | 102.04 | (0.67) | 15.88 | (0.21) | 80.77 | (0.56) | 39.22 | (0.35) | 33.19 | (n.d.) |
| | *64 min.* | 120.33 | 0.30 | (0.04) | 0.26 | (0.03) | 7.62 | (0.14) | 102.35 | (0.65) | 16.17 | (0.2) | 79.85 | (0.55) | 39.38 | (0.35) | 33.99 | (n.d.) |
| | *64 min.* | 97.10 | 0.25 | (0.04) | 0.23 | (0.04) | 7.58 | (0.16) | 103.71 | (0.77) | 14.36 | (0.22) | 79.44 | (0.65) | 39.92 | (0.41) | 34.48 | (n.d.) |
| | *72 min.* | 98.59 | 0.24 | (0.04) | 0.26 | (0.04) | 7.33 | (0.18) | 102.52 | (0.88) | 15.01 | (0.26) | 79.20 | (0.73) | 38.74 | (0.46) | 32.83 | (n.d.) |
| | *72 min.* | 66.24 | 0.32 | (0.07) | 0.16 | (0.06) | 7.68 | (0.24) | 103.76 | (1.11) | 15.26 | (0.32) | 79.72 | (0.92) | 38.76 | (0.57) | 32.33 | (n.d.) |
| | *80 min.* | 63.67 | 0.25 | (0.07) | 0.17 | (0.06) | 7.57 | (0.24) | 102.74 | (1.13) | 15.40 | (0.33) | 79.46 | (0.94) | 38.69 | (0.59) | 32.93 | (n.d.) |
| | *100 min.* | 48.68 | 0.16 | (0.08) | 0.27 | (0.08) | 7.95 | (0.29) | 103.87 | (1.32) | 14.66 | (0.38) | 77.40 | (1.08) | 38.90 | (0.69) | 31.78 | (n.d.) |
| | *180 min.* | 55.31 | 0.26 | (0.08) | 0.27 | (0.08) | 7.94 | (0.3) | 104.75 | (1.41) | 15.95 | (0.43) | 80.67 | (1.17) | 38.98 | (0.73) | 33.33 | (n.d.) |
| | *4 hours* | 54.10 | 0.13 | (0.06) | 0.24 | (0.07) | 7.65 | (0.24) | 105.70 | (1.12) | 16.15 | (0.34) | 78.74 | (0.91) | 37.43 | (0.56) | 33.47 | (n.d.) |
| | *7.5 hours* | 54.33 | 0.23 | (0.07) | 0.29 | (0.07) | 7.54 | (0.24) | 107.67 | (1.12) | 16.53 | (0.35) | 80.22 | (0.91) | 38.67 | (0.57) | 32.86 | (n.d.) |
| | *13.5 hours* | 77.74 | 0.27 | (0.05) | 0.24 | (0.05) | 7.82 | (0.18) | 107.89 | (0.88) | 16.28 | (0.28) | 80.76 | (0.72) | 37.92 | (0.44) | 32.72 | (n.d.) |
| | *16.5 hours* | 127.61 | 0.36 | (0.04) | 0.26 | (0.04) | 7.69 | (0.15) | 104.19 | (0.73) | 16.05 | (0.25) | 80.59 | (0.61) | 39.59 | (0.38) | 33.33 | (n.d.) |
| | *16.5 hours* | 123.95 | 0.31 | (0.03) | 0.27 | (0.03) | 7.90 | (0.13) | 105.19 | (0.63) | 16.52 | (0.21) | 79.33 | (0.52) | 38.15 | (0.32) | 32.85 | (n.d.) |
| | *15.5 hours* | 94.49 | 0.26 | (0.04) | 0.25 | (0.04) | 7.49 | (0.15) | 106.82 | (0.74) | 16.56 | (0.24) | 80.52 | (0.61) | 39.07 | (0.38) | 32.94 | (n.d.) |
| | *16.5 hours* | 109.61 | 0.35 | (0.04) | 0.26 | (0.04) | 7.78 | (0.17) | 106.45 | (0.82) | 15.56 | (0.25) | 79.30 | (0.66) | 38.99 | (0.42) | 33.58 | (n.d.) |
| | *20 hours* | 127.83 | 0.30 | (0.03) | 0.23 | (0.03) | 7.55 | (0.13) | 105.10 | (0.62) | 15.76 | (0.21) | 79.77 | (0.5) | 38.70 | (0.32) | 33.05 | (n.d.) |
| | *120 hours* | 8.28 | 0.06 | (0.45) | n.d. | | 6.06 | (1.14) | 108.30 | (5.02) | 13.55 | (1.4) | 77.16 | (3.99) | 36.82 | (2.5) | 33.07 | (n.d.) |
| *"Wet etch" HF distillation* | *30 min.* | 13.15 | n.d. | | 0.25 | (0.26) | 6.01 | (0.75) | 101.07 | (3.28) | 13.63 | (0.94) | 77.56 | (2.73) | 38.37 | (1.74) | 30.54 | (n.d.) |

*Stepped etching of Stardust analogue with CSSE and the RELAX mass spectrometer. All values exceed three standard errors above blank signal. "n.d" indicates the signal did not confidently exceed the blank. Ratios normalised to $^{132}Xe \equiv 100$. Errors in parentheses correspond to standard deviations. Concentration figures for $^{132}Xe$ are in $10^{-16}$ cm$^3$ $^{132}Xe$ STP. Etching conditions elaborated in Section 2.2.1 Repeated durations indicate repeated etches.*

### 5.6. Discussion

The data are conclusive in the sequence of gases being analysed in the order of a composition resembling SW-Xe before a composition resembling air-Xe. This is in contradiction with the expectation of aerogel being etched first to release air-Xe, then PCA 02007 to release a SW-Xe. The etching conditions employed during this work were comparable to the most vigorous of etches in previous work on larger and more resilient samples, so if that expected severity of etching was achieved, the sample finger is unlikely to contain any more HF-soluble material (only "Q" Vigarano II). However, the concentration of $^{132}$Xe released by the stepped heating experiments is around an order of magnitude higher than the concentration of xenon extracted from PCA 02007 by stepped etching ($1.1 \times 10^{-13}$ cm$^3$ STP of $^{132}$Xe), despite the sample finger of the etching line containing the sample amount of sample materials as the stepped heating experiments, and the stepped heating experiments not being conducted until total xenon extraction. The following section attempts to explain these observations by considering possible scenarios and their plausibility.

- *"The etching started with PCA 02007 and progressed to Aerogel, in an order reflecting the sequence of observed compositions"*

  This hypothesis assumes the air xenon composition is attributable to aerogel, and the etching of the aerogel was somehow inhibited, or delayed, until the etching of PCA 02007 had concluded. The acid vapour fills the entire volume available to it, and the aerogel definitely has a larger surface area than the PCA 02007 sample, so this theory requires some sort of blockage to have occurred, possibly during loading of the sample in the gold finger. Alternatively, the cleaning process of the sample finger before the analogue etch may not have removed all previous sample matter, which could have coated the aerogel and inhibited its etching.

A protective coating of the aerogel but not the PCA 02007 seems unlikely. Similarly, a perfect seal blocking a gas from reaching a volume containing the aerogel is unlikely. This theory also neglects the fact that the quantity of measured air-Xe was significantly lower than expected from aerogel, unless the blockage or coating somehow reappeared.

- *"The aerogel was not etched"*

  This hypothesis assumes the aerogel was either completely shielded from the acid vapour, or was not present during the etching. As discussed in the previous theory, a perfectly etch-resistant coating on the aerogel and not PCA 02007 is unlikely. The theory is most consistent with the lack of aerogel in the sample finger during etching. This could have been the result of user error during loading, or the aerogel being "sucked" out of the sample finger after it was loaded. Preferential removal of the aerogel over PCA 02007 during coarse pumping of the sample finger is consistent with its significantly lower density and larger surface area. In this case, the aerogel probably resides somewhere else within the apparatus or attached pumps, beyond the reach of the acid vapour.

  This theory is consistent with the order of analysed xenon being PCA 02007 at first, and the lack of any air xenon being released during the first few steps, which previous experiments suggested were sufficiently vigorous for aerogel etching (O'Mara et al., 2014). It does not satisfactorily explain the later etching steps with their air-Xe composition. Their composition is consistent with attribution to atmospheric blank, and such a blank would presumably be correlated with the time it was allowed to accumulate. This accumulation would have to occur within the sample and acid fingers, as these were the only volumes not accessible to the turbomolecular pump in between etching. Figure 5.16 illustrates no obvious correlation between etch duration and air-Xe concentration, the opposite would be expected if this accumulation were the cause of the signal.

The low concentration of xenon resembling SW-Xe and therefore attributable to PCA 02007 during the etching experiment (~ $1.05 \times 10^{-13}$ $cm^3$ STP of $^{132}Xe$) compared to the stepped heating experiment (~ $6.8 \times 10^{-13}$ $cm^3$ STP of $^{132}Xe$) is equally as unclear, especially given the incompletion of the stepped heating experiment suggesting that the true volume of xenon for the identical sample mass (~ 10 µg) loaded in both the etching and stepped heating was probably larger. The scales used to measure the mass of samples before loading in the stepped heating and etching experiments were not capable of resolving masses lower than the ~ 10 µg which was ultimately loaded in all samples, so the mass could have featured a greater disparity than was shown by the scales. Given this was the smallest mass increment, any mass from 5 µg < 15 µg may have returned this value, but even at the most extreme example of this range, where the stepped heating experiment contained 15 µg of PCA 02007, and the etching contained 5 µg, the volume of gas extracted in the stepped heating experiment is at least seven times the stepped etching volume. Another explanation is that PCA 02007 is a regolith breccia, and therefore may expresses heterogeneous concentrations of xenon from clast to clast within the sample, although such a heterogeneity was not evident on the scale of the multiple clasts analysed during stepped heating which returned roughly constant concentrations and compositions of xenon over numerous heating steps and clasts. Any combination of these effects, including the other proposed scenarios, can be reasonably posited as explanations responsible for such a disparity.

The adsorption of previously etched xenon onto newly etched surfaces as explained in Schwenzer et al. (2012) and Ott (2008) would presumably have manifested as a gradual progression of etched gas composition towards the 2$^{nd}$ group from the 1$^{st}$ group. This is not observed, as the etched compositions do not express intermediate compositions of either on mixing lines between the two groups. Perhaps this process could have hidden a minor SW-Xe composition in the midst of the air releases during the etches in the 2$^{nd}$ group, in

such a case this release was low enough relative to the air xenon release that it does not reside on a mixing line between the two.

Cessation of the etching experiment prior to introduction of $HNO_3$ means the ability of CSSE to separately etch HF-soluble and $HNO_3$-soluble materials is unproven. The "Q" Vigarano II sample loaded in the sample finger for etching may have been lost or coated in a similar fashion to the aerogel and PCA 02007, or may still be available for etching.

### 5.7. Conclusions

This experiment has proven that PCA 02007 xenon can be separately distinguished from air-Xe by CSSE and RELAX. The additional ability of CSSE and RELAX to separately etch and extract xenon from HF and $HNO_3$-soluble materials within one sample is unproven as the experiment stopped before it could be tested. The experiments produced unexpected results in a reduced concentration of gas relative to the expected concentrations, and an order of extracted xenon which did not meet expectations. These results are best explained as a failure on the part of the procedural process, which failed to sufficiently prove the full functionality of the CSSE apparatus prior to and during sample etching. The theoretical application of CSSE and RELAX to a Stardust sample such that HF and $HNO_3$-soluble materials may be discretely targeted for xenon measurement remains possible. The failures and successes of this work set a precedence for future application of CSSE and RELAX in determining 81P-Xe, or using CSSE in a similar application on similarly composed samples. With refinements to the procedures developed for this work, and a deeper understanding of the behaviour of the equipment, this approach can conceivably measure xenon and other noble gases contained within Stardust material collected from comet 81P/Wild 2.

## 6. Summary and conclusions

Automaton was developed specifically as a spectral decomposition modelling platform for relative abundance signatures of xenon isotopes. Automaton's coding architecture is described and the accuracy and precision of its results are validated alongside Samaritan, a similar xenon modelling platform. Automaton exhibited some modelling limitations related to uncertainty and non-minimal solutions which are identified and described. The modelling undertaken with Automaton in this work elucidates relationships amongst current and primordial xenon isotopic compositions of volatile reservoirs in the solar system, including the role of cometary xenon.

The most precise measurements of xenon contained within lunar volcanic glasses of Apollo 15 and 17 are described within this thesis, along with new methodology for confirming their volcanic origin with major element data from electron microprobe analyses (EPMA) prior to noble gas analyses. The xenon data do not contain evidence of a primordial lunar xenon composition, but the implications of its absence in the most precise analyses to date are explored. Cosmogenic xenon is measured in the volcanic glasses and used to interpret their burial history and residence near to the lunar surface.

This thesis describes the development and testing of a novel method for analysing xenon in cometary samples from 81P/Wild 2 on Earth using closed-system stepped etching. The method produced results which could not reasonably be explained when tested with an analogue of Stardust 81P/Wild 2 material, so etching of an actual Stardust 81P/Wild 2 sample was not undertaken. The original aim of further constraining cometary xenon as contained within 81P/Wild 2 was not met, but the failure of this approach does not preclude future measurement of xenon in 81P/Wild 2 samples, and the methods described in this work are useful for similar attempts in the future.

## 6.1. Future Work

### 6.1.1. Modelling mixtures of Solar System reservoirs

There are two approaches to future work based on Automaton, one approach focuses on improvements to the functionality and modelling capability of Automaton, the other approach concerns modelling scenarios which were not explored in Chapter 3.

For further work utilising Automaton in its current state, it may be applied to similar modelling using improved end member data, unknown sample compositions, and the origin of various real and hypothetical noble gas reservoirs not modelled in this work. For example, one application would be to model the origin of Q-Xe, a composition which appears to be a processed mixture of other noble gas reservoirs (explained in Section 5.4.2). Another application would be to use Automaton in conjunction with a mass spectrometer, in this role, Automaton could determine the nature of the xenon extracted from a sample between heating steps, advising further steps.

The modelling of xenon reservoirs contained in this work lacks the light isotopic composition of 67P-Xe. It would be interesting to infer the required $^{124}Xe/^{132}Xe$ and $^{126}Xe/^{132}Xe$ required from 67P-Xe to fully match the modelled reservoir composition in each modelled scenario. Determining the inferred composition of these ratios as required by the different reservoirs would allow them to be compared to one another and discussed in the context of processes which could produce such ratios. For example, if the inferred light isotopic composition of 67P-Xe was identical in each of the modelled scenarios, you could make a stronger case for the scenarios being closer to the truth. Another immediate application of Automaton with 67P-Xe would be to model its potential contribution to the

other Martian compositions as recorded in Martian meteorites (summarised in Section 1.3.4).

Further work to improve the functionality and modelling capability of Automaton will benefit from the fact Automaton was written with modular improvements in mind, so the possible applications are numerous and easily implemented. The most fruitful expansions of Automaton concern the addition of more variables. Automaton could be expanded to contain additional noble gases and their isotopes, whose isotopic compositions and element/element ratios would provide more realistic models of reservoir building. Non-noble elements and their isotopes could just as easily be added.

Less obvious revisions to Automaton's functionality could implement a means of retaining or partitioning a mixed composition, possibly helping model atmosphere specific processes, or processes which trap or remove noble gas reservoirs. Another variable may control time separating noble gas compositions which evolved from one another. For instance, the Martian atmospheric composition could contain a measure of the time required for fractionation by hydrodynamic escape to produce a certain composition. Time may also be implemented by allowing components to be added or removed after certain hypothetical time intervals are modelled. For example, modelling may favour the addition of cometary xenon after a certain amount of fractionation has occurred, possibly helping determine when the component was added to the modelled composition.

Further modelling of different scenarios using Automaton will undoubtedly lead to suggestions for other improvements to its capability and accessibility. This refinement would be accelerated by more external use of Automaton. The ultimate goal of future work with respect to Automaton would be to refine it through collaborations with other

cosmochemists, and hopefully distinguish it as a respected modelling platform in the cosmochemistry community.

### 6.1.2. Xenon isotopes in individual lunar volcanic glasses of Apollo 15 and Apollo 17

The search for an indigenous lunar xenon composition can improve upon many aspects explored in this work. For future investigations hoping to use the lunar volcanic glasses, the experiment may be better conducted in reverse, with noble gases being extracted from optically pristine glasses, then major element data being measured from the resolidified glasses. This would avoid the problems associated with removing part of the volume, such as surface area/volume determination, and removal of material containing trapped noble gases.

The request of samples containing larger lunar volcanic glasses would also be helpful for better constraining a potential trapped lunar interior xenon composition. Larger glasses should equate to larger concentrations of xenon per glass, therefore the probability of the presence and measurement of a contained indigenous lunar gas composition above the detection limit is greater.

Future work which emulates the EPMA then noble gas analysis of this work may look towards stronger materials than superglue for holding the samples in place for EPMA analysis. The polishing quality, and subsequently the major element data, suffered greatly from the softness of the superglue, a stronger material capable of being removed from samples as effectively as the superglue would be ideal.

The most obvious suggestion for future work hoping to determine an indigenous lunar mantle xenon composition is to collect samples from deeper in the lunar crust, ideally by drill core extraction. Drilling beyond the regolith into material not exposed to the adverse physical conditions of gardening and galactic cosmic ray exposure (at least ~ 400 g/cm$^2$) could target materials more likely to have retained a trapped lunar mantle xenon composition, without the problems introduced by deconvolution of other components.

As for future work hoping to measure xenon contained within the transient lunar atmosphere, larger and more pristine samples are also more likely to contain such a composition. However, a better candidate would be drilled core sample from the lunar poles, where temperatures can be low enough to condense noble gases (Butler, 1997; Hibbitts et al., 2009; Paige et al., 2010; Williams et al., 2017). Drilling into these areas may uncover solidified volatiles containing noble gases from a time when the lunar exosphere was more prevalent, or allow us to trace back the development of the contained noble gases to the early evolution of the Earth-Moon system

### 6.1.3. Towards noble gas analysis of Stardust samples with closed-system etching

To measure the xenon contained in the particles collected from 81P/Wild 2, or the atoms of xenon which were liberated and trapped within Stardust aerogel, would significantly extend our idea of the xenon contained in comets, of which our current inventory is entirely limited to 67P/Churyumov-Gerasimenko. Given the vast population of comets, and their apparent inhomogeneity in many other chemical species, a likeness or difference would be equally as significant a discovery. Until we conduct another cometary sample return mission or another remote measurement of cometary xenon, the Stardust inventory of 81P/Wild is our best opportunity to double the number of comets for which

we have characterised a xenon composition, and provide the only existing ground-truth cometary noble gas composition.

The failures and successes of this work set a precedence for future application of CSSE and RELAX in determining 81P-Xe, or using CSSE in a similar application on similarly composed samples. With refinements to the procedures developed for this work, and a deeper understanding of the behaviour of the equipment, this approach can conceivably measure xenon and other noble gases contained within Stardust material collected from comet 81P/Wild 2.

The results of this work were not successful due to the instrument and apparatus behaving abnormally, and were most likely not the result of a problem specific to the Stardust analogue. Therefore, the most obvious future work concerning this topic is to repeat the analogue experiment. A repeated experiment with identical procedures and sample masses may elucidate why the experiment in this work failed, but it would probably be more helpful to thoroughly evaluate the CSSE apparatus to determine its functionality. Removing the sample finger to see what is left of the loaded Stardust analogue would help prove or disprove the proposed results of the etching, by illustrating the fact that the aerogel is not present, for example. A similar investigation of the acid finger may be helpful, has the concentration or volume of acid changed, what are the implications for the analogue etching experiment? A more fundamental review of the functionality of the CSSE apparatus used in the analogue etch would be helpful, are the valves working as intended, are there traces of samples which have migrated from the sample finger? Repeating the experiment after a full service of the CSSE apparatus, or use of the other CSSE apparatus, would be an ideal continuation of this work. Perhaps this experiment could feature more analogue sample material, with a more precisely determined mass?

## 7. References


A'Hearn, M. F., Belton, M. J. S., Collins, S. M., Farnham, T. L., Feaga, L. M., Groussin, O., Lisse, C. M., Meech, K. J., Schultz, P. H. and Sunshine, J. M. (2008) 'Deep Impact and sample return.' *Earth, Planets and Space*, 60, pp. 61–66.

A'Hearn, M. F., Feaga, L. M., Keller, H. U., Kawakita, H., Hampton, D. L., Kissel, J., Klaasen, K. P., McFadden, L. A., Meech, K. J., Schultz, P. H., Sunshine, J. M., Thomas, P. C., Veverka, J., Yeomans, D. K., Besse, S., Bodewits, D., Farnham, T. L., Groussin, O., Kelley, M. S., Lisse, C. M., Merlin, F., Protopapa, S. and Wellnitz, D. D. (2012) 'Cometary Volatiles and the Origin of Comets.' *The Astrophysical Journal*, 758, pp. 29.

A'Hearn, M. F., Millis, R. C., Schleicher, D. O., Osip, D. J. and Birch, P. V. (1995) 'The Ensemble Properties of Comets: Results from Narrowband Photometry of 85 Comets, 1976-1992.' *Icarus*, 469, pp. 223–270.

Alaerts, L., Lewis, R. S. and Anders, E. (1979) 'Isotopic anomalies of noble gases in meteorites and their origins—III. LL-chondrites.' *Geochimica et Cosmochimica Acta*, 43, pp. 1399–1415.

Albarede, F., Ballhaus, C., Blichert-Toft, J., Lee, C. T., Marty, B., Moynier, F. and Yin, Q. Z. (2013) 'Asteroidal impacts and the origin of terrestrial and lunar volatiles.' *Icarus*, 222, pp. 44–52.

Alexander, E. C., Coscio, M. R. J., Dragon, J. C. and Saito, K. (1978) '$^{40}$Ar-$^{39}$Ar Studies of Glasses from Lunar Soils.' in *Lunar and Planetary Science IX* (abstract), pp. 7–9, Houston, USA.

Altwegg, K., Balsiger, H., Bar-Nun, A., Berthelier, J.-J., Bieler, A., Bochsler, P., Briois, C., Calmonte, U., Combi, M. R., Cottin, H., De Keyser, J., Dhooghe, F., Fiethe, B., Fuselier, S. a, Gasc, S., Gombosi, T. I., Hansen, K. C., Haessig, M., Jäckel, A., Kopp, E., Korth, A., Le Roy, L., Mall, U., Marty, B., Mousis, O., Owen, T., Rème, H., Rubin, M., Sémon, T., Tzou, C.-Y., Hunter Waite, J. and Wurz, P. (2016) 'Prebiotic chemicals—amino acid and phosphorus—in the coma of comet 67P/Churyumov-Gerasimenko.' *Science Advances*, 2(5), e1600285.

Altwegg, K., Balsiger, H., Bar-Nun, A., Berthelier, J. J., Bieler, A., Bochsler, P., Briois, C., Calmonte, U., Combi, M., De Keyser, J., Eberhardt, P., Fiethe, B., Fuselier, S., Gasc, S., Gombosi, T. I., Hansen, K. C., Hassig, M., Jackel, A., Kopp, E., Korth, A., LeRoy, L., Mall, U., Marty, B., Mousis, O., Neefs, E., Owen, T., Reme, H., Rubin, M., Semon, T., Tzou, C.-Y., Waite, H. and Wurz, P. (2015) '67P/Churyumov-Gerasimenko, a Jupiter family comet with a high D/H ratio.' *Science*, 347(6220), 1261952.

Altwegg, K., Balsiger, H., Berthelier, J. J., Bieler, A., Calmonte, U., Fuselier, S. A., Goesmann, F., Gasc, S., Gombosi, T. I., Le Roy, L., de Keyser, J., Morse, A., Rubin, M., Schuhmann, M., Taylor, M. G. G. T., Tzou, C.-Y. and Wright, I. (2017) 'Organics in comet 67P – a first comparative analysis of mass spectra from ROSINA–DFMS, COSAC and Ptolemy.' *Monthly Notices of the Royal Astronomical Society*, 469, pp. S130–S141.

Altwegg, K., Balsiger, H. and Geiss, J. (1999) ‘Composition of the Volatile Material in Halley’s Coma from in Situ Measurements.’ *In* Altwegg, K., Ehrenfreund, P., Geiss, J., and Huebner, W. F. (eds) *Composition and Origin of Cometary Materials: Proceedings of an ISSI Workshop, 14--18 September 1998, Bern, Switzerland*. Dordrecht: Springer Netherlands, pp. 3–18.

Amari, S., Matsuda, J., Stroud, R. M. and Chisholm, M. F. (2013) ‘Highly concentrated nebular noble gases in porous nanocarbon separates from the Saratov (L4) meteorite.’ *The Astrophysical Journal*, 778, 37.

Anders, E. and Grevesse, N. (1989) ‘Abundances of the elements: meteoritic and solar.’ *Geochimica et Cosmochimica Acta*, 53(1), pp. 197–214.

Anders, E. and Owen, T. (1977) ‘Mars and Earth: Origin and abundance of volatiles.’ *Science*, 198(4316), pp. 453–465.

Arndt, J., Engelhardt, W. V., Gonzalez-Cabeza, I. and Meier, B. (1984) ‘Formation of Apollo 15 green glass beads.’ *Journal of Geophysical Research*, 89(S01), pp. C225–C232.

Arndt, J. and von Engelhardt, W. (1987) ‘Formation of Apollo 17 orange and black glass beads.’ *Journal of Geophysical Research*, 92(B4) pp. E372–E376.

Arnould, M. and Goriely, S. (2003) ‘The p-process of stellar nucleosynthesis: astrophysics and nuclear physics status.’ *Physics Reports*, 384, pp. 1–84.

Asplund, M., Grevesse, N., Sauval, A. J. and Scott, P. (2009) ‘The chemical composition of the Sun.’ *Annual Review of Astronomy and Astrophysics*, 47, pp. 481–522.

Bailer-Jones, C. A. L. (2014) ‘Close encounters of the stellar kind.’ *Astronomy & Astrophysics*, 575(A35), pp. 13.

Balsiger, H., Altwegg, K., Bar-Nun, A., Berthelier, J.-J., Bieler, A., Bochsler, P., Briois, C., Calmonte, U., Combi, M., De Keyser, J., Eberhardt, P., Fiethe, B., Fuselier, S. A., Gasc, S., Gombosi, T. I., Hansen, K. C., Hässig, M., Jäckel, A., Kopp, E., Korth, A., Le Roy, L., Mall, U., Marty, B., Mousis, O., Owen, T., Rème, H., Rubin, M., Sémon, T., Tzou, C.-Y., Waite, J. H. and Wurz, P. (2015) ‘Detection of argon in the coma of comet 67P/Churyumov-Gerasimenko.’ *Science Advances*, 1(8), e1500377.

Bar-Nun, A., Dror, J., Kochavi, E. and Laufer, D. (1987) ‘Amorphous water ice and its ability to trap gases.’ *Physical Review B*, 35(5), pp. 2427–2435.

Bar-nun, A. and Kleinfeld, I. (1989) ‘On the temperature and gas composition in the region of comet formation.’ *Icarus*, 80(2), pp. 243–253.

Barnes, J. J., Franchi, I. A., Anand, M., Tartèse, R., Starkey, N. A., Koike, M., Sano, Y. and Russell, S. S. (2013) ‘Accurate and precise measurements of the D/H ratio and hydroxyl content in lunar apatites using NanoSIMS.’ *Chemical Geology*, 337–338, pp. 48–55.

Barnes, J. J., Kring, D. A., Tartèse, R., Franchi, I. A., Anand, M. and Russell, S. S. (2016) ‘An asteroidal origin for water in the Moon.’ *Nature Communications*, 7, 11684.

Barraclough, B. L. and Marti, K. (1985) ‘In search of the Moon’s indigenous volatiles: Noble gases and nitrogen in vesicular lunar glasses.’ in *Lunar and Planetary Science XVI* (abstract), pp. 31–32, Houston, USA.

Basu, A., McKay, D. S., Griffiths, S. A. and Nace, G. (1981) ‘Regolith maturation on the Earth and Moon with an example from Apollo 15.’ *Proceedings of 12th Lunar and Planetary Science Conference*, pp. 422–449.

Basu, A., McKay, D. S., Moore, H. M. and Shaffer, N. R. (1979) ‘A note on the Apollo 15 green glass vitrophyres.’ *Proceedings of 10th Lunar and Planetary Science Conference*, pp. 301–310.

Bekaert, D. V., Broadley, M. W. and Marty, B. (2020) ‘The origin and fate of volatile elements on Earth revisited in light of noble gas data obtained from comet 67P/Churyumov-Gerasimenko.’ *Scientific Reports*, 10, 5796.

Bekaert, D. V, Marrocchi, Y., Meshik, A., Remusat, L. and Marty, B. (2019) ‘Primordial heavy noble gases in the pristine Paris carbonaceous chondrite.’ *Meteoritics & Planetary Science*, 54(2), pp. 395–414.

Belton, M. J. S., Thomas, P., Veverka, J., Schultz, P., A’Hearn, M. F., Feaga, L., Farnham, T., Groussin, O., Li, J. Y., Lisse, C., McFadden, L., Sunshine, J., Meech, K. J., Delamere, W. A. and Kissel, J. (2007) ‘The internal structure of Jupiter family cometary nuclei from Deep Impact observations: The “talps” or “layered pile” model.’ *Icarus*, 187, pp. 332–344.

Bence, A. E. (1973) ‘Apollo 17 results.’ *EOS Transactions*, 54(6), pp. 580–622.
Benkert, J.-P., Baur, H., Signer, P. and Wieler, R. (1993) ‘He, Ne, and Ar from the solar wind and solar energetic particles in lunar ilmenites and pyroxenes.’ *Journal of Geophysical Research*, 98(E7), pp. 13147–13162.

Berger, E. L., Zega, T. J., Keller, L. P. and Lauretta, D. S. (2011) ‘Evidence for aqueous activity on comet 81P/Wild 2 from sulfide mineral assemblages in Stardust samples and CI chondrites.’ *Geochimica et Cosmochimica Acta*, 75, pp. 3501–3513.

Bernatowicz, T. J. and Fahey, A. J. (1986) ‘Xe isotopic fractionation in a cathodeless glow discharge.’ *Geochimica et Cosmochimica Acta*, 50, pp. 445–452.

Bernatowicz, T. J., Hohenberg, C. M., Hudson, B., Kennedy, B. M. and Podosek, F. A. (1978) ‘Excess fission xenon at Apollo 16.’ *Proceedings of 9th Lunar and Planetary Science Conference*, 2, pp. 1571–1597.

Blake, D., Allamandola, L., Sandford, S., Hudgins, D. and Freund, F. (1991) ‘Clathrate hydrate formation in amorphous cometary ice analogs in vacuo.’ *Science*, 254, pp. 548–551.

Bockelée-Morvan, D. and Biver, N. (2017) ‘The composition of cometary ices.’ *Philosophical Transactions of the Royal Society A: Mathematical, Physical and Engineering Sciences*, 375, 20160252.

Bockelée-Morvan, D., Gautier, D., Hersant, F., Huré, J.-M. and & Robert, F. (2002) ‘Turbulent radial mixing in the solar nebula as the source of crystalline silicates in comets.’ *Astronomy & Astrophysics*, 384, pp. 1107–1118.

Bodmer, R. and Bochsler, P. (1998) ‘Fractionation of minor ions in the solar wind acceleration process.’ *Physics and Chemistry of the Earth*, 23(5–6), pp. 683–688.

Bodmer, R. and Bochsler, P. (2000) ‘Influence of Coulomb collisions on isotopic elemental fractionation in the solar wind acceleration process.’ *Journal of Geophysical Research*, 105, pp. 47–60.

Bogard, D. D., Clayton, R. N., Marti, K., Owen, T. and Turner, G. (2001) ‘Martian Volatiles: Isotopic Composition, Origin, and Evolution.’ *In* Kallenbach, R., Geiss, J., and Hartmann, W. K. (eds) *Chronology and Evolution of Mars: Proceedings of an ISSI Workshop, 10-14 April 2000, Bern, Switzerland.* Dordrecht: Springer Netherlands, pp. 425–458.

Bogard, D. D. and Hirsch, W. C. (1978) ‘Depositional and irradiational history and noble gas contents of orange-black droplets in the 74002/1 core from Shorty Crater.’ *Proceedings of 9th Lunar and Planetary Science Conference*, pp. 1981–2000.

Bogard, D. D. and Johnson, P. (1983) ‘Martian Gases in an Antarctic Meteorite?’ *Science*, 221, pp. 651–654.

Bogard, D. D., Nyquist, L. E., Hirsch, W. C. and Moore, D. R. (1973) ‘Trapped solar and cosmogenic noble gas abundances in Apollo 15 and 16 deep drill samples.’ *Earth and Planetary Science Letters*, 21, pp. 52–69.

Bogard, D. D., Nyquist, L. E. and Johnson, P. (1984) ‘Noble gas contents of shergottites and implications for the Martian origin of SNC meteorites.’ *Geochimica et Cosmochimica Acta*, 48, pp. 1723–1739.

Bondi, A. (1964) ‘Van Der Waals volumes and radii.’ *The Journal of Physical Chemistry*, 68(3), pp. 441–451.

Borg, L. E., Connelly, J. N., Boyet, M. and Carlson, R. W. (2011) ‘Chronological evidence that the Moon is either young or did not have a global magma ocean.’ *Nature*, 477, pp. 70–73.

Bottke, W. F., Vokrouhlický, D., Marchi, S., Swindle, T., Scott, E. R. D., Weirich, J. R. and Levison, H. (2015) ‘Dating the Moon-forming impact event with asteroidal meteorites.’ *Science*, 348, pp. 321–323.

Brady, P. V. and Walther, J. V. (1989) ‘Controls on silicate dissolution rates in neutral and basic pH solutions at 25°C.’ *Geochimica et Cosmochimica Acta*, 53, pp. 2823–2830.

Brown, C. D. and Gooding, T. (n.d.) How to make a polished standard mount. [Online] [Accessed on 17th September 2019] http://avdhandt.umn.edu/sites/avdhandt.dl.umn.edu/files/media/smithsonian_how_to_make_a_standard_mount_1.pdf.

Brown, M. E. (2001) ‘The Inclination Distribution of the Kuiper Belt.’ *The Astronomical Journal*, 121, pp. 2804–2814.

Brownlee, D. (2014) ‘The Stardust Mission: Analyzing Samples from the Edge of the Solar System.’ *Annual Review of Earth and Planetary Sciences*, 42, pp. 179–205.

Brownlee, D. E. (1985) ‘Cosmic Dust: Collection and Research.’ *Annual Review of Earth and Planetary Sciences*, 13, pp. 147–173.

Brownlee, D., Tsou, P., Aléon, J., Alexander, C. M. O., Araki, T., Bajt, S., Baratta, G. A, Bastien, R., Bland, P., Bleuet, P., Borg, J., Bradley, J. P., Brearley, A., Brenker, F., Brennan, S., Bridges, J. C., Browning, N. D., Brucato, J. R., Bullock, E., Burchell, M. J., Busemann, H., Butterworth, A., Chaussidon, M., Cheuvront, A., Chi, M., Cintala, M. J., Clark, B. C., Clemett, S. J., Cody, G., Colangeli, L., Cooper, G., Cordier, P., Daghlian, C., Dai, Z., D’Hendecourt, L., Djouadi, Z., Dominguez, G., Duxbury, T., Dworkin, J. P., Ebel, D. S., Economou, T. E., Fakra, S., Fairey, S. A. J., Fallon, S., Ferrini, G., Ferroir, T., Fleckenstein, H., Floss, C., Flynn, G., Franchi, I. A., Fries, M., Gainsforth, Z., Gallien, J.-P., Genge, M., Gilles, M. K., Gillet, P., Gilmour, J., Glavin, D. P., Gounelle, M., Grady, M. M., Graham, G. A., Grant, P. G., Green, S. F., Grossemy, F., Grossman, L., Grossman, J. N., Guan, Y., Hagiya, K., Harvey, R., Heck, P., Herzog, G. F., Hoppe, P., Hörz, F., Huth, J., Hutcheon, I. D., Ignatyev, K., Ishii, H., Ito, M., Jacob, D., Jacobsen, C., Jacobsen, S., Jones, S., Joswiak, D., Jurewicz, A., Kearsley, A. T., Keller, L. P., Khodja, H., Kilcoyne, A. L. D., Kissel, J., Krot, A., Langenhorst, F., Lanzirotti, A., Le, L., Leshin, L. A., Leitner, J., Lemelle, L., Leroux, H., Liu, M.-C., Luening, K., Lyon, I., Macpherson, G., Marcus, M. A., Marhas, K., Marty, B., Matrajt, G., McKeegan, K., Meibom, A., Mennella, V., Messenger, K., Messenger, S., Mikouchi, T., Mostefaoui, S., Nakamura, T., Nakano, T., Newville, M., Nittler, L. R., Ohnishi, I., Ohsumi, K., Okudaira, K., Papanastassiou, D. A., Palma, R., Palumbo, M. E., Pepin, R. O., Perkins, D., Perronnet, M., Pianetta, P., Rao, W., Rietmeijer, F. J. M., Robert, F., Rost, D., Rotundi, A., Ryan, R., Sandford, S. a, Schwandt, C. S., See, T. H., Schlutter, D., Sheffield-Parker, J., Simionovici, A., Simon, S., Sitnitsky, I., Snead, C. J., Spencer, M. K., Stadermann, F. J., Steele, A., Stephan, T., Stroud, R., Susini, J., Sutton, S. R., Suzuki, Y., Taheri, M., Taylor, S., Teslich, N., Tomeoka, K., Tomioka, N., Toppani, A., Trigo-Rodríguez, J. M., Troadec, D., Tsuchiyama, A., Tuzzolino, A. J., Tyliszczak, T., Uesugi, K., Velbel, M., Vellenga, J., Vicenzi, E., Vincze, L., Warren, J., Weber, I., Weisberg, M., Westphal, A. J., Wirick, S., Wooden, D., Wopenka, B., Wozniakiewicz, P., Wright, I., Yabuta, H., Yano, H., Young, E. D., Zare, R. N., Zega, T., Ziegler, K., Zimmerman, L., Zinner, E. and Zolensky, M. (2006) ‘Comet 81P/Wild 2 under a microscope.’ *Science*, 314, pp. 1711–1716.

Burbidge, E. M., Burbidge, G. R., Fowler, W. A. and Hoyle, F. (1957) ‘Synthesis of the Elements in Stars.’ *Reviews of Modern Physics*, 29, pp. 547–650.

Burchell, M. J., Fairey, S. A. J., Wozniakiewicz, P., Brownlee, D. E., Hörz, F., Kearsley, A. T., See, T. H., Tsou, P., Westphal, A., Green, S. F., Trigo-Rodríguez, J. M. and Domingúez, G. (2008) ‘Characteristics of cometary dust tracks in Stardust aerogel and laboratory calibrations.’ *Meteoritics & Planetary Science*, 43, pp. 23–40.

Burnett, D. S., Barraclough, B. L., Bennett, R., Neugebauer, M., Oldham, L. P., Sasaki, C. N., Sevilla, D., Smith, N., Stansbery, E., Sweetnam, D. and Wiens, R. C. (2003) ‘The Genesis Discovery mission: Return of solar matter to earth.’ *Space Science Reviews*, 105, pp. 509–534.

Busemann, H., Baur, H. and Wieler, R. (2000) ‘Primordial noble gases in “phase Q” in carbonaceous and ordinary chondrites studied by closed-system stepped etching.’ *Meteoritics & Planetary Science*, 35, pp. 949–973.

Busemann, H., Nguyen, A. N., Cody, G. D., Hoppe, P., Kilcoyne, A. L. D., Stroud, R. M., Zega, T. J. and Nittler, L. R. (2009) 'Ultra-primitive interplanetary dust particles from the comet 26P/Grigg-Skjellerup dust stream collection.' *Earth and Planetary Science Letters*, 288, pp. 44–57.

Busemann, H., Spring, N., Crowther, S. A., Claydon, J. L., Gilmour, J. D. and Nittler, L. R. (2010) 'Abundant primordial xenon in interplanetary dust particles from the comet Grigg-Skjellerup collection.' in *41st Lunar and Planetary Science Conference* (abstract), Texas, USA.

Butler, J. (1997) 'The migration of volatiles on the surfaces of Mercury and the Moon' *Journal of Geophysical Research*, 102, pp. 283–291.

Butler, P. J., Anderson, M., Johnston, K. and Phinney, W. C. (1971) '*Apollo 15 Lunar Sample Information Catalog Part 1: 15015-15299.*', National Aeronautics and Space Administration, pp. 186–188.

Butler, P. J. and Meyer, C. J. (1976) 'Sulfur prevails in coatings on glass droplets: Apollo 15 green and brown glasses and Apollo 17 orange and black (devitrified) glasses.' *Proceedings of 7th Lunar and Planetary Science Conference*, pp. 1561–1581.

Byle, J. (1983) 'Galactic perturbations on nearly-parabolic cometary orbits.' *The Moon and the Planets*, 29, pp. 121–137.

Cameron, A. (1997) 'The Origin of the Moon and the Single Impact Hypothesis.' *Icarus*, 126, pp. 126–137.

Canup, R. M. (2004) 'Simulations of a late lunar-forming impact.' *Icarus*, 168, pp. 433–456.

Canup, R. M. (2012) 'Forming a Moon with an Earth-like Composition via a Giant Impact.' *Science*, 338, pp. 1052–1055.

Canup, R. M. and Asphaug, E. (2001) 'Origin of the Moon in a giant impact near the end of the Earth's formation.' *Nature*, 412, pp. 708–712.

Caracausi, A., Avice, G., Burnard, P. G., Füri, E. and Marty, B. (2016) 'Chondritic xenon in the Earth's mantle.' *Nature*. 533, pp. 82–85.

Carter, J. L., Taylor, J. and Padovani, E. (1973) 'Morphology and chemistry of particles from Apollo 17 soils 74220, 74241 and 75081.' *EOS Transactions*, 54, pp. 582–583.

Carusi, A., Perozzi, E. and Valsecchi, G. B. (1987) 'High-order librations of Halley-type comets.' *Astronomy & Astrophysics*, 187, pp. 889–905.

Charnoz, S. and Morbidelli, A. (2007) 'Coupling dynamical and collisional evolution of small bodies. II. Forming the Kuiper belt, the Scattered Disk and the Oort Cloud.' *Icarus*, 188, pp. 468–480.

Chassefière, E. and Leblanc, F. (2004) 'Mars atmospheric escape and evolution; interaction with the solar wind.' *Planetary and Space Science*, 52, pp. 1039–1058.

Chou, C. L., Boynton, W. V., Sundberg, L. L. and Wasson, J. T. (1975) 'Volatiles on the surface of Apollo 15 green glass and trace-element distributions among Apollo 15 soils.' In *Proceedings of 6th Lunar Science Conference*, pp. 1701–1727.

Ciesla, F. J. (2007) 'Outward transport of high-temperature materials around the midplane of the solar nebula.' *Science*, 318, pp. 613–615.

Cochran, A. L., Levasseur-Regourd, A. C., Cordiner, M., Hadamcik, E., Lasue, J., Gicquel, A., Schleicher, D. G., Charnley, S. B., Mumma, M. J., Paganini, L., Bockelée-Morvan, D., Biver, N. and Kuan, Y. J. (2015) 'The Composition of Comets.' *Space Science Reviews*, 197, pp. 60.

Cohen, B., Swindle, T. and Kring, D. (2005) 'Geochemistry and $^{40}$Ar-$^{39}$Ar geochronology of impact-melt clasts in feldspathic lunar meteorites: Implications for lunar bombardment history.' *Meteoritics & Planetary Science*, 40, pp. 755–777.

Cohen, B. A. (2013) 'The Vestan cataclysm: Impact-melt clasts in howardites and the bombardment history of 4 Vesta.' *Meteoritics and Planetary Science*, 48, pp. 771–785.

Connelly, J. N., Bizzarro, M., Krot, A. N., Nordlund, A., Wielandt, D. and Ivanova, M. A. (2012) 'The absolute chronology and thermal processing of solids in the solar protoplanetary disk.' *Science*, 338, pp. 651–655.

Conrad, P. G., Malespin, C. A., Franz, H. B., Pepin, R. O., Trainer, M. G., Schwenzer, S. P., Atreya, S. K., Freissinet, C., Jones, J. H., Manning, H., Owen, T., Pavlov, A. A., Wiens, R. C., Wong, M. H. and Mahaffy, P. R. (2016) 'In situ measurement of atmospheric krypton and xenon on Mars with Mars Science Laboratory.' *Earth and Planetary Science Letters*, 454, pp. 1–9.

Cowan, J. J., Thielemann, F. and Truran, J. W. (1991) 'The R-process and nucleochronology.' *Physics Reports*, 208, pp. 267–394.

Crovisier, J. (2007) 'Cometary diversity and cometary families.' *Icarus*, 223, pp. 298–307.

Crowther, S. A. and Gilmour, J. D. (2013) 'The Genesis solar xenon composition and its relationship to planetary xenon signatures.' *Geochimica et Cosmochimica Acta*, 123, pp. 17–34.

Crowther, S. A., Mohapatra, R. K., Turner, G., Blagburn, D. J., Kehm, K. and Gilmour, J. D. (2008) 'Characteristics and applications of RELAX, an ultrasensitive resonance ionization mass spectrometer for xenon.' *Journal of Analytical Atomic Spectrometry*, 23, pp. 921–1044.

Crozaz, G. (1978) 'Regolith depositional history at Shorty Crater.' *Proceedings of 9th Lunar and Planetary Science Conference*, pp. 2001–2009.

Curran, N. M., Nottingham, M., Alexander, L., Crawford, I. A., Füri, E. and Joy, K. H. (2020) 'A database of noble gases in lunar samples in preparation for mass spectrometry on the Moon.' *Planetary and Space Science*, 182, 104823.

Dauphas, N. and Morbidelli, A. (2013) 'Geochemical and planetary dynamical views on the origin of Earth's atmosphere and oceans.' in Turekian, K. and Holland, H. *Treatise on Geochemistry: Second Edition*, Elsevier Science.

Delano, J. W. (1979) ‘Apollo 15 green glass - Chemistry and possible origin.’ *Proceedings of 10th Lunar and Planetary Science Conference*, pp. 275–300.

Delano, J. W. (1980) ‘Chemistry and liquidus phase relations of Apollo 15 red glass: Implications for the deep lunar interior.’ *Proceedings of 11th Lunar and Planetary Science Conference*, pp. 251–288.

Delano, J. W. (1986) ‘Pristine lunar glasses: Criteria, data, and implications.*’ Journal of Geophysical Research: Solid Earth*, 91, pp. D201–D213.

Delano, J. W. and Lindsley, D. H. (1983) ‘Mare glasses from Apollo 17: Constraints on the Moon’s bulk composition.’ *Journal of Geophysical Research*, 88(S01), pp. B3–B16.

Delano, J. W. and Livi, K. (1981) ‘Lunar volcanic glasses and their constraints on mare petrogenesis.’ *Geochimica et Cosmochimica Acta*, 45, pp. 2137–2149.

Delano, J. W., Zellner, N. E. B., Barra, F., Olson, E., Swindle, T. D., Tibbetts, N. J. and Whittet, D. C. B. (2007) ‘An integrated approach to understanding Apollo 16 impact glasses: Chemistry, isotopes, and shape.’ *Meteoritics and Planetary Science*, 42, pp. 993–1004.

Delsemme, A. H. (1987) ‘Galactic tides affect the Oort cloud: an observational confirmation.’ *Astronomy & Astrophysics*, 187, pp. 913–918.

Delsemme, A. H. and Swings, P. (1952) ‘Hydrates de gaz dans les noyaux cométaires et les grains interstellaires.’ *Annales d’Astrophysique*, 15, pp. 1–6.

Desch, S. J. (2007) ‘Mass distribution and planet formation in the solar nebula.’ *The Astrophysical Journal*, 671, pp. 878–893.

Dones, L., Brasser, R., Kaib, N. and Rickman, H. (2015) ‘Origin and evolution of the cometary reservoirs.’ *Space Science Reviews*, 197, pp. 191–269.

Dones, L., Weissman, P. R., Levison, H. F. and Duncan, M. J. (2004) ‘Oort cloud formation and dynamics.’ *Comets II*, pp. 153–174.

Drake, M. J., Swindle, T. D., Owen, T. and Musselwhite, D. S. (1994) ‘Fractionated Martian atmosphere in the nakhlites?’ *Meteoritics*, 29, pp. 854–859.

Duncan, M. and Levison, H. (1997) ‘A disk of scattered icy objects and the origin of Jupiter-family comets.’ *Science*, 276, pp. 1670–1672.

Dybczyński, P. a. and Królikowska, M. (2016) ‘Towards a better understanding of the apparent source/sources of long period comets.’ *Planetary and Space Science*, 123, pp. 77–86.

Eberhardt., P., Eugster, O., Geiss, J., Grögler, N., Jungck, N., Maurer, P., Morgeli, M. and Stettler, A. (1975) ‘Shorty crater, noble gases and chronology.’ *Meteoritics*, 10, pp. 93–94.

Eberhardt, P., Geiss, J. and Graf, H. (1971) ‘On the origin of excess $^{131}$Xe in lunar rocks.’ *Earth and Planetary Science Letters*, 12, pp. 260–262.

Eberhardt, P., Geiss, J., Graf, H., Grogler, N., Krahenbuhl, U., Schwaller, H., Schwarzmuller, J. and Stettler, A. (1970) 'Trapped solar wind noble gases, exposure age and K/Ar-age in Apollo 11 lunar fine material.' *Proceedings of 11th Lunar and Planetary Science Conference*, 2, pp. 1037–1070.

Elkins, L. T., Fernandes, V. A., Delano, J. W. and Grove, T. L. (2000) 'Origin of lunar ultramafic green glasses: Constraints from phase equilibrium studies.' *Geochimica et Cosmochimica Acta*, 64, pp. 2339–2350.

Elsila, J. E., Glavin, D. P. and Dworkin, J. P. (2009) 'Cometary glycine detected in samples returned by Stardust.' *Meteoritics and Planetary Science*, 44, pp. 1323–1330.

Engrand, C. and Maurette, M. (1998) 'Carbonaceous micrometeorites from Antarctica.' Meteoritics & Planetary Science, 33, pp. 565–580.

Etique, P., Signer, P. and Wieler, R. (1981) 'An in-depth study of neon and argon in lunar soil plagioclases, revisited: Implanted solar flare noble gases.' in *Lunar and Planetary Science XII* (abstract), pp. 265–267.

Eugster, O. (1985) 'Multistage exposure history of the 74261 soil constituents.' *Proceedings of 16th Lunar and Planetary Science Conference*, 90, pp. D95–D102.

Eugster, O., Eberhardt, P., Geiss, J. and Grogler, N. (1978) 'The solar wind and cosmic-ray exposure history of soil from drive tube 74001, an unmixed lunar regolith.' in *Lunar and Planetary Science IX* (abstract), pp. 306–308, Houston, USA.

Eugster, O., Eberhardt, P., Geiss, J., Grögler, N., Jungck, M. and Mörgeli, M. (1977) 'The cosmic-ray exposure history of Shorty Crater samples; The age of Shorty Crater.' *Proceedings of 8th Lunar and Planetary Science Conference*, pp. 3059–3082.

Eugster, O., Grögler, N., Eberhardt, P., Geiss, J. and Kiesl, W. (1982) 'Double drive tube 74001/2: A two-stage exposure model based on noble gases, chemical abundances and predicted production rates.' *Proceedings of 12$^{th}$ Lunar and Planetary Science Conference*, 12B, pp. 541–558.

Feng, Q., Chen, K., Ma, D., Lin, H., Liu, Z., Qin, S. and Luo, Y. (2018) 'Synthesis of high specific surface area silica aerogel from rice husk ash via ambient pressure drying.' *Colloids and Surfaces A: Physicochemical and Engineering Aspects*, 539, pp. 399–406.

Fernandes, V. A., Anand, M., Burgess, R. and Taylor, L. A. (2004) 'Ar-Ar studies of Dhofar clast-rich feldspathic highland meteorites: 025, 026, 280, 303.' in *Lunar and Planetary Science XXXV* (abstract), Houston, USA.

Fernandes, V. A. and Burgess, R. (2005) 'Volcanism in Mare Fecunditatis and Mare Crisium: Ar-Ar age studies.' *Geochimica et Cosmochimica Acta*, 69, pp. 4919–4934.

Fernandes, V. A., Fritz, J., Weiss, B. P., Garrick-Bethell, I. and Shuster, D. L. (2013) 'The bombardment history of the Moon as recorded by $^{40}$Ar-$^{39}$Ar chronology.' *Meteoritics and Planetary Science*, 48, pp. 241–269.

Fernández, J. A., Gallardo, T. and Brunini, A. (2004) 'The scattered disk population as a source of Oort cloud comets: Evaluation of its current and past role in populating the Oort cloud.' *Icarus*, 172, pp. 372–381.

Filacchione, G., De Sanctis, M. C., Capaccioni, F., Raponi, A., Tosi, F., Ciarniello, M., Cerroni, P., Piccioni, G., Capria, M. T., Palomba, E., Bellucci, G., Erard, S., Bockelee-Morvan, D., Leyrat, C., Arnold, G., Barucci, M. A., Fulchignoni, M., Schmitt, B., Quirico, E., Jaumann, R., Stephan, K., Longobardo, A., Mennella, V., Migliorini, A., Ammannito, E., Benkhoff, J., Bibring, J. P., Blanco, A., Blecka, M. I., Carlson, R., Carsenty, U., Colangeli, L., Combes, M., Combi, M., Crovisier, J., Drossart, P., Encrenaz, T., Federico, C., Fink, U., Fonti, S., Ip, W. H., Irwin, P., Kuehrt, E., Langevin, Y., Magni, G., McCord, T., Moroz, L., Mottola, S., Orofino, V., Schade, U., Taylor, F., Tiphene, D., Tozzi, G. P., Beck, P., Biver, N., Bonal, L., Combe, J.-P., Despan, D., Flamini, E., Formisano, M., Fornasier, S., Frigeri, A., Grassi, D., Gudipati, M. S., Kappel, D., Mancarella, F., Markus, K., Merlin, F., Orosei, R., Rinaldi, G., Cartacci, M., Cicchetti, A., Giuppi, S., Hello, Y., Henry, F., Jacquinod, S., Reess, J. M., Noschese, R., Politi, R. and Peter, G. (2016) 'Exposed water ice on the nucleus of comet 67P/Churyumov–Gerasimenko.' *Nature*, 529, pp. 368–372.

Fleischer, R. L. and Hart, H. R., J. (1974) 'Uniformity of the uranium content of lunar green and orange glasses.' *Proceedings of 5th Lunar and Planetary Science Conference*, 3, pp. 2251–2255.

Floss, C., Stadermann, F. J., Kearsley, A. T., Burchell, M. J. and Ong, W. J. (2013) 'The abundance of presolar grains in comet 81P/Wild 2.' *The Astrophysical Journal*, 763, 140.

Fouchard, M., Rickman, H. and Valsecchi, G. B. (2013) 'Planetary perturbations for Oort Cloud comets. I. Distributions and dynamics.' *Icarus*, 222, pp. 20–31.

Francis, P. J. (2005) 'The demographics of long-period comets.' *The Astrophysical Journal*, 635, p. 1348.

Füri, E., Barry, P. H., Taylor, L. A. and Marty, B. (2015) 'Indigenous nitrogen in the Moon: Constraints from coupled nitrogen-noble gas analyses of mare basalts.' *Earth and Planetary Science Letters*, 431, pp. 195–205.

Füri, E., Deloule, E., Gurenko, A. and Marty, B. (2014) 'New evidence for chondritic lunar water from combined D/H and noble gas analyses of single Apollo 17 volcanic glasses.' *Icarus*, 229, pp. 109–120.

Füri, E., Zimmermann, L. and Saal, A. E. (2018) 'Apollo 15 green glass He-Ne-Ar signatures – In search for indigenous lunar noble gases.' *Geochemical Perspectives Letters*, 8, pp. 1–5.

Galbreath, K. C., Shearer, C. K., Papike, J. J. and Shimizu, N. (1990) 'Inter- and intra-group compositional variations in Apollo 15 pyroclastic green glass: An electron- and ion-microprobe study.' *Geochimica et Cosmochimica Acta*, 54, pp. 2565–2575.

Geller, J. D. and Engle, P. D. (2002) 'Sample preparation for electron probe microanalysis - Pushing the limits.' *Journal of Research of the National Institute of Standards and Technology*, 107, p. 627–638.

Gibb, E. L., Whittet, D. C. B., Boogert, A. C. A. and Tielens, A. G. G. M. (2004) 'Interstellar ice: The Infrared Space Observatory legacy.' *The Astrophysical Journal Supplement Series*, 151, pp. 35–73.

Gilmour, J. (2018) *An irrational approach to isotopic analysis*. DOI: 10.13140/RG.2.2.27449.01126

Gilmour, J., Whitby, J. and Turner, G. (1998) 'Xenon isotopes in irradiated ALH84001: Evidence for shock-induced trapping of ancient Martian atmosphere.' *Geochimica et Cosmochimica Acta*, 62, pp. 2555–2571.

Gilmour, J., Crowther, S., Busfield, A., Holland, G. and Whitby, J. (2009) 'An early I-Xe age for CB chondrite chondrule formation, and a re-evaluation of the closure age of Shallowater enstatite.' *Meteoritics & Planetary Science*, 44, pp. 573–579.

Gilmour, J. D. (2010) '"Planetary" noble gas components and the nucleosynthetic history of solar system material.' *Geochimica et Cosmochimica Acta*, 74, pp. 380–393.

Gilmour, J. D., Holland, G., Verchovsky, A. B., Fisenko, A. V., Crowther, S. A. and Turner, G. (2016) 'Xenon and iodine reveal multiple distinct exotic xenon components in Efremovka "nanodiamonds."' *Geochimica et Cosmochimica Acta*, 177, pp. 78–93.

Gilmour, J. D., Lyon, I. C., Johnston, W. A. and Turner, G. (1994) 'RELAX: An ultrasensitive, resonance ionization mass spectrometer for xenon.' *Reviews of Scientific Instruments*, 65, pp. 617–625.

Gilmour, J. D., Pravdivtseva, O. V., Busfield, A. and Hohenburg, C. M. (2006) 'The I-Xe chronometer and the early solar system.' *Meteoritics & Planetary Science*, 41, pp. 19–31.

Gilmour, J. D. and Turner, G. (2007) 'Constraints on nucleosynthesis from xenon isotopes in presolar Material.' *The Astrophysical Journal*, 657, pp. 600–608.

Gilmour, J. D., Verchovsky, A. B., Fisenko, A. V., Holland, G. and Turner, G. (2005) 'Xenon isotopes in size separated nanodiamonds from Efremovka: $^{129}$Xe*, Xe-P3, and Xe-P6.' *Geochimica et Cosmochimica Acta*, 69, pp. 4133–4148.

Gilmour, J. D., Whitby, J. A. and Turner, G. (1999) 'Martian atmospheric xenon contents of Nakhla mineral separates: Implications for the origin of elemental mass fractionation.' *Earth and Planetary Science Letters*, 166, pp. 139–147.

Glass, B. P. (1976) 'Major element composition of glasses from Apollo 11, 16, and 17 soil samples.' *Proceedings of 7th Lunar and Planetary Science Conference*, pp. 679–693.

Gloeckler, G. and Geiss, J. (2000) 'Deuterium and Helium-3 in the Protosolar Cloud.' *The Light Elements and their Evolution, Proceedings of IAU Symposium*, 198, p. 224–233.

Goldstein, J. I., Newbury, D. E., Echlin, P., Joy, D. C., Lyman, C. E., Lifshin, E., Sawyer, L. and Michael, J. R. (2003) 'Electron beam–specimen interactions.' In *Scanning Electron Microscopy and X-ray Microanalysis, Third Edition*. Springer US, pp. 61–98.

Gombosi, D. J., Baldwin, S. L., Watson, E. B., Swindle, T. D., Delano, J. W. and Roberge, W. G. (2015) 'Argon diffusion in Apollo 16 impact glass spherules: Implications for $^{40}$Ar/$^{39}$Ar dating of lunar impact events.' *Geochimica et Cosmochimica Acta*, 148, pp. 251–268.

Gomes, R., Levison, H. F., Tsiganis, K. and Morbidelli, A. (2005) 'Origin of the cataclysmic Late Heavy Bombardment period of the terrestrial planets.' *Nature*, 435, pp. 466–469.

Gomes, R. S., Fern Ndez, J. a, Gallardo, T. and Brunini, A. (2008) 'The Scattered Disk: Origins, dynamics, and end states.' *The Solar System Beyond Neptune*, p. 259–273.

Grimberg, A., Baur, H., Bochsler, P., Bühler, F., Burnett, D. S., Hays, C. C., Heber, V. S., Jurewicz, A. J. G. and Wieler, R. (2006) 'Solar wind neon from Genesis: Implications for the lunar noble gas record.' *Science*, 314, pp. 1133–1135.

Grochala, W. (2007) 'Atypical compounds of gases, which have been called "noble."' *Chemical Society reviews*, 36, pp. 1632–55.

Gross, J., Treiman, A. H. and Harlow, G. E. (2017) 'Reported sulfate mineral in lunar meteorite PCA 02007 is impact glass.' *Meteoritics & Planetary Science*, 52, pp. 191–194.

Gudipati, M. S., Abou Mrad, N., Blum, J., Charnley, S. B., Chiavassa, T., Cordiner, M. A., Mousis, O., Danger, G., Duvernay, F., Gundlach, B., Hartogh, P., Marboeuf, U., Simonia, I., Simonia, T., Theulé, P. and Yang, R. (2015) 'Laboratory Studies Towards Understanding Comets.' *Space Science Reviews*, 197, pp. 101–150.

Guilbert-Lepoutre, A., Besse, S., Mousis, O., Ali-Dib, M., Höfner, S., Koschny, D. and Hager, P. (2015) 'On the Evolution of Comets.' *Space Science Reviews*, 197, pp. 271–296.

Haggerty, S. (1974) 'Apollo 17 orange glass: Textural and morphological characteristics of devitrification.' *Proceedings of 5th Lunar and Planetary Science Conference*, 1, pp. 193–205.

Halliday, A. N. (2000) 'Terrestrial accretion rates and the origin of the Moon.' *Earth and Planetary Science Letters*, 176, pp. 17–30.

Hanner, M. S. and Zolensky, M. E. (2010) 'The mineralogy of cometary dust.' *Astromineralogy*, pp. 203–232.

Harper, C. L. and Jacobsen, S. B. (1996) 'Noble gases and Earth's accretion.' *Science*, 273, pp. 1814–1818.

Hartmann, W. K. and Davis, D. R. (1975) 'Satellite-sized planetesimals and lunar origin.' *Icarus*, 24, pp. 504–515.

Heber, V. S. (2002) *PhD Thesis: Ancient solar wind noble gases in lunar and meteoritic archives and tests for modern solar wind collection with the GENESIS mission*. Swiss Federal Instituite of Technology Zurich.

Heber, V. S., Baur, H., Bochsler, P., McKeegan, K. D., Neugebauer, M., Reisenfeld, D. B., Wieler, R. and Wiens, R. C. (2012) 'Isotopic mass fractionation of solar wind: Evidence from fast and slow solar wind collected by the Genesis mission.' *The Astrophysical Journal*, 759, 121.

Heber, V. S., Wieler, R., Baur, H., Olinger, C., Friedmann, T. A. and Burnett, D. S. (2009) 'Noble gas composition of the solar wind as collected by the Genesis mission.' *Geochimica et Cosmochimica Acta*, 73, 7414–7432.

Heiken, G. H., McKay, D. S. and Brown, R. (1974) ‘Lunar deposits of possible pyroclastic origin.’ *Geochimica et Cosmochimica Acta*, 38, pp. 1703–1718.

Heymann, D. and Dziczkaniec, M. (1979) ‘Xenon from intermediate zones of supernovae.’ *Proceedings of 10th Lunar and Planetary Science Conference*, pp. 1943–1959.

Hibbitts, C. A., Dyar, M. D., Orlando, T. M., Grieves, G. and Szanyi, J. (2009) ‘Cold trapping of volatiles in the lunar regolith.’ in *40th Lunar and Planetary Science Conference* (abstract), Texas, USA.

Hillebrandt, W. (1978) ‘The rapid neutron-capture process and the synthesis of heavy and neutron-rich elements.’ *Space Science Reviews*, 21, pp. 639–702.

Hintenberger, H., Weber, H. W. and Schultz, L. (1974) ‘Solar, spallogenic, and radiogenic rare gases in Apollo 17 soils and breccias.’ *Proceedings of 5th Lunar and Planetary Science Conference*, 2, pp. 2005–2022.

Hohenberg, C. M., Hudson, B., Kennedy, B. M. and Podosek, F. A. (1981) ‘Xenon spallation systematics in Angra Dos Reis.’ *Geochimica et Cosmochimica Acta*, 45, pp. 1909–1915.

Hohenberg, C. M., Marti, K., Podosek, F. A., Reedy, R. and Shrick, J. R. (1978) ‘Comparisons between observed and predicted cosmogenic gases in lunar samples.’ *Proceedings of the 9th Lunar and Planetary Sciences Conference*, pp. 2311–2344.

Hohenberg, C. M., Thonnard, N. and Meshik, A. (2002) ‘Active capture and anomalous adsorption: New mechanisms for the incorporation of heavy noble gases.’ *Meteoritics & Planetary Science*, 37, pp. 257–267.

Horner, J., Evans, N. W. and Bailey, M. E. (2004) ‘Simulations of the population of Centaurs - I. The bulk statistics.’ *Monthly Notices of the Royal Astronomical Society*, 354, pp. 798–810.

Hsieh, H. H. and Haghighipour, N. (2016) ‘Potential Jupiter-Family comet contamination of the main asteroid belt.’ *Icarus*, 277, pp. 19–38.

Huebner, W. F. (2006) ‘Heat and gas diffusion in comet nuclei.’ *Space Science Reviews*, 4, pp. 869–904.

Huebner, W. F. and Benkhoff, J. (1997) ‘On the relationship of chemical abundances in the nucleus to those in the coma.’ *Earth, Moon and Planets*, 77, pp. 217–222.

Huebner, W. F. and Benkhoff, J. (1999) ‘From coma abundances to nucleus composition’ in Altwegg, K., Ehrenfreund, P., Geiss, J., and Huebner, W. F. (eds) *Composition and Origin of Cometary Materials: Proceedings of an ISSI Workshop, 14-18 September 1998, Bern, Switzerland*, Springer Netherlands, pp. 117–130.

Huebner, W. F. (2008) ‘Origins of cometary materials’ in Balsiger, H., Altwegg, K., Huebner, W., Owen, T., and Schulz, R. (eds) *Origin and early evolution of comet nuclei*. Springer Science+Business Media, pp. 5–25.

Hughes, S., Delano, J. and Schmitt, R. (1990) ‘Chemistries of individual mare volcanic glasses: Evidence for distinct source regions of hybridized mantle and a KREEP component in Apollo 14 magmatic sources.’ *Proceedings of 20th Lunar and Planetary Science Conference*, pp. 127–138.

Hughes, S. S., Delano, J. W. and Schmitt, R. A. (1988) ‘Apollo 15 yellow-brown volcanic glass: Chemistry and petrogenetic relations to green volcanic glass and olivine-normative mare basalts.’ *Geochimica et Cosmochimica Acta*, 52, pp. 2379–2391.

Hughes, S. S., Delano, J. W. and Schmitt, R. A. (1990) ‘Chemistries of individual mare volcanic glasses: Evidence for distinct regions of hybridised mantle and a KREEP component in Apollo 14 magmatic sources.*’ Proceedings of 20th Lunar and Planetary Science Conference*, pp. 127–138.

Hui, H., Hess, K. U., Zhang, Y., Nichols, A. R. L., Peslier, A. H., Lange, R. A., Dingwell, D. B. and Neal, C. R. (2018) ‘Cooling rates of lunar orange glass beads.’ *Earth and Planetary Science Letters*, 503, pp. 88–94.

Huneke, J. C. (1978) ‘Ar-40 - Ar-39 microanalysis of single 74220 glass balls and 72435 breccia clasts.’ *Proceedings of 9th Lunar and Planetary Science Conference*, 2, pp. 2345–2362.

Huneke, J. C., Podosek, F. A. and Wasserburg, G. J. (1973) ‘An argon bouillabaisse including ages from the Luna 20 site.’ *Abstracts of the Lunar and Planetary Science Conference*, 4, 403–404.

Hunten, D. M. (1973) ‘The escape of light gases from planetary atmospheres.’ *Journal of the Atmospheric Sciences*, 30, pp. 1481–1494.

Hunten, D. M, Pepin, R. O. and Walker, J. C. G. (1987) ‘Mass fractionation in hydrodynamic escape.’ *Icarus*, 69, pp. 532–549.

Husain, L. and Schaeffer, O. A. (1973) ‘Lunar volcanism: Age of the glass in the Apollo 17 orange soil.’ *Science*, 180, pp. 1358–1360.

Huss, G. and Alexander, E. (1987) ‘On the presolar origin of the “normal planetary” noble gas component in meteorites.’ *Journal of Geophysical Research*, 92, pp. E710–E716.

Huss, G. R. and Lewis, R. S. (1994) ‘Noble gases in presolar diamonds I: Three distinct components and their implications for diamond origins.’ *Meteoritics*, 29, pp. 791–810.

Huss, G. R., Lewis, R. S. and Hemkin, S. (1996) ‘The “normal planetary” noble gas component in primitive chondrites: Compositions, carrier, and metamorphic history.’ *Geochimica et Cosmochimica Acta*, 60, pp. 3311–3340.

Imae, N. (2013) ‘Cometary dust in Antarctic micrometeorites.’ *Proceedings of the International Astronomical Union*, 8(S288), pp. 123–129.

Ishii, H. A., Bradley, J. P., Dai, Z. R., Chi, M., Kearsley, A. T., Burchell, M. J., Browning, N. D. and Molster, F. (2008) ‘Comparison of Comet 81P/Wild 2 Dust with Interplanetary Dust from Comets.’ *Science*, 319, pp. 447–450.

Ishii, H., Brennan, S., Bradley, J., Luening, K., Ignatyev, K. and Pianetta, P. (2008) 'Recovering the elemental composition of comet Wild 2 dust in five Stardust impact tracks and terminal particles in aerogel.' *Meteoritics & Planetary Science*, 43, pp. 215–231.

Jakosky, B. M., Brain, D., Chaffin, M., Curry, S., Deighan, J., Grebowsky, J., Halekas, J., Leblanc, F., Lillis, R., Luhmann, J. G., Andersson, L., Andre, N., Andrews, D., Baird, D., Baker, D., Bell, J., Benna, M., Bhattacharyya, D., Bougher, S., Bowers, C., Chamberlin, P., Chaufray, J. Y., Clarke, J., Collinson, G., Combi, M., Connerney, J., Connour, K., Correira, J., Crabb, K., Crary, F., Cravens, T., Crismani, M., Delory, G., Dewey, R., DiBraccio, G., Dong, C., Dong, Y., Dunn, P., Egan, H., Elrod, M., England, S., Eparvier, F., Ergun, R., Eriksson, A., Esman, T., Espley, J., Evans, S., Fallows, K., Fang, X., Fillingim, M., Flynn, C., Fogle, A., Fowler, C., Fox, J., Fujimoto, M., Garnier, P., Girazian, Z., Groeller, H., Gruesbeck, J., Hamil, O., Hanley, K. G., Hara, T., Harada, Y., Hermann, J., Holmberg, M., Holsclaw, G., Houston, S., Inui, S., Jain, S., Jolitz, R., Kotova, A., Kuroda, T., Larson, D., Lee, Y., Lee, C., Lefevre, F., Lentz, C., Lo, D., Lugo, R., Ma, Y. J., Mahaffy, P., Marquette, M. L., Matsumoto, Y., Mayyasi, M., Mazelle, C., McClintock, W., McFadden, J., Medvedev, A., Mendillo, M., Meziane, K., Milby, Z., Mitchell, D., Modolo, R., Montmessin, F., Nagy, A., Nakagawa, H., Narvaez, C., Olsen, K., Pawlowski, D., Peterson, W., Rahmati, A., Roeten, K., Romanelli, N., Ruhunusiri, S., Russell, C., Sakai, S., Schneider, N., Seki, K., Sharrar, R., Shaver, S., Siskind, D. E., Slipski, M., Soobiah, Y., Steckiewicz, M., Stevens, M. H., Stewart, I., Stiepen, A., Stone, S., Tenishev, V., Terada, N., Terada, K., Thiemann, E., Tolson, R., Toth, G., Trovato, J., Vogt, M., Weber, T., Withers, P., Xu, S., Yelle, R., Yiğit, E. and Zurek, R. (2018) 'Loss of the Martian atmosphere to space: Present-day loss rates determined from MAVEN observations and integrated loss through time.' *Icarus*, 315, pp. 146–157.

Jarosewich, E. (2002) 'Smithsonian microbeam standards.' *Journal of Research of the National Institute of Standards and Technology*, 107, pp. 681–685.

Jeffery, P. M. and Reynolds, J. H. (1961) 'Origin of excess $^{129}$Xe in stone meteorites.' *Journal of Geophysical Research*, 66, pp. 3582–3583.

Jewitt, D. C. (2004) 'From cradle to grave: The rise and demise of the comets.' in Festou, M., Keller, H. U., and Weaver, H. A. (eds) *Comets II*, University of Arizona Press, pp. 659–676.

Karouji, Y., Arai, T. and Ebihara, M. (2006) 'Chemical composition of another KREEP-rich lunar regolith breccia Yamato 983885.' in *Lunar and Planetary Science XXXVII* (abstract), Houston, USA.

Kehm, K., Crowther, S., Gilmour, J. D., Mohapatra, R. K. and Hohenberg, C. M. (2009) 'Upper limit concentrations of trapped xenon in individual interplanetary dust particles from the stratosphere.' *Meteoritics and Planetary Science*, 44, pp. 249–259.

Kehm, K., Flynn, G. J., Sutton, S. R. and Hohenberg, C. M. (2002) 'Combined noble gas and trace element measurements on individual stratospheric interplanetary dust particles.' *Meteoritics & Planetary Science*, 37, pp. 1323–1335.

Kirsten, T., Horn, P., Heymann, D., Hübner, W. and Storzer, D. (1973) 'Apollo 17 crystalline rocks and soils: Rare gases, ion tracks, and ages.' *EOS Transactions*, 54, pp. 595–596.

Korotev, R. L., Zeigler, R. A., Jolliff, B. L., Irving, A. J. and Bunch, T. E. (2009) ‘Compositional and lithological diversity among brecciated lunar meteorites of intermediate iron concentration.’ *Meteoritics and Planetary Science*, 44, pp. 1287–1322.

Koscheev, A. P., Gromov, M. D., Mohapatra, R. K. and Ott, U. (2001) ‘History of trace gases in presolar diamonds inferred from ion-implantation experiments.’ *Nature*, 412, pp. 615–617.

Kring, D. A. (2006) Parameters of lunar soils upper crust of the Moon. Lunar exploration initiative. [Online] [Accessed on 18th August 2020] https://www.lpi.usra.edu/science/kring/lunar_exploration/briefings/lunar_soil_physical_properties.pdf.

Kuga, M., Cernogora, G., Marrocchi, Y., Tissandier, L. and Marty, B. (2017) ‘Processes of noble gas elemental and isotopic fractionations in plasma-produced organic solids: Cosmochemical implications.’ *Geochimica et Cosmochimica Acta*, 217, pp. 219–230.

Lakatos, S., Heymann, D. and Yaniv, A. (1973) ‘Green spherules from Apollo 15: Inferences about their origin from inert gas measurements.’ *The Moon*, 7, pp. 132–148.

Lamb, S. A., Howard, W. M., Truran, J. W. and Iben, I., J. (1977) ‘Neutron-capture nucleosynthesis in the helium-burning cores of massive stars.’ *The Astrophysical Journal*, 217, p. 213–221.

Laufer, D., Kochavi, E. and Bar-Nun, A. (1987) ‘Structure and dynamics of amorphous water ice.’ *Physical Review B*, 36, pp. 9219–9227.

Lawton, T. (2020) Automaton 1.4. Mendeley Data. [Online] http://dx.doi.org/10.17632/zt25vm4m4f.1.

Leroux, H. (2012) ‘Fine-grained material of 81P/Wild 2 in interaction with the Stardust aerogel.’ *Meteoritics and Planetary Scienc*e, 47, pp. 613–622.

Leroux, H., Rietmeijer, F. J. M., Velbel, M. A., Brearley, A. J., Jacob, D., Langenhorst, F., Bridges, J. C., Zega, T. J., Stroud, R. M., Cordier, P., Harvey, R. P., Lee, M., Gounelle, M. and Zolensky, M. E. (2008) ‘A TEM study of thermally modified comet 81P/Wild 2 dust particles by interactions with the aerogel matrix during the Stardust capture process.’ *Meteoritics & Planetary Science*, 43, pp. 97–120.

Levison, H. (1996) ‘Comet taxonomy.’ *Completing the Inventory of the Solar System, Astronomical Society of the Pacific Conference Proceedings*, pp. 173–191.

Levison, H. F. and Morbidelli, A. (2003) ‘The formation of the Kuiper belt by the outward transport of bodies during Neptune’s migration.’ *Nature*, 426, pp. 419–421.

Lewis, R. S., Ming, T., Wacker, J. F., Anders, E. and Steel, E. (1987) ‘Interstellar diamonds in meteorites.’ *Nature*, 326, pp. 160–162.

Lewis, R. S., Srinivasan, B. and Anders, E. (1975) ‘Host phase of a strange xenon component in Allende.’ *Science*, 190, pp. 1251–1262.

Leya, I., Neumann, S., Wieler, R. and Michel, R. (2001) 'The production of cosmogenic nuclides by galactic cosmic-ray particles for 2π exposure geometries.' *Meteoritics & Planetary Science*, 36, pp. 1547–1561.

Lodders, K. (2003) 'Solar System abundances and condensation temperatures of the elements.' *The Astrophysical Journal*, 591, pp. 1220–1247.

Lodders, K., Palme, H. and Gail, H.-P. (2009) 'Abundances of the elements in the Solar System.' in Trümper, J. E. (ed) *Astronomy, Astrophysics, and Cosmology (Solar System)*, Springer, pp. 712–770.

Ludwig, K. R. (2008) 'Isoplot 3.70 A Geochronological Toolkit for Microsoft Excel.' *Berkely Geochronology Centre Special Publication No. 4*, pp. 1–76.

Lux G. (1987) 'The behavior of noble gases in silicate liquids: Solution, diffusion, bubbles and surface effects, with applications to natural samples.' *Geochimica et Cosmochimica Acta*, 51, pp. 1549–1560.

Mahaffy, P. R., Benna, M., King, T., Harpold, D. N., Arvey, R., Barciniak, M., Bendt, M., Carrigan, D., Errigo, T., Holmes, V., Johnson, C. S., Kellogg, J., Kimvilakani, P., Lefavor, M., Hengemihle, J., Jaeger, F., Lyness, E., Maurer, J., Melak, A., Noreiga, F., Noriega, M., Patel, K., Prats, B., Raaen, E., Tan, F., Weidner, E., Gundersen, C., Battel, S., Block, B. P., Arnett, K., Miller, R., Cooper, C., Edmonson, C. and Nolan, J. T. (2015) 'The Neutral Gas and Ion Mass Spectrometer on the Mars Atmosphere and Volatile Evolution Mission.' *Space Science Reviews*, 195, pp. 49–73.

Mahaffy, P. R., Niemann, H. B., Alpert, A., Atreya, S. K., Demick, J., Donahue, T. M., Harpold, D. N. and Owen, T. C. (2000) 'Noble gas abundance and isotope ratios in the atmosphere of Jupiter from the Galileo Probe Mass Spectrometer.' *Journal of Geophysical Research*, 105, p. 15061–15071.

Mahaffy, P. R., Webster, C. R., Cabane, M., Conrad, P. G., Coll, P., Atreya, S. K., Arvey, R., Barciniak, M., Benna, M., Bleacher, L., Brinckerhoff, W. B., Eigenbrode, J. L., Carignan, D., Cascia, M., Chalmers, R. A., Dworkin, J. P., Errigo, T., Everson, P., Franz, H., Farley, R., Feng, S., Frazier, G., Freissinet, C., Glavin, D. P., Harpold, D. N., Hawk, D., Holmes, V., Johnson, C. S., Jones, A., Jordan, P., Kellogg, J., Lewis, J., Lyness, E., Malespin, C. A., Martin, D. K., Maurer, J., McAdam, A. C., McLennan, D., Nolan, T. J., Noriega, M., Pavlov, A. A., Prats, B., Raaen, E., Sheinman, O., Sheppard, D., Smith, J., Stern, J. C., Tan, F., Trainer, M., Ming, D. W., Morris, R. V., Jones, J., Gundersen, C., Steele, A., Wray, J., Botta, O., Leshin, L. A., Owen, T., Battel, S., Jakosky, B. M., Manning, H., Squyres, S., Navarro-González, R., McKay, C. P., Raulin, F., Sternberg, R., Buch, A., Sorensen, P., Kline-Schoder, R., Coscia, D., Szopa, C., Teinturier, S., Baffes, C., Feldman, J., Flesch, G., Forouhar, S., Garcia, R., Keymeulen, D., Woodward, S., Block, B. P., Arnett, K., Miller, R., Edmonson, C., Gorevan, S. and Mumm, E. (2012) 'The sample analysis at Mars investigation and instrument suite.' *Space Science Reviews*, 170, pp. 401–478.

Mahajan, R. R. (2015) 'Lunar meteorite Yamato-983885: Noble gases, nitrogen and cosmic ray exposure history.' *Planetary and Space Science*, 117, pp. 24–34.

Mandt, K. E., Mousis, O., Marty, B., Cavalié, T., Harris, W., Hartogh, P. and Willacy, K. (2015) 'Constraints from comets on the formation and volatile acquisition of the planets and satellites.' *Space Science Reviews*, pp. 297–342.

Mao, H. K., Virgo, D. and Bell, P. M. (1973) ‘Sample 74220: analysis of the Apollo 17 orange soil from Shorty Crater.’ *EOS Transactions*, 54, pp. 598–600.

Marrocchi, Y. and Marty, B. (2013) ‘Experimental determination of the xenon isotopic fractionation during adsorption.’ *Geophysical Research Letters*, 40, pp. 4165–4170.

Marti, K. (1967) ‘Trapped xenon and the classification of chondrites.’ *Earth and Planetary Science Letters*, 2, pp. 193–196.

Marti, K. and Mathew, K. J. (1998) ‘Noble gas components in planetary atmospheres and interiors in relation to solar wind and meteorites.’ *Proceedings of the Indian Academy of Sciences - Earth and Planetary Sciences*, 107, pp. 425–431.

Marty, B. (2012) ‘The origins and concentrations of water, carbon, nitrogen and noble gases on Earth.’ *Earth and Planetary Science Letters*, 313–314, pp. 56–66.

Marty, B., Altwegg, K., Balsiger, H., Bar-Nun, A., Bekaert, D. V., Berthelier, J.-J., Bieler, A., Briois, C., Calmonte, U., Combi, M., De Keyser, J., Fiethe, B., Fuselier, S. A., Gasc, S., Gombosi, T. I., Hansen, K. C., Hässig, M., Jäckel, A., Kopp, E., Korth, A., Le Roy, L., Mall, U., Mousis, O., Owen, T., Rème, H., Rubin, M., Sémon, T., Tzou, C.-Y., Waite, J. H. and Wurz, P. (2017) ‘Xenon isotopes in 67P/Churyumov-Gerasimenko show that comets contributed to Earth’s atmosphere.’ *Science*, 356, pp. 1069–1072.

Marty, B., Avice, G., Sano, Y., Altwegg, K., Balsiger, H., Hässig, M., Morbidelli, A., Mousis, O. and Rubin, M. (2016) ‘Origins of volatile elements (H, C, N, noble gases) on Earth and Mars in light of recent results from the ROSETTA cometary mission.’ *Earth and Planetary Science Letters*, 441, pp. 91–102.

Marty, B. and Dauphas, N. (2002) ‘Formation and early evolution of the atmosphere.’ In Fowler, C. M. R., Ebinger, C. J., and Hawkesworth, C. J. (eds) *The Early Earth: Physical, Chemical and Biological Development*, The Geological Society of London, pp. 213–229.
Marty, B. and Marti, K. (2002) ‘Signatures of early differentiation of Mars.’ *Earth and Planetary Science Letters*, 196, pp. 251–263.

Marty, B., Palma, R. L., Pepin, R. O., Zimmermann, L., Schlutter, D. J., Burnard, P. G., Westphal, A. J., Snead, C. J., Bajt, S., Becker, R. H. and Simones, J. E. (2008) ‘Helium and neon abundances and compositions in cometary matter.’ *Science*, 319, pp. 75–78.

Mathew, K. J., Kim, J. S. and Marti, K. (1998) ‘Martian atmospheric and indigenous components of xenon and nitrogen in the Shergotty, Nakhla, and Chassigny group meteorites.’ *Meteoritics & Planetary Science*, 33, pp. 655–664.

Mathew, K. J. and Marti, K. (2001) ‘Early evolution of Martian volatiles: Nitrogen and noble gas components in ALH84001 and Chassigny.’ *Journal of Geophysical Research*, 106 pp. 1401–1422.

Mathew, K. J. and Marti, K. (2002) ‘Martian atmospheric and interior volatiles in the meteorite Nakhla.’ *Earth and Planetary Science Letters*, 199, pp. 7–20.

Mathews, G. J. and Cowan, J. J. (1990) ‘New insights into the astrophysical r-process.’ *Nature*, 345, pp. 491–494.

Matsuda, J.-I., Lewis, R. S., Takahashi, H. and Anders, E. (1980) 'Isotopic anomalies of noble gases in meteorites and their origins—VII. C3V carbonaceous chondrites.' *Geochimica et Cosmochimica Acta*, 44, pp. 1861–1874.

Matsuda, J. I., Morishita, K., Tsukamoto, H., Miyakawa, C., Nara, M., Amari, S., Uchiyama, T. and Takeda, S. (2010) 'An attempt to characterize phase Q: Noble gas, Raman spectroscopy and transmission electron microscopy in residues prepared from the Allende meteorite.' *Geochimica et Cosmochimica Acta*, 74, pp. 5398–5409.

Matsuda, J. and Yoshida, T. (2001) 'The plasma model for the origin of phase Q: an experimental approach and the comparison with the labyrinth model.' in *64th Annual Meteoritical Society Meeting* (abstract), Vatican City.

Maurette, M., Duprat, J., Engrand, C., Gounelle, M., Kurat, G., Matrajt, G., Toppani, A., Engrand, E., Gounelle, M., Kurat, G., Matrajt, G. and Toppani, A. (2000) 'Accretion of neon, organics, CO2, nitrogen and water from large interplanetary dust particles on the early Earth.' *Planetary and Space Science*, 48, pp. 1117–1137.

Mazor, E., Heymann, D. and Anders, E. (1970) 'Noble gases in carbonaceous chondrites.' *Geochimica et Cosmochimica Acta*, 34, pp. 781–824.

McElroy, M. B., Kong, T. Y. and Yung, Y. L. (1977) 'Photochemistry and evolution of Mars' atmosphere: A Viking perspective.' *Journal of Geophysical Research*, 82, pp. 4379–4388.

Mckeegan, K. D., Aléon, J., Bradley, J., Brownlee, D., Busemann, H., Butterworth, A., Chaussidon, M., Fallon, S., Floss, C., Gilmour, J., Gounelle, M., Graham, G., Guan, Y., Heck, P. R., Snead, C. J., Stadermann, F. J., Stroud, R., Tsou, P. and Westphal, A. (2006) 'Isotopic compositions of cometary matter returned by Stardust.' *Science*, 314, pp. 1724–1728.

Meech, K. J., Yang, B., Kleyna, J., Hainaut, O. R., Berdyugina, S., Keane, J. V, Micheli, M., Morbidelli, A. and Wainscoat, R. J. (2016) 'Inner solar system material discovered in the Oort cloud.' *Science Advances*, 2, e1600038.

Meshik, A., Pravdivtseva, O. and Burnett, D. (2019) 'Isotopic composition of solar wind xenon captured by Genesis: Verification and possible implication for indigenous lunar xenon.' in *50th Lunar and Planetary Science Conference* (abstract), Texas, USA.

Meshik, A., Hohenberg, C., Pravdivtseva, O. and Burnett, D. (2014) 'Heavy noble gases in solar wind delivered by Genesis mission.' *Geochimica et Cosmochimica Acta*, 127, pp. 326–347.

Meshik, A., Schovsbo, N. H. and Pravdivtseva, O. (2019) 'Xenon isotopes in the Scandinavian Alum Shale: A clue for the origin of P1(Q) and P3 xenon components in nanodiamond-rich residues from primitive meteorites.' in *82nd Annual Meeting of The Meteoritical Society* (abstract), Sapporo, Japan.

Messenger, S. (2002) 'Opportunities for the stratospheric collection of dust from short-period comets.' *Meteoritics & Planetary Science*, 37, pp. 1491–1505.

Meyer, J. C., Mckay, D. S., Anderson, D. H. and Butler, J. P. (1975) 'The source of sublimates on the Apollo 15 green and Apollo 17 orange glass samples.' *Proceedings of 6th Lunar and Planetary Science Conference*, p.1673-1699.

Mohapatra, R. K., Herrmann, S., Ott, U., Westphal, A. and Clark, I. D. (2013) 'Stardust Aerogel - A Noble Gas Experiment.' in *44th Lunar and Planetary Science Conference* (abstract), Texas, USA.

Mohapatra, R., Ott, U. and Clark, I. (2011) 'Cometary noble gases trapped by the Stardust aerogel.' in *74th Annual Meteoritical Society Meeting* (abstract), London, UK.

Morbidelli, A., Levison, H. F., Tsiganis, K. and Gomes, R. (2005) 'Chaotic capture of Jupiter's Trojan asteroids in the early Solar System.' *Nature*, 435, pp. 462–465.

Morbidelli, A., Emel'yanenko, V. V. and Levison, H. F. (2004) 'Origin and orbital distribution of the trans-Neptunian scattered disc.' *Monthly Notices of the Royal Astronomical Society*, 355, pp. 935–940.

Morgan, J. W., Krähenbühl, U., Ganapathy, R., Anders, E. and Marvin, U. (1973) 'Trace element abundances and petrology of separates from Apollo 15 soils.' *Proceedings of 4th Lunar and Planetary Science Conference*, 2, pp. 1379–1398.

Morris, R. (1976) 'Surface exposure indices of lunar soils: A comparative FMR study.' *Proceedings of 7th Lunar and Planetary Science Conference*, pp. 315–335.

Morris, R. V. (1978) 'The surface exposure (maturity) of lunar soils: Some concepts and Is/FeO compilation.' *Proceedings of 9th Lunar and Planetary Science Conference*, pp. 2287–2297.

Mumma, M. J. and Charnley, S. B. (2011) 'The Chemical Composition of Comets—Emerging Taxonomies and Natal Heritage.' *Annual Review of Astronomy and Astrophysics*, 49, pp. 471–524.

Murty, S. V. S. and Mohapatra, R. K. (1997) 'Nitrogen and heavy noble gases in ALH 84001: Signatures of ancient Martian atmosphere.' *Geochimica et Cosmochimica Acta*, 61, pp. 5417–5428.

Nagle, J. S. (1981) 'Apollo 15 green glass: A mare margin deposit.' *Proceedings of 12th Lunar and Planetary Science Conference*, pp. 750–752.

Needham, D. H. and Kring, D. A. (2017) 'Lunar volcanism produced a transient atmosphere around the ancient Moon.' *Earth and Planetary Science Letters*, 478, pp. 175–178.

Nier, A. O. and Schlutter, D. J. (1993) 'The thermal history of interplanetary dust particles collected in the Earth's stratosphere.' *Meteoritics*, 28, pp. 675–681.

O'Mara, A, Busemann, H., Clay, P. L., Crowther, S. A., Gilmour, J. D. and Wieler, R. (2014) 'Xenon Release by the In-Vacuum Etching of Aerogel: Implications for the Study of Noble Gases in Comet Wild 2 Stardust.' in *77th Annual Meeting of the Meteoritical Society* (abstract), Houston, USA.

Oort, J. H. (1950) ‘The structure of the cloud of comets surrounding the Solar System and a hypothesis concerning its origin.’ *Bulletin of the Astronomical Institutes of the Netherlands*, 11, pp. 91–110.

Öpik, E. (1932) ‘Note on Stellar Perturbations of Nearly Parabolic Orbits.’ *Proceedings of the American Academy of Arts and Sciences*, 67, pp. 169–183.

Ott, U. (1988) ‘Noble gases in SNC meteorites: Shergotty, Nakhla, Chassigny.’ *Geochimica et Cosmochimica Acta*, 52, pp. 1937–1948.

Ott, U. (2008) ‘An almost infinite sink for tightly bound xenon: Etched Shergotty and (less so) etched Nakhla.’ in *39th Lunar and Planetary Science Conference* (abstract), Texas, USA.

Ott, U. (2014) ‘Planetary and pre-solar noble gases in meteorites.’ *Chemie der Erde*, 74, pp. 519–544.

Ott, U. and Begemann, F. (1985) ‘Are all the “Martian” meteorites from Mars?’ *Nature*, 317, pp. 509–512.

Ott, U., Mack, R. and Sherwood, C. (1981) ‘Noble-gas-rich separates from the Allende meteorite.’ *Geochimica et Cosmochimica Acta*, 45, pp. 1751–1788.

Ott, U., Swindle, T. D. and Schwenzer, S. P. (2019) ‘Noble gases in Martian meteorites.’ in Filiberto, J. and Schwenzer, S. P. (eds) *Volatiles in the Martian Crust*, Elsevier, pp. 35–70.

Owen, T. (2008) ‘The contributions of comets to planets, atmospheres, and life: Insights from Cassini-Huygens, Galileo, Giotto, and inner planet missions.’ *Space Science Reviews*, 138, pp. 301–316.

Owen, T. and Bar-Nun, A. (1995) ‘Comets, impacts, and atmospheres.’ *Icarus*, pp. 215–226.

Owen, T., Bar-Nun, A. and Kleinfeld, I. (1992) ‘Possible cometary origin of heavy noble gases in the atmospheres of Venus, Earth and Mars.’ *Nature*, 358, pp. 43–46.

Owen, T. and Biemann, K. (1976) ‘Composition of the atmosphere at the surface of Mars: Detection of argon-36 and preliminary analysis.’ *Science*, 193, pp. 801–803.

Owen, T., Biemann, K., Rushneck, D. R., Biller, J. E., Howarth, D. W. and Lafleur, A. L. (1976) ‘The atmosphere of Mars: Detection of krypton and xenon.’ *Science*, 194, pp. 1293–1295.

Owen, T., Biemann, K., Rushneck, D. R., Biller, J. E., Howarth, D. W. and Lafleur, A. L. (1977) ‘The composition of the atmosphere at the surface of Mars.’ *Journal of Geophysical Research*, 82, pp. 4635–4639.

Ozima, M., Wieler, R., Marty, B. and Podosek, F. A. (1998) ‘Comparative studies of solar, Q-gases and terrestrial noble gases, and implications on the evolution of the solar nebula.’ *Geochimica et Cosmochimica Acta*, 62, pp. 301–314.

Ozima and Podosek (1999) ‘Formation age of Earth from $^{129}I/^{127}I$ and $^{244}Pu/^{238}U$ systematics and the missing Xe.’ *Journal of Geophysical Research*, 104, pp. 25493–25499.

Paige, D., Siegler, M., Zhang, J., Hayne, P., Foote, E., Bennett, K., Vasavada, A., Greenhagen, B., Schofield, J., McCleese, D., Foote, M., DeJong, E., Bills, B., Hartford, W., Murray, B. C., Allen, C., Snook, K., Soderblom, L., Calcutt, S., Taylor, F., Bowles, N., Bandfield, J., Elphic, R., Ghent, R., Glotch, T., Wyatt, M. and Lucey, P. (2010) ‘Diviner Lunar Radiometer observations of cold traps in the Moon’s south polar region.’ *Science*, 330, pp. 479–482.

Palma, R. L., Pepin, R. O. and Schlutter, D. (2009) ‘A preliminary light noble gas investigation of Stardust samples.’ in *72nd Annual Meteoritical Society Meeting* (abstract), Nancy, France.

Palma, R. L., Pepin, R. O., Schlutter, D. J., Stodolna, J. and Westphal, A. (2013) ‘Q-gases in an unusual IDP: A noble gas link to carriers in Stardust track 41.’ in *44th Lunar and Planetary Science Conference* (abstract), Texas, USA.

Palma, R. L., Pepin, R. O., Westphal, A., Schlutter, D. and Gainsforth, Z. (2010) ‘Helium and neon in Stardust aerogel samples from cell 2044 adjacent to track 41.’ in *73rd Meeting of the Meteoritical Society* (abstract), New York.

Palma, R. L., Pepin, R. O., Westphal, A., Schlutter, D. and Gainsforth, Z. (2012) ‘Helium and neon in “blank” Stardust aerogel samples.’ in *43rd Lunar and Planetary Science Conference* (abstract), Texas, USA.

Palma, R L, Pepin, R. O., Westphal, A., Schlutter, D. and Gainsforth, Z. (2013) ‘A light noble gas inventory of Stardust cell C2044.’ in *44th Lunar and Planetary Science Conference* (abstract), Texas, USA.

Pan, Y., He, S., Cheng, X., Li, Z., Li, C., Huang, Y. and Gong, L. (2017) ‘A fast synthesis of silica aerogel powders-based on water glass via ambient drying.’ *Journal of Sol-Gel Science and Technology*, 82, pp. 594–601.

Paquette, J. A., Engrand, C., Stenzel, O., Hilchenbach, M. and Kissel, J. (2016) ‘Searching for calcium-aluminum-rich inclusions in cometary particles with Rosetta/COSIMA.’ *Meteoritics & Planetary Science*, 13, pp. 1–13.

Pepin, R. O. (1991) ‘On the origin and early evolution of terrestrial planet atmospheres and meteoritic volatiles.’ *Icarus*, 92, pp. 2–79.

Pepin, R. O. (2000) ‘On the isotopic composition of primordial xenon in terrestrial planet atmospheres.’ *Space Science Reviews*, 92, pp. 371–395.

Pepin, R. O., Becker, R. H. and Rider, P. E. (1995) ‘Xenon and krypton isotopes in extraterrestrial regolith soils and in the solar wind.’ *Geochimica et Cosmochimica Acta*, 59, pp. 4997–5022.

Pepin, R. O. and Phinney, D. (1982) ‘Components of xenon in the solar system.’ *Unpublished preprint*.

Pepin, R. O. and Porcelli, D. (2002) ‘Origin of noble gases in the terrestrial planets.’ *Reviews in Mineralogy and Geochemistry*, 47, pp. 191–246.

Pepin, R. O. and Porcelli, D. (2006) ‘Xenon isotope systematics, giant impacts, and mantle degassing on the early Earth.’ *Earth and Planetary Science Letters*, 250, pp. 470–485.

Philpotts, J. A., Schuhmann, S., Kouns, C. W., Lum, R. K. L. and Winzer, S. (1974) ‘Origin of Apollo 17 rocks and soils.’ *Proceedings of 5th Lunar and Planetary Science Conference*, 2, pp. 1255–1267.

Pierre, A. C. and Pajonk, M. (2002) ‘Chemistry of Aerogels and Their Applications.’ *Chemical Reviews*, 102, pp. 4243–4265.

Podosek, F. A. and Huneke, J. C. (1973) ‘Argon in Apollo 15 green glass spherules (15426): $^{40}$Ar-$^{39}$Ar age and trapped argon.’ *Earth and Planetary Science Letters*, 19, pp. 413–421.

Podosek, F. A. and Ozima, M. (2000) ‘The xenon age of the Earth.’ in Canup, R. M. and Righter, K. (eds) *Origin of the Earth and Moon*, University of Arizona Press, pp. 63–72.

Porcelli, D. and Ballentine, C. J. (2002) ‘Models for Distribution of Terrestrial Noble Gases and Evolution of the Atmosphere.’ *Reviews in Mineralogy and Geochemistry*, 47, pp. 411–480.

Pozuelos, F. J., Moreno, F., Aceituno, F., Casanova, V., Sota, A., López-Moreno, J. J., Castellano, J., Reina, E., Climent, A., Fernández, A., San Segundo, A., Häusler, B., González, C., Rodriguez, D., Bryssinck, E., Cortés, E., Rodriguez, F. A., Baldris, F., García, F., Gómez, F., Limón, F., Tifner, F., Muler, G., Almendros, I., de los Reyes, J. A., Henríquez, J. A., Moreno, J. A., Báez, J., Bel, J., Camarasa, J., Curto, J., Hernández, J. F., González, J. J., Martín, J. J., Salto, J. L., Lopesino, J., Bosch, J. M., Ruiz, J. M., Vidal, J. R., Ruiz, J. M., Sánchez, J., Temprano, J., Aymamí, J. M., Lahuerta, L., Montoro, L., Campas, M., García, M. A., Canales, O., Benavides, R., Dymock, R., García, R., Ligustri, R., Naves, R., Lahuerta, S. and Pastor, S. (2014) ‘Dust environment and dynamical history of a sample of short-period comets.’ *Astronomy & Astrophysics*, 571, A64.

Prinz, M., Dowty, E. and Keil, K. (1973) ‘A model for the origin of orange and green glasses and the filling of mare basins.’ *EOS Transactions*, 54, p. 605.

Pujol, M., Marty, B. and Burgess, R. (2011) ‘Chondritic-like xenon trapped in Archean rocks: A possible signature of the ancient atmosphere.’ *Earth and Planetary Science Letters*, 308, pp. 298–306.

Ragettli, R. A., Hebeda, E. H., Signer, P. and Wieler, R. (1994) ‘Uranium-xenon chronology: precise determination of $\lambda_{sf*}$ $^{136}Y_{sf}$ for spontaneous fission of $^{238}$U.’ *Earth and Planetary Science Letters*, 128, pp. 653–670.

Raymond, S. N., Quinn, T. and Lunine, J. I. (2004) ‘Making other earths: Dynamical simulations of terrestrial planet formation and water delivery.’ *Icarus*, 168, pp. 1–17.

Reid, A. M., Lofgren, G. E., Heiken, G. H., Brown, R. W. and Moreland, G. (1973) ‘Apollo 17 orange glass, Apollo 15 green glass and Hawaiian lava fountain glass.’ *EOS Transactions*, 54, pp. 606–607.

Reinhard, R. (1986) ‘The Giotto encounter with comet Halley.’ *Nature*, 321, pp. 313–318.

Renne, P. R., Balco, G., Ludwig, K. R., Mundil, R. and Min, K. (2011) 'Response to the comment by W.H. Schwarz et al. on "Joint determination of $^{40}$K decay constants and $^{40}$Ar*/$^{40}$K for the Fish Canyon sanidine standard, and improved accuracy for $^{40}$Ar/$^{39}$Ar geochronology" by P.R. Renne et al. (2010).' *Geochimica et Cosmochimica Acta*, 75, pp. 5097–5100.

Reufer, A., Meier, M. M. M., Benz, W. and Wieler, R. (2012) 'A hit-and-run giant impact scenario.' *Icarus*, 221(1) pp. 296–299.

Reynolds, J. H. (1956) 'High sensitivity mass spectrometer for noble gas analysis.' *Review of Scientific Instruments*, 27, pp. 928–934.

Reynolds, J. H. (1960) 'Determination of the age of the elements.' *Physical Review Letters*, 4, pp. 8–10.

Reynolds, J. H. (1963) 'Xenology.' *Journal of Geophysical Research*, 68, pp. 2939–2956.

Reynolds, J. H., Alexander, E. C., Davis, P. K. and Srinivasan, B. (1974) 'Studies of K-Ar dating and xenon from extinct radioactivities in breccia 14318; implications for early lunar history.' *Geochimica et Cosmochimica Acta*, 38, pp. 401–417.

Reynolds, J. H. and Turner, G. (1964) 'Rare gases in the chondrite Renazzo.' *Journal of Geophysical Research*, 69, pp. 3263–3281.

Ridley, W. I., Reid, A. M., Warner, J. L. and Brown, R. W. (1973) 'Apollo 15 green glasses.' *Physics of the Earth and Planetary Interiors*, 7, pp. 133–136.

Riebe, M. E. I., Busemann, H., Wieler, R. and Maden, C. (2017) 'Closed System Step Etching of CI chondrite Ivuna reveals primordial noble gases in the HF-solubles.' *Geochimica et Cosmochimica Acta*, 205, pp. 65–83.

Righter, K. (2013) 'Curator's comments.' *Antarctic Meteorite Newsletter*, 36(1), pp. 1–22.

Roedder, E. and Weiblen, P. W. (1973) 'Origin of orange glass spherules in Apollo-17 sample 74220.' *EOS Transactions*, 54, pp. 612–613.

Roskosz, M., Leroux, H. and Watson, H. C. (2008) 'Thermal history, partial preservation and sampling bias recorded by Stardust cometary grains during their capture.' *Earth and Planetary Science Letters*, 273, pp. 195–202.

Rubin, M., Altwegg, K., Balsiger, H., Bar-Nun, A., Berthelier, J.-J., Briois, C., Calmonte, U., Combi, M., De Keyser, J., Fiethe, B., Fuselier, S. A., Gasc, S., Gombosi, T. I., Hansen, K. C., Kopp, E., Korth, A., Laufer, D., Le Roy, L., Mall, U., Marty, B., Mousis, O., Owen, T., Rème, H., Sémon, T., Tzou, C.-Y., Waite, J. H. and Wurz, P. (2018) 'Krypton isotopes and noble gas abundances in the coma of comet 67P/Churyumov-Gerasimenko.' *Science Advances*, 4, eaar6297.

Russell, S. S., Folco, L., Grady, M. M., Zolensky, M. E., Jones, R., Righter, K., Zipfel, J. and Grossman, J. N. (2004) 'The meteoritical bulletin, No. 88, 2004 July.' *Meteoritics & Planetary Science*, 39(S8), pp. A215–A272.

Saal, A. E., Hauri, E. H., Cascio, M. Lo, Van Orman, J. A., Rutherford, M. C. and Cooper, R. F. (2008) 'Volatile content of lunar volcanic glasses and the presence of water in the Moon's interior.' *Nature*, 454, pp. 192–195.

De Sanctis, M. C., Lasue, J., Capria, M. T., Magni, G., Turrini, D. and Coradini, A. (2010) 'Shape and obliquity effects on the thermal evolution of the Rosetta target 67P/Churyumov-Gerasimenko cometary nucleus.' *Icarus*, 207, pp. 341–358.

Sandford, S. A., Aleon, J., Alexander, C. M. O., Araki, T., Bajt, S., Baratta, G. A., Borg, J., Bradley, J. P., Brownlee, D. E., Brucato, J. R., Burchell, M. J., Busemann, H., Butterworth, A., Clemett, S. J., Cody, G., Colangeli, L., Cooper, G., D'Hendecourt, L., Djouadi, Z., Dworkin, J. P., Ferrini, G., Fleckenstein, H., Flynn, G. J., Franchi, I. A., Fries, M., Gilles, M. K., Glavin, D. P., Gounelle, M., Grossemy, F., Jacobsen, C., Keller, L. P., Kilcoyne, A. L. D., Leitner, J., Matrajt, G., Meibom, A., Mennella, V., Mostefaoui, S., Nittler, L. R., Palumbo, M. E., Papanastassiou, D. A., Robert, F., Rotundi, A., Snead, C. J., Spencer, M. K., Stadermann, F. J., Steele, A., Stephan, T., Tsou, P., Tyliszczak, T., Westphal, A. J., Wirick, S., Wopenka, B., Yabuta, H., Zare, R. N. and Zolensky, M. E. (2006) 'Organics captured from comet 81P/Wild 2 by the Stardust Spacecraft.' *Science*, 314, pp. 1720–1724.

Saxena, P., Elkins-Tanton, L., Petro, N. and Mandell, A. (2017) 'A model of the primordial lunar atmosphere.' *Earth and Planetary Science Letters*, 474, pp. 198–205.

Schlebusch, C. M., Skoglund, P., Sjödin, P., Gattepaille, L. M., Hernandez, D., Jay, F., Li, S., Jongh, M. De, Singleton, A., Blum, M. G. B., Soodyall, H. and Jakobsson, M. (2010) 'Constraints on the formation age of cometary material from the NASA Stardust mission.' *Science*, 328, pp. 483–486.

Schwarzschild, M. and Härm, R. (1967) 'Hydrogen mixing by helium-shell flashes.' *The Astrophysical Journal*, 150, p. 961–970.

Schwenzer, S. P., Herrmann, S. and Ott, U. (2012) 'Noble gas adsorption with and without mechanical stress: Not Martian signatures but fractionated air.' *Meteoritics and Planetary Science*, 47, pp. 1049–1061.

Scott, E. R. D. and Krot, A. N. (2005) 'Thermal processing of silicate dust in the solar nebula: Clues from primitive chondrite matrices.' *The Astrophysical Journal*, 623, p. 571–578.

Seko, A. and Kobayashi, H. (1973) 'Application of channel multiplier plates as image information preprocessors.' *Review of Scientific Instruments*, 44, pp. 400–405.

Shearer, C. K. and Papike, J. J. (1993) 'Basaltic magmatism on the Moon: A perspective from volcanic picritic glass beads.' *Geochimica et Cosmochimica Acta*, 57, pp. 4785–4812.

Shearer, C. K., Papike, J. J., Galbreath, K. C. and Shimizu, N. (1991) 'Exploring the lunar mantle with secondary ion mass spectrometry: a comparison of lunar picritic glass beads from the Apollo 14 and Apollo 17 sites.' *Earth and Planetary Science Letters*, 102, pp. 134–147.

Shu, F. H., Shang, H. and Lee, T. (1996) 'Toward an astrophysical theory of chondrites.' *Science*, 271, pp. 1545–1552.

Signer, P., Baur, H. and Weiler, R. (1991) ‘Closed system stepped etching; an alternative to stepped heating.’ *Proceedings of the Alfred O. Nier Symposium on Inorganic Mass Spectrometry*, pp. 181–202.

Sill, G. T. and Wilkening, L. L. (1978) ‘Ice clathrate as a possible source of the atmospheres of the terrestrial planets.’ *Icarus*, 33, pp. 13–22.

Simon, S. B., Joswiak, D. J., Ishii, H. a., Bradley, J. P., Chi, M., Grossman, L., Aléon, J., Brownlee, D. E., Fallon, S., Hutcheon, I. D., Matrajt, G. and McKeegan, K. D. (2008) ‘A refractory inclusion returned by Stardust from comet 81P/Wild 2.’ *Meteoritics & Planetary Science*, 1877(11), pp. 1861–1877.

Spangler, R. R., Warasila, R. and Delano, J. W. (1984) ‘$^{39}$Ar-$^{40}$Ar ages for the Apollo 15 green and yellow volcanic glasses.’ *Journal of Geophysical Research*, 89(S02), p. B487–B497.

Steele, A. M., Colson, R., Korotev, R. L. and Haskin, L. A. (1992) ‘Apollo 15 green glass: Compositional distribution and petrogenesis.’ *Geochimica et Cosmochimica Acta*, 56, pp. 4075–4090.

Stern, S. A. (2003) ‘The evolution of comets in the Oort cloud and Kuiper belt.’ *Nature*, 424, pp. 639–642.

Stern, S. A. and Shull, J. M. (1988) ‘The influence of supernovae and passing stars on comets in the Oort cloud.’ *Nature*, 332, pp. 407–411.

Stern, S. A., Slater, D. C., Festou, M. C., Parker, J. W., A’Hearn, G. R. G. M. F. and Wilkinson, E. (2000) ‘The discovery of argon in comet C/1995 O1 (Hale-Bopp).’ *The Astrophysical Journal Letters*, 544(2), L169.

Swindle, T. D. (2002) ‘Noble gases in the Moon and meteorites: Radiogenic components and early volatile chronologies.’ *Reviews in Mineralogy and Geochemistry*, 47, pp. 101–124.

Swindle, T. D., Caffee, M. W., Hohenberg, C. M., Hudson, G. B., Laul, J. C., Simon, S. B. and Papike, J. J. (1985) ‘Noble gas component organization in Apollo 14 breccia 14318: $^{129}$I and $^{244}$Pu regolith chronology.’ *Journal of Geophysical Research*, 90, pp. C517–C539.

Swindle, T. D. and Jones, J. H. (1997) ‘The xenon isotopic composition of the primordial Martian atmosphere: Contributions from solar and fission components.’ *Journal of Geophysical Research*, 102(E1), pp. 1671–1678.

Swindle, T. D., Treiman, A. H., Lindstrom, D. J., Burkland, M. K., Cohen, B. A., Grier, J. A., Li, B. and Olson, E. K. (2000) ‘Noble gases in iddingsite from the Lafayette meteorite: Evidence for liquid water on Mars in the last few hundred million years.’ *Meteoritics & Planetary Science*, 35, pp. 107–115.

Takaoka, N. (1972) ‘An interpretation of general anomalies of xenon and the isotopic composition of primitive xenon.’ *Journal of the Mass Spectrometry Society of Japan*, 20(4), pp. 287–302.

Tatsumoto, M., Premo, W. R. and Unruh, D. M. (1987) 'Origin of lead from green glass of Apollo 15426: a search for primitive lunar lead.' *Journal of Geophysical Research*, 92(B4), pp. 361–371.

Taylor, L. A., Anand, M., Neal, C., Patchen, A. and Kramer, G. (2004) 'Lunar meteorite PCA 02007: A feldspathic regolith breccia with mixed mare/highland components.' in *Lunar and Planetary Science XXXV* (abstract), Texas, USA.

Tera, F., Papanastassiou, D. A. and Wasserburg, G. J. (1974) 'Isotopic evidence for a terminal lunar cataclysm.' *Earth and Planetary Science Letters*, 22, pp. 1–21.

Thiemens, M. M., Sprung, P., Fonseca, R. O. C., Leitzke, F. P. and Münker, C. (2019) 'Early Moon formation inferred from hafnium–tungsten systematics.' *Nature Geoscience*, 12, pp. 696–700.

Touboul, M., Kleine, T., Bourdon, B., Palme, H. and Wieler, R. (2007) 'Late formation and prolonged differentiation of the Moon inferred from W isotopes in lunar metals.' *Nature*, 450, pp. 1206–1209.

Treiman, A. H. (1998) 'The history of Allan Hills 84001 revised: multiple shock events.' *Meteoritics and Planetary Science*, 33, pp. 753–764.

Truran, J. and Iben, I. (1977) 'On s-process nucleosynthesis in thermally pulsing stars.' *The Astrophysical Journal*, 216, pp. 797–810.

Tsou, P. (1990) 'Intact capture of hypervelocity projectiles.' *International Journal of Impact Engineering*, 10, pp. 615–627.

Tsou, P., Brownlee, D. E., Anderson, J. D., Bhaskaran, S., Cheuvront, A. R., Clark, B. C., Duxbury, T., Economou, T., Green, S. F., Hanner, M. S., Hörz, F., Kissel, J., McDonnell, J. A. M., Newburn, R. L., Ryan, R. E., Sandford, S. A., Sekanina, Z., Tuzzolino, A. J., Vellinga, J. M. and Zolensky, M. E. (2004) 'Stardust encounters comet 81P/Wild 2.' *Journal of Geophysical Research*, 109, E12S01.

Tsou, P., Brownlee, D. E., Sandford, S. A., Hörz, F. and Zolensky, M. E. (2003) 'Wild 2 and interstellar sample collection and Earth return.' *Journal of Geophysical Research*, 108(E10), 8113.

Turcotte, S. and Wimmer-Schweingruber, R. F. (2002) 'Possible in situ tests of the evolution of elemental and isotopic abundances in the solar convection zone.' *Journal of Geophysical Research*, 107(A12), 1442.

Vaniman, D. T. and Papike, J. J. (1977a) 'The Apollo 17 drill core - Modal petrology and glass chemistry /sections 70007, 70008, 70009.' *Proceedings of 8th Lunar Science Conference*, pp. 3161–3193.

Vaniman, D. T. and Papike, J. J. (1977b) 'Very low TI /VLT/ basalts - A new mare rock type from the Apollo 17 drill core.' *Proceedings of 8th Lunar Science Conference*, pp. 1443–1471.

Vogel, N., Heber, V. S., Baur, H., Burnett, D. S. and Wieler, R. (2011) 'Argon, krypton, and xenon in the bulk solar wind as collected by the Genesis mission.' *Geochimica et Cosmochimica Acta*, 75, pp. 3057–3071.

Wacker, J. (1989) ‘Laboratory simulation of meteoritic noble gases. III. Sorption of neon, argon, krypton, and xenon on carbon: Elemental fractionation.’ *Geochimica et Cosmochimica Acta*, 53, pp. 1421–1433.

Walsh, K. J., Morbidelli, A., Raymond, S. N., O’Brien, D. P. and Mandell, A. M. (2011) ‘A low mass for Mars from Jupiter’s early gas-driven migration.’ *Nature*, 475, pp. 206–209.

Warner, R. D., Taylor, G. J. and Keil, K. (1979) ‘Composition of glasses in Apollo 17 samples and their relation to known lunar rock types.’ *Proceedings of 10th Lunar and Planetary Science Conference*, pp. 1437–1456.

Weidenschilling, S. (1997) ‘The origin of comets in the solar nebula: A unified model.’ *Icarus*, 127, pp. 290–306.

Weiler, R., Baur, H. and Signer, P. (1986) ‘Noble gases from solar energetic particles revealed by closed system stepwise etching of lunar soil minerals.’ *Geochimica et Cosmochimica Acta*, 50, pp. 1997–2017.

Weissman, P. (1986) ‘Are cometary nuclei primordial rubble piles?’ *Nature*, 320, pp. 242–244.

Wieler, R. (2002) ‘Noble Gases in the Solar System.’ *Reviews in Mineralogy and Geochemistry*, 47, pp. 21–70.

Wieler, R., Anders, E., Baur, H., Lewis, R. S. and Signer, P. (1991) ‘Noble-Gases in “phase-Q”: Closed-system etching of an Allende residue.’ *Geochimica et Cosmochimica Acta*, 55, pp. 1709–1722.

Wieler, R., Anders, E., Baur, H., Lewis, R. S. and Signer, P. (1992) ‘Characterisation of Q-gases and other noble gas components in the Murchison meteorite.’ *Geochimica et Cosmochimica Acta*, 56, pp. 2907–2921.

Wieler, R. and Baur, H. (1994) ‘Krypton and xenon from the solar wind and solar energetic particles in two lunar ilmenites of different antiquity.’ *Meteoritics*, 29, pp. 570–580.

Wieler, R. and Franchi, I. A. (2006) ‘Trapping and modification processes of noble gases and nitrogen in meteorites and their parent bodies.’ *Meteorites and the Early Solar System II*, pp. 499–521.

Wieler, R., Grimberg, A. and Heber, V. S. (2007) ‘Consequences of the non-existence of the “SEP” component for noble gas geo-and cosmochemistry.’ *Chemical Geology*, 244, pp. 382–390.

Wieler, R., Kehm, K., Meshik, A. P. and Hohenberg, C. M. (1996) ‘Secular changes in the xenon and krypton abundances in the solar wind recorded in single lunar grains.’ *Nature*, 384, pp. 46–49.

Wiley, W. C. and McLaren, I. H. (1955) ‘Time-of-flight mass spectrometer with improved resolution.’ *Review of Scientific Instruments*, 26, pp. 1150–1157.

Will, P., Maden, C. and Busemann, H. (2016) 'Noble gases in recently found hot and cold desert lunar meteorites.' in *79th Annual Meeting of the Meteoritical Society*, Berlin, Germany.

Will, P., Maden, C. and Busemann, H. (2017) 'Primordial noble gases in "phase Q" from the CV3 chondrite Vigarano studied by closed-system step etching (CSSE).' in *80th Annual Meeting of The Meteoritical Society*, Santa Fe, USA.

Williams, J. P., Paige, D. A., Greenhagen, B. T. and Sefton-Nash, E. (2017) 'The global surface temperatures of the moon as measured by the diviner lunar radiometer experiment.' *Icarus*, 283, pp. 300–325.

Wiza, J. L. (1979) 'Microchannel plate detectors.' *Nuclear Instruments and Methods*, 162, pp. 587–601.

Wogelius, R. A. and Walther, J. V. (1992) 'Olivine dissolution kinetics at near-surface conditions.' *Chemical Geology*, 97, pp. 101–112.

Wong, M. H., Atreya, S. K., Mahaffy, P. N., Franz, H. B., Malespin, C., Trainer, M. G., Stern, J. C., Conrad, P. G., Manning, H. L. K., Pepin, R. O., Becker, R. H., McKay, C. P., Owen, T. C., Navarro-González, R., Jones, J. H., Jakosky, B. M. and Steele, A. (2013) 'Isotopes of nitrogen on Mars: Atmospheric measurements by Curiosity's mass spectrometer.' *Geophysical Research Letters*, 40(23), pp. 6033–6037.

Wooden, D. H. (2008) 'Cometary refractory grains: Interstellar and nebular sources' in Balsiger, H., Altwegg, K., Huebner, W., Owen, T., and Schulz, R. (eds) *Origin and Early Evolution of Comet Nuclei: Workshop honouring Johannes Geiss on the occasion of his 80th birthday*, Springer New York, pp. 75–108.

Young, E. D., Galy, A. and Nagahara, H. (2002) 'Kinetic and equilibrium mass-dependent isotope fractionation laws in nature and their geochemical and cosmochemical significance.' *Geochimica et Cosmochimica Acta*, 66(6), pp. 1095–1104.

Zellner, N. E. B. (2019) 'Lunar impact glasses: Probing the Moon's surface and constraining its impact history.' *Journal of Geophysical Research*, 124(11), pp. 2686–2702.

Zellner, N. E. B. and Delano, J. W. (2015) '$^{40}Ar/^{39}Ar$ ages of lunar impact glasses: Relationships among Ar diffusivity, chemical composition, shape, and size.' *Geochimica et Cosmochimica Acta*, 161, pp. 203–218.

Zellner, N. E. B., Delano, J. W., Swindle, T. D., Barra, F., Olsen, E. and Whittet, D. C. B. (2009) 'Apollo 17 regolith, 71501,262: A record of impact events and mare volcanism in lunar glasses.' *Meteoritics and Planetary Science*, 44(6), pp. 839–851.

Zellner, N. E. B., Norman, M. D. and Jourdan, F. (2018) 'Volcanic events at the Apollo 15 landing site: Eruption ages from old to young.' in *49$^{th}$ Lunar and Planetary Sciences Conference* (abstract), Texas, USA.

Zellner, N. E. B., Spudis, P. D., Delano, J. W. and Whittet, D. C. B. (2002) 'Impact glasses from the Apollo 14 landing site and implications for regional geology.' *Journal of Geophysical Research*, 107(E11), pp. 12-1-12–13.

Ziegler, J. F., Ziegler, M. D. and Biersack, J. P. (2010) 'SRIM - The stopping and range of ions in matter (2010).' *Nuclear Instruments and Methods in Physics Research, Section B: Beam Interactions with Materials and Atoms*, 268(11–12), pp. 1818–1823.

Zolensky, M. E., Zega, T. J., Yano, H., Wirick, S., Westphal, A. J., Weisberg, M. K., Weber, I., Warren, J. L., Velbel, M. A, Tsuchiyama, A., Tsou, P., Toppani, A., Tomioka, N., Tomeoka, K., Teslich, N., Taheri, M., Susini, J., Stroud, R., Stephan, T., Stadermann, F. J., Snead, C. J., Simon, S. B., Simionovici, A., See, T. H., Robert, F., Rietmeijer, F. J. M., Rao, W., Perronnet, M. C., Papanastassiou, D. A., Okudaira, K., Ohsumi, K., Ohnishi, I., Nakamura-Messenger, K., Nakamura, T., Mostefaoui, S., Mikouchi, T., Meibom, A., Matrajt, G., Marcus, M. A., Leroux, H., Lemelle, L., Le, L., Lanzirotti, A., Langenhorst, F., Krot, A. N., Keller, L. P., Kearsley, A. T., Joswiak, D., Jacob, D., Ishii, H., Harvey, R., Hagiya, K., Grossman, L., Grossman, J. N., Graham, G. A., Gounelle, M., Gillet, P., Genge, M. J., Flynn, G., Ferroir, T., Fallon, S., Ebel, D. S., Dai, Z. R., Cordier, P., Clark, B., Chi, M., Butterworth, A. L., Brownlee, D. E., Bridges, J. C., Brennan, S., Brearley, A., Bradley, J. P., Bleuet, P., Bland, P. A. and Bastien, R. (2006) 'Mineralogy and Petrology of Comet 81P/Wild 2 Nucleus Samples.' *Science*, 314, pp. 1735–1739.

Zolensky, M., Nakamura-Messenger, K., Rietmeijer, F., Leroux, H., Mikouchi, T., Ohsumi, K., Simon, S., Grossman, L., Stephan, T., Weisberg, M., Velbel, M., Zega, T., Stroud, R., Tomeoka, K., Ohnishi, I., Tomioka, N., Nakamura, T., Matrajt, G., Joswiak, D., Brownlee, D., Langenhorst, F., Krot, A., Kearsley, a, Ishii, H., Graham, G., Dai, Z. R., Chi, M., Bradley, J., Hagiya, K., Gounelle, M., Keller, L. and Bridges, J. (2008) 'Comparing Wild 2 particles to chondrites and IDPs.' *Meteoritics and Planetary Science*, 43(1–2) pp. 261–272.

## 8. Appendix

| | |
|---|---|
| 67P | Comet 67P/Churyumov-Gerasimenko, preliminary target of Rosetta mission |
| 81P | Comet 81P/Wild 2, preliminary target of Stardust mission |
| amu | Atomic mass unit |
| AU | Astronomical unit |
| BSE | Backscattered Electron |
| CAI | Calcium-aluminium-rich inclusion |
| CaO | Calcium oxide, used in neutralisation of acid during etching |
| CF | ConFlat stainless-steel blade and copper gasket seal used in vacuum systems |
| $cm^3$ STP | Cubic centimetres at Standard Temperature (273.15 K) and Pressure (100 kPa) |
| CSSE | Closed-system stepped etching |
| Ef | Equilibrium fractionation model of isotopic fractionation |
| EPMA | Electron Probe MicroAnalysis, instrument for major element measurement |
| GCR | Galactic Cosmic Rays |
| Gf | Gravitational fractionation model of isotopic fractionation |
| Gyr | Billion years |
| HCl | Hydrochloric acid, used in isolation of phase "Q" |
| HF | Hydrofluoric acid, used in isolation of phase "Q" and etching experiments |
| IDP | Interplanetary Dust Particle |
| Kf | Kinetic fractionation model of isotopic fractionation |
| MCP | MicroChannel Plate |
| Myr | Million years |
| PCA | Pecora Hills Escarpment, region in Antarctica where meteorites are collected |
| PDF | Probability Density Function |
| PPB | Parts per billion |
| PPM | Parts per million |
| Q | Quintessence, phase or noble gas composition ubiquitous in carbonaceous chondrites |
| QMS | Quadrupole Mass Spectrometer |
| REE | Rare Earth Element(s) |
| RELAX | Refrigerator Enhanced Laser Analyser for Xenon |
| RIMSKI | Resonance Ionisation Mass Spectrometer for Krypton Isotopes |
| SEP | Solar Energetic Particles, defunct term for deeply implanted solar wind |
| SRIM | Stopping and Range of Ions in Matter, program which simulates title |
| SW | Solar wind |
| UHV | Ultra High Vacuum, vacuum lower than $10^{-8}$ mbar |
| VLT | Very Low Titanium, compositional group of volcanic glasses of Apollo 17 |
| YAG | Yttrium Aluminium Garnet, synthetic crystal used in laser systems |

***A.1*** *Various acronyms used throughout thesis and their definition.*

Cool acid and sample fingers to desired step temperatures (Note - most step variations are done by changing etching duration)

1. If conducting a short step, prepare two dewars of liquid nitrogen (~ 20%) and ethanol (~ 80%) at −70 ℃ ± 10 ℃ in preparation for acid finger and U-tube cooling

2. Open the G2B valve gently (to avoid sucking of sample into valve), exposing the sample to acid vapour for the desired step duration (ensure valve is actually open, as there is relatively little feedback)

3. Cool the acid finger to −70 ℃ ± 10 ℃ for 2 hours after step duration to reduce partial pressure of HF in system (this requires constant attention)

4. After 1.5 hours since the start of acid condensation, cool the sample finger to −15 ℃ with a Peltier device for the remaining 30 minutes

5. Prepare a dewar of LN and ethanol at −70 ℃ ± 10 ℃ and apply to the U-tube

6. Close the G2B valve after 2 hours of acid condensation, 30 minutes after the sample finger cooling

7. Expose sample gas to the CaO getter via the pre-cooled U-tube by opening G1B + 5 + 6 for 2 minutes

8. Expand the sample gas to the SAES getter by opening valve 7 for 3 minutes

9. Close G1B and expose the sample gas to RELAX and its procedures, isolate the CSSE apparatus and getter after mass spectrometer isolation (by closing of valve 8)

10. Cool the detour cold finger to −70 ℃ ± 10 ℃, thaw the U-bend and pump out the system through the detour line (opening valves 4, 3, 2, and then valve 1 after 2 minutes) – only if the CSSE apparatus is isolated.

***2A.1*** *Example of etching procedure developed and enacted during this work.*

***3A.1*** *Synthetic xenon isotope compositions for Automaton validation with Samaritan.*

| Input data (%) | | | Modelled number of atoms for each xenon isotope | | | | | | | | | | | | | | | | | |
|---|---|---|---|---|---|---|---|---|---|---|---|---|---|---|---|---|---|---|---|---|
| Q | SW | Ba | 124 | σ | 126 | σ | 128 | σ | 129 | σ | 130 | σ | 131 | σ | 132 | σ | 134 | σ | 136 | σ |
| 5 | 95 | 0 | 4797 | 69 | 4164 | 65 | 84100 | 290 | 1038945 | 1019 | 164750 | 406 | 825910 | 909 | 1000000 | 1000 | 369640 | 608 | 301105 | 549 |
| 15 | 85 | 0 | 4771 | 69 | 4153 | 64 | 83900 | 290 | 1036635 | 1018 | 164450 | 406 | 825130 | 908 | 1000000 | 1000 | 370520 | 609 | 302715 | 550 |
| 25 | 75 | 0 | 4745 | 69 | 4142 | 64 | 83700 | 289 | 1034325 | 1017 | 164150 | 405 | 824350 | 908 | 1000000 | 1000 | 371400 | 609 | 304325 | 552 |
| 35 | 65 | 0 | 4719 | 69 | 4130 | 64 | 83500 | 289 | 1032015 | 1016 | 163850 | 405 | 823570 | 908 | 1000000 | 1000 | 372280 | 610 | 305935 | 553 |
| 45 | 55 | 0 | 4693 | 69 | 4119 | 64 | 83300 | 289 | 1029705 | 1015 | 163550 | 404 | 822790 | 907 | 1000000 | 1000 | 373160 | 611 | 307545 | 555 |
| 55 | 45 | 0 | 4667 | 68 | 4108 | 64 | 83100 | 288 | 1027395 | 1014 | 163250 | 404 | 822010 | 907 | 1000000 | 1000 | 374040 | 612 | 309155 | 556 |
| 65 | 35 | 0 | 4641 | 68 | 4097 | 64 | 82900 | 288 | 1025085 | 1012 | 162950 | 404 | 821230 | 906 | 1000000 | 1000 | 374920 | 612 | 310765 | 557 |
| 75 | 25 | 0 | 4615 | 68 | 4085 | 64 | 82700 | 288 | 1022775 | 1011 | 162650 | 403 | 820450 | 906 | 1000000 | 1000 | 375800 | 613 | 312375 | 559 |
| 85 | 15 | 0 | 4589 | 68 | 4074 | 64 | 82500 | 287 | 1020465 | 1010 | 162350 | 403 | 819670 | 905 | 1000000 | 1000 | 376680 | 614 | 313985 | 560 |
| 95 | 5 | 0 | 4563 | 68 | 4063 | 64 | 82300 | 287 | 1018155 | 1009 | 162050 | 403 | 818890 | 905 | 1000000 | 1000 | 377560 | 614 | 315595 | 562 |
| 5 | 85 | 10 | 56044 | 237 | 98714 | 314 | 229621 | 479 | 1086882 | 1043 | 266779 | 517 | 1157335 | 1076 | 1000000 | 1000 | 339273 | 582 | 271075 | 521 |
| 15 | 75 | 10 | 56018 | 237 | 98703 | 314 | 229421 | 479 | 1084572 | 1041 | 266479 | 516 | 1156555 | 1075 | 1000000 | 1000 | 340153 | 583 | 272685 | 522 |
| 25 | 65 | 10 | 55992 | 237 | 98692 | 314 | 229221 | 479 | 1082262 | 1040 | 266179 | 516 | 1155775 | 1075 | 1000000 | 1000 | 341033 | 584 | 274295 | 524 |
| 35 | 55 | 10 | 55966 | 237 | 98680 | 314 | 229021 | 479 | 1079952 | 1039 | 265879 | 516 | 1154995 | 1075 | 1000000 | 1000 | 341913 | 585 | 275905 | 525 |
| 45 | 45 | 10 | 55940 | 237 | 98669 | 314 | 228821 | 478 | 1077642 | 1038 | 265579 | 515 | 1154215 | 1074 | 1000000 | 1000 | 342793 | 585 | 277515 | 527 |
| 55 | 35 | 10 | 55914 | 236 | 98658 | 314 | 228621 | 478 | 1075332 | 1037 | 265279 | 515 | 1153435 | 1074 | 1000000 | 1000 | 343673 | 586 | 279125 | 528 |
| 65 | 25 | 10 | 55888 | 236 | 98646 | 314 | 228421 | 478 | 1073022 | 1036 | 264979 | 515 | 1152655 | 1074 | 1000000 | 1000 | 344553 | 587 | 280735 | 530 |
| 75 | 15 | 10 | 55862 | 236 | 98635 | 314 | 228221 | 478 | 1070712 | 1035 | 264679 | 514 | 1151875 | 1073 | 1000000 | 1000 | 345433 | 588 | 282345 | 531 |
| 85 | 5 | 10 | 55836 | 236 | 98624 | 314 | 228021 | 478 | 1068402 | 1034 | 264379 | 514 | 1151095 | 1073 | 1000000 | 1000 | 346313 | 588 | 283955 | 533 |

*Synthesised mixtures of xenon isotopic compositions composed of linear combinations of end members in input data columns. Xenon isotope data are from isotope ratios normalised to $^{132}Xe$, multiplied by 1,000,000. Errors are defined as square root of each isotopic atom count.*

***3A.2*** *Synthetic xenon isotope compositions with various uncertainties for modelling with Automaton.*

| Synthesised mixtures | | Xenon isotopic ratios normalised to $^{132}Xe \equiv 1$ for synthesised mixtures of variable uncertainty | | | | | | | | | | | | | | | |
|---|---|---|---|---|---|---|---|---|---|---|---|---|---|---|---|---|---|
| # | Atoms of $^{132}Xe$ | 124 | σ | 126 | σ | 128 | σ | 129 | σ | 130 | σ | 131 | σ | 134 | σ | 136 | σ |
| Mixture 1: 40 % Q-Xe, 60 % SW-Xe | $10^4$ | 0.005 | 0.00068762 | 0.004 | 0.00064357 | 0.083 | 0.00300592 | 1.031 | 0.01446904 | 0.164 | 0.00436460 | 0.823 | 0.01225074 | 0.373 | 0.00715290 | 0.307 | 0.00633111 |
| | $10^5$ | 0.005 | 0.00021744 | 0.004 | 0.00020351 | 0.083 | 0.00095056 | 1.031 | 0.00457551 | 0.164 | 0.00138021 | 0.823 | 0.00387402 | 0.373 | 0.00226195 | 0.307 | 0.00200207 |
| | $10^6$ | 0.005 | 0.00006876 | 0.004 | 0.00006436 | 0.083 | 0.00030059 | 1.031 | 0.00144690 | 0.164 | 0.00043646 | 0.823 | 0.00122507 | 0.373 | 0.00071529 | 0.307 | 0.00063311 |
| | $10^7$ | 0.005 | 0.00002174 | 0.004 | 0.00002035 | 0.083 | 0.00009506 | 1.031 | 0.00045755 | 0.164 | 0.00013802 | 0.823 | 0.00038740 | 0.373 | 0.00022619 | 0.307 | 0.00020021 |
| | $10^8$ | 0.005 | 0.00000688 | 0.004 | 0.00000644 | 0.083 | 0.00003006 | 1.031 | 0.00014469 | 0.164 | 0.00004365 | 0.823 | 0.00012251 | 0.373 | 0.00007153 | 0.307 | 0.00006331 |
| | $10^9$ | 0.005 | 0.00000217 | 0.004 | 0.00000204 | 0.083 | 0.00000951 | 1.031 | 0.00004576 | 0.164 | 0.00001380 | 0.823 | 0.00003874 | 0.373 | 0.00002262 | 0.307 | 0.00002002 |
| | $10^{10}$ | 0.005 | 0.00000069 | 0.004 | 0.00000064 | 0.083 | 0.00000301 | 1.031 | 0.00001447 | 0.164 | 0.00000436 | 0.823 | 0.00001225 | 0.373 | 0.00000715 | 0.307 | 0.00000633 |
| | $10^{11}$ | 0.005 | 0.00000022 | 0.004 | 0.00000020 | 0.083 | 0.00000095 | 1.031 | 0.00000458 | 0.164 | 0.00000138 | 0.823 | 0.00000387 | 0.373 | 0.00000226 | 0.307 | 0.00000200 |
| | $10^{12}$ | 0.005 | 0.00000007 | 0.004 | 0.00000006 | 0.083 | 0.00000030 | 1.031 | 0.00000145 | 0.164 | 0.00000044 | 0.823 | 0.00000123 | 0.373 | 0.00000072 | 0.307 | 0.00000063 |
| | $10^{13}$ | 0.005 | 0.00000002 | 0.004 | 0.00000002 | 0.083 | 0.00000010 | 1.031 | 0.00000046 | 0.164 | 0.00000014 | 0.823 | 0.00000039 | 0.373 | 0.00000023 | 0.307 | 0.00000020 |
| | $10^{14}$ | 0.005 | 0.00000001 | 0.004 | 0.00000001 | 0.083 | 0.00000003 | 1.031 | 0.00000014 | 0.164 | 0.00000004 | 0.823 | 0.00000012 | 0.373 | 0.00000007 | 0.307 | 0.00000006 |
| Mixture 2: 80 % Q-Xe, 20 % SW-Xe | $10^4$ | 0.005 | 0.00067994 | 0.004 | 0.00064002 | 0.083 | 0.00299036 | 1.022 | 0.01437125 | 0.163 | 0.00434633 | 0.820 | 0.01221703 | 0.376 | 0.00719581 | 0.313 | 0.00641297 |
| | $10^5$ | 0.005 | 0.00021502 | 0.004 | 0.00020239 | 0.083 | 0.00094564 | 1.022 | 0.00454459 | 0.163 | 0.00137443 | 0.820 | 0.00386336 | 0.376 | 0.00227551 | 0.313 | 0.00202796 |
| | $10^6$ | 0.005 | 0.00006799 | 0.004 | 0.00006400 | 0.083 | 0.00029904 | 1.022 | 0.00143712 | 0.163 | 0.00043463 | 0.820 | 0.00122170 | 0.376 | 0.00071958 | 0.313 | 0.00064130 |
| | $10^7$ | 0.005 | 0.00002150 | 0.004 | 0.00002024 | 0.083 | 0.00009456 | 1.022 | 0.00045446 | 0.163 | 0.00013744 | 0.820 | 0.00038634 | 0.376 | 0.00022755 | 0.313 | 0.00020280 |
| | $10^8$ | 0.005 | 0.00000680 | 0.004 | 0.00000640 | 0.083 | 0.00002990 | 1.022 | 0.00014371 | 0.163 | 0.00004346 | 0.820 | 0.00012217 | 0.376 | 0.00007196 | 0.313 | 0.00006413 |
| | $10^9$ | 0.005 | 0.00000215 | 0.004 | 0.00000202 | 0.083 | 0.00000946 | 1.022 | 0.00004545 | 0.163 | 0.00001374 | 0.820 | 0.00003863 | 0.376 | 0.00002276 | 0.313 | 0.00002028 |
| | $10^{10}$ | 0.005 | 0.00000068 | 0.004 | 0.00000064 | 0.083 | 0.00000299 | 1.022 | 0.00001437 | 0.163 | 0.00000435 | 0.820 | 0.00001222 | 0.376 | 0.00000720 | 0.313 | 0.00000641 |
| | $10^{11}$ | 0.005 | 0.00000022 | 0.004 | 0.00000020 | 0.083 | 0.00000095 | 1.022 | 0.00000454 | 0.163 | 0.00000137 | 0.820 | 0.00000386 | 0.376 | 0.00000228 | 0.313 | 0.00000203 |
| | $10^{12}$ | 0.005 | 0.00000007 | 0.004 | 0.00000006 | 0.083 | 0.00000030 | 1.022 | 0.00000144 | 0.163 | 0.00000043 | 0.820 | 0.00000122 | 0.376 | 0.00000072 | 0.313 | 0.00000064 |
| | $10^{13}$ | 0.005 | 0.00000002 | 0.004 | 0.00000002 | 0.083 | 0.00000009 | 1.022 | 0.00000045 | 0.163 | 0.00000014 | 0.820 | 0.00000039 | 0.376 | 0.00000023 | 0.313 | 0.00000020 |
| | $10^{14}$ | 0.005 | 0.00000001 | 0.004 | 0.00000001 | 0.083 | 0.00000003 | 1.022 | 0.00000014 | 0.163 | 0.00000004 | 0.820 | 0.00000012 | 0.376 | 0.00000007 | 0.313 | 0.00000006 |
| Mixture 3: 65 % Q-Xe, 25 % SW-Xe, 10 % Ba-X | $10^4$ | 0.056 | 0.00242924 | 0.099 | 0.00329207 | 0.228 | 0.00529714 | 1.073 | 0.01491441 | 0.265 | 0.00578958 | 0.739 | 0.01133195 | 0.345 | 0.00680639 | 0.281 | 0.00599622 |
| | $10^5$ | 0.056 | 0.00076819 | 0.099 | 0.00104104 | 0.228 | 0.00167510 | 1.073 | 0.00471635 | 0.265 | 0.00183083 | 0.739 | 0.00358348 | 0.345 | 0.00215237 | 0.281 | 0.00189617 |
| | $10^6$ | 0.056 | 0.00024292 | 0.099 | 0.00032921 | 0.228 | 0.00052971 | 1.073 | 0.00149144 | 0.265 | 0.00057896 | 0.739 | 0.00113319 | 0.345 | 0.00068064 | 0.281 | 0.00059962 |
| | $10^7$ | 0.056 | 0.00007682 | 0.099 | 0.00010410 | 0.228 | 0.00016751 | 1.073 | 0.00047164 | 0.265 | 0.00018308 | 0.739 | 0.00035835 | 0.345 | 0.00021524 | 0.281 | 0.00018962 |
| | $10^8$ | 0.056 | 0.00002429 | 0.099 | 0.00003292 | 0.228 | 0.00005297 | 1.073 | 0.00014914 | 0.265 | 0.00005790 | 0.739 | 0.00011332 | 0.345 | 0.00006806 | 0.281 | 0.00005996 |
| | $10^9$ | 0.056 | 0.00000768 | 0.099 | 0.00001041 | 0.228 | 0.00001675 | 1.073 | 0.00004716 | 0.265 | 0.00001831 | 0.739 | 0.00003583 | 0.345 | 0.00002152 | 0.281 | 0.00001896 |
| | $10^{10}$ | 0.056 | 0.00000243 | 0.099 | 0.00000329 | 0.228 | 0.00000530 | 1.073 | 0.00001491 | 0.265 | 0.00000579 | 0.739 | 0.00001133 | 0.345 | 0.00000681 | 0.281 | 0.00000600 |
| | $10^{11}$ | 0.056 | 0.00000077 | 0.099 | 0.00000104 | 0.228 | 0.00000168 | 1.073 | 0.00000472 | 0.265 | 0.00000183 | 0.739 | 0.00000358 | 0.345 | 0.00000215 | 0.281 | 0.00000190 |
| | $10^{12}$ | 0.056 | 0.00000024 | 0.099 | 0.00000033 | 0.228 | 0.00000053 | 1.073 | 0.00000149 | 0.265 | 0.00000058 | 0.739 | 0.00000113 | 0.345 | 0.00000068 | 0.281 | 0.00000060 |
| | $10^{13}$ | 0.056 | 0.00000008 | 0.099 | 0.00000010 | 0.228 | 0.00000017 | 1.073 | 0.00000047 | 0.265 | 0.00000018 | 0.739 | 0.00000036 | 0.345 | 0.00000022 | 0.281 | 0.00000019 |
| | $10^{14}$ | 0.056 | 0.00000002 | 0.099 | 0.00000003 | 0.228 | 0.00000005 | 1.073 | 0.00000015 | 0.265 | 0.00000006 | 0.739 | 0.00000011 | 0.345 | 0.00000007 | 0.281 | 0.00000006 |

*Synthesised data for three end member mixtures (end member compositions listed in Table 3.1), with increasingly large numbers of $^{132}Xe$ atoms, before expansion and modelling with Automaton. Errors of isotopes in each synthesised mixture are equal to the square root of the modelled number of atoms.*

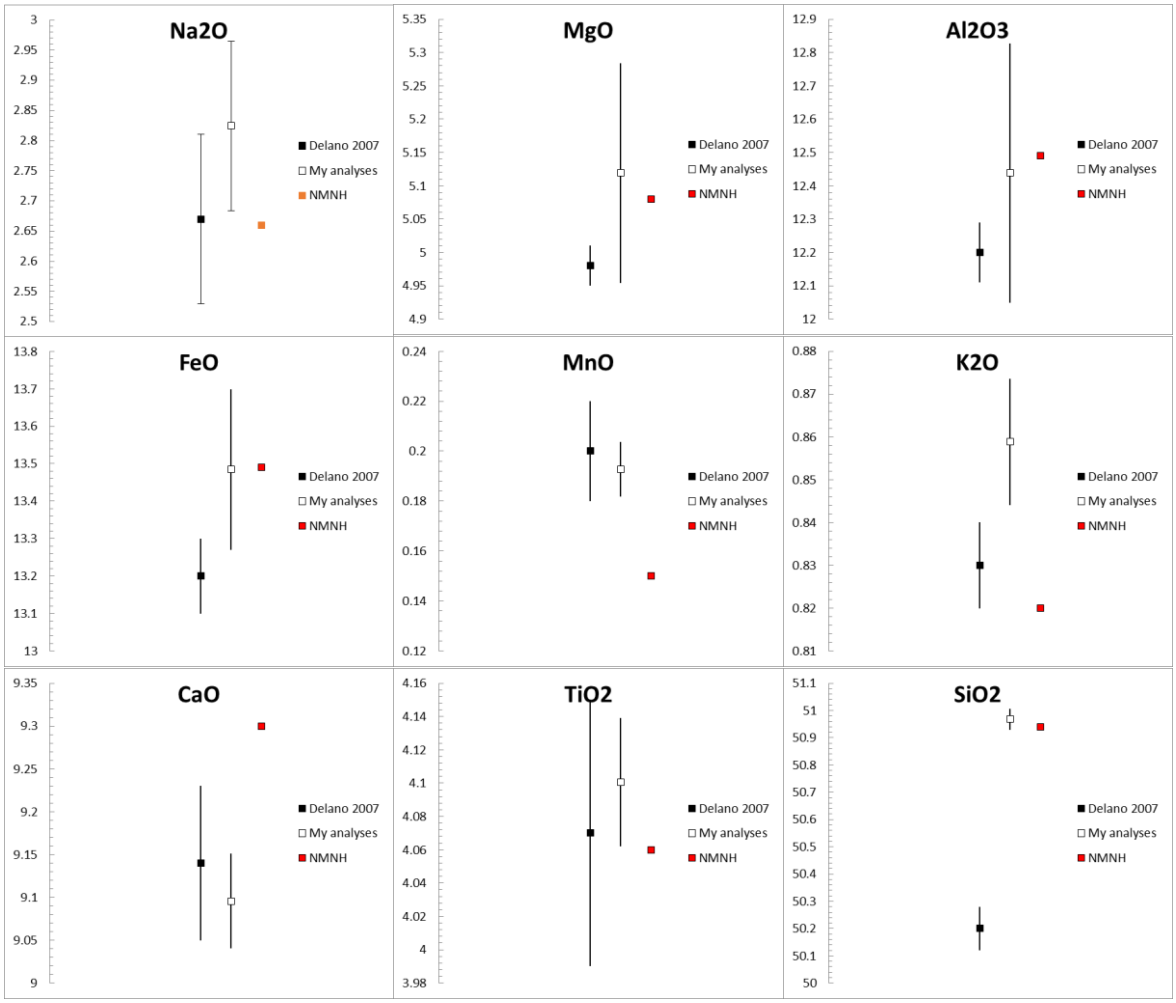


***4A.1*** *A99 EPMA standard oxide variation compared to Delano et al. (2007) and the NHMH samples (Jarosewich 2002).*

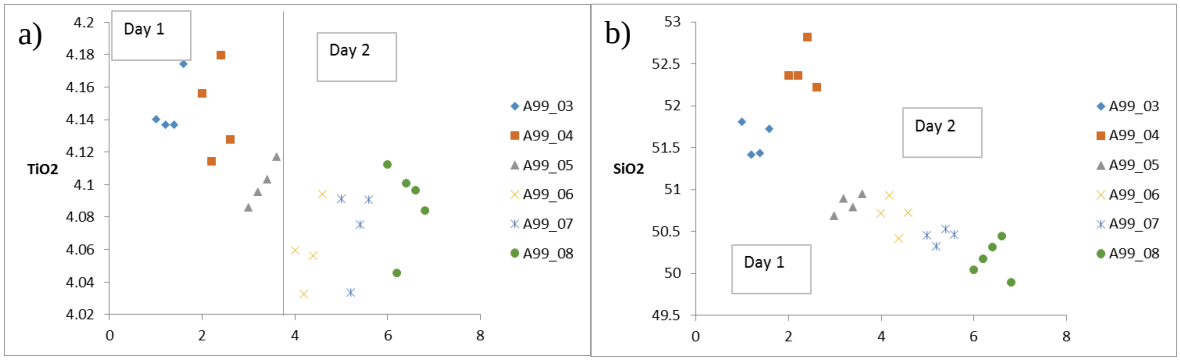


***4A.2*** *A99 EPMA Standard variability in measured values for $TiO_2$ (a) and $SiO_2$ (b) during sample analyses (plotted in sequence on the X axis).*

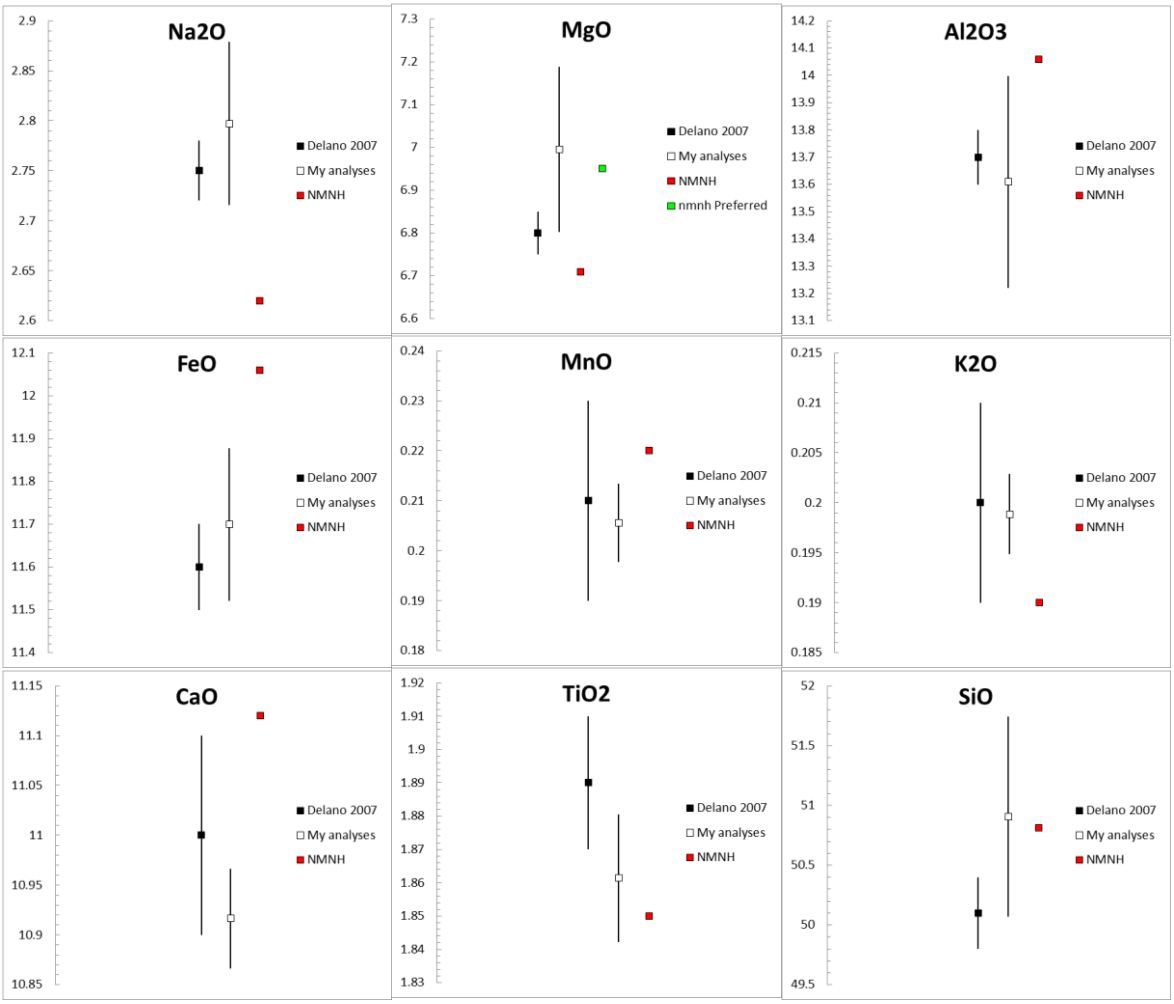


***4A.3*** *VG2 EPMA standard oxide variation compared to Delano et al. (2007) and the NHMH samples (Jarosewich 2002).*

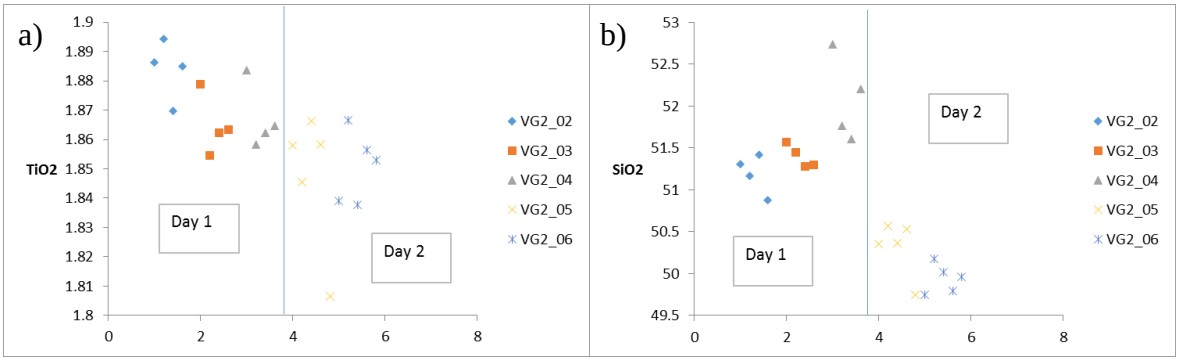


***4A.4*** *VG2 EPMA Standard variability in measured values for $TiO_2$ (a) and $SiO_2$ (b) during sample analyses (plotted in sequence on the X axis).*

**4A.5** *Table containing xenon atoms measured in individual heating steps of 15426 glasses.*

| 15426,189 Subsample | Stepped heating conditions | 124 | | 126 | | 128 | | 129 | | 130 | | 131 | | 132 | | 134 | | 136 | |
|---|---|---|---|---|---|---|---|---|---|---|---|---|---|---|---|---|---|---|---|
| | 10% 20 µs | - | - | - | - | - | - | - | - | - | - | - | - | 504 | 240 | - | - | - | - |
| | 10% 23 µs | 622 | 108 | 855 | 110 | 2168 | 178 | 3541 | 295 | 1698 | 151 | 9337 | 351 | 3182 | 294 | 1024 | 174 | 886 | 156 |
| | 10% 29 µs | 1060 | 116 | 1311 | 127 | 2291 | 165 | 3918 | 274 | 1975 | 144 | 11722 | 337 | 2876 | 265 | 1224 | 162 | 744 | 139 |
| A | 10% 39 µs | 8369 | 360 | 13579 | 649 | 21989 | 431 | 28842 | 511 | 15601 | 348 | 104285 | 951 | 20613 | 452 | 5607 | 247 | 3567 | 209 |
| | 10% 60 µs | 244 | 110 | 408 | 100 | 1098 | 156 | 1202 | 272 | 805 | 134 | 3894 | 284 | 672 | 260 | 771 | 182 | 190 | 146 |
| | 10% 99 µs | - | - | - | - | 134 | 112 | - | - | 210 | 106 | - | - | - | - | 533 | 162 | - | - |
| | 20% CW | - | - | 191 | 82 | 451 | 141 | - | - | 232 | 105 | - | - | - | - | 518 | 163 | 249 | 142 |
| | 30% CW | - | - | - | - | 391 | 115 | - | - | - | - | - | - | - | - | - | - | - | - |
| | 10% 20 µs | - | - | - | - | 936 | 149 | 3889 | 309 | 963 | 134 | 3231 | 275 | 3463 | 308 | 1564 | 193 | 1192 | 171 |
| B | 10% 83 µs | 12853.59 | 718 | 13083.44 | 810 | 150381 | 1781 | 1844747 | 6114 | 300543 | 2475 | 1490691 | 5364 | 1753837 | 5413 | 658415 | 3573 | 525821 | 3180 |
| | 10% 83 µs | - | - | 68 | 77 | 176 | 117 | 2148 | 265 | 288 | 107 | 1804 | 239 | 2481 | 274 | 621 | 157 | 677 | 152 |
| | 30% CW | - | - | 65 | 75 | 605 | 111 | 1063 | 229 | 278 | 96 | 885 | 195 | 840 | 225 | 344 | 138 | 559 | 126 |
| | 10% 20 µs | - | - | - | - | - | - | 1460 | 279 | 193 | 109 | 1030 | 242 | 1667 | 286 | 248 | 171 | 603 | 166 |
| | 10% 23 µs | 87 | 69 | - | - | - | - | 1154 | 271 | 466 | 116 | 495 | 224 | 1060 | 278 | 517 | 176 | 447 | 155 |
| | 10% 29 µs | - | - | 74 | 50 | - | - | 2661 | 296 | 536 | 121 | 2704 | 272 | 1848 | 286 | 1060 | 183 | 711 | 161 |
| D | 10% 39 µs | 216 | 101 | - | - | 209 | 149 | 2465 | 330 | 921 | 154 | 3765 | 329 | 2055 | 325 | 846 | 209 | 658 | 187 |
| | 10% 60 µs | 525 | 148 | 258 | 87 | 710 | 187 | 4302 | 394 | 874 | 171 | 5409 | 398 | 3918 | 394 | 1159 | 231 | 1759 | 241 |
| | 10% 99 µs | 169 | 150 | 310 | 141 | 343 | 180 | 2959 | 378 | 582 | 182 | 2749 | 344 | 2852 | 384 | 1779 | 276 | 1372 | 245 |
| | 30% CW | - | - | 222 | 113 | 297 | 158 | 2631 | 339 | - | - | 3351 | 325 | 3382 | 363 | 1567 | 246 | 1557 | 225 |
| | 10% 20 µs | - | - | - | - | 358 | 128 | - | - | - | - | - | - | - | - | - | - | - | - |
| F | 10% 83 µs | 586 | 114 | 954 | 124 | 1255 | 162 | 2574 | 289 | 1240 | 144 | 7472 | 343 | 1610 | 278 | 414 | 164 | 487 | 150 |
| | 30% CW | - | - | - | - | 270 | 102 | - | - | - | - | - | - | - | - | - | - | - | - |
| | 10% 20 µs | - | - | - | - | - | - | 674 | 229 | - | - | - | - | - | - | - | - | - | - |
| | 10% 23 µs | - | - | 118 | 52 | 373 | 130 | 1121 | 272 | 310 | 112 | 1216 | 241 | 795 | 269 | 464 | 166 | 413 | 148 |
| | 10% 29 µs | 261 | 75 | 378 | 74 | 1327 | 159 | 3695 | 305 | 824 | 130 | 7368 | 340 | 3261 | 305 | 1297 | 182 | 1156 | 168 |
| H | 10% 39 µs | 779 | 109 | 1546 | 146 | 2418 | 182 | 3631 | 298 | 1729 | 149 | 13797 | 405 | 3449 | 297 | 1207 | 177 | 515 | 146 |
| | 10% 60 µs | 1820 | 153 | 3092 | 213 | 5136 | 232 | 6657 | 330 | 3766 | 197 | 27415 | 522 | 4693 | 310 | 1372 | 178 | 1086 | 155 |
| | 10% 99 µs | - | - | 64 | 67 | - | - | - | - | 248 | 87 | - | - | - | - | - | - | - | - |
| | 30% CW | - | - | 79 | 58 | - | - | - | - | - | - | 567 | 220 | 639 | 260 | - | - | 225 | 138 |
| | 10% 20 µs | - | - | - | - | - | - | - | - | - | - | - | - | - | - | - | - | - | - |
| | 10% 23 µs | 96 | 73 | - | - | 328 | 123 | 616 | 253 | 144 | 105 | 1207 | 229 | - | - | 263 | 154 | 429 | 146 |
| | 10% 29 µs | 373 | 79 | 348 | 62 | 937 | 135 | 2580 | 266 | 1162 | 121 | 6223 | 293 | 1682 | 255 | 572 | 157 | 728 | 140 |
| J | 10% 39 µs | 507 | 88 | 980 | 114 | 1724 | 164 | 1751 | 266 | 1032 | 127 | 9172 | 347 | 1440 | 265 | 476 | 158 | 233 | 132 |
| | 10% 60 µs | 912 | 107 | 1877 | 148 | 2696 | 173 | 2735 | 260 | 2161 | 142 | 14952 | 369 | 2518 | 262 | 684 | 149 | 382 | 122 |
| | 10% 99 µs | - | - | 56 | 63 | - | - | - | - | - | - | - | - | - | - | - | - | - | - |
| | 30% CW | - | - | - | - | - | - | - | - | - | - | - | - | - | - | - | - | - | - |
| | 10% 20 µs | - | - | - | - | - | - | - | - | - | - | - | - | - | - | - | - | - | - |
| | 10% 23 µs | - | - | - | - | - | - | - | - | - | - | - | - | - | - | - | - | - | - |
| | 10% 29 µs | - | - | - | - | - | - | - | - | - | - | - | - | - | - | - | - | - | - |
| L | 10% 39 µs | 118 | 61 | 59 | 47 | - | - | - | - | - | - | - | - | - | - | 372 | 149 | 251 | 130 |
| | 10% 60 µs | 255 | 69 | 790 | 92 | 1060 | 123 | 4587 | 272 | 1299 | 116 | 8915 | 295 | 3841 | 268 | 1442 | 158 | 1022 | 139 |
| | 10% 99 µs | 1109 | 117 | 1513 | 132 | 2362 | 167 | 2777 | 268 | 1733 | 140 | 13820 | 375 | 1991 | 262 | 759 | 157 | 390 | 134 |
| | 30% CW | - | - | 76 | 59 | 250 | 121 | - | - | 155 | 98 | - | - | - | - | - | - | - | - |
| | 10% 20 µs | - | - | 172 | 72 | - | - | 1205 | 257 | 229 | 96 | 712 | 216 | 995 | 255 | 368 | 153 | 362 | 138 |
| | 10% 23 µs | 154 | 60 | 89 | 64 | 1916 | 151 | 19531 | 432 | 2962 | 167 | 14772 | 380 | 17439 | 419 | 6960 | 262 | 5592 | 235 |
| Z | 10% 29 µs | 958 | 112 | 1684 | 145 | 3868 | 203 | 20049 | 459 | 4547 | 207 | 27333 | 510 | 18853 | 452 | 6724 | 272 | 5609 | 249 |
| | 10% 39 µs | 3111 | 183 | 4844 | 273 | 8090 | 252 | 14072 | 370 | 6757 | 224 | 46865 | 585 | 11159 | 349 | 3722 | 203 | 2896 | 179 |
| | 10% 60 µs | - | - | 66 | 59 | 122 | 102 | - | - | - | - | - | - | - | - | - | - | - | - |
| | 30% CW | - | - | - | - | 280 | 111 | - | - | - | - | - | - | - | - | - | - | - | - |
| | 10% 20 µs | 507 | 90 | - | - | 668 | 127 | 4145 | 298 | 992 | 125 | 2998 | 255 | 3481 | 293 | 1679 | 184 | 1280 | 169 |
| | 10% 23 µs | 1627 | 135 | 1322 | 122 | 11524 | 308 | 140635 | 1032 | 22147 | 409 | 111843 | 923 | 129297 | 980 | 47115 | 606 | 38323 | 548 |
| | 10% 29 µs | 2401 | 171 | 3019 | 210 | 19368 | 417 | 187339 | 1268 | 31099 | 513 | 162449 | 1180 | 171953 | 1198 | 63225 | 746 | 52568 | 682 |
| Multi-spherule | 10% 39 µs | 7580 | 322 | 11698 | 560 | 22944 | 414 | 74058 | 723 | 21404 | 379 | 145840 | 1005 | 64496 | 683 | 23179 | 414 | 17354 | 362 |
| | 10% 60 µs | 701 | 100 | 862 | 100 | 2101 | 163 | 6217 | 321 | 2135 | 157 | 12561 | 372 | 5932 | 320 | 2173 | 192 | 1861 | 174 |
| | 10% 99 µs | 91 | 72 | - | - | - | - | - | - | - | - | - | - | - | - | - | - | - | - |
| | 30% CW | - | - | - | - | 351 | 113 | - | - | - | - | - | - | - | - | - | - | - | - |
| RELAX Detection limit | | 0 | 23 | 0 | 18 | 761 | 41 | 3494 | 159 | 454 | 44 | 2693 | 120 | 3501 | 156 | 1271 | 73 | 1018 | 54 |

***Table 4A.5*** *Description.*

*Atoms in excess of procedural blank. Dashes refer to signals which did not exceed this criterion. "Multi-spherule" refers to collection of 8 spherules. RELAX detection limit is concentration and composition of procedural blank plus three standard errors. Heating conditions refer to laser pulse duration in μs per 10 kHz cycle and Fiber laser input power as percentage, CW refers to continuous wave, explained in Section 4.4.3.*

***Table 4A.6*** *Description.*

*Atoms in excess of blank + 3σ. Dashes refer to signals which did not exceed this criterion. "Multi-spherule" refers to collection of 7 spherules. Errors are σ instrumental counting errors in atoms. RELAX detection limit is concentration and composition of procedural plank plus three standard errors. Heating conditions refer to laser pulse duration in μs per 10 kHz cycle and Fiber laser input power as percentage, CW refers to continuous wave, explained in Section 4.4.3. *Multiple steps up to CW measured simultaneously.*

***4A.6** Table containing xenon atoms measured in individual heating steps of 74220 glasses.*

| 74220,989 Subsample | Stepped heating conditions | 124 | | 126 | | 128 | | 129 | | 130 | | 131 | | 132 | | 134 | | 136 | |
|---|---|---|---|---|---|---|---|---|---|---|---|---|---|---|---|---|---|---|---|
| A | 10% 20 µs | - | - | - | - | 350 | 112 | - | - | - | - | - | - | - | - | - | - | - | - |
| | Multiple* | 2510 | 187 | 2458 | 191 | 32398 | 556 | 443773 | 2016 | 68392 | 779 | 359951 | 1816 | 453660 | 1946 | 176541 | 1275 | 146945 | 1166 |
| C | 10% 20 µs | - | - | 194 | 77 | - | - | - | - | - | - | - | - | - | - | - | - | - | - |
| | 10% 23 µs | - | - | - | - | - | - | - | - | - | - | - | - | - | - | - | - | - | - |
| | 10% 29 µs | 203 | 61 | 315 | 65 | - | - | - | - | 425 | 105 | 1056 | 225 | - | - | - | - | - | - |
| | 10% 39 µs | 110 | 117 | 621 | 153 | 1579 | 235 | 2340 | 340 | 1178 | 182 | 5132 | 367 | 2579 | 352 | 1056 | 231 | 371 | 201 |
| | 10% 60 µs | 213 | 83 | - | - | - | - | - | - | 209 | 111 | 494 | 235 | - | - | - | - | 192 | 152 |
| | 30% CW | - | - | - | - | - | - | 735 | 294 | 488 | 144 | 510 | 256 | 1118 | 309 | 546 | 197 | - | - |
| D | 10% 20 µs | - | - | - | - | 373 | 128 | 1118 | 255 | 330 | 114 | 1272 | 233 | 1201 | 256 | 528 | 160 | 485 | 152 |
| | 10% 23 µs | 103 | 72 | 75 | 65 | - | - | 1958 | 268 | - | - | 1781 | 253 | 2614 | 286 | 1270 | 185 | 551 | 152 |
| | 10% 29 µs | 199 | 102 | - | - | 1690 | 196 | 4262 | 343 | 1151 | 157 | 5713 | 344 | 3899 | 347 | 1709 | 219 | 1053 | 205 |
| | 10% 39 µs | 2714 | 207 | 4208 | 283 | 5961 | 275 | 9073 | 393 | 4157 | 234 | 21983 | 526 | 6998 | 372 | 2030 | 212 | 1803 | 199 |
| | 10% 60 µs | 374 | 91 | 254 | 61 | 1449 | 151 | 2361 | 262 | 870 | 126 | 4599 | 269 | 2468 | 268 | 1018 | 168 | 730 | 147 |
| | 30% CW | - | - | - | - | 759 | 135 | 820 | 244 | - | - | 898 | 217 | 1096 | 255 | 399 | 154 | - | - |
| F | 10% 20 µs | - | - | 106 | 54 | 206 | 105 | - | - | - | - | - | - | - | - | - | - | - | - |
| | 10% 23 µs | - | - | - | - | - | - | - | - | - | - | - | - | - | - | - | - | - | - |
| | 10% 29 µs | 127 | 75 | 132 | 65 | 177 | 104 | - | - | - | - | 721 | 201 | - | - | - | - | - | - |
| | 10% 39 µs | 471 | 99 | 862 | 119 | 1899 | 187 | 1476 | 285 | 989 | 139 | 5595 | 333 | 946 | 280 | 258 | 162 | 363 | 155 |
| | 10% 60 µs | - | - | 106 | 78 | 237 | 123 | - | - | 232 | 99 | - | - | - | - | - | - | - | - |
| | 30% CW | - | - | 160 | 66 | - | - | - | - | 238 | 94 | - | - | 520 | 231 | 468 | 156 | 233 | 121 |
| G | 10% 20 µs | - | - | - | - | - | - | - | - | - | - | - | - | - | - | - | - | - | - |
| | 10% 32 µs | 1138 | 130 | 2300 | 184 | 2817 | 195 | 4505 | 315 | 2132 | 163 | 10360 | 374 | 2439 | 286 | 693 | 167 | 777 | 152 |
| | 10% 57 µs | 529 | 102 | 1471 | 135 | 2098 | 168 | 2440 | 261 | 1545 | 131 | 7662 | 296 | 2026 | 259 | 452 | 156 | 465 | 136 |
| | 10% 83 µs | - | - | - | - | 122 | 120 | - | - | - | - | - | - | - | - | - | - | - | - |
| | 12% CW | - | - | - | - | 184 | 114 | - | - | 151 | 94 | - | - | - | - | 312 | 161 | - | - |
| | 20% CW | - | - | 133 | 71 | 316 | 111 | - | - | 208 | 84 | - | - | - | - | - | - | - | - |
| | 30% CW | - | - | - | - | 554 | 132 | - | - | 296 | 107 | - | - | - | - | - | - | - | - |
| H | 10% 20 µs | - | - | - | - | 174 | 108 | - | - | - | - | - | - | - | - | - | - | - | - |
| | 10% 23 µs | - | - | - | - | 5915 | 324 | 494 | 294 | 281 | 127 | - | - | 1285 | 313 | 748 | 202 | - | - |
| | 10% 23 µs | - | - | 106 | 64 | - | - | 884 | 255 | - | - | 877 | 220 | - | - | 736 | 171 | 642 | 146 |
| | 10% 29 µs | 86 | 60 | - | - | 168 | 108 | - | - | - | - | - | - | - | - | 383 | 152 | - | - |
| | 10% 99 µs | 204 | 70 | 290 | 78 | 410 | 123 | - | - | 275 | 102 | 1132 | 223 | - | - | 317 | 149 | - | - |
| | 30% CW | - | - | - | - | - | - | - | - | - | - | - | - | - | - | - | - | - | - |
| I | 10% 20 µs | 99 | 72 | - | - | - | - | - | - | - | - | - | - | - | - | - | - | - | - |
| | 10% 23 µs | - | - | - | - | - | - | - | - | - | - | - | - | - | - | - | - | - | - |
| | 10% 29 µs | - | - | - | - | - | - | - | - | - | - | - | - | - | - | 262 | 143 | - | - |
| | 10% 39 µs | - | - | 222 | 68 | 298 | 115 | 1651 | 252 | 423 | 103 | 1822 | 223 | 1219 | 249 | 866 | 155 | 526 | 134 |
| | 10% 60 µs | 1116 | 132 | 2008 | 177 | 2869 | 203 | 2785 | 291 | 1740 | 156 | 8268 | 345 | 1584 | 273 | 382 | 156 | 547 | 153 |
| | 10% 99 µs | - | - | 81 | 84 | 195 | 114 | - | - | - | - | - | - | - | - | - | - | - | - |
| | 30% CW | - | - | 152 | 80 | - | - | - | - | 161 | 90 | - | - | - | - | - | - | - | - |
| X | 10% 20 µs | - | - | 132 | 63 | - | - | - | - | 257 | 98 | 404 | 201 | - | - | 231 | 149 | 288 | 134 |
| | 10% 23 µs | - | - | - | - | - | - | - | - | - | - | - | - | - | - | - | - | - | - |
| | 10% 29 µs | - | - | - | - | - | - | - | - | 314 | 96 | 531 | 208 | - | - | - | - | - | - |
| | 10% 99 µs | 406 | 86 | 531 | 90 | 503 | 134 | 1227 | 270 | 838 | 130 | 2700 | 266 | 970 | 269 | 256 | 154 | 411 | 151 |
| | 30% CW | - | - | - | - | - | - | - | - | 152 | 106 | - | - | - | - | - | - | - | - |
| Multi-spherule | 10% 20 µs | - | - | - | - | - | - | - | - | - | - | - | - | - | - | - | - | - | - |
| | 10% 23 µs | - | - | - | - | - | - | - | - | - | - | - | - | - | - | - | - | - | - |
| | 10% 29 µs | - | - | 143 | 53 | 129 | 103 | 1707 | 261 | 377 | 99 | 1656 | 229 | 1525 | 262 | 357 | 149 | 618 | 142 |
| | 10% 39 µs | 462 | 86 | 510 | 88 | 1103 | 154 | 2730 | 286 | 860 | 127 | 4224 | 285 | 2537 | 287 | 725 | 169 | 772 | 152 |
| | 10% 60 µs | 926 | 118 | 1379 | 138 | 1739 | 168 | 2820 | 291 | 1155 | 142 | 5925 | 314 | 1510 | 273 | 394 | 154 | 447 | 142 |
| | 10% 99 µs | - | - | 146 | 69 | - | - | - | - | - | - | - | - | - | - | - | - | - | - |
| | 30% CW | - | - | - | - | - | - | - | - | - | - | - | - | - | - | - | - | - | - |
| RELAX Detection limit | | 0 | 23 | 0 | 18 | 761 | 41 | 3494 | 159 | 454 | 44 | 2693 | 120 | 3501 | 156 | 1271 | 73 | 1018 | 54 |

***5A.1*** *Blank corrected atoms of xenon isotopes measured from stepped heating of PCA 02007 with RELAX.*

| Stepped heating conditions | 124 | | 126 | | 128 | | 129 | | 130 | | 131 | | 132 | | 134 | | 136 | |
|---|---|---|---|---|---|---|---|---|---|---|---|---|---|---|---|---|---|---|
| 10% 20 µs | 608 | 78 | 634 | 73 | 10654 | 271 | 131657 | 945 | 21659 | 387 | 104909 | 846 | 126736 | 864 | 46144 | 555 | 37099 | 495 |
| 10% 22 µs | 7503 | 522 | 6920 | 507 | 128177 | 2063 | 1698144 | 6191 | 284055 | 3565 | 1299140 | 5667 | 1535379 | 4085 | 541150 | 3542 | 431664 | 3062 |
| 10% 22 µs | 483 | 65 | 379 | 59 | 8143 | 222 | 101026 | 801 | 17213 | 324 | 80220 | 712 | 97462 | 747 | 34611 | 461 | 28284 | 415 |
| 10% 24 µs | 10800 | 672 | 10972 | 698 | 185374 | 2808 | 2389551 | 8202 | 404106 | 4758 | 1817700 | 7273 | 2118429 | 4434 | 733179 | 4277 | 590815 | 3747 |
| 10% 24 µs | 561 | 73 | 644 | 73 | 10856 | 281 | 140614 | 1001 | 23815 | 439 | 112606 | 899 | 134614 | 914 | 48208 | 583 | 40013 | 530 |
| 10% 24 µs | 2182 | 182 | 1877 | 169 | 35889 | 653 | 492014 | 2163 | 81821 | 1151 | 388103 | 1978 | 467195 | 1657 | 167326 | 1251 | 136806 | 1122 |
| 10% 25 µs | 14389 | 873 | 14159 | 872 | 241885 | 3657 | 3013916 | 10782 | 512309 | 5953 | 2287598 | 9485 | 2589888 | 5794 | 900771 | 5448 | 716124 | 4764 |
| 10% 25 µs | 92 | 44 | 73 | 45 | 2471 | 148 | 27864 | 577 | 4646 | 204 | 23057 | 507 | 27854 | 572 | 9788 | 319 | 8715 | 300 |
| 10% 26 µs | 220 | 57 | 87 | 43 | 1626 | 110 | 17170 | 470 | 2734 | 145 | 13784 | 398 | 17349 | 467 | 6435 | 250 | 5274 | 228 |
| 10% 27 µs | 220 | 57 | 174 | 51 | 2677 | 146 | 28674 | 568 | 4713 | 198 | 23088 | 495 | 28781 | 563 | 10261 | 315 | 8176 | 283 |
| 10% 28 µs | 343 | 57 | 262 | 50 | 4508 | 160 | 54949 | 618 | 8867 | 224 | 43207 | 538 | 52450 | 593 | 18959 | 344 | 15309 | 311 |
| 10% 28 µs | 13695 | 809 | 14287 | 843 | 228146 | 3346 | 2926067 | 9199 | 454542 | 4755 | 2203715 | 8210 | 2534036 | 5511 | 913343 | 5155 | 735815 | 4463 |
| 10% 28 µs | 373 | 63 | 182 | 45 | 5462 | 194 | 69387 | 740 | 11426 | 282 | 54166 | 649 | 66471 | 708 | 24492 | 429 | 19181 | 380 |
| 10% 29 µs | 2718 | 184 | 2263 | 162 | 41451 | 698 | 540021 | 2121 | 91159 | 1057 | 429949 | 2000 | 518912 | 1589 | 191769 | 1312 | 155567 | 1163 |
| 10% 29 µs | 550 | 70 | 789 | 82 | 13362 | 313 | 171757 | 1084 | 28581 | 460 | 137661 | 986 | 166631 | 983 | 61895 | 656 | 49243 | 583 |
| 10% 29 µs | 6121 | 505 | 5658 | 478 | 81948 | 1628 | 1133755 | 5022 | 176335 | 2592 | 882509 | 4609 | 1071725 | 4010 | 384855 | 3007 | 313230 | 2694 |
| 10% 29 µs | 4080 | 295 | 4014 | 296 | 70343 | 1193 | 929802 | 3680 | 150792 | 1861 | 726141 | 3380 | 868428 | 2787 | 315389 | 2186 | 258899 | 1979 |
| 10% 30 µs | 7668 | 593 | 8044 | 599 | 125337 | 2132 | 1659100 | 6551 | 270346 | 3429 | 1269606 | 5826 | 1513773 | 4688 | 542314 | 3821 | 440069 | 3380 |
| 10% 30 µs | 728 | 75 | 525 | 61 | 10484 | 244 | 133566 | 864 | 21665 | 352 | 106157 | 774 | 127484 | 779 | 48169 | 515 | 38664 | 460 |
| 10% 31 µs | 2828 | 229 | 3005 | 236 | 48168 | 872 | 644223 | 2767 | 103823 | 1446 | 506174 | 2567 | 615882 | 2158 | 226015 | 1716 | 181801 | 1498 |
| 10% 31 µs | 119 | 51 | 98 | 49 | 2582 | 162 | 12010 | 475 | 1881 | 147 | 9333 | 400 | 12275 | 474 | 4703 | 257 | 3646 | 230 |
| 10% 33 µs | 4316 | 309 | 2836 | 212 | 64852 | 1095 | 865280 | 3399 | 140523 | 1753 | 681331 | 3124 | 820869 | 2504 | 301426 | 2067 | 242006 | 1811 |
| 10% 35 µs | 2572 | 233 | 2078 | 195 | 39504 | 794 | 535150 | 2632 | 86562 | 1229 | 425114 | 2424 | 513912 | 2216 | 185082 | 1598 | 149943 | 1428 |
| 10% 37 µs | 3413 | 251 | 3203 | 255 | 53940 | 957 | 714114 | 3040 | 115835 | 1454 | 565208 | 2802 | 687620 | 2332 | 250074 | 1838 | 202705 | 1637 |
| 10% 39 µs | 2197 | 172 | 1856 | 154 | 34026 | 636 | 454300 | 2068 | 72983 | 929 | 359128 | 1893 | 433357 | 1669 | 161172 | 1274 | 131296 | 1132 |
| 10% 42 µs | 3619 | 283 | 3521 | 280 | 51266 | 964 | 670805 | 3075 | 109675 | 1593 | 530579 | 2814 | 639654 | 2495 | 233665 | 1890 | 187494 | 1650 |
| 10% 45 µs | 2234 | 218 | 2326 | 230 | 32947 | 718 | 423042 | 2356 | 66380 | 1049 | 333703 | 2147 | 408572 | 2065 | 147819 | 1442 | 118548 | 1283 |

*Atoms in excess of blank + 3σ. Errors are σ instrumental counting errors in atoms. Heating conditions refer to laser pulse duration in µs per 10 kHz cycle and Fiber laser input power as percentage, CW refers to continuous wave, explained in Section 4.3.3.*

***5A.2** Blank corrected atoms of xenon isotopes measured from stepped heating of "Q" Vigarano II with RELAX.*

| Stepped heating conditions | 124 | | 126 | | 128 | | 129 | | 130 | | 131 | | 132 | | 134 | | 136 | |
|---|---|---|---|---|---|---|---|---|---|---|---|---|---|---|---|---|---|---|
| 10% 20 µs | 8637 | 673 | 8658 | 697 | 226070 | 4273 | 2299606 | 9177 | 299669 | 3447 | 1558537 | 7692 | 1828919 | 6539 | 672598 | 5008 | 549792 | 4380 |
| 10% 20 µs | 1483 | 156 | 1886 | 181 | 51771 | 1111 | 380804 | 2194 | 51944 | 837 | 268108 | 1883 | 332602 | 1872 | 128046 | 1344 | 103964 | 1180 |
| 10% 21 µs | 4793 | 363 | 4902 | 363 | 116346 | 2229 | 1258185 | 5066 | 166468 | 1923 | 885259 | 4344 | 1067290 | 3737 | 412829 | 3004 | 340799 | 2627 |
| 10% 21 µs | 2032 | 167 | 1982 | 170 | 46348 | 948 | 507762 | 2294 | 66664 | 858 | 363195 | 1985 | 447013 | 1821 | 173129 | 1413 | 143979 | 1241 |
| 10% 22 µs | 4516 | 299 | 4533 | 311 | 96255 | 1735 | 1200803 | 4100 | 163870 | 1614 | 855381 | 3563 | 1034311 | 2663 | 399001 | 2453 | 333800 | 2130 |
| 10% 22 µs | 2493 | 223 | 2392 | 226 | 54732 | 1141 | 658540 | 2979 | 89461 | 1148 | 478790 | 2622 | 583974 | 2388 | 222661 | 1819 | 185750 | 1609 |
| 10% 22 µs | 803 | 86 | 845 | 97 | 41362 | 832 | 530171 | 2207 | 73110 | 862 | 390258 | 1953 | 473612 | 1703 | 187472 | 1398 | 154586 | 1216 |
| 10% 23 µs | 5041 | 500 | 5261 | 552 | 101457 | 2296 | 1389422 | 6802 | 182715 | 2540 | 1018727 | 5919 | 1211819 | 5538 | 466066 | 4076 | 392607 | 3653 |
| 10% 23 µs | 3607 | 270 | 3201 | 252 | 64277 | 1252 | 860367 | 3352 | 117628 | 1307 | 634239 | 2950 | 761461 | 2452 | 295470 | 2057 | 249773 | 1818 |
| 10% 23 µs | 3021 | 240 | 2346 | 207 | 46806 | 977 | 637530 | 2764 | 89299 | 1088 | 483047 | 2475 | 569056 | 2176 | 223370 | 1725 | 187027 | 1519 |
| 10% 24 µs | 5917 | 518 | 5531 | 493 | 99529 | 2110 | 1340355 | 5997 | 183046 | 2313 | 1003634 | 5297 | 1179847 | 4727 | 456003 | 3623 | 382292 | 3221 |
| 10% 24 µs | 4723 | 304 | 3782 | 264 | 77790 | 1402 | 1022858 | 3466 | 143617 | 1378 | 773209 | 3113 | 916571 | 2284 | 359453 | 2157 | 299964 | 1857 |
| 10% 24 µs | 2807 | 225 | 2436 | 209 | 47570 | 980 | 628433 | 2692 | 88612 | 1062 | 480218 | 2414 | 573198 | 2118 | 223422 | 1692 | 188459 | 1500 |
| 10% 25 µs | 7763 | 603 | 6801 | 549 | 127621 | 2566 | 1682679 | 6983 | 231707 | 2707 | 1252048 | 6140 | 1491810 | 5328 | 567342 | 4199 | 473782 | 3692 |
| 10% 25 µs | 3866 | 301 | 2709 | 229 | 65332 | 1318 | 849753 | 3574 | 119320 | 1412 | 649031 | 3193 | 796429 | 2780 | 300171 | 2220 | 253161 | 1966 |
| 10% 25 µs | 3602 | 269 | 3075 | 240 | 66017 | 1279 | 869088 | 3382 | 120918 | 1324 | 659048 | 3024 | 802551 | 2492 | 306823 | 2113 | 255048 | 1836 |
| 10% 25 µs | 2758 | 236 | 2525 | 218 | 49138 | 1015 | 642559 | 2783 | 89659 | 1087 | 493799 | 2508 | 599202 | 2202 | 228321 | 1750 | 190458 | 1538 |
| 10% 25 µs | 6394 | 560 | 5372 | 492 | 99525 | 2178 | 1355236 | 6384 | 186539 | 2484 | 1011918 | 5584 | 1229242 | 5134 | 463287 | 3848 | 386244 | 3427 |
| 10% 25 µs | 2077 | 174 | 1847 | 163 | 36997 | 802 | 486987 | 2281 | 68775 | 896 | 371925 | 2047 | 457394 | 1879 | 174439 | 1445 | 146298 | 1280 |
| 10% 25 µs | 5598 | 356 | 4536 | 308 | 90572 | 1639 | 1159519 | 4011 | 168967 | 1641 | 895855 | 3625 | 1077026 | 2656 | 415729 | 2522 | 342469 | 2154 |
| 10% 26 µs | 3033 | 242 | 2777 | 226 | 50100 | 1004 | 659145 | 2706 | 93784 | 1079 | 509448 | 2447 | 625948 | 2099 | 238130 | 1724 | 197314 | 1504 |
| 10% 26 µs | 4110 | 294 | 3198 | 257 | 64689 | 1272 | 834447 | 3352 | 118895 | 1333 | 639214 | 3009 | 784239 | 2547 | 298011 | 2105 | 246260 | 1836 |
| 10% 27 µs | 5201 | 348 | 4016 | 294 | 90390 | 1666 | 1136892 | 4104 | 164524 | 1664 | 875426 | 3695 | 1056994 | 2848 | 405421 | 2570 | 340210 | 2241 |
| 10% 28 µs | 6277 | 527 | 4261 | 465 | 96988 | 2037 | 1312076 | 5760 | 179392 | 2238 | 1001334 | 5177 | 1215371 | 4589 | 453078 | 3527 | 378592 | 3130 |
| 10% 28 µs | 4355 | 289 | 3285 | 233 | 70588 | 1291 | 915738 | 3187 | 129212 | 1273 | 699105 | 2877 | 857491 | 2151 | 325373 | 2004 | 270484 | 1730 |

*Atoms in excess of blank + 3σ. Errors are σ instrumental counting errors in atoms. Heating conditions refer to laser pulse duration in µs per 10 kHz cycle and Fiber laser input power as percentage, CW refers to continuous wave, explained in Section 4.3.3.*